Effects of a Quasi-Static Variation of the Angle of Attack in the Ventilation Inception of a Surface-Piercing Hydrofoil

MSc Thesis

5756804
Carlos Navas Rodriguez

Delft University of Technology

TU Delft

(This page is intentionally left blank)

Effects of a Quasi-Static Variation of the Angle of Attack in the Ventilation Inception of a Surface-Piercing Hydrofoil

by

Carlos Navas Rodriguez

In partial fulfilment of the requirements for the degree of

Master of Science

In Marine Technology

at the Department of Maritime and Transport Technology, Faculty of Mechanical Engineering, Delft University of Technology.

to be defended publicly on Friday, January 10, 2025 at 14:00.

This thesis (MT.24/25.023.M) is classified as confidential in accordance with the general conditions for projects performed by TU Delft

Responsible Supervisors:	Dr. D. Fiscaletti,	TU Delft
Daily Supervisor:	Dr. G. Jacobi,	TU Delft
Thesis exam committee:		
Chair Member:	Dr. D. Fiscaletti,	TU Delft
Staff Member:	Dr. G. Jacobi,	TU Delft
Staff Member:	Dr. M. Aguiar Ferreira,	TU Delft
Staff Member:	Dr. Ir. Ido Akkerman,	TU Delft
Company Member:	L. Minerva,	MARIN
Project duration:	November 20, 2023 – January 10, 2025	
Student number:	5756804	

Cover: NACA0010-34 at FV Regime, $Fn_h = 2.5$, $AR_h = 1.0$

TU Delft

Acknowledgements

This dissertation constitutes my final work to obtain the Master in Marine Technology at Delft University of Technology. The research was performed in collaboration with the Ship Hydrodynamics Section of the University of Delft under the supervision of Danielle Fiscalleti and Gunnar Jacobi. My interest in hydrofoils stems from a lifelong passion for sailing, especially high-performance sailing, where hydrofoils play a critial role in enabling the boat's "flying" conditions. During my master's studies at TU Delft, I developed a strong enthusiasm for fluid dynamics, making the study of ventilation in hydrofoils an ideal research focus.

I would like to thank Gunnar Jacobi for his invaluable support before, during, and after the experimental campaign, as well as his willingness to answer all of my questions. My gratitude also goes to Danielle Fiscalleti for his guidance and patience and for allowing me to pursue my thesis on a topic aligned with my career aspirations.

A special thanks go to Manuel Ferreira for his guidance throughout the shared experimental campaign, his willingness to teach me and explain anything related to fluids and for being more than just a research colleague but someone I could rely on; I enjoyed the long hours in the towing tank. Also, a word of appreciation to Sedat, Jasper, Peter, Sebastian, Frits, Pascal, Angelica, and Tom for their dedication and hard work during the towing tank experiments. Their efforts made me feel fully integrated into the research team, and I am truly grateful for their support.

Finally, I am incredibly grateful to my family, my girlfriend and friends for their support throughout my academic journey. I am especially thankful to my parents, who have supported every decision I have made and whose effort and dedication made it possible for me to pursue my dreams in the Netherlands. I also want to thank the wonderful friends I met in Delft, especially "The Climbing Boys" and "The Gymbros," who made the journey of earning a master's degree more enjoyable. I truly cherished our Friday nights and the climbing sessions, which allowed me to take a break from the stresses of my studies.

I hope you enjoy reading this dissertation.

Carlos Navas Rodriguez
Delft, January 2025

Abstract

This thesis investigates the mechanisms of ventilation inception on surface-piercing hydrofoils under quasi-static variations of the angle of attack (AoA). Two hydrofoil geometries, a Semi-Ogive profile with a blunt trailing edge and a streamlined NACA 0010-34, were tested in a towing tank across a range of Froude numbers (Fn_h) and aspect ratios (AR). The study introduces a novel experimental methodology, quasi-static testing, which eliminates inertial effects associated with acceleration by maintaining constant Fn_h while varying AoA. This approach contrasts with traditional "static tests" found in the literature.

A new flow regime map in the $\alpha - Fn_h$ parametric space was developed, tracing distinct ventilation inception boundaries for the two hydrofoils and offering a more detailed representation of transitions between flow regimes. The findings challenge the validity of previous methodologies, which assumed that ventilation inception boundaries were dominated by stall angles and fixed AoA, overlooking the dynamics of ventilation inception. At low Fn_h, leading-edge (LE) ventilation appears as the dominant mechanism, slightly enhancing lift by stabilizing flow on the suction surface. As Fn_h increases, transitions to Rayleigh-Taylor (RT) instabilities become evident, particularly at moderate Reynolds numbers. At high Fn_h (≥ 2.5), RT instabilities prevail, with trailing-edge (TE) effects becoming significant for the Semi-Ogive hydrofoil. In contrast, the streamlined NACA 0010-34 primarily exhibits RT-driven mechanisms.

The results demonstrate that this new methodology yields precise and repeatable inception boundaries, representing a significant improvement over historical techniques. Notably, contrary to prior assumptions, the AoA at which ventilation inception occurs exceeds 15° and is no longer constant across various Fn_h. Additionally, trailing-edge geometry was found to influence ventilation inception, particularly at higher AR, as evidenced by the diverging trends observed between the two hydrofoil profiles. Furthermore, the experimental results align well with semi-empirical models for lift and drag coefficients at $Fn_h \geq 1.0$, reinforcing the robustness of the findings.

These contributions provide more in-depth insights into ventilation inception dynamics and offer valuable guidance for the design of hydrofoils in marine applications.

Contents

Acknowledgements i

Abstract ii

Nomenclature xii

1 Introduction 1
- 1.1 Introduction to Multi-phase Flow in Lifting Surfaces . . . 1
- 1.2 Background Information . . . 2
- 1.3 Problem Statement . . . 6
- 1.4 Research Objective . . . 7
- 1.5 Research Questions . . . 7
- 1.6 Plan of Approach . . . 7
- 1.7 Structure . . . 8

2 Theoretical Background 9
- 2.1 Introduction to hydrofoils . . . 9
- 2.2 Multi-phase Flows . . . 10
  - 2.2.1 Two-Dimensional Cavity Flows . . . 10
  - 2.2.2 Three-Dimensional Multi-Phase Flows . . . 11
- 2.3 Ventilation . . . 13
  - 2.3.1 Flow Regimes . . . 14
  - 2.3.2 Flow Stability . . . 17
  - 2.3.3 Hydrodynamic Loads . . . 18
  - 2.3.4 Ventilation Formation . . . 19
  - 2.3.5 Ventilation Elimination . . . 21
  - 2.3.6 Hysteresis of Ventilation . . . 23
  - 2.3.7 Scale Effects . . . 23
- 2.4 Geometry Definition . . . 24
  - 2.4.1 Previous Research Geometries . . . 24
- 2.5 Conclusion . . . 27
  - 2.5.1 Knowledge Gaps . . . 27

3 Experimental Approach 29
- 3.1 Hydrofoil Models and Fixture . . . 29
  - 3.1.1 Geometry Considerations . . . 29
  - 3.1.2 Semi-Ogive . . . 31
  - 3.1.3 NACA0010-34 . . . 32
  - 3.1.4 Geometry Comparison . . . 33
  - 3.1.5 Model Set-up . . . 34
- 3.2 Facilities . . . 35
- 3.3 Reference Frame . . . 35
- 3.4 Instrumentation, Alignment and Calibration . . . 36
  - 3.4.1 Force and Moment Measurements . . . 36
  - 3.4.2 Position and Angle Measurements . . . 38

3.4.3 Flow Speed and Droplet Release Measurement . . . 38
3.4.4 Setup Alignment . . . 39
3.4.5 6-DOF Calibration . . . 41
3.4.6 Camera Systems and Synchronization . . . 43
3.4.7 Stereo Camera Calibration . . . 45
3.4.8 Data Acquisition System . . . 45
3.4.9 Instrumentation overview . . . 46
3.5 Force Predictions . . . 46
3.6 Method . . . 49
3.6.1 General Considerations . . . 49
3.6.2 Static Tests . . . 50
3.6.3 Quasi-Static Tests . . . 51
3.6.4 Experimental Matrix . . . 55
3.7 Post-processing . . . 55
3.7.1 Filtering . . . 56
3.7.2 Force Rotation . . . 56
3.7.3 Ventilation . . . 56
3.8 Uncertainty Analysis . . . 56

4 Results **59**
4.1 Semi-Ogive Validation . . . 59
4.2 Flow Regimes . . . 62
4.2.1 $AoA - Fn_h$ inception boundary . . . 63
4.2.2 Repeatability of the AoA . . . 64
4.2.3 Flow Regime Transition . . . 65
4.3 Ventilation Inception Mechanisms . . . 67
4.3.1 Types of inception mechanisms . . . 67
4.3.2 Triggering Mechanisms . . . 70
4.3.3 Influence of the Fn_h and Re_c on the Inception Mechanisms . . . 76
4.3.4 Influence of the Inception Mechanisms and Fn_h on the AoA . . . 80
4.4 Integration of Past Experimental Results - Flow Regime Map . . . 80
4.5 Lift and Drag Semi-empirical Formulation . . . 82
4.5.1 Semi-empirical Lift and Drag Formula . . . 83
4.5.2 Comparison with Experimental C_L and C_D . . . 85

5 Conclusions and Recommendations **88**
5.1 Conclusions on the Research Question . . . 88
5.2 Future Recommendations . . . 91

References **93**

A Foil Theory **97**
A.1 Kutta-Joukowki Theorem . . . 97
A.1.1 Thin foil theory . . . 98
A.2 Lifting-line theory . . . 99
A.3 Foil Characteristics . . . 100
A.3.1 Characteristic Graphs of a foil . . . 100

B Construction Drawings **103**
B.1 Semi-Ogive Hydrofoil . . . 103
B.2 NACA0010-34 Hydrofoil . . . 110

C Experimental Run Log **115**

List of Figures

2.1 The geometry of a 2D foil. Reprinted from Kulkarni et al. [44] 10
2.2 Flow regimes of a 2D foil section.(a) Fully wetted, (b) Base-cavitation or base-ventilation, (c) Partial-cavitation or partial ventilation, (d) Supercavitation or super-ventilation. Figure reproduced from Young et al. [6]. 11
2.3 Coordinate system for a surface-piercing Hydrofoil. Figure reprinted from Elisa [45]. 12
2.4 Drawdown to chord length ratio, d/c. Figure reprinted from Swales et al. [12] . 13
2.5 Reflection of oncoming flow by the closure line of the cavity. Figure reprinted from Harwood [15] with modifications from De lange and De Bruin [46]. 14
2.6 Representation of the re-entrant jet on spanwise-varying cavity. Figure reprinted from Harwood [15]. 15
2.7 Fully wetted (FW) flow over the suction surface. Figure reproduced from Harwood et al. [2]. 15
2.8 Partial ventilated (PV) flow. Figure reproduced from Harwood et al. [2]. 16
2.9 Fully ventilated (FV) flow. Figure reproduced from Harwood et al. [2]. 16
2.10 Partially cavitating (PC) flow. Figure reproduced from Harwood et al. [2]. . . 16
2.11 Stability map for a hydrofoil with $AR_h = 1.0$ with overlaid transition events. The flows are plotted as a function of the AoA and Fn_h. Figure reprinted from Harwood [15]. 17
2.12 The hysteresis loop in the characteristic lift curved and the stability map. Reprinted from Young et al. and Fridsma [6] [20]. 18
2.13 Ventilation formation and elimination mechanisms on a surface-piercing hydrofoil. Figure reprinted from Young et al. [6] 21
2.14 Representation of the cavity closure line. Figure reprinted from Harwood et al. [1] 22
2.15 Formation points in $\alpha - Fn_h$ space. Data from previous studies are plotted as symbols: H, Y & C: Harwood et al. (2016) [2]; H, Q & Z: Huang et al. (2022) [27]; B & S: Breslin and Skalak (1959) [7]; R, M & W: Rothblum et al. (1969) [11]; W: Waid (1968) [16]; S & W: Swales et al. (1974) [12]; We: Wetzel (1957) [9]; K: Kiceniuk (1954) [19].[1] Tests conducted at atmospheric pressure. [2] Tests conducted at reduced pressure. 25
2.16 Zoom-in view of inception points in $\alpha - Fn_h$ space. 26
2.17 Inception points in $\alpha - Fn_h$ space. Data from previous studies are plotted as symbols and grouped depending on the geometry: H, Y & C: Harwood et al. (2016) [2]; H, Q & Z: Huang et al. (2022) [27]; B & S: Breslin and Skalak (1959) [7]; R, M & W: Rothblum et al. (1969) [11]; W: Waid (1968) [16]; S & W: Swales et al. (1974) [12]; We: Wetzel (1957) [9]; K: Kiceniuk (1954) [19].[1] Tests conducted at atmospheric pressure. [2] Tests conducted at reduced pressure. . . 27
2.18 Zoom-in view of inception points in $\alpha - Fn_h$ space. Data from previous studies are plotted as symbols and grouped depending on the geometry. 28
2.19 Zoom-in view of inception points in $\alpha - V$ space. Data from previous studies are plotted as symbols and grouped depending on the geometry 28

3.1 Cross-section shape of the Semi-ogive Hydrofoil. Figure reproduced from Harwood et al. [2]. 31
3.2 Construction process of the Semi-Ogive Hydrofoil. 32
3.3 Cross-section shape of the Semi-ogive Hydrofoil with structural characteristics. 32
3.4 The process of painting the Semi-Ogive hydrofoil. 33
3.5 Cross-section shape of the NACA0010-34 Hydrofoil. 34
3.6 Cross-section shape of the NACA0010-34 Hydrofoil with structural characteristics 34
3.7 Comparison of the hydrofoil models cross-section shapes. 34
3.8 Rendering of the experimental setup underneath the carriage and the main variables that define the flow. The coordinate system used in the experiments is set at the coordinate system of the force balance. The X-axis is pointing upstream, and the Y-axis is in the direction of positive lift. The direction of the Z-axis follows the right-hand rule. 35
3.9 Grid on the foil suction surface of model NACA0010-34. The grid waterline is thicker for a better measurement. 36
3.10 Experimental setup featuring the positioning of the semi-ogive hydrofoil and the camera module The NACA0010-34 hydrofoil is arranged in the same configuration. 37
3.11 Towing Tank No.1. [49] 38
3.12 Reference frame detailed representation in the Semi-ogive hydrofoil 39
3.13 Force measurement instruments 40
3.14 6-DOF configuration 41
3.15 Signal amplifiers and data acquisition (DAQ) system used to amplify and capture force measurements from multiple sensors. 42
3.16 Certus reference plate 42
3.17 6-DOF Gauge Calibration 43
3.18 Cameras module for both underwater and above-water views The underwater cameras are mounted on torpedo-shaped structures equipped with streamlined bodies to minimize wave interference. Additional instrumentation, such as LED strips, is also shown. 44
3.19 Views from LaVision® cameras installed during the experimental campaign. Both cameras look at the suction side of the hydrofoil. 45
3.20 Views from Basler® cameras installed during the experimental campaign. Both cameras look at the suction side of the hydrofoil. 46
3.21 Programmable Timing Unit that controls the trigger signals received by the cameras. 47
3.22 Type 31 3D calibration plate in front of the hydrofoil. 48
3.23 Schematic overview of the intruments 49
3.24 Predicted forces for the load gauges in the 6-DOF force balance across a range of configurations from 0 to 90 degrees. 50
3.25 Experimental procedure performed by Harwood et al. [2], illustrated in the $\alpha - Fn_h$ parametric space. The two stages are represented as acceleration (red) and deceleration (blue). The inception boundary is based on experiments by Harwood et al. [2]. 51
3.26 Experimental procedure illustrated in the $\alpha - Fn_h$ parametric space. The three stages are represented as follow: acceleration (green), AoA variation (red) and deceleration (blue). The inception boundary is based on experiments by Harwood et al. [2]. 52

3.27 Variations in AoA and speed throughout run 1152. Green dots represent the acquired images, and the horizontal line indicates the point of ventilation inception. The three stages are denoted as acceleration (Acc), AoA variation (AoA var) and deceleration (Decel). White and grey backgrounds indicate a transition within stages. 53
3.28 Measured hydrodynamic lift and drag for the NACA hydrofoil at an $AR = 1$ and $Fn_h = 1.5$, for the "Static" and "Quasi-static" tests. The data is fitted with a linear trend for lift and quadratic for drag. 54
3.29 Measured hydrodynamic lift and drag for the Semi-ogive hydrofoil at an $AR = 1$ and $Fn_h = 1.5$, for the "Static" and "Quasi-static" tests. The data is fitted with a linear trend for lift and quadratic for drag. 54

4.1 Measured hydrodynamic lift and drag coefficients for the semi-ogive hydrofoil at an $AR = 1$ and $Fn_h = 1.5$, compared against historical experimental data under identical conditions and geometry. The experimental data aligns within an 8% uncertainty band around the polynomial fit of Harwood et al. [2] data. H, Y & C: Harwood et al. (2016) [2]. 60
4.2 Measured hydrodynamic lift and drag coefficients for the semi-ogive hydrofoil at an $AR = 1.5$ and $Fn_h = 1.5$, compared against historical experimental data under identical conditions and geometry. The experimental data aligns within an 8% uncertainty band around the polynomial fit of Harwood et al. [2] data. H, Y & C: Harwood et al. (2016) [2]. 61
4.3 Rayleigh-Taylor (RT) ventilation inception observed during the acceleration phase by Harwood et al. [2], with an aspect ratio, $Ar_h = 1.5$. The Froude number, Fn_h, represents the value at the instant of each photograph. 62
4.4 Rayleigh-Taylor (RT) ventilation inception observed during the acceleration phase at an angle of attack, $\alpha = 12°$, with an aspect ratio, $Ar_h = 1.5$, Run 1108. The Froude number, Fn_h, represents the value at the instant of each photograph. This approach follows the methodology described by Harwood et al. [2]. 63
4.5 Ventilation inception angle of attack as a function of the depth Froude Number for $AR = 1$. The hatched region indicates the transition between PV and FV regimes. Uncertainty on the measurement is plotted as a shaded area on each point. 64
4.6 Ventilation inception angle of attack as a function of the depth Froude Number for $AR = 1.5$. The hatched region indicates the transition between PV and FV regimes. Uncertainty on the measurement is plotted as a shaded area on each point. 64
4.7 Visualization of the flow transition for the Semi-Ogive hydrofoil at various Fn_h with $AR = 1$. Each frame represents the flow state for each tested Fn_h value after ventilation, showing the progressive transition from partially ventilated (PV) to fully ventilated (FV) regimes. 66
4.8 Schematic of LE ventilation inception across different Froude numbers. The blue lines represent streamlines, highlighting the flow field around the hydrofoil. Green areas with hatching indicate regions of entrained air. Black hatching denotes boundary layer separation zones, and red arrows show the paths of air ingress. T_0 represents the moment of inception. The diagram is inspired by the schematics in Harwood et al. [2]. 67

4.9 Leading edge - LSB ventilation inception, $Fn_h = 0.5$; $AR_h = 1$; Run 1024; Semi-Ogive. The time is given at the instant of each photograph relative to the initiation of the mechanism. 68
4.10 Leading edge ventilation inception, $Fn_h = 1.0$; $AR_h = 1$; Run 1036; Semi-Ogive. The time is given at the instant of each photograph relative to the initiation of the mechanism. 68
4.11 Leading edge ventilation inception, $Fn_h = 1.25$; $AR_h = 1$; Run 1058; Semi-Ogive. The time is given at the instant of each photograph relative to the initiation of the mechanism. 69
4.12 Schematic of Rayleigh-Taylor ventilation inception. T_0 represents the moment of inception and T_1 is when enough air has entered for ventilation to trigger. The diagram is inspired by the schematics in Harwood et al. [2]. 69
4.13 Rayleigh-Taylor ventilation inception, $Fn_h = 2.0$; $AR_h = 1$; Run 2042; NACA 0010-34. The time is given at the instant of each photograph relative to the initiation of the mechanism. 70
4.14 Rayleigh-Taylor ventilation inception, $Fn_h = 2.0$; $AR = 1$; Run 1086; Semi-Ogive. The time is given at the instant of each photograph relative to the initiation of the mechanism. The white circles show the droplet's instability, and the red arrows indicate the flow direction. 71
4.15 Schematic of tip-vortex ventilation inception. The diagram is inspired by the schematics in Harwood et al. [2]. 72
4.16 Schematic of TE ventilation inception. The diagram is inspired by the schematics in Harwood et al. [2]. 72
4.17 Tip-Vortex inception, $Fn_h = 2.5$; $AR_h = 1$; 1090; Semi-Ogive. The time is given at the instant of each photograph relative to the initiation of the mechanism. . 72
4.18 RT-TE inception, $Fn_h = 2.5$; $AR_h = 1$; 1090; Semi-Ogive. The time is given at the instant of each photograph relative to the initiation of the mechanism. . . . 72
4.19 LE-LSB ventilation inception, $Fn_h = 0.75$; $AR_h = 1$; Run 2050; NACA 0010-34. The flow can be seen as instabilities grow near the leading edge. The time is given from the start of the recording. 73
4.20 LE ventilation inception, $Fn_h = 1$; $AR_h = 1$; Run 1036; Semi-Ogive. The run-up can be seen to collapse onto the LE. The red circle indicate the perturbation that ultimately triggers ventilation. The time is given from the start of the recording. 74
4.21 LE ventilation inception, $Fn_h = 1.5$; $AR_h = 1$; Run 1038; Semi-Ogive. The run-up can be noticed to be releasing droplets toward the free surface and the LE. The red circle indicate the perturbation that ultimately triggers ventilation. The time is given from the start of the recording. 75
4.22 The surface drawdown ratio, d/c, at the point of ventilation inception is presented as a function of Fn_h and U for both hydrofoil shapes (Semi-Ogive and NACA 0010-34) and aspect ratios (AR). 77
4.23 Inception Mechanisms as a Function of Froude Number fpr $AR = 1$ and $AR = 1.5$. Each dot represents an experimental run, excluding those without camera availability. The graph distinguishes two primary mechanisms and three combinations: LE-LSB (Leading Edge inception by laminar separation bubble), LE (Leading Edge inception), LE-RT (Combined Leading Edge and Rayleigh-Taylor inception), RT (Rayleigh-Taylor inception), and RT-TE (Combined Rayleigh-Taylor and Trailing Edge inception). 78

4.24 Ventilation inception angle as a function of the chord Reynolds Number. Hatched lines indicate a transitional region were there is a combination of LE and RT ventilation 79
4.25 Frame prior to ventilation, $Fn_h = 1.5$; $AR_h = 1$; Run 1090, Run 2132. The ventilated wake behind the Semi-ogive can be noted, while there is no wake behind the NACA profile. 79
4.26 Ventilation inception angle of attack as a function of the depth Froude Number for $AR = 1$. The arrows indicate the trends of the AoA as a function of the Fn_h and the inception mechanism. 81
4.27 Ventilation inception angle of attack as a function of the depth Froude Number for $AR = 1.5$. The arrows indicate the trends of the AoA as a function of the Fn_h and the inception mechanism. 81
4.28 Flow regime map for the Semi-Ogive hydrofoil as a function of α and Fnh at a fixed aspect ratio of $AR_h = 1.0$. The inception boundary delineates the transition between fully wetted and partial or full ventilation regimes. Symbols mark experimentally observed boundaries for the Semi-Ogive hydrofoil, including boundaries documented in previous research by Harwood et al. [2] marked as H, Y & C. The dashed lines indicate projected trends for the inception and bifurcation boundaries based on empirical data. This figure is adapted from Harwood et al. [2]. 83
4.29 Fow regime map for the Semi-Ogive hydrofoil as a function of α and Fnh at a fixed aspect ratio of $AR_h = 1.5$. Data are from the experimental campaign and previous research [2]. Figure inspired from Harwood et al. [2]. 84
4.30 Maximum lift coefficients at the ventilation inception boundary, $(C_{L_{incep}})$, as a function of the Froude number, (Fn_h), for both hydrofoil geometries (Semi-Ogive and NACA 0010-34) and aspect ratios ($AR_h = 1$ and $AR_h = 1.5$). The plot includes a predicted curve at atmospheric pressure, calculated using Equation 4.5. 85
4.31 Maximum drag coefficients at the ventilation inception boundary, $(C_{D_{incep}})$, as a function of the Froude number, (Fn_h), for both hydrofoil geometries (Semi-Ogive and NACA 0010-34) and aspect ratios ($AR_h = 1$ and $AR_h = 1.5$). The plot includes a predicted curve at atmospheric pressure, calculated using Equation 4.4. 86
4.32 Maximum lift coefficients at the ventilation inception boundary, $C_{L_{incep}}$, as a function of the Froude number, Fn_h. This figure compares the experimental results with prior experimental data. Harwood: Harwood et al. [2], Breslin: Breslin & Skalak [7], Vaughan & Ramsen [51], Swales: Swales et al. [12]. Reprinted with modifications from Damley-Strnad et al. [48]. 87

A.1 Superposition of flow around a foil 98
A.2 Superposition of an infinite number of horseshoe vortices along the lifting line. Reprinted from Anderson [53]. 99
A.3 Elliptic loading and constant downwash. Reprinted from Anderson [53]. 99
A.4 Schematic of lift-coefficient variation with angle of attack for an airfoil. Figure reproduced from Anderson[53]. 100
A.5 Schematic of the variation of lift-to-drag ratio with angle of attack. Reprinted with modifications from Anderson et al. [53] 101

List of Tables

1.1 Summary of previous studies on natural ventilation at surface-piercing and submerged hydrofoils and strut-foil systems. The facility types are keyed as follows: TT-towing tank, FSWT-free surface water tunnel, RAT-rotatory arm tank, DPTT-depressurized towing tank, FSCC-free surface cavitation channel, and NS-numerical solver. When the values of the parameters were not explicitly given, they are inferred from the respective reports. Reprinted with modifications from Harwood et al. [2] 6

3.1 Foil Characteristics 29
3.2 Tabulated material properties of hydrofoil construction materials 31
3.3 Tabulated physical properties of the two tested hydrofoils. The moments of inertia and rigidities are calculated only for the structural RHS reinforcements. 33
3.4 Load cell configuration in the 6-DOF load gauge 37
3.5 Corrections applied to the Hexapod configuration 41
3.6 Cell gauge full-range 49
3.7 List of static tests. The angle of attack is fixed at this test. 50
3.8 Relative error in the Lift-AoA slope 54
3.9 Test Conditions at $AR = 1$ for the Semi-ogive and NACA0010-34 hydrofoils, respectively. 55
3.10 Test Conditions at $AR = 1.5$ for the Semi-ogive and NACA0010-34 hydrofoils, respectively. 55
3.11 Test matrix 55
3.12 Estimated uncertainties in baseline variables, measured and derived quantities. Baseline variables and measured quantities are obtained a 95% confidence interval. 58

4.1 Measured percentage deviation between the experimental results and Harwood's data. 62
4.2 Measured $\overline{\alpha_i}$, σ, and σ_M for the Semi-Ogive and NACA 0010-34 hydrofoils at various Fn_h across test conditions for $AR = 1$. 65
4.3 Measured $\overline{\alpha_i}$, σ, and σ_M for the Semi-Ogive and NACA 0010-34 hydrofoils at various Fn_h across test conditions for $AR = 1.5$. 65

C.1 Run list - Fixed Angle of Attack 116
C.2 Run List - Angle of Attack Quasi-Static Variation 117

Nomenclature

Abbreviations

Abbreviation	Definition
AoA	Angle of Attack
CFD	Computational Fluid Dynamics
DAQ	Data Acquisition System
FV	Fully Ventilated
FW	Fully Wetted
LE	Leading Edge
OLS	Ordinary Least-Squares
PC	Partially Cavitating
PV	Partially Ventilated
PTU	Programmable Timing Unit
RT	Rayleigh-Taylor
TE	Trailing Edge
6DOF	6 Degrees of Freedom
3DOF	3 Degrees of Freedom

Symbols

Symbol	Definition	Unit
a	Acceleration	[m/s^2]
AR	Aspect ratio	-
AR_h	Immersed aspect ratio	-
A_s	Section Area	[mm^2]
c	Chord length	[m]
C_D	Drag coefficient	-
C_L	Lift coefficient	-
C_M	Moment coefficient	-
D	3D Drag Force	[N]
d	Free surface Drawdown	[m]
E	Young's Modulus	[GPa]
Fn_c	Chord-wise Froude number	-
Fn_h	Immersion depth Froude number	-
f	frequency	[s^{-1}]
Fn	Froude number	-
F_x	Force in x-direction (Drag)	[N]
F_y	Force in y-direction (Lift)	[N]
G	Shear Modulus	[GPa]

Symbol	Definition	Unit
g	Gravitational acceleration	[m/s^2]
h	Immersion depth	[m]
I_x	Moment of inertia in x-direction	[cm^4]
I_t	Moment of inertia in y-direction	[cm^4]
L	3D Lift force	[N]
L_c	Cavity length	[m]
M	Yaw Moment	[N/m]
Ma	Mach number	-
m	mass	[kg]
P	Pressure	[Pa]
Re	Reynolds Number	-
R	Nose radius	[deg]
s	Span	[m]
T_w	Water temperature	$^\circ C$
t	thickness	[mm]
V	Velocity	[m/s]
We	Weber number	-
z'	Cavity depth	[m]
α	Angle of attack	[deg]
α_b	Bifurcation angle	[deg]
$\Delta\sigma$	Cavitation number	-
α_i	Inception angle	[deg]
θ	Local angle of cavity closure line	[deg]
ρ	Density	[kg/m^3]
Γ	Sectional bound circulation	[m^3/s]
γ	Surface tension	[N/m]
ν	Poisson Ratio	-
κ	Length from free surface to L_c	[m]
σ	Cavitation number	-
σ_y	Yield Strength	[MPa]

1

Introduction

The maritime industry constantly evolves, with increasing demands for faster, more efficient, and environmentally sustainable vessels. Among the new technologies are larger ship propellers and hydrofoils, designed to enhance propulsion efficiency and reduce hydrodynamic drag. However, as these technologies advance, they bring new challenges, particularly in multi-phase flow phenomena such as ventilation. Ventilation, where air is drawn into the water around a propeller or hydrofoil, can lead to significant performance losses, including reduced lift and potential structural damage. These effects are more likely to happen in surface-piercing hydrofoils, which operate near the water's surface and are highly susceptible to ventilation.

The Ship Hydrodynamics Section of Delft University of Technology aims to address these challenges by studying the multi-phase phenomenon of ventilation around surface-piercing hydrofoils. This research focuses on designing and building experimental models to conduct tests in the Towing Tank, developing a new experimental methodology to study ventilation inception, and acquiring images to visually classify the transitioning regimes. A quasi-static variation of the angle of attack (AoA) while maintaining a constant Froude number (Fn_h) is proposed as an innovative methodology to study ventilation inception.

The selected geometry for these experiments is a semi-ogive strut, previously studied by Harwood et al. [1, 2]. Additionally, an experimental campaign will be conducted in parallel with a modified NACA0010-34 hydrofoil to study the influence of waves on ventilation inception for leading edge (LE) and Rayleigh-Taylor (RT) inception mechanisms. The calm water data from these experiments will be used in this research to provide a comprehensive understanding of ventilation phenomena.

This research is motivated by the need to fill the gaps in our understanding of ventilation and improve our ability to predict it for designing and operating more efficient and durable hydrofoils and propellers. The insights gained from this study are expected to improve the existing knowledge of ventilation and contribute to the reliability and performance of high-speed marine vessels.

1.1. Introduction to Multi-phase Flow in Lifting Surfaces

Multi-phase flows are systems consisting of two or more thermodynamic phases. These phases can include combinations of liquids, gases, and solids [3]. Phase distribution, interface dynamics, and phase change processes influence these phases' behaviour and interactions. Common

examples include liquid-gas mixtures, liquid-solid suspensions, and gas-solid flows [3]. Multi-phase phenomena involve interactions between a solid surface, such as a foil, and multiple fluid phases, typically liquid and gas, leading to complex and often undesirable performance, stability, and durability effects. Typical multi-phase flows in lifting surfaces are ventilation and cavitation [3].

Ventilation is a multi-phase phenomenon where atmospheric air is drawn into the liquid flow around fully or partially submerged bodies, such as hydrofoils or high-speed watercraft. This can occur due to surface piercing, where part of the lifting surface moves through the air-water interface, or due to pressure differences that draw air into the water [4, 5]. The resulting air cavities persist due to the continuous supply of atmospheric air, leading to equalization of pressure within the cavity to atmospheric pressure [6]. This process can lead to significant losses in lift force, reductions in speed, maneuverability, and stability [7, 8]. For ventilation to occur, the local pressure on the suction side of the body must be lower than atmospheric pressure, there must be a separated flow region, and a continued path for air ingress must be available [7, 9, 10, 11, 12].

Cavitation is the formation and collapse of vapour bubbles in a liquid due to a local drop below the liquid's saturated vapour pressure [13, 11, 14]. When these vapour bubbles collapse, they can generate significant pressure pulses, leading to noise, vibration, and potential damage to the lifting surface. Unlike ventilation, which involves non-condensable gas, cavitation involves the transition between liquid and vapour phases through vaporization and condensation. Thus, dynamics involving ventilated and vaporous cavities may vary [15]. Vaporous cavitation can also promote the inception of atmospheric ventilation, and the two phenomena can coincide [10, 11, 16, 12, 17, 15]. However, these conditions require sufficiently high speeds for the cavity pressure to decrease until the vapour pressure of the fluid or a forced decrease in pressure within the cavity prompts cavitation.

1.2. Background Information

Experimental studies on ventilation were extensively conducted during the 80ies and 90ies, and in recent years, there has been a renewed focus on understanding and predicting ventilation phenomena. Various researchers identified the conditions under which ventilation develops and its effect on hydrofoils and surface-piercing bodies. A summary of previous studies is presented in Table 1.1.

In the early studies, Perry [18] focused on understanding the forces and ventilation mechanisms on struts that pierce the water surface. They found that if the surface tension was broken, the aerated wake behind the bluff bodies could affect the entire body's ventilation. Similarly, Kiceniuk [19] observed the same behaviour in streamlined bodies when the angle of attack reached or exceeded the stall angle. Both studies observed that once the cavity was established, it remained stable across various angles, including sub-stall angles of attack. The ventilated cavity was initially created by air entering into low-pressure regions of the separated flow. However, if the cavity was sufficiently big, a new stable state was reached, with a cavity developing beyond the original wetted zone and original wake.

Wetzel [9] conducted fundamental experiments using various cylindrical rods and NACA profiles to investigate the scale effects associated with ventilation phenomena. Surface tension and viscosity were altered by heating the water and adding detergents. This was done to study their impact on the transition between wetted and ventilated flows. The results indicated that both Reynolds and Weber numbers significantly influence this transition, particularly for

small rods. Harwood [15] indicated that the effect of the Weber number was negligible above a critical value of $We = \rho_f U^2 l/\gamma \approx 250$. Wetzel [9] described two types of ventilation: "flash" and "creeping." "Flash" ventilation occurred suddenly and was associated with a noticeable hysteresis effect, especially in small-diameter rods and at angles below the stall boundary. In contrast, "creeping" ventilation occurred at angles of attack surpassing the stall angle, with the air pocket forming gradually. Wetzel [9] found that creeping ventilation could be correlated with the depth-based Froude number and the submergence ratio. This type of ventilation was linked to a critical Froude number of approximately 1.7 and occurred particularly in larger diameter rods or smaller rods at higher submergence ratios.

Wadlin [10] performed experiments on a surface-piercing strut to understand the relation between ventilation and boundary layer separation. Wadlin used an oil-flow technique to reveal areas of high-energy attached flow and low-energy-separated flow on the suction side. The results showed that laminar separation bubbles (LSB) form near the leading edge at low angles of attack, and turbulent separation occurs near the trailing edge at higher angles of attack. However, these separated regions did not extend to the free surface. Wadlin injected air artificially into the separated flow, creating a cavity of the same size as the preceding LSB. Wadlin concluded that both low pressure and separated flow are required for ventilation to occur. Wadlin highlighted the importance of considering the scale effect when interpreting the experimental results. The behaviour observed in model tests did not translate to a full-scale condition. Finally, they suggested that for ventilation to start, a low-pressure path had to be available to allow air ingress into the cavity.

Breslin and Skalak [7] conducted investigations on yawed surface-piercing hydrofoils, both with and without cambered sections. They reported a significant reduction in lift (up to 70%) and a smaller reduction in drag during ventilated flow. The study introduced the terms "inception" and "closure" to describe the generation and disappearance of ventilation. Their findings corroborate the observations made by Kiceniuk [19] and Wetzel [9], showing that ventilation could be triggered at sub-stall angles by disturbing the free surface upstream of the hydrofoil's leading edge. Additionally, it was documented that cavities remained stable even if the yaw angle decreased towards zero degrees, an effect also noted by Fridma [20], who termed this hysteresis range as "unstable". Breslin's report introduced two Froude-number-based criteria for achieving stable ventilated flow. These are:

$$C_{L_w} \geq 5Fn_h^{-2} \tag{1.1}$$

$$Fn_h \geq 3. \tag{1.2}$$

Rothblum et al. [11] conducted high-speed experiments on a family of symmetric biogival-section hydrofoils, observing the same types of ventilation as Breslin and Skalak [7]. Rothblum noted that hysteresis caused the ventilated flow to persist down for a zero-degree angle of attack. At high speeds, significant reversal of side forces occurred on surface-piercing struts, with ventilation most likely to occur on blunt-nosed struts. Rothblum suggested that at moderate angles of attack, flow over the hydrofoil's suction surface induced a downward acceleration of the free surface, creating Taylor instabilities, which are fluid instabilities caused by surface waves, leading to the growth of disturbances and potentially turbulent motion in the direction of the denser fluid (Emmons et al. [21]). Additionally, Rothblum defined boundaries for different foil shapes and configurations based on the lift coefficient and Froude number, illustrating the conditions under which fully-ventilated flows remained stable. The same biogival family was used in the experiments conducted by Waid [16], who studied the interaction of ventilated and vaporous cavities in a depressurized towing tank. The main mechanism for air ingress

was observed to be through Taylor's instabilities. These findings suggest that Taylor-induced ventilation formation or RT inception occurs only at high Froude or low cavitation numbers.

Rothblum [22] studied the effects of surface roughness, surface wettability, and speed on the formation of ventilated cavities using various section profiles with different surface coatings and finishes. The study determined that roughened surfaces and higher speeds weaken the sealing effect of the unseparated flow at the free surface. These findings are supported by Fuwa et al. [23], who found similar results. They reported that surface roughness affected drag, particularly the frictional drag component, due to boundary layer transition. Additionally, Fuwa's study highlighted that surface roughness increased the wetted area and contributed to higher frictional drag. Rothblum's study suggested that surface wettability and surface tension were negligible factors.

Swales et al. [12] used the same models as Rothblum et al. [11]. The main findings indicated that sub-atmospheric pressures and flow separation preceded ventilation formation. They identified two requirements for sustaining ventilation: pressure below atmospheric levels on the suction side and flow separation around the foil. Swales reported that Taylor instabilities induced ventilation for streamlined sections, whereas sharp-nosed sections ventilated through a long leading-edge bubble and an associated leading-edge vortex, termed "nose inception."

More recent studies have delved into the transitional region and the underlying physics of the ventilation phenomenon. Pogozelski et al. [24] investigated flow structures around a surface-piercing symmetric body, finding that at low Froude numbers, the bow wave exhibited capillary waves that became unstable with higher Froude numbers. At $Fn_L > 0.357$, the bow wave separated at the toe, generating a bubbly wake. The wave contained strong counter-rotating vorticity, leading to boundary layer separation near the free surface. The study emphasized the significant impact of shoulder wave breaking on flow structures and highlighted discrepancies with previous studies due to unaccounted energy dissipation. Additionally, it emphasized the importance of flow visualization techniques, especially Particle Image Velocimetry (PIV), in understanding ventilation mechanisms.

Young and Brizzolara [17] investigated the hydrodynamic response of a surface-piercing hydrofoil using both numerical and experimental methods. Their study extended a 3-D boundary element method (BEM) to model the effects of cavitation and ventilation. The research found that lift coefficients varied depending on whether the cavity was closed or open to the free surface. Good agreement was observed between numerical predictions and experimental measurements in both fully attached and fully ventilated regimes. The study identified major flow regimes around hydrofoils—fully attached, transitional, and fully ventilated—based on the separation and aeration on the suction side.

Harwood et al. [1, 2] conducted an experimental study on atmospheric ventilation of a surface-piercing hydrofoil, further developing the criteria implemented by Young and Brizzolara [17]. They classified steady flow regimes and examined the conditions for ventilation formation and elimination. Three distinct flow regimes were identified: fully wetted (FW), partially ventilated (PV), and fully ventilated (FV). They also developed a scaling relationship for the washout stage of ventilation elimination and mapped the flow regimes as a function of the yaw angle and depth-based Froude number. A review of the scaling relation on ventilated flow was presented by Young et al.[6].

The most recent research focuses on predicting ventilation through CFD simulations. Charlou and Wackers [25] conducted numerical experiments on the same model as Harwood's model to study the transition between wetted and ventilated flow regimes. Andrun et al. [26] utilized

CFD simulations to investigate natural ventilation on surface-piercing hydrofoils. They discussed the use of fences to prevent ventilation and improve hydrofoil stability. However, their simulations overestimated the drag forces. Other studies, [27, 28, 29, 30] have highlighted the importance of modeling Froude numbers, flow separation, and leading-edge geometry. They have reported that ventilation affects cavitation behaviours, with base ventilation suppressing natural cavitation and emphasising challenges in simulating complex multi-phase flows. Design modifications and understanding flow regimes were also key to controlling ventilation phenomena.

Mcgregor et al. [31] were the first to study the effects of waves on ventilation through a series of experiments in a towing tank facility. Their principal findings indicated a reduction in the inception angle of attack (AoA) with increased wave amplitude, orbital velocity, or steepness. While wave effects are beyond the scope of this work, excellent reviews on the topic can be found in Young et al. [32, 33, 31]. Additionally, the hydroelastic effects in ventilated flows, reviewed by Harwood et al. [34, 35, 15], are outside the scope of this thesis, which focuses on the hydrodynamic response of a rigid hydrofoil.

The analysis of existing literature indicates a prevalent experimental method for investigating ventilation inception in calm waters by increasing the Fn_h with a constant AoA, yet this approach does not avoid the inertial effects of foil acceleration. This tendency leads to a new experimental approach that takes this inertial effect off the equation. This innovative approach builds upon the work of Harwood et al. [2, 15] and incorporates the observations made by Charlou and Wackers [25].

Table 1.1: Summary of previous studies on natural ventilation at surface-piercing and submerged hydrofoils and strut-foil systems. The facility types are keyed as follows: TT-towing tank, FSWT-free surface water tunnel, RAT-rotatory arm tank, DPTT-depressurized towing tank, FSCC-free surface cavitation channel, and NS-numerical solver. When the values of the parameters were not explicitly given, they are inferred from the respective reports. Reprinted with modifications from Harwood et al. [2]

Citation	Section Shape	Facility Type	c(d) (cm)	v (m/s)	AR_h	Fn_c	Fn_h	σ_v
Coffee and McKann (1953) [36]	NACA 661 012	TT	10-20	9.14 - 24.38	1-6	6.48-24.42	2.64-24.42	0.33-2.3
	NACA 664012	TT	1	9.14 - 24.38	1-6	9.16-24.42	3.74-24.42	0.33-2.3
Kiceniuk (1954) [19]	Circ. arc	FSWT	3	1.50 - 8.22	0.98-1.46	6.16-12.27	5.1-12.42	4.1-16
Perry (1954) [18]	Rect. bars	FSWT	2.5	1.50 - 8.22	1.2-16.8	3.05-16.49	0.74-15.05	2.9-84
Wetzel (1957) [9]	Cyl. rods	RAT	0.1 - 5.1	0 - 45.74	1-100	1.3-65.32	0.13-65.32	5.3 to >100
	NACA 0012	RAT	5.1	0.73 - 6.05	0.5-5	1.05-8.64	0.47-12.21	5.3 to >100
	NACA 0024	RAT	5.1	0.73 - 6.05	0.5-4.5	1.29-8.64	0.61-12.21	5.3 to >100
Ramsen (1957) [37]	Flat Plate	TT	36-91	1.91 - 41.23	0.01-0.42	1.02-13.8	1.56-117	0.33-2.3
Wadlin (1958) [10]	Wedge	TT	18-18	3.66 - 76.28	0.5-1.5	2.76-57.4	2.25-81.2	0.33-2.3
Breslin and Skalak (1959) [7]	NACA 4412	RAT	7.6	0.76 - 9.18	0.5-2	0.88-10.58	0.62-14.96	2.3 to >100
	Circ. Arc	RAT	6.4	0.76 - 9.18	0.5-2	0.96-11.59	0.68-16.38	2.3 to >100
Fridma (1963) [20]	Wedge at 30 deg dihedral	TT	5.1	3.05 - 12.19	1-3	4.32-17.27	2.49-17.27	1.32-21
Waid (1968) [16]	Biogive family	DPTT	30.5	6.1 - 9.14	1-1.5	3.53-5.29	2.88-5.29	0.16-5.3
Rothblum et al. (1969) [11]	Biogive family	TT	30.5	2.06- 25.72	1-3	1.19-16.35	0.69-16.35	0.24-46
Mcgregor et al. (1973) [31]	Blunt biogive	TT	10	1.52-6.09	1-1.5	1.54-6.15	1.26-6.15	5.3-84
	NACA 0012	TT	10	1.52-6.09	1.5	1.54-6.15	1.26-5.03	5.3-84
	6º wedge	TT	7.5	1.32- 6.1	1.5	1.54-7.11	1.26-5.8	5.3-84
Swales et al. (1974) [12]	Sharp biogive	FSCC	10	1.5-6.1	2	1.5-6.11	1.06-4.32	0.08-87
	NACA 0012	FSCC	10	1.5-6.1	2	1.5-6.11	1.06-4.32	0.08-87
	NACA 016-021	FSCC	10	1.5-6.1	2	1.5-6.11	1.06-4.32	0.08-87
Fuwa et al. (1993) [23]	Biogive	TT	30.5-61	1.9-25.2	2	0.78-14.57	0.55-10.3	0.31-54
	Circ. Arc	TT	30	0.17 - 5.14	1.5	0.1-3	0.08-2.45	7.4 to >100
	Circ. Arc	TT	80	0.28-8.40	1.5	0.1-3	0.08-2.45	2.8 to >100
Pogozelski et al. (1997)[24]	Streamlined body at 0 def	TT	91.4	0.15-1.52	1.5	0.05-0.51	0.04-0.42	84 to >100
Harwood et al. (2016) [2]	Semi-ogive	TT	27.9	0.6-6	0.5-1.5	1.21-3.68	0.5-5	5.3 to >100
Ageorges et al. (2019) [38]	Cyl. rods	TT	1.4-16	0.25-1.5	1.44-16.5	0.20-2.41	0.20-2.41	-
Wang et al. (2022) [28]	Biogive Family	NS	27.9	50	1	30.2	30.2	0.0784
Huang et al. (2022)[27]	Triangle	TT & NS	0.05	0.36-22.96	0.5-1.5	0.51-32.79	0.51-43.34	0.37 to >100
Zhi et al. (2022) [39]	Semi-ogive	NS	27.9	0-4.13	1	0-2.5	0-2.5	-
Wang et al. (2024) [40]	NACA0012	TT	0.05	5.0-25.0	0.25-2.0	7.14-35.69	5.05-50.47	0.31-7.83

1.3. Problem Statement

Extensive research has been conducted on the inception of ventilation, with significant advancements in understanding atmospheric ventilation on rigid surfaces and hydroelastic responses [1, 2, 34, 35]. However, a common experimental approach—maintaining a constant angle of attack (AoA) while slowly accelerating the strut—may not fully capture the dynamic nature of ventilation inception. Charlou and Wackers [25] demonstrated through CFD simulations on a ventilated surface-piercing hydrofoil that the inception points vary depending on whether AoA or Froude number is kept constant. Additionally, the literature lacks detailed imaging, such as underwater and above-water videography, and stereo imaging on the suction side of the strut, which are crucial for accurately defining the cavity and validating CFD simulations. There is also an absence of tools to track the cavity closure line or the free surface, leaving gaps in the understanding of ventilation mechanisms.

After defining the problem statement, the research objectives and guidelines for the study's structure must be provided.

1.4. Research Objective

This research focuses on the inception of ventilation in surface-piercing hydrofoils, a topic of significant interest since the mid-20th century due to the rise of high-speed crafts and the associated drag-reduction benefits of hydrofoils. While recent studies have characterized atmospheric ventilation, the methodologies have largely remained unchanged, typically involving a constant AoA with increased Fn_h. To address these gaps and provide a more fundamental understanding of ventilation mechanisms, this study aims to experimentally investigate ventilation inception in a surface-piercing hydrofoil using a novel approach.

The research is conducted in collaboration with the Ship Hydrodynamics group at the University of Delft, where there is growing interest in ventilated flows. The analysis takes place at the towing tank facilities of the Faculty of Mechanical Engineering at the University of Delft. The following study objectives are defined:

Experimental study on the influence of a quasi-static variation of the angle of attack in the inception of ventilation.

1.5. Research Questions

The research objective is always accompanied by a series of questions that provide a more structured manner towards achieving the objective. The main question of the research is the following:

How is the inception of ventilation affected by a quasi-static variation of the angle of attack?

A series of sub-questions accompany the main research question to facilitate a comprehensive examination of the initial question's scope and potential branches. The following itemization encloses the formulation of sub-questions:

- How repetitive is the AoA at which ventilation inception occurs for a given Fn_h and AR_h?
- How do varying Froude numbers affect the inception AoA for a given geometry?
- How is the inception mechanisms affected by the Fn_h and the Re_c?
- How does varying the hydrofoil geometry, particularly the trailing edge shape, impact the inception AoA and mechanism at moderate to low Fn_h?

The sub-questions will be addressed through the analysis of experimental results. These questions focus primarily on interpreting the data obtained from the experiments. The project planning and research scope are essential for understanding the study's goals and constraints.

1.6. Plan of Approach

The research begins with thoroughly reviewing the existing literature on ventilation inception and elimination on lifting surfaces, particularly surface-piercing struts. The literature review aims to summarize the current understanding of the ventilation phenomenon, identify the experimental methods used in previous studies, analyze the various geometries studied, and ultimately select the most suitable method and geometry for the upcoming experimental studies.

After reviewing the literature, the focus of the research will shift towards designing and building the surface-piercing hydrofoil, defining the experimental matrix, and preparing the setup to conduct the experiments. The study aims to build upon existing knowledge of ventilation inception. Part of the experiments will be designed to verify the constructed geometry with previous research, while the other part will focus on developing the experimental methodology. Upon completing the experiments and obtaining the results, the focus will shift to post-processing the collected data and developing a code to analyse the videography.

This research is conducted in collaboration with the University of Delft's Ship Hydrodynamics group. This experimental study marks the first step in a series of new research initiatives of interest to the group. The experiments will yield a significant amount of videography and data, which can be utilized for future research on the topic, such as CFD validation.

1.7. Structure

The thesis is divided into several chapters, each focusing on a specific task in the project:

- Chapter 2 is a description of the findings of the literature review performed before the execution process of the project.
- Chapter 3 covers the experimental preparation of the towing tank testing. A description of the instruments used is given, as well as the methodologies and the test matrices.
- Chapter 4 is a presentation and discussion of the results obtained from the towing tank testing
- Chapter 5 provides a summary of the work carried out in the project and future recommendations.

2

Theoretical Background

This chapter elaborates on the theory behind the research. To start, an explanation of foil theory is given, covering the physical aspects and theory of hydrofoils, as well as the study of lift, drag and the behaviour of foils in different fluid conditions. Next, the fundamental concepts of multi-phase flows in 2D and 3D cavities will be introduced. This is followed by a discussion on the understanding of the ventilation phenomenon, covering the main leading parameters for ventilation inception, the different mechanisms for ventilation inception and the different flow regimes. The theoretical background continues with a review of foil geometries in previous research, covering the different parameters that affect the inception of ventilation. The theoretical background is concluded with the identification of the research gaps.

2.1. Introduction to hydrofoils

This section provides an introduction to hydrofoils, their physical aspects and their theoretical background. An extended version covering foil theory can be found in Appendix A, including the study of lift, drag and the behaviour of hydrofoils in different fluid conditions.

An airfoil is a streamlined surface designed to generate lifting force perpendicular to the direction of the surrounding airflow [41]. The cross-sectional shape of an airfoil creates a pressure difference between the upper and lower surfaces, resulting in an upward lift force. The lift is defined as the component of force acting in the plane of symmetry in a direction perpendicular to the line of flight [41, 42]. A hydrofoil is an airfoil operating in water. Aerodynamic foil principles can, therefore, be utilized to characterize a hydrofoil [43].

The typical airfoil section notation is shown in Figure 2.1. The chord (c) of the foil is the shortest distance from the leading edge to the trailing edge, and the angle of attack (α) is the angle between the chord line and the flow direction. [43]

The mean line of the section is called the camber line, which is the maximum separation between this line and the chord line [43]. The foil dimensions are usually taken at 1/4 of c from the foil's leading edge (where the hydrodynamic centre is defined). Thus, the thickness is determined at this position.

The two-dimensional hydrodynamic forces, lift (L), drag (D), and moment (M), can be computed as non-dimensional numbers, which depend on the density ρ, the velocity V and the size and shape of the body [42].

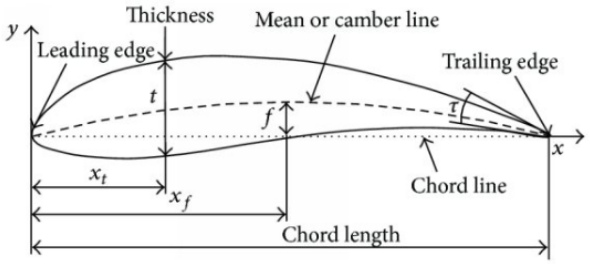

Figure 2.1: The geometry of a 2D foil. Reprinted from Kulkarni et al. [44]

$$C_{L_{2D}} = \frac{l}{\frac{1}{2}\rho V^2 c} \tag{2.1}$$

$$C_{D_{2D}} = \frac{d}{\frac{1}{2}\rho V^2 c} \tag{2.2}$$

$$C_{M_{2D}} = \frac{m}{\frac{1}{2}\rho V^2 c^2} \tag{2.3}$$

2.2. Multi-phase Flows

This section reviews the fundamental concepts and mechanisms of multi-phase flows in 2D and 3D cavities. subsection 2.2.1 reviews the hydrodynamics of two-dimensional cavity flows, and subsection 2.2.2 describes three-dimensional cavity flows.

2.2.1. Two-Dimensional Cavity Flows

The classic lift geometry is a two-dimensional foil section representing a standard three-dimensional strut. The two-dimensional theory usually serves as a first approach to understanding three-dimensional flows. Thus, it is helpful to introduce the different 2D flow regimes.

The two-dimensional force coefficients for lift, drag, and moment on a foil section, as defined in section 2.1, are described as follows.

$$C_{l_{2D}} = \frac{l}{\rho_f V^2 c/2} \tag{2.4a}$$

$$C_{d_{2D}} = \frac{d}{\rho_f V^2 c/2} \tag{2.4b}$$

$$C_{m_{2D}} = \frac{m}{\rho_f V^2 c^2/2} \tag{2.4c}$$

Where l, d and m are the lift, drag and moment per unit span, V is the velocity, ρ_f is the density of the fluid, and c is the chord length.

Flow regimes around a foil section are classified by Franc and Michel [14] as fully wetted, base-cavitating, partially cavitating, or supercavitating states. This terminology applies to any multi-phase flow, whether cavitation or ventilation. Illustrations of these regimes can be found

in Figure 2.2. The regimes are driven by the length of the cavity L_c and the non-dimensional cavity length L_c/c, which is relative to the chord length. The AoA governs this parameter and can be scaled with the cavitation number σ_c [14].

$$\sigma_c = \frac{P_\infty - P_c}{\rho_f V^2/2} \tag{2.5}$$

Where P_∞ is the free-stream pressure, and P_c is the pressure inside of the cavity. In the case of a cavitation cavity, P_c corresponds to the saturated vapour pressure; for a ventilated cavity, it refers to the atmospheric pressure [6].

In the context of a ventilated foil, as discussed in works by Harwood et al. [1, 2, 15], these regimes are categorized as thoroughly wetted (FW), partially ventilated (PV), and fully ventilated (FV). Further details on these concepts are provided in section 2.3.

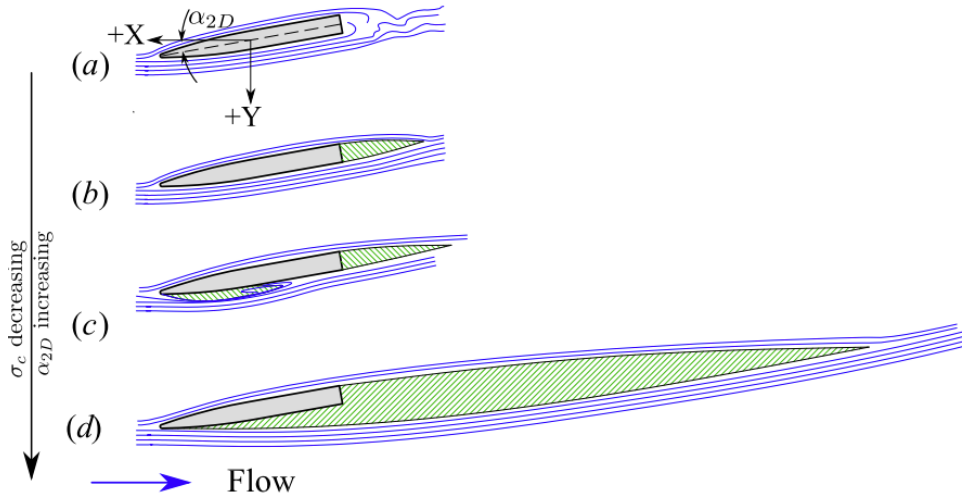

Figure 2.2: Flow regimes of a 2D foil section.(a) Fully wetted, (b) Base-cavitation or base-ventilation, (c) Partial-cavitation or partial ventilation, (d) Supercavitation or super-ventilation. Figure reproduced from Young et al. [6].

2.2.2. Three-Dimensional Multi-Phase Flows

In 3D flow, different sections along the span of a lifting surface can experience varied flow conditions simultaneously. For instance, some sections might be fully wetted while others might be ventilated or cavitated. These spanwise variations are influenced by factors such as geometry, inflow conditions, cross-flow effects, proximity to the free surface, buoyancy or rotational effects. The coordinate system of a 3D surface-piercing hydrofoil is illustrated in Figure 2.3. For a surface-piercing hydrofoil, gravity often dominates the pressure gradient, resulting in a hydrostatic pressure distribution along the span. This gradient causes the sectional cavitation number (σ_c) to vary with the depth (z) below the free surface.

$$\sigma_c(z) = \frac{P_{atm} + \rho_f g z - P_c}{0.5\rho_f V^2} = \frac{2gz}{V^2} \tag{2.6}$$

The geometric aspect ratio of a lifting surface is defined as

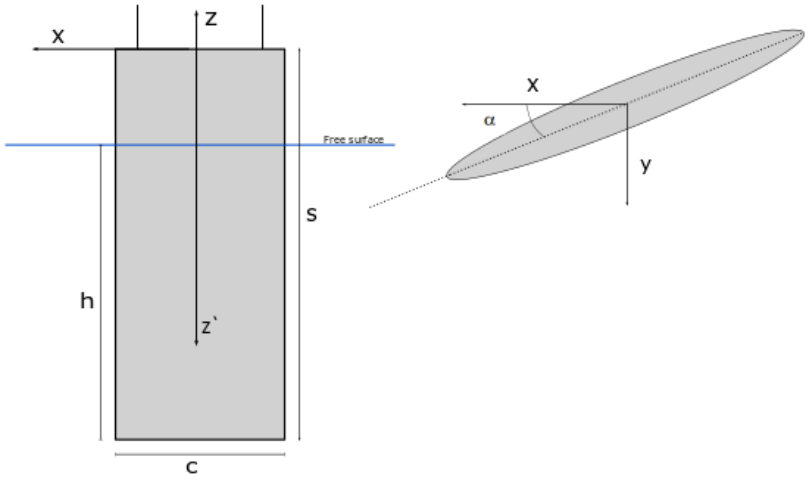

Figure 2.3: Coordinate system for a surface-piercing Hydrofoil. Figure reprinted from Elisa [45].

$$AR_s = \frac{S}{c} \tag{2.7}$$

where S is the span and c is the chord length. The submerged aspect ratio is given by

$$AR_h = \frac{h}{c} \tag{2.8}$$

where h is the submerged depth of the body, note that for a straight lifting surface piercing the surface vertically, Equations 2.7 and 2.8 are equivalent.

The depth-based Froude number is critical for analyzing ventilation near the free surface. This parameter indicates the ratio of dynamic to hydrostatic forces. It is defined as

$$Fn_h = \frac{V}{\sqrt{gh}} \tag{2.9}$$

The chord-based Froude number can be related to the depth-based Froude number by the expression [6].

$$Fn_h = Fn_c AR_h^{-\frac{1}{2}} \tag{2.10}$$

The three-dimensional lift, drag and yaw moment coefficients are defined as: [4]

$$C_{L_{3D}} = \frac{L}{\frac{1}{2}\rho V^2 hc} \tag{2.11a}$$

$$C_{D_{3D}} = \frac{-D}{\frac{1}{2}\rho V^2 hc} \tag{2.11b}$$

$$C_{M_{3D}} = \frac{M}{\frac{1}{2}\rho V^2 hc^2} \tag{2.11c}$$

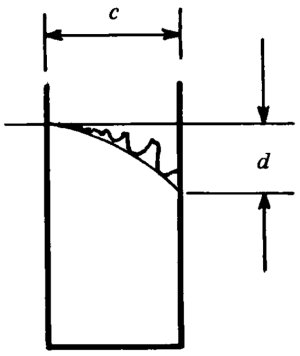

Figure 2.4: Drawdown to chord length ratio, d/c. Figure reprinted from Swales et al. [12]

Lift (L), drag (D), and yawing moment (M) are taken with respect to the rotation axis of the surface-piercing hydrofoil.

The drawdown to chord length ratio, d/c, is a measurement of the position of the free surface when ventilation triggers as a function of the chord length of the strut as depicted in Figure 2.4. The parameter d is the surface drawdown on the low-pressure side, defined as the vertical distance between the level of the nominal free surface and the intersection of the envelope of the perturbations with the trailing edge [12].

Three-Dimensional Re-entrant Jets

When the angle of the cavity-closure line relative to the inflow is considered, the kinematics of the re-entrant jet are notably affected. If the inflow velocity is decomposed into normal and tangential components to the cavity-closure line, conservation of momentum shows that the tangential component remains constant, reflecting the incoming flow about the separation boundary [46]. A streamline intersecting the cavity closure at an angle ϕ will emerge in the re-entrant jet at an angle 2ϕ (see Figure 2.5) [15, 6]. In two-dimensional flows, this reflection maintains the jet's velocity equal to the incoming flow, but in three-dimensional flows, the jet's behaviour is more complex due to spanwise velocity components. This interaction can either stabilize or destabilize the cavity. The mirror-like reflection model, although idealized, helps in understanding these jets, particularly noting that in growing cavities, the jet is weaker due to the lower relative velocity to the moving closure line. These three-dimensional effects are critical for surface-piercing hydrofoils, which often have non-normal closure lines to the local flow.

2.3. Ventilation

Atmospheric ventilation, as mentioned in section 1.1, refers to the phenomenon of a non-condensable gas, air, being drawn down along the low-pressure areas on a strut [4, 5]. In a surface-piercing hydrofoil, there is a perturbation in the flow, which allows the air to break the seal of the water surface, after which the entire cavity can be formed [43]. This phenomenon can especially happen when the strut operates at high speeds or large yaw angles beyond the stall angle. This leads to a breakdown of the lift-generating capacity of the hydrofoil, disrupting the smooth flow of water. Examples of marine systems where atmospheric ventilation can occur include propellers, rudders, fins, stabilisers, or ship hulls [47]. This section will delve into the understanding of ventilation based on previously published studies.

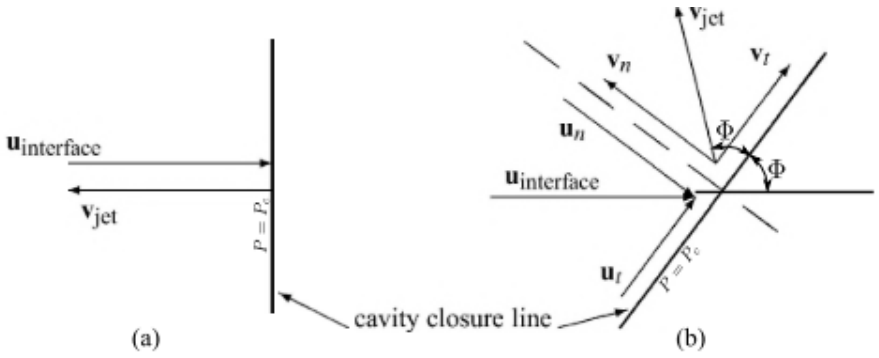

Figure 2.5: Reflection of oncoming flow by the closure line of the cavity. Figure reprinted from Harwood [15] with modifications from De lange and De Bruin [46].

As described in section 1.1, ventilation is a multi-phase flow similar to cavitation, with the primary difference being that a ventilated flow involves multiple fluids [45]. The effect of ventilation on lifting surfaces mainly results in a decrease in lifting force, as water is replaced by a less dense gas, such as air. However, ventilation can sometimes be beneficial. If the foil is designed to ensure that the cavity closes well downstream of the body, it will form a supercavity, leading to significant reductions in frictional drag on high-speed bodies [15]. However, the uncontrolled or unanticipated formation of a ventilated cavity can cause stability or structural concerns. Therefore, it is essential to understand the physics of ventilation inception.

Before ventilation, three requirements must be accomplished for the cavity to develop and be sustained:

- Sub-atmospheric pressure at the suction side of the foil
- Flow separation region at the suction side of the foil
- Continued path of ingress for the air to enter the cavity.

2.3.1. Flow Regimes

Harwood et al. [1] established three steady-state flow regimes associated with ventilated flows recognised by their flow stability. These flows were identified as fully wetted (FW), partially ventilated (PV) and fully ventilated (FV). The criteria to determine the flow regimes may be summarised as: [15]

D = 0			Fully wetted (FW) flow
D = h	AND	$\phi < 45°$	Fully ventilated (FV) flow
0 < D < h	OR	$\phi \geq 45°$	Partially ventilated (PV) flow
D = 0	AND	Water vapor present	Partially cavitating (PC) flow

where D is the depth of the cavity measured vertically from the free surface and ϕ is the angle of the cavity closure line. Note that Harwood [15] described an additional regime known as partially cavitating (PC) flow. However, this regime requires a depressurised water channel to inhibit cavitation at low cavitation numbers. Therefore, it is beyond the scope of this research.

Re-entrant Jet effect on Flow Regimes

The effects of the re-entrant jet on 2D and 3D flows were discussed in Sections 5.2.4 and 5.3.1. For the specific case of a surface-piercing hydrofoil, a representation of the jet is shown in

Figure 2.6. The incoming flow encounters the cavity closure line at a local angle ϕ and is reflected at twice this angle.

Harwood et al. [1] studied the re-entrant jet's influence on the flow regimes' stability. They outlined three stability conditions: globally stable, locally stable, and unstable. A flow regime is globally stable if it remains unchanged after any perturbation. It is locally stable if small perturbations don't affect it, but large perturbations cause a transition to another regime. The coexistence of locally and globally stable regimes was defined as bi-stable conditions. A regime is considered unstable if it cannot sustain itself without perturbations. In this case, when the cavity closure line angle ϕ exceeds 45°, the re-entrant jet moves upstream, causing large-scale shedding and instability. If ϕ is below 45°; the jet is redirected downstream, maintaining stability. Thus, a ventilated cavity is stable if $\phi < 45°$ and unstable if $\phi \geq 45°$.

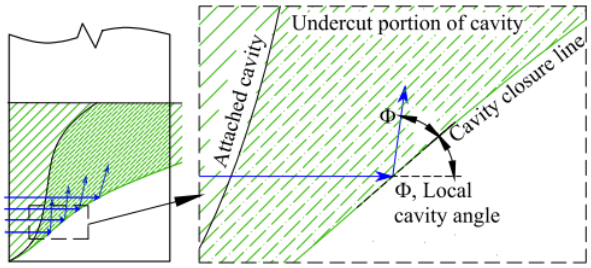

Figure 2.6: Representation of the re-entrant jet on spanwise-varying cavity. Figure reprinted from Harwood [15].

Fully wetted flow

A fully ventilated (FW) flow is a non-ventilated regime with no significant gas entrainment [1]. In this regime, a small separated wake may be present for blunt trailing edge (TE) profiles, but as they are confined to a small area, they do not affect the hydrodynamic performance of the foil. Similarly, there is no noticeable impact on the free surface deformation or flow separation [18]. An example of FW flow is illustrated in Figure 2.7.

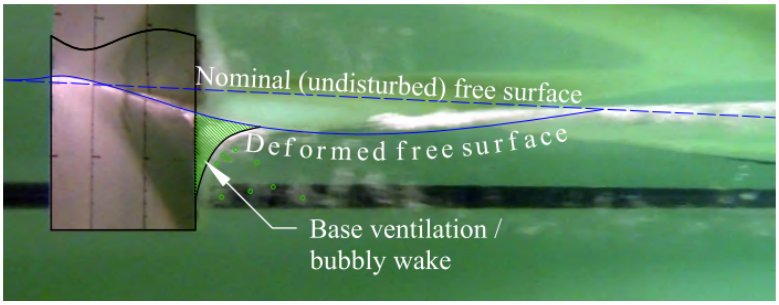

Figure 2.7: Fully wetted (FW) flow over the suction surface. Figure reproduced from Harwood et al. [2].

Partially ventilated flow

Partially ventilated (PV) flow is defined as a regime where one of the conditions for an FV regime is not met. Consequently, the cavity will not extend sufficiently to reach the foil's immersion depth, or the projected cavity closure angle will be $\phi \geq 45°$. Figure 2.8 presents two different PV regimes. In the first case, the cavity depth and length are unstable. On the other hand, a significant portion of the re-entrant jet is directed towards the LE. This will result in unsteady shedding structures.

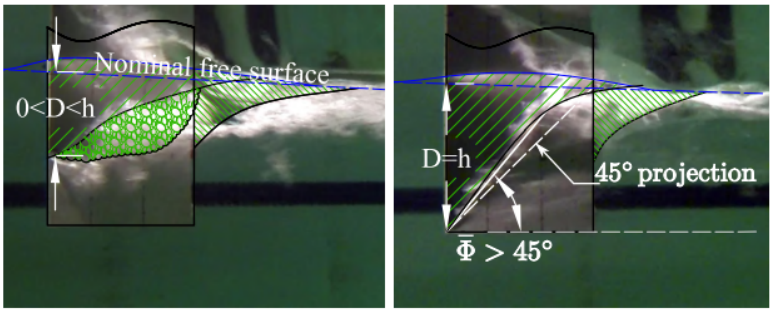

Figure 2.8: Partial ventilated (PV) flow. Figure reproduced from Harwood et al. [2].

Fully ventilated flow

Fully ventilated (FV) flow is defined as a regime where the ventilated cavity has extended to the entire span of the suction surface, and the incoming flow is redirected at $\phi << 45°$. Figure 2.9 gives an example of a fully ventilated regime.

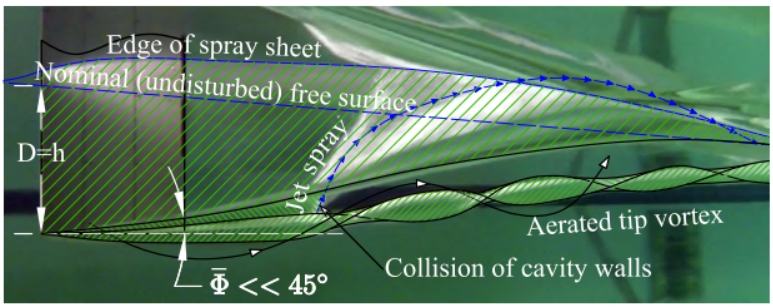

Figure 2.9: Fully ventilated (FV) flow. Figure reproduced from Harwood et al. [2].

Partially Cavitating Flow

Partial cavitation refers to a regime where the cavity is primarily filled with vaporous cavitation. This phenomenon was observed in experiments conducted by Harwood et al. [2], where air was evacuated from a depressurized towing tank to a pressure of 44 mbar. Similarly, Rothblum et al. [11] observed this regime by accelerating a foil to high Froude numbers at a sub-stall angle of attack (AoA) of $\alpha \leq 15°$. Figure 2.10 illustrates an example of a partially cavitating regime, showing both a vaporous cavity and a ventilated base cavity at the trailing edge (TE).

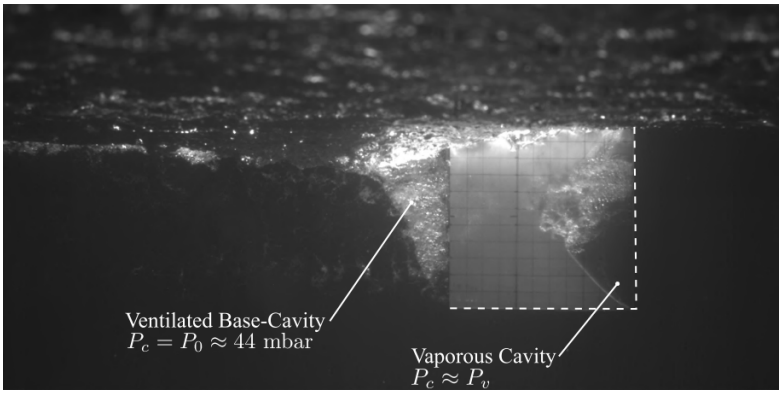

Figure 2.10: Partially cavitating (PC) flow. Figure reproduced from Harwood et al. [2].

2.3.2. Flow Stability

The four regimes defined by Harwood et al. [2] are mapped as a function of α and Fn_h for an immersed aspect ratio of $AR_h = 1.0$ in Figure 2.11. The map represents the flow regimes observed in experiments conducted by Harwood et al. [2], where the hydrofoil was accelerated quasi-statically while maintaining a constant value of α. Stability regions are defined for each regime, with boundaries indicating where flows are stable, locally stable, or unstable. Three bi-stable areas are observed, where two different regimes are stable; typically, one will be locally stable and the other globally stable. This can be correlated with the hysteric loop observed by Fridsma [20], see Figure 2.12.

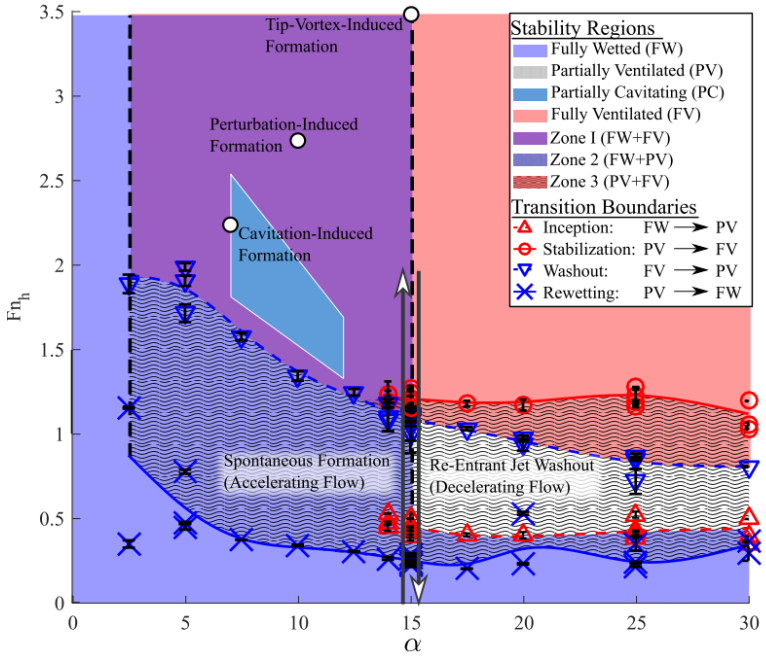

Figure 2.11: Stability map for a hydrofoil with $AR_h = 1.0$ with overlaid transition events. The flows are plotted as a function of the AoA and Fn_h. Figure reprinted from Harwood [15].

Harwood et al. [2] identified three types of boundaries. The transition boundaries separate the flow regimes along the Fn_h axis, representing the experimentally observed transitions between flow regimes. The bifurcation boundary vertically separates the region where only FW flow is stable from the bi-stable regions (zones 1 and 2). The bifurcation angle (α_b) is the lowest angle at which FW and FV flows can coexist [48]. The stall boundary defines the limit for stable FW flow and indicates where the exclusively stable FV regime begins.

Charlou and Wackers [25] conducted numerical experiments on the same geometry as Harwood et al. [2] to study the transition between wetted and ventilated flow regimes. The study employed two different methods. First, they slowly accelerated the strut at a fixed angle, yielding results consistent with Harwood's findings. The second method fixed the speed while gradually increasing the angle of attack. Surprisingly, at a fixed Froude number (Fn_h) of 2.5, ventilation inception occurred at 27.5° instead of 15° as predicted by Harwood et al. [2], which the study suggested was due to unsteady fluctuations in the wake. The difference between the two methods was attributed to the wave characteristics behind the LE: at $Fn_h < 2.5$, the wave was shorter but steeper, making ventilation inception easier at lower speed. Therefore, the inception occurred spontaneously during the slow acceleration. These findings contradict the vertical bifurcation and stall boundaries proposed by Harwood, indicating that further

experiments are necessary to understand ventilation inception.

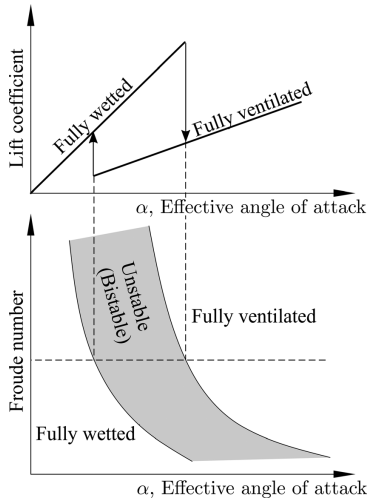

Figure 2.12: The hysteresis loop in the characteristic lift curved and the stability map. Reprinted from Young et al. and Fridsma [6] [20].

2.3.3. Hydrodynamic Loads

As observed in previous research, ventilation formation primarily affects hydrodynamic forces by reducing lift. The impact on drag force and yaw moment is less significant but should be further discussed. This section will explore the influence of various parameters and flow regimes on the hydrodynamic loads.

The lift force exhibits significant variations depending on whether the flow regime is fully wetted, partially ventilated, or fully ventilated. Breslin and Skalak [7] found that transitioning to the fully ventilated regime can reduce the lift coefficient by up to 70% compared to the fully wetted regime. Harwood et al. [2] observed that this reduction in lift is more pronounced at higher angles of attack. The Froude number can also affect the lift coefficient. Harwood's experiments demonstrated that as Fn_h increases, the lift coefficient in the fully ventilated regime decreases due to reduced lift-induced drag. If ventilation exists for $Fn_h \leq 1$, it often manifests as leading-edge laminar separation, which can increase lift due to increased effective camber and decreased span-wise flow separation [7, 2]. The aspect ratio influences the lift coefficient slope in the FW regime due to finite-aspect ratio effects. However, the FV's slope is independent of the AR_h [4].

Harwood et al. [2] reported the drag force to follow the classic quadratic trend with α. They noticed that the global drag was not affected by variations in the flow regime. Instead, the lift-induced drag component decreases with lift while the pressure drag increases due to the generation of large-side spray sheets [15]. This was first observed by Breslin et Skalak [7], who reported that ventilation causes an increase in form drag and a reduction of frictional drag. Harwood [15] noted that both the lift and drag coefficient will decrease with increasing Fn_h, which reflected the importance of the lift-induced drag.

The yawing moment measured approximately at the mid-chord is reported by Harwood et al. and Young et al. [2, 6] to be affected by the transition from fully wetted (FW) to fully ventilated (FV) regimes. The magnitude of the yawing moment is reduced due to the movement of the centre of pressure towards the mid-chord. The moment is also decreased by increasing Fn_h in the bi-stable region. Harwood et al. [2] noted that as the Fn_h increased, the lift and moment

coefficients tended to stabilise and reach a maximum value.

2.3.4. Ventilation Formation

Experiments by Harwood et al. [2] described the different formation mechanisms for ventilation. The concept of ventilation formation represents the transition from a fully wetted regime to a fully ventilated regime. The process was subdivided into two sequential stages. Inception is the transition from FW to PV, and it constitutes the process when the aerated cavity forms on the suction surface. As the speed increases, the flow will stabilise. The stabilisation is the transition from PV to FV.

Ventilation formation typically occurs when a low-pressure path created by a vortex core allows air to enter the separated low-pressure regions [12]. The mechanisms inhibiting this process were described by Harwood et al. [2] as spontaneous formation and perturbation-induced formation. Wetzel [9] described this process as creeping and flash ventilation.

Spontaneous or spontaneous-induced inceptions are mechanisms where ventilation is self-generated and develops naturally without external intervention. These include Leading-edge formation, tip-vortex formation, and Rayleigh-Taylor ventilation. The presence of vaporous cavities can also lead to cavitation-induced ventilation. Contrariwise, if the vortex is introduced artificially through disturbances in the incoming flow, it is called perturbation-induced formation. Figure 2.13 summarises ventilation formation and elimination, depicting the transition between the three flow regimes [6].

Rayleigh-Taylor at acceleration

The mechanism of spontaneous ventilation was first observed by Kiceniuk, Breslin and Skalak, and Swales et al. [19, 7, 12] and later classified by Harwood et al. [2]. This mechanism activates when the fixed angle of attack is set at or above the stall angle for an increasing speed. At this angle, boundary layer separation is forced, leading to a reduction in lift. Initially, the flow is attached, but a large vortex starts to develop at the leading edge (LE), generating flow separation in this region [2]. The low pressure associated with the speed creates a depression in the free surface, eventually reaching the separated flow region. Meanwhile, minor vorticity disturbances are generated at the free surface depression that is quickly magnified [12, 24]. These vortices, also called Rayleigh-Taylor instabilities, can breach the free surface seal, allowing a path for air ingress. If there is sufficient air ingress, the regime transitions to a ventilated flow, either PV or FV. Typically, after inception, the flow is classified as PV. Only after the flow velocity increases will the separated flow propagate enough to allow the cavity to reach fully ventilated conditions. Harwood et al. [2] describe this process as quasi-static, where the development of the cavity takes place on a time scale governed by the acceleration of the hydrofoil.

Tip-vortex and Trailing Edge Formation

Tip-vortex inception is another form of spontaneous ventilation. A strong tip vortex draws in air from far behind, eventually reaching the tip and entering the low-pressure region at the leading edge (LE). This interaction causes a rapid transition to fully ventilated (FV) flow and significantly shifts the hydrodynamic coefficient. Young et al. [6] suggested that this rapid transition likely occurs due to the flow's susceptibility to ventilation. Similar mechanisms were observed in the works of Ramsen, Breslin and Skalak, Swales et al., and Wetzel [37, 7, 12, 9], with Wetzel describing this tip-vortex ventilation phenomenon as 'flash ventilation.'

In the experiments conducted by Harwood et al. [2], the air entered the tip vortex through the bubbly wake generated by the blunt trailing edge (TE). In this case, the tip vortex was induced by the blunt TE of their geometry, rather than entering from far behind as in typical tip-vortex ventilation. This mechanism was observed only at high Froude numbers and angles of attack near the stall boundary. Trailing edge formation is similar to the observation made by Harwood et al. [2]. However, in hydrofoils or wedges with a blunt trailing edge, the ventilation wake provides an aeration path that ultimately reaches the leading-edge separation bubble without passing through the tip vortex.

Rayleigh-Taylor ventilation Formation

Rayleigh-Taylor ventilation, also known as Taylor ventilation, occurs at higher velocities and moderate angles of attack. This phenomenon was observed in the works of Waid, Rothblum et al., Rothblum, and Swales et al. [16, 11, 22, 12]. The mechanism is related to the leading edge formation, but the air ingress process is more complex. The air channel is generated by Taylor instabilities on the free surface near the trailing edge (TE). These instabilities grow when the interface, the free surface, is accelerated downwards in the direction of the denser fluid, the water. Emmons et al. also predicted that for the growth of unstable surface waves, an additional Helmholtz-type instability would develop on the surface [21]. For Rayleigh-Taylor ventilation, the low-pressure area on the suction side of the hydrofoil induces a downward acceleration of the free surface, creating a depression. If this downward acceleration is sufficient, small disturbances on the free surface, such as ripples or capillary waves, can rapidly grow in amplitude, become unstable and collapse once the low-pressure region and downward acceleration subside. The vortices generated by these perturbations can lead to air ingress [6]. Young et al. described this process as occurring over a relatively large time scale. This extended time frame is because the vertical elements generated by these instabilities allow only a small amount of air ingress at a time [22]. Consequently, a series of small perturbations are required to develop the cavity fully. This ventilation mechanism is described by Harwood et al. [2] as tail ventilation

Cavitation-induced Formation

The cavitation-induced formation was observed in the works of Waid, Rothblum et al., Rothblum, and Swales et al. [16, 11, 22, 12] at very high speeds. Cavitation promotes ventilation by creating a separated region filled with vapour at low pressure. In experiments by Harwood [15], cavitation specifically favoured Rayleigh-Taylor ventilation, as vaporous cavitation disappeared near the free surface. In experiments by Wang et al. [40], they found that cavitation-induced ventilation was influenced by the tip-immersed depth and forward speed.

Leading Edge Ventilation Formation

At angles of attack below the stall boundary, natural perturbations cannot break the surface seal. Therefore, the FW flow can remain stable long after the conditions for FV are established. Harwood et al. [2] suggested that this delay was due to a thin layer of high-momentum flow at the free surface. Consequently, the flow can remain in the fully wetted region even after conditions for full ventilation are met in some surface areas. Ventilation caused by external disturbances is known as perturbation-induced formation or forced inception. Previous research has identified various methods to perturb the surface, such as jet sprays, sharp objects, and thin wire intrusions [7, 12, 2]. A recurring observation from these studies is that an immediate transition to a fully ventilated regime occurs as the surface is pierced. Harwood et al. [2] noted that for a surface-piercing hydrofoil, a thin layer of separated flow exists at the leading

edge, allowing air ingress and later cavity expansion. Leading edge ventilation occurs when natural disturbances—such as capillary waves or ripples generated by the leading edge run-up or naturally, have sufficient momentum to disrupt the free surface around the LE and reach the small separation bubble at the LE, ultimately causing ventilation inception. Typically, this formation can transition the flow into partial ventilation (PV) or full ventilation (FV), depending on the Froude number, Fn_h.

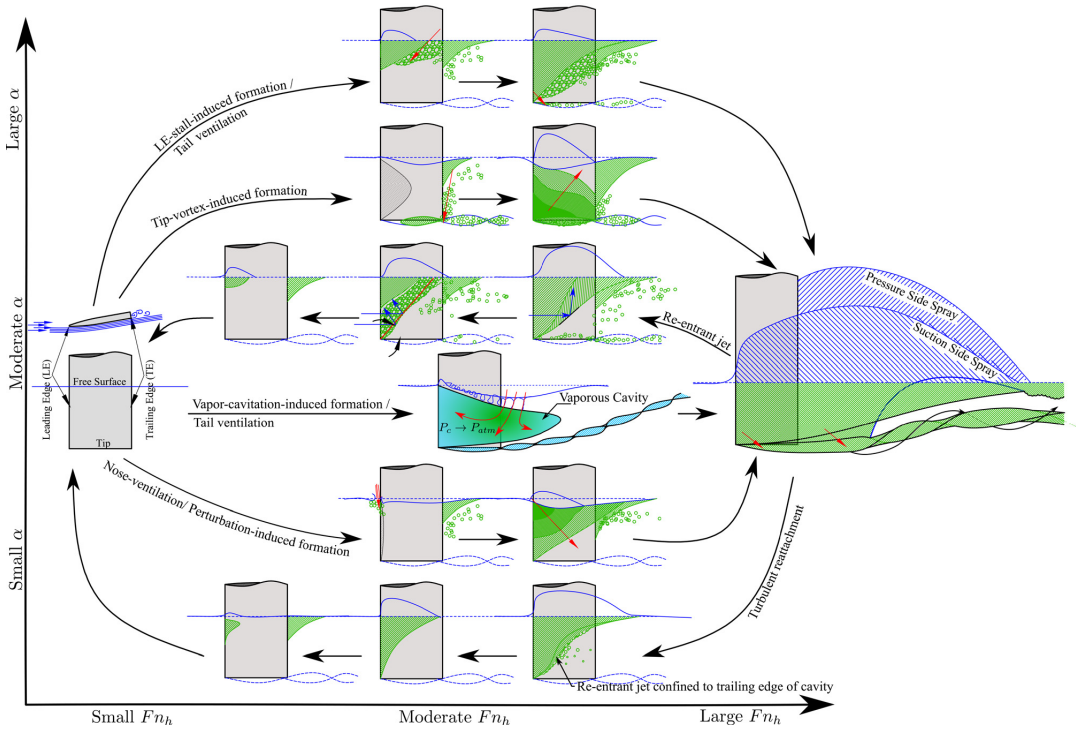

Figure 2.13: Ventilation formation and elimination mechanisms on a surface-piercing hydrofoil. Figure reprinted from Young et al. [6]

2.3.5. Ventilation Elimination

Elimination is the process where the ventilated cavity is destabilised and reduced [15]. Harwood et al., and Breslin and Skalak [2, 7] described this process to occur when the velocity or the angle of attack (AoA) were reduced. It involves transitioning from a fully ventilated (FV) regime to a partially ventilated (PV) regime and eventually to a fully wetted (FW) regime. Harwood et al. [1] explained ventilation elimination in two stages: washout and re-wetting. Washout is the transition from FV flow to PV flow, usually due to not meeting the criteria for FV flow, and involves large-scale shedding of the cavity. Re-wetting is the transition from PV flow to FW flow, completing the transition to fully attached flow when there is no visual evidence of air entrainment on the suction or pressure surfaces. However, bubbly flow may persist after the trailing edge. Harwood et al. [2] observed that the connection between the cavity and the free surface is terminated as speed is reduced.

Cavitation elimination typically occurs by the action of a re-entrant jet when the steepness of the closure line exceeds 45 degrees, $\phi > 45°$, as the strut decelerates. For $\alpha > 5°$, the re-entrant jet has enough momentum to impact the upstream cavity boundary, leading to the shedding of a portion of the cavity and leaving the flow partially ventilated. At very small angles of attack, $\alpha < 5°$, the jet is confined to the trailing edge and lacks the momentum to shed the cavity [14, 6]. Consequently, reattachment is more gradual as the cavity slowly reduces to a

separated bubble. Harwood et al. [2] described the two mechanisms of ventilation elimination as Re-entrant jet elimination and turbulent reattachment. These processes are sketched in Figure 2.13.

Breslin and Skalak [7] first introduced the washout boundary. However, Harwood et al. [1, 2] noticed that this formulation over-predicted the washout boundary. Therefore, they presented an expression for the critical washout Froude number (Fn_h) in relation to the slope of the cavity closure line. The following expression represents this slope.

$$m = \frac{(1-\kappa)h}{L_c} \tag{2.12}$$

Where κ is the non-dimensional immersion depth, which was taken by Harwood et al. [1] as $\kappa = 0.5$, and L_c is the cavity length for that immersion. A representation of these values is presented in Figure 2.14.

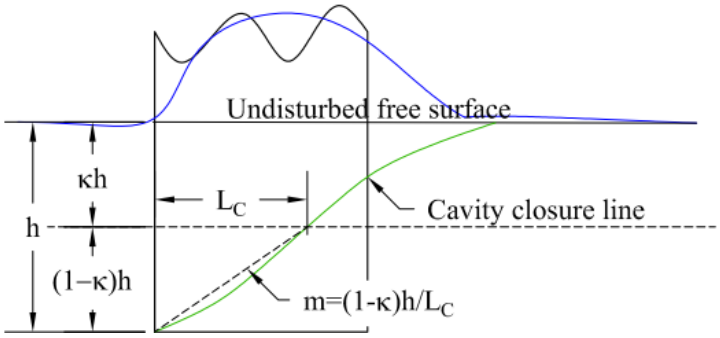

Figure 2.14: Representation of the cavity closure line. Figure reprinted from Harwood et al. [1]

The non-dimensional approximation for the cavity length was also defined by Harwood et al. [2].

$$\frac{L_c}{c} = 4.62\frac{\alpha_{eff}}{\sigma_c} \tag{2.13}$$

The effective angle of attack can be approximated by the finite aspect-ratio correction presented by Fridsma [20].

$$\alpha_{eff} \approx \alpha\frac{2AR_h}{2AR_h + 1} \tag{2.14}$$

By combining equations 2.13 and 2.14 and solving for the critical washout Froude number (Fn_h), the following expression is obtained.

$$Fn_h = \sqrt{\frac{\kappa(1-\kappa)^{\frac{1}{b}}}{\alpha^{\frac{1}{b}}}\frac{(2AR_h+1)}{AR_h^{\frac{b-1}{b}}}\frac{1}{\alpha}} \tag{2.15}$$

where a and b are constants [14]. This expression was modified by Harwood et al. [2] in order to include the three-dimensional lift coefficient.

$$Fn_h = \frac{\pi}{4}\sqrt{\frac{\frac{\pi}{2}AR_h^4 - 4AR_h^3 + 18AR_h^2 + 8AR_h}{2.31C_{L_{3D}}(\pi AR_h^3 - 2\pi AR_h^2 + 3\pi AR_h + 4)}} \tag{2.16}$$

2.3.6. Hysteresis of Ventilation

Hysteresis in ventilated cavities is a phenomenon caused by transitions between different flow regimes. When flow conditions change, overlapping flow regimes can lead to bi-stability, which induces hysteresis in hydrodynamic loads. This occurs because the stabilisation boundary does not coincide with the washout boundary. Instead, once the flow transitions to the FV regime, decelerating the flow will cause it to remain in the FV regime at a lower speed than the stabilisation boundary.

Rothblum et al. [11] reported this phenomenon and found that they could not reestablish the non-ventilated condition before inception by simply restoring the previous conditions. Fridsma [20] also highlighted the instability of the bi-stability region (see Figure 2.12). Additionally, Harwood et al. [2] noted that the bi-stability region ends at the bifurcation boundary at a specific angle of attack (AoA). Their experiments determined this angle to be approximately $\alpha_b \approx 2.5°$, although the geometry may influence this boundary.

2.3.7. Scale Effects

Previous literature has examined the scaling factors affecting the hydrodynamic response of ventilated flows. For instance, Young et al. [6] developed scaling relations for model-scale testing of ventilated lifting surfaces. Similar to observations by Rothblum et al. [11], they found that keeping the cavitation number (σ_c) and the chord-based Froude number (Fn_c) constant between models is required for achieving a similar hydrodynamic response in ventilation studies. This similarity is further supported by keeping geometric similarities, such as the aspect ratio (AR_h) and the shape of the models. Additionally, the geometric angle of attack should remain consistent.

However, maintaining these values constant can be challenging because other parameters may not scale proportionately with the model. This discrepancy and its implications will be further discussed in this section.

The Reynolds number (Re_c) influences the location and extent of flow separation and the formation of vortical structures. In RT ventilation formation during acceleration, the effect of Re_c depends on the type of flow separation and the characteristics of the boundary layer, whether laminar or turbulent. At low angles of attack and moderate Re_c values (between 10^5 and 10^6), the transition from laminar to turbulent flow can occur spontaneously by creating a laminar separation bubble (LSB). This bubble develops due to flow reversal caused by an adverse pressure gradient. At higher Re_c the LSB may "burst" or fail to reattach, causing a direct transition from laminar to fully separated flow [6].

Young et al. [6] observed that hydrodynamic loads varied with the Reynolds number for $Re_c < 3 \times 10^6$. Their study concluded that scaled models might affect ventilation formation, particularly at $Re_c < 3 \times 10^6$. The Reynolds number was scaled according to Equation 2.17, with $\lambda_{Fn_c} = 1$.

$$Re_{c_{scaled}} = Re_{c_{full}} \cdot \lambda_L^{3/2} \tag{2.17}$$

where the Re_c is derived as follows.

$$Re = \frac{Vc}{\nu} \tag{2.18}$$

The influence of the Weber number was studied by Wetzel [9]. This parameter represents the ratio between inertia and surface tension. Their experiments noted that the effect of surface tension was negligible for $We \geq 250$. However, for small bodies with $We \leq 250$, surface tension affected the surface wave and spray sheet pattern [6]. Surface tension could also dissipate small perturbations, such as Taylor instabilities, which would eventually delay ventilation inception. The following expression can define the Webber number.

$$We = \frac{\rho u^2 c}{\gamma} \tag{2.19}$$

Other parameters also influence the scaling of the ventilated flow. For instance, Young et al. [6] observed that the Mach number (Ma) impacts the cavity shedding frequency in cases involving vaporous cavitation. However, these effects are negligible when $Ma < 0.1$. The waves and surface disturbances are also parameters that affect the inception of ventilation. Rothblum et al. [11] noted that these disturbances weaken the free-surface seal. Similar to this, Mcgregor et al. [31] found that the inception AoA decreased with increased wave steepness, orbital velocity, and amplitude. Therefore, the scaling of waves must be considered when working with scaled models.

2.4. Geometry Definition

This section reviews the geometries from previous research and provides an initial geometry selection based on several parameters.

2.4.1. Previous Research Geometries

As discussed in section 1.2, several studies have experimentally investigated the mechanics of ventilation. These studies have introduced various geometries with unique parameters. Therefore, it is beneficial for the experimental campaign to gather all available information to define the geometry for the case study. For instance, in Figure 2.15, a summary of previously used geometries is presented. For each geometry and study, the formation points have been defined in the parametric space represented by $\alpha - Fn_h$.

Figure 2.15 shows that previous studies have reported depth-based Froude numbers in the range of $1 \leq Fn_h \leq 25$, except for the study by Huang et al. [27], which aimed to investigate the inception of ventilation through cavitation-induced formation and therefore required higher speeds. For the case study, the aim is to investigate fluids in the range of low-to-moderate Froude numbers ($0.5 \leq Fn_h \leq 4$), also due to the speed restrictions imposed by the facilities ($V \leq 6$ m/s). As reported by Harwood [15], this range is where flows are more prone to exhibit pronounced spanwise variation in the cavity topology, and therefore multiple flow regimes may exist. Thus, Figure 2.16 provides a more detailed view of the experiments that reported most formation points for $Fn_h \leq 4$. The Figure is set to a maximum of $Fn_h \leq 10$

In Figure 2.16, the studies with all the formation points obtained bellow $Fn_h \leq 10$ were included, summarizing the possible geometries to 8 specific, corresponding to 8 different studies. It is noticeable that the majority of the studies have reported some formation points at $0.5 \leq Fn_h \leq 4$. However, this is achieved by having an $AoA \geq 20°$. The study by Breslin and Skalak

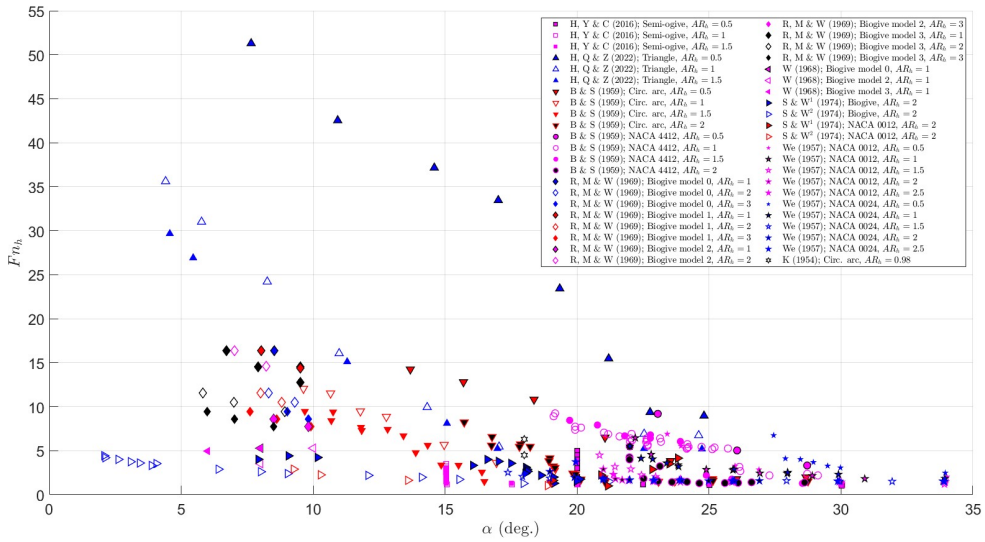

Figure 2.15: Formation points in $\alpha - Fn_h$ space. Data from previous studies are plotted as symbols: H, Y & C: Harwood et al. (2016) [2]; H, Q & Z: Huang et al. (2022) [27]; B & S: Breslin and Skalak (1959) [7]; R, M & W: Rothblum et al. (1969) [11]; W: Waid (1968) [16]; S & W: Swales et al. (1974) [12]; We: Wetzel (1957) [9]; K: Kiceniuk (1954) [19].[1] Tests conducted at atmospheric pressure. [2] Tests conducted at reduced pressure.

[7] has most of the points above the intended Fn_h boundary and will not be considered for the geometry selection. For the different studies, it is noted that the one with lower formation points in both Fn_h and AoA is the study by Harwood et al. [2], without taking into account the points with reduced pressure reported by Swales et al. [12]. The lower formation points indicate that lower hydrodynamic loads are reached, and therefore, a wider range of Froude numbers can be tested. The geometry studied by Harwood et al. [2] is a semi-ogive with a blunt trailing edge. The primary formation mechanism reported was the spontaneous formation, likely due to the sharp-nose leading edge (LE) and tip-vortex formation at moderate Froude numbers ($Fn_h \geq 2.5$) due to the blunt trailing edge (TE) that allows a wake to be attached.

To determine which geometry is most suitable for the intended test campaign, the formation points for different conditions have been grouped and plotted in Figure 2.17 for all previously studied geometries and in Figure 2.18 for those with formation points below Froude numbers $Fn_h \leq 10$. Figure 2.18 reveals two main areas: those with a more rounded leading edge (LE), specifically streamlined NACA bodies, which reported higher formation inception points both in Fn_h and AoA; and those with a sharper LE, including the bi-ogive, semi-ogive, and Circular-Arc families, which have formation points below $AoA \leq 20°$.

Another factor to consider is the chord length of the strut. If only the sharp-nose geometries are considered, then two main choices arise, a geometry with a chord length around $c = 0.3$ m or a geometry with a chord length around $c = 0.1$ m. The main parameter affected by the chord length is the Reynolds number. For models at $Re < 3 \times 10^6$, Young et al. [6] reported that ventilation inception is influenced somehow by the Reynolds Number. Additionally, around Reynolds numbers of $5 \times 10^5 < Re < 1 \times 10^6$, the transition from laminar to turbulent flow occurs, which Harwood et al. [2] noted as appearing in laminar separation bubbles (LSB).

The study intends to investigate LE ventilation and Rayleigh ventilation formation; therefore, the effects associated with Reynolds number (Re) should be minimized as much as possible. This can be achieved in two ways: by increasing the chord length or by increasing the speed

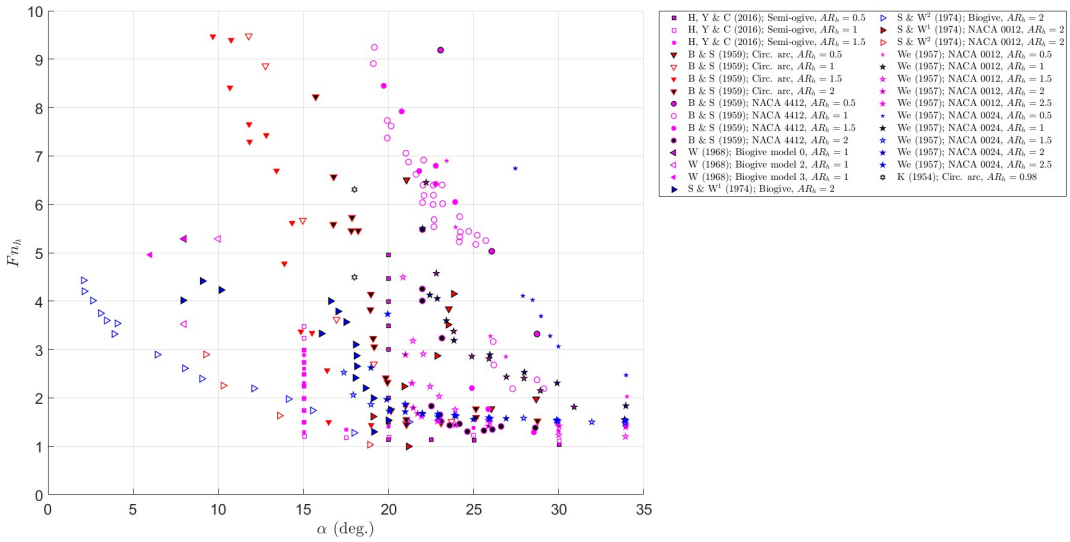

Figure 2.16: Zoom-in view of inception points in $\alpha - Fn_h$ space.

for smaller models. However, there is a limitation in the towing tank with a maximum speed of $V \leq 6$ m/s. Another method to induce the transition from laminar to turbulent flow is using turbulent tripping tape, which can prompt this transition. However, previous studies have not used it, as the experiments were performed at Reynolds numbers over the transition from laminar to turbulent, and the sharp LE provided a fixed point of flow separation.

Figure 2.19 represents the geometry formation points in the $\alpha - V$ parametric space, with the same areas as in Figure 2.18 reported. It can be noted that the geometries provided by Breslin and Skalak [7] surpass the limit imposed by the facility in the majority of cases. Furthermore, the main inception points are within the speed range of $1\text{m/s} \leq V \leq 3\text{m/s}$, which indicates that the formation points for the models with a chord length of $(c = 0.1m)$ may be affected by the transition from laminar to turbulent flow.

Ultimately, a model with a chord length of $c = 0.3$ m is the best choice. For these models, the laminar to turbulent transition will occur at around $V \approx 1.5$ m/s, providing a broader range to study the intended formation mechanisms. On the other hand, models with $c = 0.1$ m will transition at $V \approx 3$ m/s, which already uses half of the available speed range in the towing tank. Among the choices, the geometry provided by Harwood et al. [2] is the one that has been more extensively studied and characterized. This geometry resembles those used in previous studies by Rothblum et al. [11], Waid [16], and Swales et al. [12] and was intended to be an improved version of these geometries. Therefore, it was selected for the intended test campaign. A more detailed rationale for this selection will be discussed in further chapters.

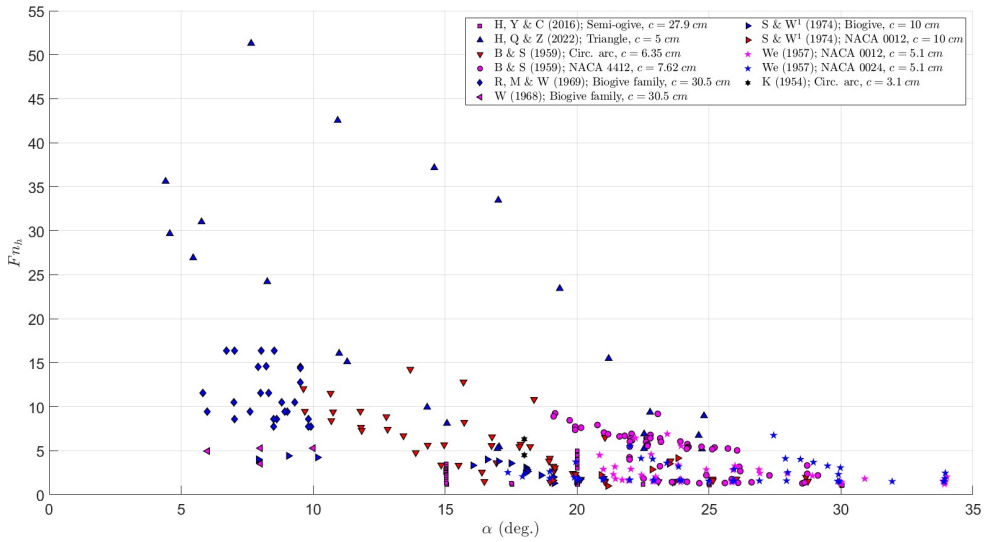

Figure 2.17: Inception points in $\alpha - Fn_h$ space. Data from previous studies are plotted as symbols and grouped depending on the geometry: H, Y & C: Harwood et al. (2016) [2]; H, Q & Z: Huang et al. (2022) [27]; B & S: Breslin and Skalak (1959) [7]; R, M & W: Rothblum et al. (1969) [11]; W: Waid (1968) [16]; S & W: Swales et al. (1974) [12]; We: Wetzel (1957) [9]; K: Kiceniuk (1954) [19].[1] Tests conducted at atmospheric pressure. [2] Tests conducted at reduced pressure.

2.5. Conclusion

The literature analysis has provided an overview of ventilation phenomena in hydrofoils, combining insights from previous studies. The investigation has covered several aspects as follows:

The investigation starts with an introduction to hydrofoils, focusing on their design and function. It explored how hydrofoils generate lift and the principles governing their behaviour in different fluid conditions. Secondly, the analysis discussed the various types of multiphase flows, focusing on ventilation. The study provided insight into how ventilation is formed and eliminated, the effects of ventilation on hydrodynamic loads, and the implications of ventilated cavities in lifting surfaces. Lastly, the investigation reviewed previous geometries used in ventilation experiments to determine which geometry has a lower inception point.

2.5.1. Knowledge Gaps

Overall, previous studies have advanced our understanding of ventilation. The literature review provides a discussion of the existing knowledge on ventilation. However, several gaps are found regarding the ventilation phenomenon. These gaps can be summarised as follows:

- Experimental studies evaluating the impact of varying the angle of attack (AoA) on the inception of ventilation are limited.
- Comparative experimental investigations into the effects of different trailing-edge geometries are lacking.
- High-quality videography documenting the inception of ventilation and the associated flow regimes remains scarce.
- The quantification of the ventilated region, as well as the previous instants prior to ventilation inception using automated, vision-based techniques is a very recent advancement

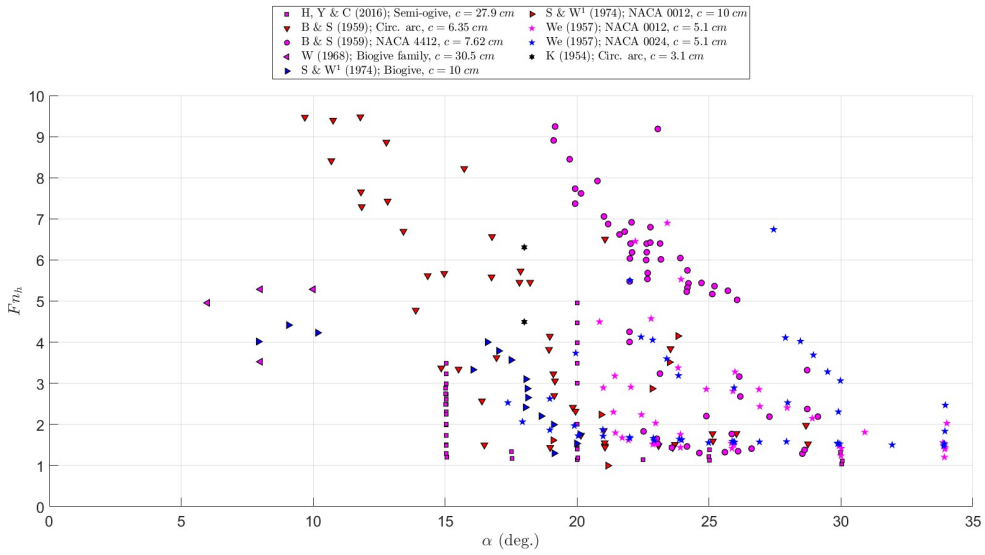

Figure 2.18: Zoom-in view of inception points in $\alpha - Fn_h$ space. Data from previous studies are plotted as symbols and grouped depending on the geometry.

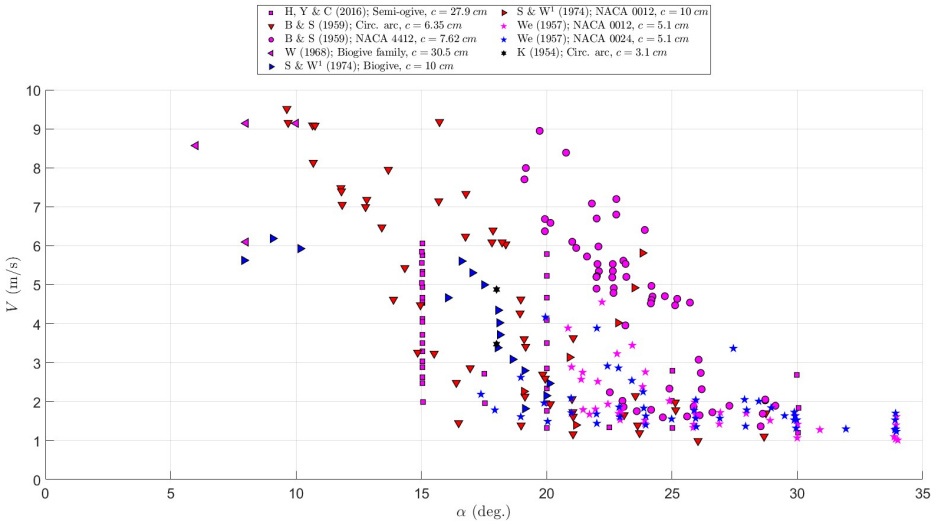

Figure 2.19: Zoom-in view of inception points in $\alpha - V$ space. Data from previous studies are plotted as symbols and grouped depending on the geometry

and requires further development.

The first and second research gap identified in this analysis closely correlates with the experiments conducted by Harwood et al. [2]. The intention is to build upon the findings of this research. While the geometry selection has already been introduced, it will be further detailed in the remaining part of the project. The third and fourth research gaps are associated with analysing early studies on ventilation inception, where these issues have been identified [25, 39, 28, 40, 38, 27].

3

Experimental Approach

Two hydrofoil models were tested in the Towing Tank at Delft University of Technology. This chapter details the experimental program. First, the hydrofoil models will be described, including their geometry and construction. Next, the facilities and the force predictions will be covered. The instrument selection, alignment and calibration process will be explained in detail, along with the overall test program and methodology. Finally, the chapter will conclude with an overview of the post-processing approach and an analysis of measurement uncertainties. This chapter results from a simultaneous process where the parameters defined in the various sections are influenced by each other.

3.1. Hydrofoil Models and Fixture

Two foils with comparable chord lengths and spans were constructed, with their critical characteristics summarized in Table 3.1. Construction drawings for the models and fixtures are in Appendix B. The following section provides a detailed explanation of the geometry selection, the construction process, and the experimental facility setup.

Table 3.1: Foil Characteristics

		Semi-Ogive	NACA0010-34	Unit
Chord length	c	279.4	300	mm
Total span	s	680	700	mm
Submerged depth	h	279.4, 419.1	300, 450	mm
Aspect ratio	AR_h	1, 1.5	1, 1.5	-
Max. thickness	t	27.9	30	mm
Velocity	V	0.83 - 4.14	0.86 - 4.29	m/s
Froude nr.	Fn_h	0.5 - 2.5	0.5 - 2.5	-
Yaw angle	α	0 - 30	0 - 30	deg.

3.1.1. Geometry Considerations

Chord

Building on the discussion in section 2.4, chord selection is influenced by how the Reynolds number affects the ventilation onset. The chord length can be scaled appropriately based on two factors: the critical Reynolds number, set to 5×10^5, which marks the transition from

laminar to turbulent flow near the leading edge, and the tested speeds. Previous geometries can be categorized into two main groups, $c = 0.1$m and $c = 0.3$m, representing the two primary options for chord selection.

For the first option, $c = 0.1$m, the transition to turbulent flow occurs at a speed of $V = 3$m/s following Equation 3.1, while for the second option, $c = 0.3$m, the transition occurs at $V = 1.5$m/s. Taking into account a maximum allowable lift of 800 N (see section 3.2), a chord length of 0.1m can theoretically reach speeds of up to 16m/s but is limited by the maximum carriage speed ($V \leq 6$m/s), achieving a Froude number of 6 and generating a lift force of 110 N. In contrast, a chord length of 0.3m can reach speeds of 4.5m/s, resulting in a Froude number 2.5 and producing a lift force of 500 N.

$$V_{crit} = \frac{Re_{crit} \cdot \nu}{c} \tag{3.1}$$

Therefore, considering these factors, selecting a chord length of 0.3m is more suitable for the experiments. This choice reduces the number of cases with laminar flow to only those below $Fn_h = 1\ m/s$ while losing only points above 4.5 m/s that are less relevant. It also minimizes the points affected by the Reynolds number effect, thereby reducing the number of points where ventilation is expressed as laminar separation bubbles.

Span

Several factors determine the span of the hydrofoils: the maximum allowable deflection, the required clearance to prevent water spray or run-up from reaching the force balance, and the maximum positioning height of the Hexapod.

The waterline is positioned 500 mm below the force balance at a height of 2.2 meters, the maximum height at which the Hexapod can be set. The hydrofoils are optimized to maintain a 500 mm clearance from the force balance, mainly when the aspect ratio (AR) is 1.

According to experimental observations by Harwood et al. [2], at least 0.75c of the foil must be above the waterline to prevent water run-up from affecting the force balance at the tested speeds (see section 3.6). The selected chord length corresponds to 225 mm of foil above the waterline. This requirement becomes more critical when AR increases to 1.5, where the clearance reduces to 350 mm.

To ensure rigidity, the maximum deflection is limited to 5 mm. A maximum allowable span is calculated to be 857 mm (see Equation 3.2) by applying the general deflection formula for a cantilever beam, with an estimated load of 500N distributed over the submerged area. Further details on the model construction can be found in subsection 3.1.5.

In the final design, the foils from the fixed position were chosen to span 700 mm. This provides 400 mm of foil above the waterline for AR = 1 and 250 mm for AR = 1.5, satisfying both clearance and deflection requirements. The design's maximum deflection for a lift force of 600N is 3.86 mm, ensuring the foils' structural integrity while maximizing the available clearance from the Hexapod.

$$\delta = \frac{qL_1^2}{6EI} \cdot (3L - L_1) \tag{3.2}$$

3.1.2. Semi-Ogive

The cross-section of the semi-ogive hydrofoil closely resembles the design used by Harwood et al. [2] in their experiments, as illustrated in Figure 3.1. The geometry remains uniform along the span, with an approximate chord length of $c = 279.4$mm and a maximum thickness of $T = 0.1c = 28$mm. The section features a leading-edge radius of $0.01c$ and a blunt trailing edge. This type of geometry was previously studied in experiments by Rothblum et al., Swales et al., Waid, and McGregor et al. [11, 12, 16, 31] and has also been applied in CFD simulations following Harwood's experiments.

The design offers several advantages, including a negligible pressure gradient over the aft half of the section and a sharp leading edge that acts as a fixed point for flow separation, eliminating the need for turbulent tripping. The choice of a sharp leading edge aligns with the experimental focus on studying ventilation inception through leading edge ventilation and Rayleigh-Taylor ventilation. Additionally, the blunt trailing edge facilitates ventilation via the classic "creeping" mechanism described by Wetzel [9], Trailing edge or tip-vortex formation, as defined by Harwood et al. [2].

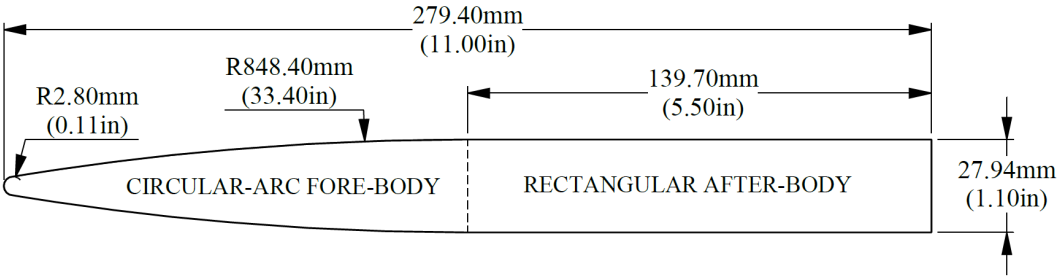

Figure 3.1: Cross-section shape of the Semi-ogive Hydrofoil. Figure reproduced from Harwood et al. [2].

The hydrofoil was constructed at the TU Delft towing tank workshop, using a 3D printer (Original Prusa MK3) to create four sections along the span with PETg. Its cost-effectiveness and ease of machining drove the decision to use 3D printing. Although PETg alone does not provide sufficient rigidity, the hydrofoil was designed to be reinforced. After printing, the sections were joined and structurally strengthened at the mid-chord by three steel rectangular hollow sections (RHS) measuring 40x20 mm with a 3 mm thickness to ensure the necessary stiffness. Additionally, two carbon fibre rods were installed near the leading edge (LE) and trailing edge (TE) to reduce torsional moments. The fully assembled foil is depicted in Figure 3.2, while the cross-sectional shape is illustrated in Figure 3.3. Table 3.2 lists the material properties of the S235 Steel and PETg, and Table 3.3 gives the physical properties of the two hydrofoil models.

Table 3.2: Tabulated material properties of hydrofoil construction materials

Property	Symbol	Units	S235 Steel	PETg
Density	ρ	kg/m^3	7.850	1.270
Young's Modulus	E	GPa	210	2.0
Shear Modulus	G	GPa	80	0.7
Poisson's Ratio	ν	-	0.33	0.40
Yield Strength	σ_y	MPa	235	50

The surface of the hydrofoil was machined and coated with epoxy-based paint to prevent water ingress into the model. Yellow was selected to provide maximum contrast against the towing tank walls. The surface was meticulously smoothed to eliminate imperfections that could

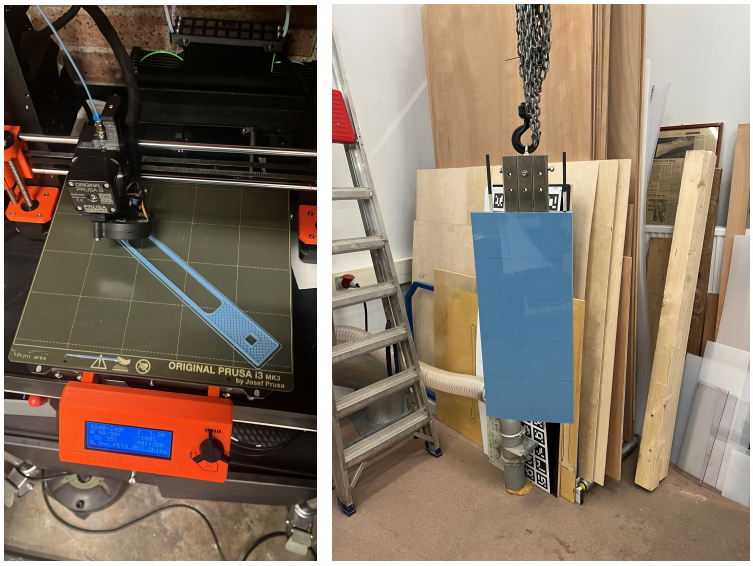

(a) 3D Printer **(b)** Semi-ogive Hydrofoil without coating

Figure 3.2: Construction process of the Semi-Ogive Hydrofoil.

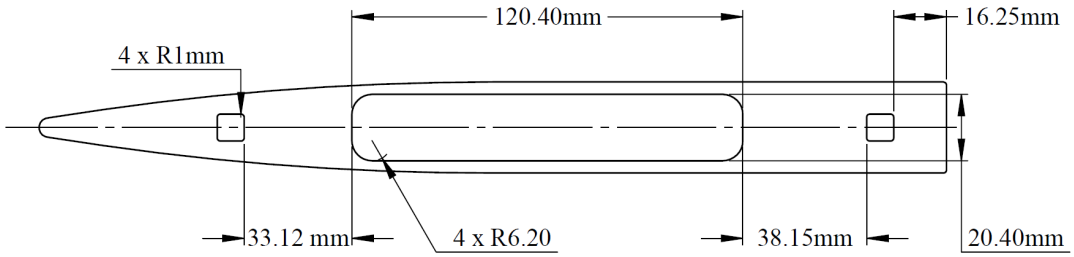

Figure 3.3: Cross-section shape of the Semi-ogive Hydrofoil with structural characteristics.

trigger premature ventilation. Finally, a grid with a pitch of c/14 was painted onto the foil using a precision meter to assess the ventilated flow better, as illustrated in Figure 3.4.

3.1.3. NACA0010-34

The NACA0010-34 cross-section was selected based on the requirements of the parallel experimental campaign and is illustrated in Figure 3.5. The geometry features a chord length of $c = 300$mm and a maximum thickness of $T = 0.1c = 30$mm This section has a leading edge that is three times sharper than the standard NACA0010 profile, with the centre of efforts at $0.4c$.

The sharp leading edge, similar to a semi-ogive hydrofoil, acts as a fixed point for flow separation, enabling separation at an angle of 8° This design is selected to facilitate LE formation by enabling earlier flow separation, which is consistent with the objectives of the experimental campaign. Additionally, the sharp trailing edge and streamlined aft-body contribute to Rayleigh-Taylor ventilation by generating an additional low-pressure region and preventing tip-vortex-induced ventilation at higher speeds, which was observed by Harwood et al. when using a blunt trailing edge [2].

The model was produced at an external facility using a resin-based 3D printer, fabricated as a single piece and reinforced by three steel rectangular hollow sections (RHS) measuring 40x20 mm with a 3 mm thickness like the Semi-ogive hydrofoil. The cross-sectional shape and

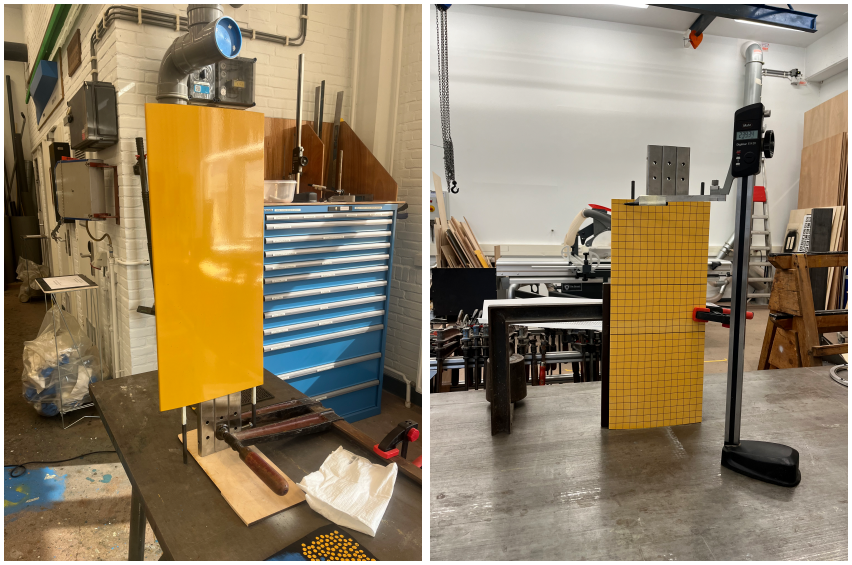

(a) Semi-Ogive Hydrofoil Painted

(b) Final aspect of the Semi-Ogive Hydrofoil

Figure 3.4: The process of painting the Semi-Ogive hydrofoil.

Table 3.3: Tabulated physical properties of the two tested hydrofoils. The moments of inertia and rigidities are calculated only for the structural RHS reinforcements.

		Semi-ogive	NACA 0010-34	Unit
Chord length th	c	279.4	300	mm
Section Area	A_s	6741.36	6340.74	mm^2
Mass	m	9.54	8.93	kg
Volume	V	3727.03	3579.51	cm^3
Mass Center (Aft of LE)	CG	0.60	0.37	X_{CG}/c
Moment of Inertia	I_x	5..05	5.05	cm^4
Moment of Inertia	I_y	111.9	111.9	cm^4
Flexural Rigidity	EI	234960.66	234960.66	$N - m^2$
Torsional Rigidity	GJ	93552.21	93552.21	$N - m^2/rad$

structural characteristics are shown in Figure 3.6. The surface coating applied to the hydrofoil follows the same procedure as the previous design, ensuring a smooth, waterproof finish with good contrast over the walls. Further, a grid with a pitch of c/15 was drawn on the surface.

3.1.4. Geometry Comparison

Figure 4.25 presents an overlay of the two tested cross-sectional shapes. The most notable difference between the two designs is the contrast between the blunt and streamlined trailing edges. Both designs feature a similar leading edge, with a sharp nose that maximizes flow separation at small angles of attack, followed by a sharply contoured aft body. These design characteristics facilitate ventilation through spontaneously induced mechanisms, such as Leading edge and Rayleigh-Taylor ventilation. Additionally, the blunt trailing edge fosters an additional form of ventilation at higher speeds via tip-vortex inception, where air is drawn into the tip vortex through the bubbly wake formation at the trailing edge, rather than downstream, as observed in previous studies by Harwood et al. [2] Note that both foils are assumed to be

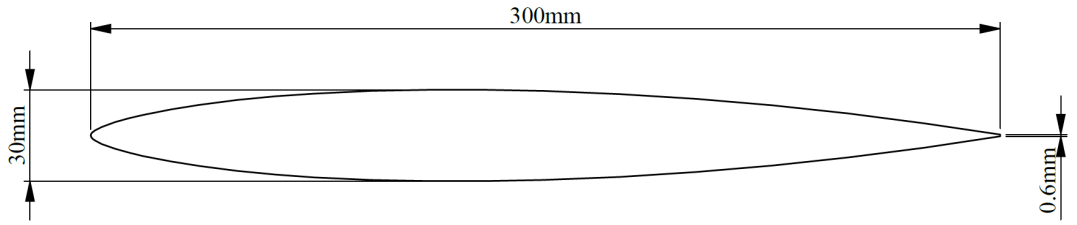

Figure 3.5: Cross-section shape of the NACA0010-34 Hydrofoil.

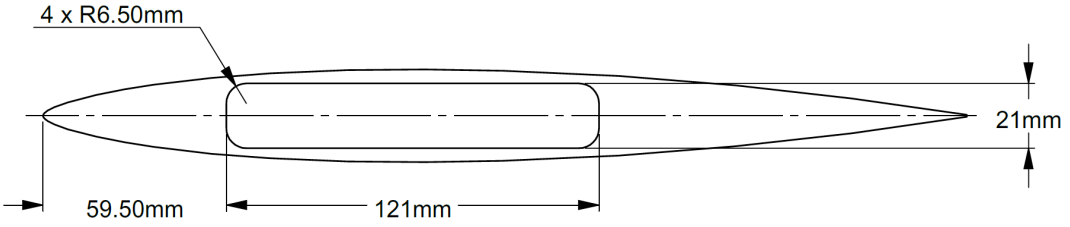

Figure 3.6: Cross-section shape of the NACA0010-34 Hydrofoil with structural characteristics

rigid because of the steel reinforcement.

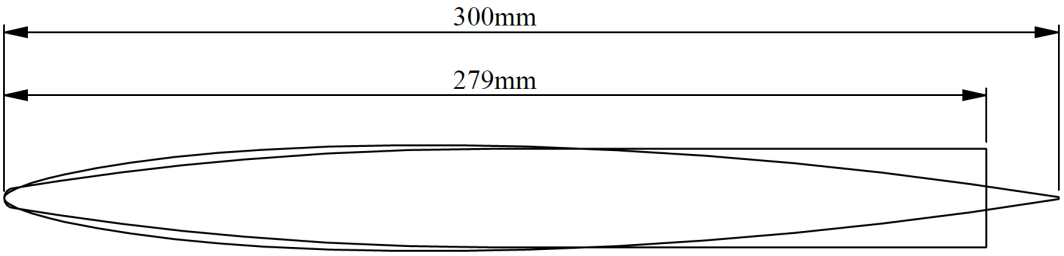

Figure 3.7: Comparison of the hydrofoil models cross-section shapes.

3.1.5. Model Set-up

The hydrofoils were clamped at the root and mounted vertically in a cantilevered configuration to pierce the water's free surface, as shown in Figure 3.8 and Figure 3.10; the camera module setup will be discussed in the following sections. The foils were designed to fit an existing 6DOF load gauge (force balance) clamped to the Hexapod. The setup is configured so that the angle of attack (α), the speed (U), and the immersion depth (h) can be independently varied. The hydrofoils were secured to the force balance by a built-in disk that fit the force balance, along with six ITEM 80x80 brackets that fixed the position of the hydrofoils. The force balance was then secured to the Hexapod Appendix B shows the technical drawing of the experimental setup.

The immersion depth of the hydrofoils was visually measured against a reference grid and monitored through the 90° underwater camera, as shown in Figure 3.9. Two thicker lines were marked on the grid, corresponding to the two aspect ratios (AR) to be tested The width of the grid lines determined the maximum uncertainty in-depth measurement, which was ±3mm, due to the challenge of precisely positioning the hydrofoils. Additionally, the water level fluctuated naturally, with approximately 1 mm of water evaporating each morning and the consequent filling of the towing tank, contributing to minor variations in the immersion depth. The immersion depth and angle of attack were controlled by adjusting the Hexapod, which operates with a 6-degree-of-freedom (6DOF) configuration.

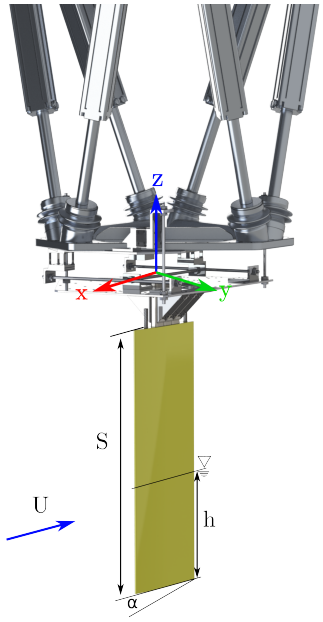

Figure 3.8: Rendering of the experimental setup underneath the carriage and the main variables that define the flow. The coordinate system used in the experiments is set at the coordinate system of the force balance. The X-axis is pointing upstream, and the Y-axis is in the direction of positive lift. The direction of the Z-axis follows the right-hand rule.

3.2. Facilities

The experimental campaign took place over two months in the spring of 2024 at the testing facilities of Delft University of Technology. Specifically, the experiments were conducted in Towing Tank No. 1 at the Ship Hydromechanics Laboratory, see Figure 3.11. The tank is 142 meters long, 4.22 meters wide, and has a maximum water depth of 2.5 meters, though the water level was set to 2.2 meters for the campaign's duration. The tank features a gantry-type carriage equipped with a laser-aided positioning drive system. The carriage is capable of reaching speeds of up to 7 m/s; however, a maximum speed of 4.29 m/s ($Fn = 2.5$) was used due to the force limitations of the balance, as detailed in section 3.5. The speed and acceleration of the carriage were configured on a dedicated computer, while the carriage was controlled via a switch just behind the model.

3.3. Reference Frame

The standard coordinate system in the TU Delft Towing Tank is defined as indicated in Figure 3.8: the x-axis points in the direction of the carriage's motion, the y-axis aligns with the direction of positive lift, and the z-axis points vertically upward The angle of attack is measured in a clockwise direction when viewed from above This coordinate system is located within the carriage and moves along with it The origin of the carriage's coordinate system corresponds to the reference frame of the force balance, as shown in Figure 3.12, where the yaw moment is set to zero. Since the force balance rotates with the Hexapod, the measured forces must be corrected for the angle of attack to express them in the reference frame.

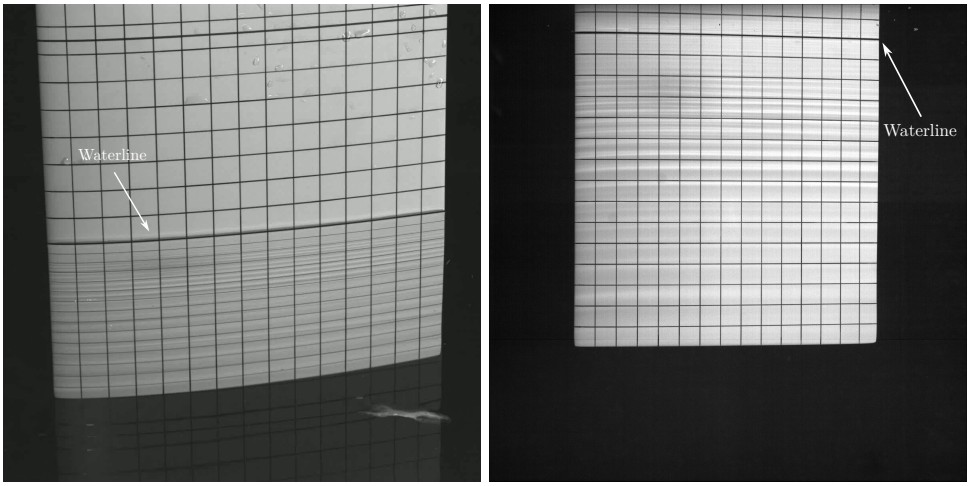

(a) Above-water camera **(b)** Underwater camera

Figure 3.9: Grid on the foil suction surface of model NACA0010-34. The grid waterline is thicker for a better measurement.

3.4. Instrumentation, Alignment and Calibration

In this experimental campaign, several instruments were employed to capture, measure, and record the necessary data. The instrumentation setup remained consistent throughout the testing campaign and was identical for both hydrofoil configurations. The setup includes dedicated instruments for force and moment measurements, systems for executing controlled movements, separate systems for detecting and tracking these movements and videography systems for visual data capture. This section describes the equipment used, categorized by the measured quantities and the complementary systems required for their operation. Furthermore, it explains the alignment of the systems with the hydrofoil and outlines the calibration procedures for each instrument.

3.4.1. Force and Moment Measurements

6-DOF load gauge

The 6-DOF load gauge used for the experiments was previously built by the personnel at the TU Delft Towing tank. It consists of two rigid plates with a wooden core, reinforced by two thin steel layers, and is equipped with six load cells. These load cells can be exchanged so that the maximum force capacities vary, allowing the 6-DOF system to be customized according to the specific requirements of each experiment Figure 3.13 and 3.14 shows an overall view of the sensor and a detailed view of the cell loads.

Figure 3.13a shows the connections of the load gauges to the mounting plate. The load gauge is positioned transversely to the action plane of the steel rods, which are aligned along the axis of force application. The thin ends of these rods are meant to constrain movement to a single axis, thereby minimizing any additional unwanted forces. The load gauges are arranged as follows: one gauge measures force in the x-direction (F1X), two gauges measure in the y-direction (F2Y and F3Y), and the remaining three gauges measure force in the z-direction (F4Z, F5Z, and F6Z) However, for this experimental campaign, the primary interest was to measure F_x, F_y and M_z Consequently, The load gauges measuring in the z-direction were replaced with non-instrumented load cells, or dummy gauges, resulting in a final configuration with a 3-DOF load gauge system This adjustment will enhance the force capacity of these load

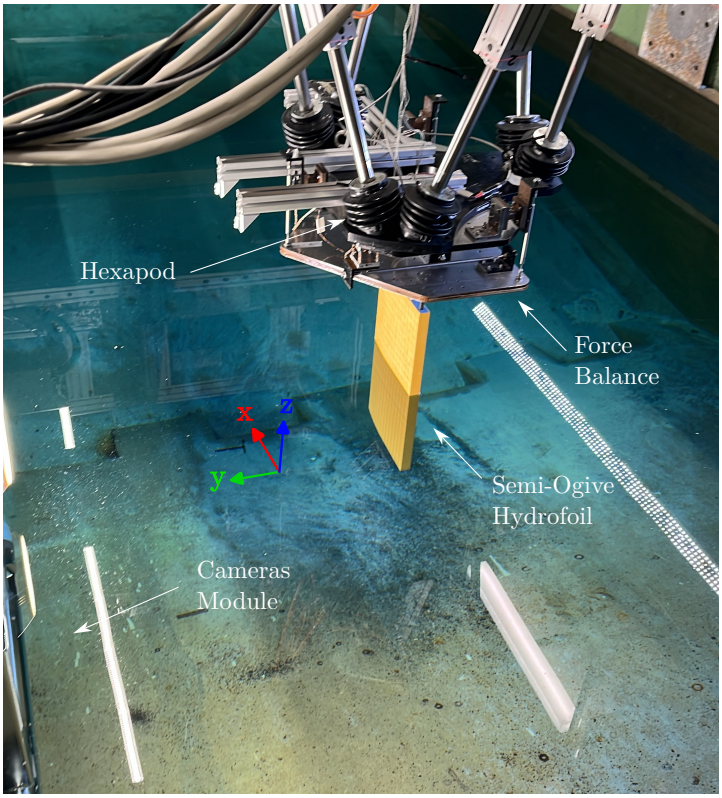

Figure 3.10: Experimental setup featuring the positioning of the semi-ogive hydrofoil and the camera module The NACA0010-34 hydrofoil is arranged in the same configuration.

cells, mainly as they will register the highest expected loads, see section 3.5. The positioning of the load cells relative to the reference coordinate system is shown in Table 3.4.

Table 3.4: Load cell configuration in the 6-DOF load gauge

	F1X	F2Y	F3Y	F4Z	F5Z	F6Z
X	0	0.2	-0.2	-0.26	0	0.26
Y	0	0	0	-0.15	0.3	-0.15
Z	0	0	0	0	0	0

Amplifiers

The strain in the load cell gauges is measured as a change in resistance. However, this signal is relatively small, making direct recording challenging. To resolve this, a Peekel PICAS Multi-Channel Compact Amplifier System was employed to amplify the signal before transmitting it to the data acquisition system The amplifier converts the resistance changes into a corresponding voltage output, ranging between -10V and 10V Figure 3.15 illustrates the setup, where both the PICAS amplifier and the rack-mounted data acquisition unit (DAQ) are shown. The latter gathers the amplified signals for further processing and analysis on the measuring computer.

Figure 3.11: Towing Tank No.1. [49]

3.4.2. Position and Angle Measurements

Hexapod

The Hexapod is a six-legged robot centrally mounted on the carriage, as shown in Figure 3.10. Each of the robot's legs consists of linear electric actuators, controlled using the commercial software provided by Symétrie®. The system is made to allow movements in six degrees of freedom.

The specific model used in this setup is the Notus hexapod. The dedicated software offers advanced positioning capabilities. This includes simulating particular rotations around the Z-axis (yaw) while dynamically compensating for movements and rotations in other axes. The Hexapod can also be programmed to follow predefined movement sequences specified with time and coordinates. This functionality is essential for the upcoming test campaign, as outlined in section 3.6.

Certus

The Certus system was used to measure the hydrofoil's rotation and position with respect to the reference frame. This instrument operates based on three infrared cameras that interpolate the location of the reference plate. The reference plate is mounted in the 6-DOF sensor, as depicted in Figure 3.16.

The origin of the Certus system was set when the foil aligned with the experimental reference frame. Since the yaw angle was the primary parameter of interest, its rate of change was recorded. As a result, the first reading in the dataset was replaced by the initial yaw angle.

3.4.3. Flow Speed and Droplet Release Measurement

Peristaltic Pump

A peristaltic pump was initially used to release droplets at a known distance from the hydrofoil's leading edge to introduce controlled perturbations that could trigger ventilation. By controlling

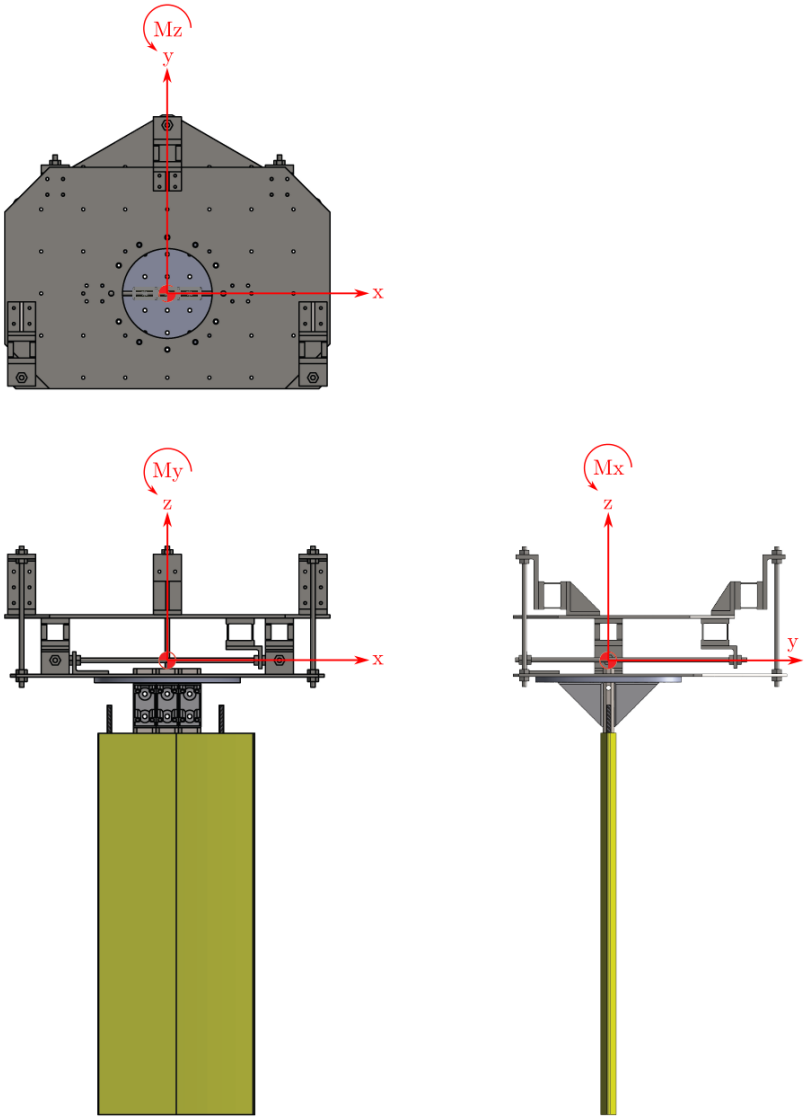

Figure 3.12: Reference frame detailed representation in the Semi-ogive hydrofoil

the size of the ripple, LE ventilation could be regulated rather than relying on naturally occurring droplets due to the rump-up at the leading edge. However, after multiple runs, the inception angle showed no variation with or without the pump, leading to the discontinuation of this approach (see Appendix C remarks for additional details).

3.4.4. Setup Alignment

The alignment procedure ensures that all systems, including the hydrofoil, align correctly with the reference frame. This subsection will explain the alignment processes for each system within the experimental setup. Additionally, an estimation of the measurement accuracy for each system will be provided, along with the overall accuracy for each principal axis. The alignment procedure follows a hierarchical order, starting with the Certus system, then the Hexapod and force balance, and concluding with the alignment of the hydrofoil.

The Certus system was aligned in two steps. First, the Y and Z axes were aligned. This was done by placing the reference plate on a pole at the bottom of the tank. By moving the

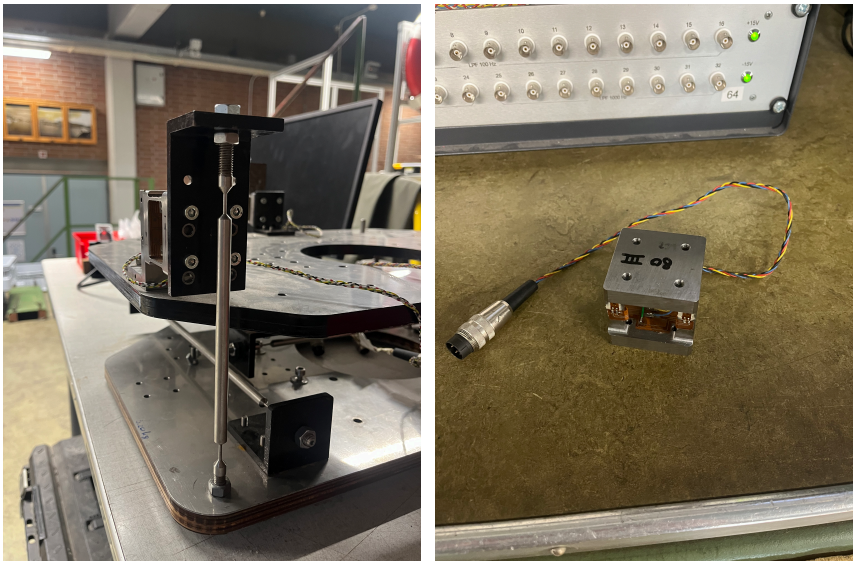

(a) Force sensor mounted on the 6-DOF frame

(b) Single load gauge

Figure 3.13: Force measurement instruments

carriage over a distance of $\pm 500mm$, the misalignment on the Y and Z axis could be measured. Then, the x-axis was defined by moving the pole over the bottom of the towing tank. The reference plate should be located in the same x and y plane as the first measurement, as the bottom of the towing tank is said to be flat. A maximum deviation of 0.1° is expected due to the misalignment of the carriage wheels. The pole was moved 300 mm, over which the height does not differ more than 0.25 mm. That being the case, a maximum deviation of 0.04° on the roll axis is expected. Therefore, an overall accuracy of $\pm 0.04^{\circ}$ can be assumed.

The Hexapod was calibrated using the Certus system. The Hexapod was moved along the three principal axes of the reference frame, and the deviations were measured. Euler angles were then calculated for each axis rotation. These corrections were subsequently applied to the Hexapod's configuration to ensure precise alignment.

The 6-DOF gauge was aligned by performing oscillations of $\pm 100mm$ and $f = 1.2s$ along the X and Y axes and looking for minimal combined deviation across both axes. The initial position was set at the aligned position of the Hexapod and Certus. At this stage, the system was configured without the hydrofoil. There is a final deviation of 0.1848 Rz for F_x and -0.1743 Rz for F_y, which are associated with the misalignment of the load gauges during the assembly of the 6-DOF plate. Overall, these values were obtained for a yaw offset -0.196° with respect to the initial position. The slightest deviation and cross-coupling for both axes was found in this position. However, due to the non-symmetry across the x-axis of the force balance a second alignment was performed. The force balance was calibrated using a laser orientated on the x-axis. The final correction was found to be -0.28°. This correction was introduced in the configuration of the Hexapod.

Once all systems were correctly aligned, the hydrofoils were adjusted by identifying the angle of attack (AOA) at which the lift reached zero, thereby eliminating misalignment. The procedure involved running the carriage at a fixed speed and varying the AOA in steps within the range of $-3^{\circ} < \text{AOA} < 3^{\circ}$. Output forces were plotted against the AOA, and a linear fit was applied to the lift data. The intersection of the fitted line with zero lift indicated the misalignment angle of -0.10° in yaw for both hydrofoils. Manual measurements were taken for pitch and

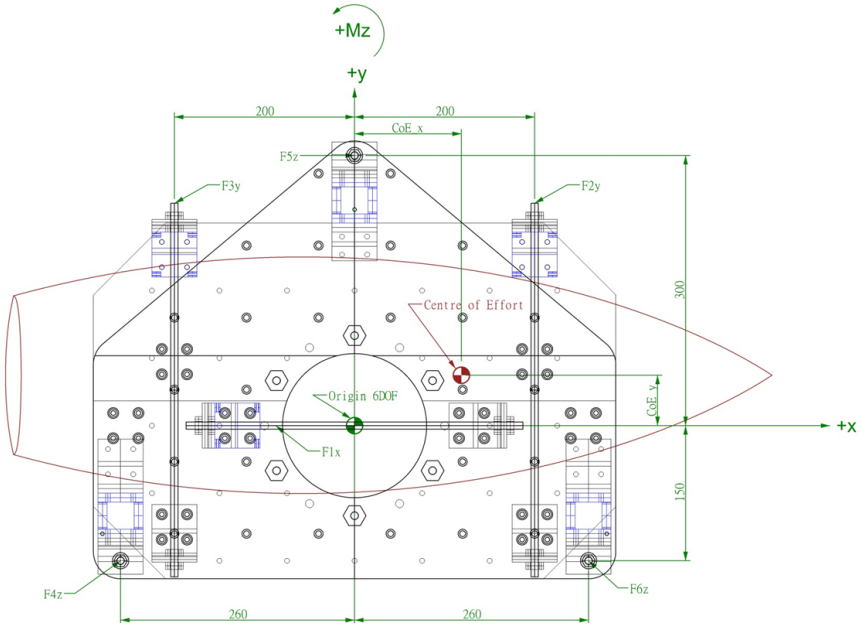

Figure 3.14: 6-DOF configuration

roll misalignments, recorded as $-0.45°$ and $-0.2°$, respectively. Note that the alignment of the systems was maintained when switching between hydrofoils, with only the hydrofoils being re-aligned. Due to the minimal variation in misalignment between the two hydrofoils, the corrections were kept the same.

Summing up all identified misalignments, Table 3.5 presents the complete set of corrections to be applied to the Hexapod configuration, ensuring that the hydrofoils are aligned with the reference frame.

Table 3.5: Corrections applied to the Hexapod configuration

	Units	Roll	Pitch	Yaw
Correction	deg	-0.2	-0.45	-0.37

3.4.5. 6-DOF Calibration

The calibration process for the 6-DOF load gauge involved two primary stages: first, the individual calibration of each load cell, followed by the combined calibration of the entire 6-DOF system, as illustrated in Figure 3.17. Given that the selected load cells have a linear relationship between voltage and load, this calibration aimed to establish this linear correlation and quantify the measurement uncertainty for each load cell and the complete 6-DOF system.

The load cells were securely bolted, and weights were gradually added to a hook suspended below them. Calibration was performed in positive and negative directions to assess the bidirectional response. After each weight was added, readings were taken following a set delay to minimize drift in the measured quantities. The measurements were taken for loading and unloading to assess the hysteresis effect. Once all measurements were recorded, a linear fit was applied to the data, allowing the error relative to the expected values to be assessed and the linearity error to be calculated.

Figure 3.15: Signal amplifiers and data acquisition (DAQ) system used to amplify and capture force measurements from multiple sensors.

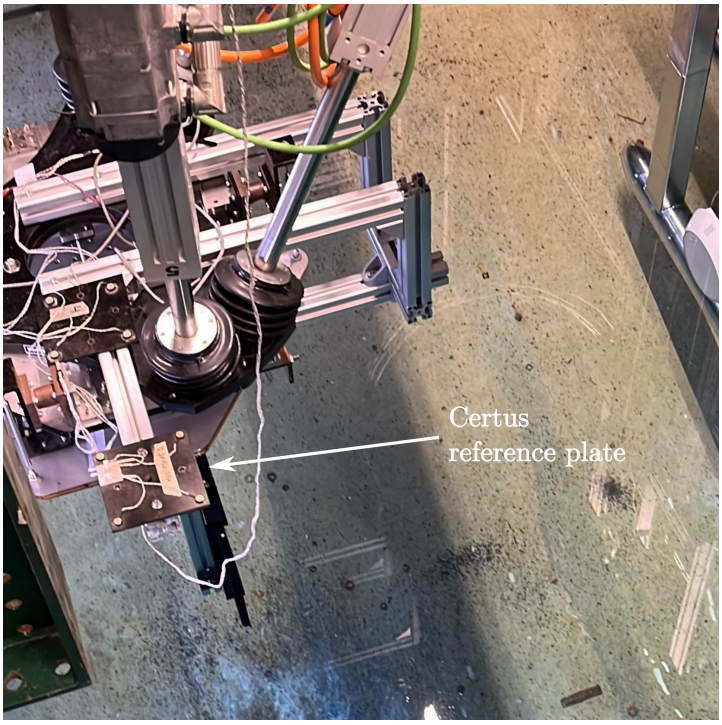

Figure 3.16: Certus reference plate

$$\begin{bmatrix} F_x \\ F_y \\ M_z \end{bmatrix} = \begin{bmatrix} F2Y & F3Y & F1X \end{bmatrix} \begin{bmatrix} -0.4126 & 143.7645 & 28.7233 \\ 0.6965 & 144.9642 & -28.9496 \\ 69.7757 & -0.0272 & 0.0527 \end{bmatrix} \tag{3.3}$$

After individually calibrating each load cell, the 6-DOF system was assembled within a reference frame to minimize potential interference between the load gauges. To calibrate the system, weights were applied through distinct load configurations to capture the FX, FY, and MZ components. This approach allowed for an evaluation of cross-interference among the load cells. The calibration procedure was repeated over multiple runs to assess repeatability and quantify measurement error. Finally, an ordinary least-squares (OLS) fit was applied to the measured data against the predicted forces, yielding the calibration matrix shown in Equation 3.3. This matrix converts the load gauge readings into forces along the principal axes while accounting for interference between the load cells. The uncertainty on the measurement will be discussed in section 3.8.

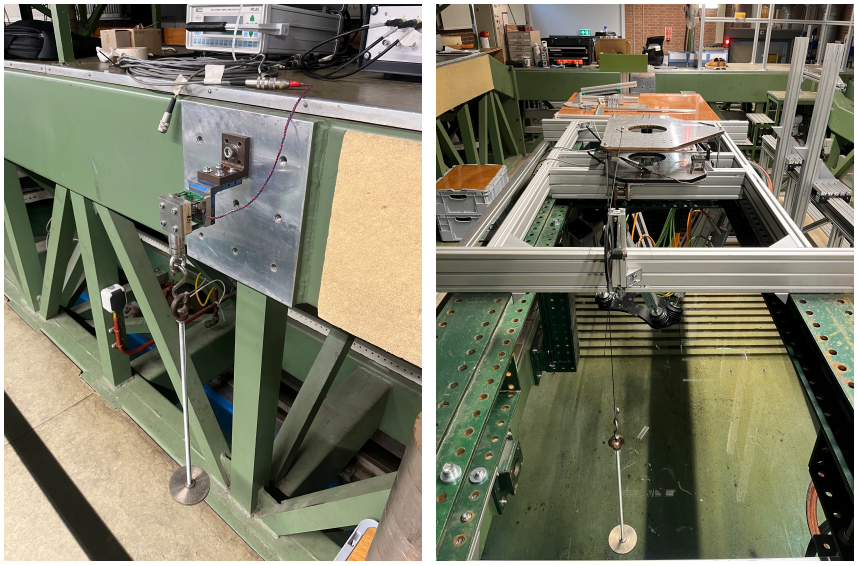

(a) Single cell load calibration **(b)** Full board calibration

Figure 3.17: 6-DOF Gauge Calibration

3.4.6. Camera Systems and Synchronization

Low-speed videography for the towing-tank experiments was captured using four cameras: two LaVision® cameras for underwater visualization and two Basler® cameras for above-water shots The LaVision cameras recorded at a resolution of 2048 × 2048 pixels at 100 Hz, while the Basler cameras recorded at 1920 × 1200 pixels In some trials, the frame rate was reduced to 50 Hz to capture the entire run, as noted in the comments of Appendix C. The positioning of the cameras is shown in Figure 3.18, following the model setup described in Figure 3.10.

The camera setup consisted of two camera sets configured to achieve stereo vision of the free surface and ventilated areas Two cameras were positioned at 90 degrees to the hydrofoil's field of view, while the other two were angled to create stereo vision The field of view for the underwater cameras was adjusted to ensure that the free surface and the foil's tip were visible at all angles for $AR = 1$ However, this configuration did not allow visibility of the tip at $AR = 1.5$, due to limited field of view For the above-water cameras, the field of view was

off-centred on the foil in the direction of the incoming flow to capture the wake Views from each camera are depicted in Figure 3.19 and 3.20.

The camera module was securely fixed to the towing tank's carriage and reinforced to maintain rigidity and minimize vibrations during testing. To protect the underwater cameras, they were housed in streamlined "torpedoes," which acted as waterproof enclosures. Additional streamlined bodies were fitted to the base of these torpedoes to minimize interference with the hydrofoils. The lighting setup used LED strips and an LED panel. These were strategically positioned to illuminate the hydrofoil and ensure optimal camera visibility, avoiding the reflections as much as possible.

LaVision® cameras were controlled using their commercial DaVis software, while Basler® cameras were managed through an in-house script. Both camera systems were synchronized using a common trigger signal provided by the DaVis software via the Programmable Timing Unit (PTU), see Figure 3.21. This trigger signal was also routed to an Arduino® Uno, which generated a 5V pulse reflecting the timing of the trigger signal into the Data Acquisition (DAQ) system. This allowed the measured forces to match their corresponding camera frames accurately. The files containing the frames were saved after each run, with filenames corresponding to the run time and number, ensuring proper identification and tracking. All frame manipulation was completed using a combination of DaVis and Python™.

An additional Nikon® Z 6II camera was used during specific runs to capture a detailed view of the trailing edge during ventilation formation. This was done solely to record supplementary visual footage and was not part of the former videography setup for the experimental campaign.

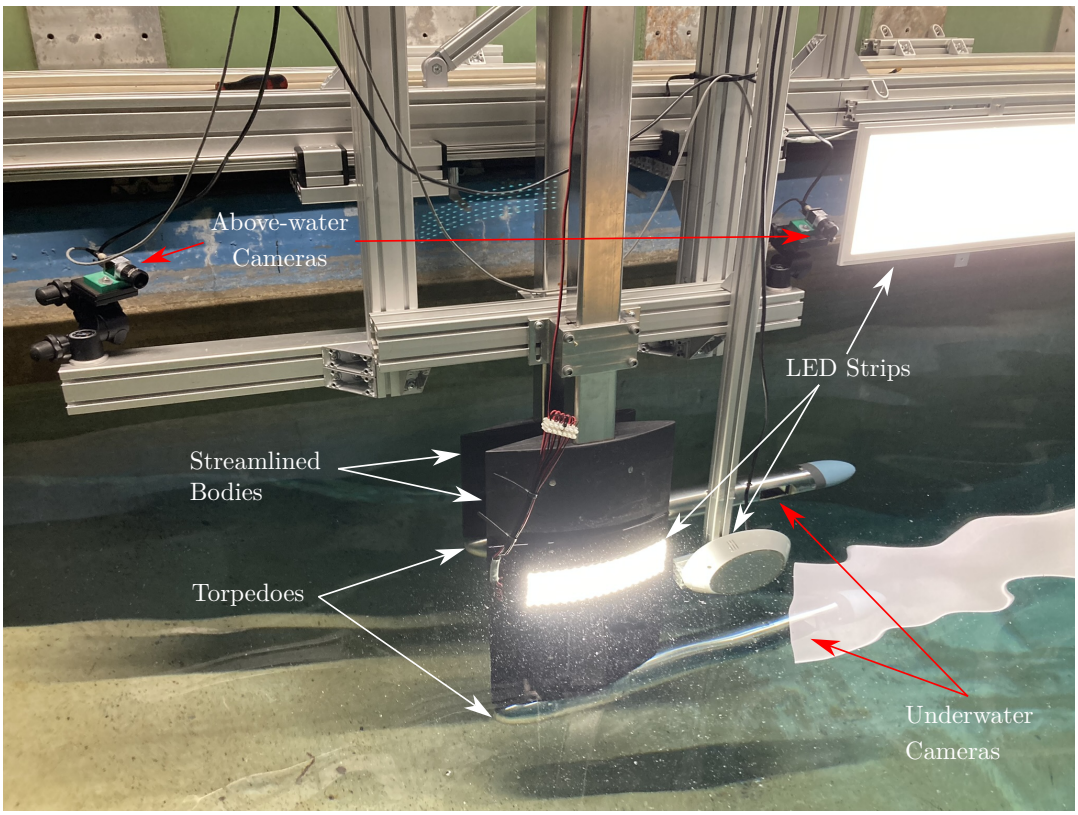

Figure 3.18: Cameras module for both underwater and above-water views The underwater cameras are mounted on torpedo-shaped structures equipped with streamlined bodies to minimize wave interference. Additional instrumentation, such as LED strips, is also shown.

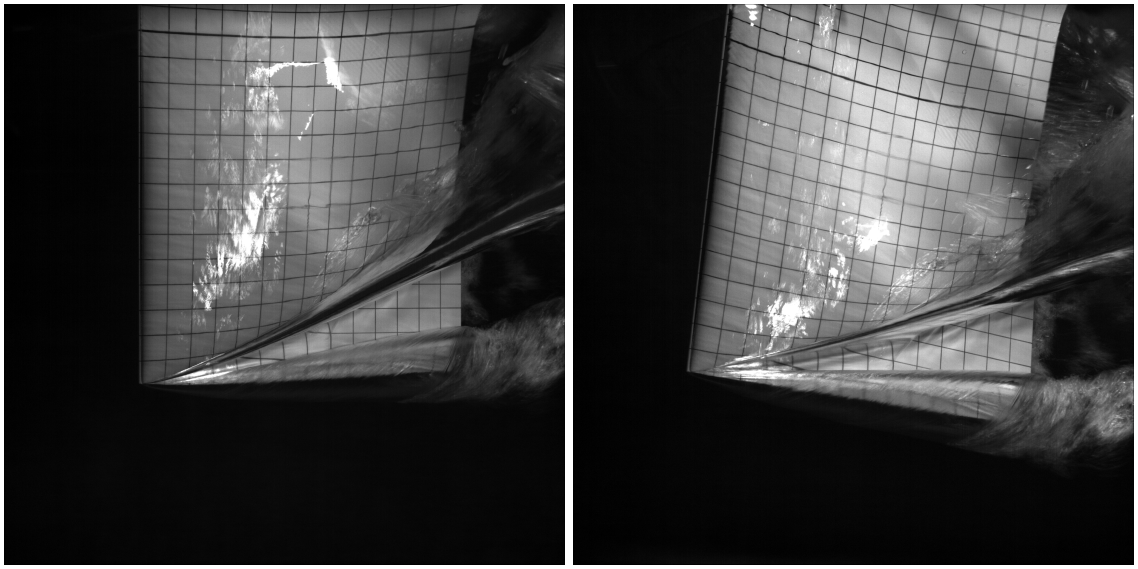

(a) 90 degrees underwater camera **(b)** Angled underwater camera

Figure 3.19: Views from LaVision® cameras installed during the experimental campaign. Both cameras look at the suction side of the hydrofoil.

3.4.7. Stereo Camera Calibration

Stereo camera calibration is a process used to precisely determine the relative position and orientation of cameras with respect to a 3D calibration plate This step is crucial for accurately capturing 3D points from the acquired images, enabling the precise reconstruction of different structures in the pictures Through this procedure, an epipolar plane is established, allowing any visible point to be located along an epipolar line The cameras were calibrated using a Type 31 3D calibration plate for stereo calibration, as shown in Figure 3.22. The calibration plate features several rows of points at known heights, facilitating the calibration process.

For the LaVision® cameras, their commercial software DaVis automatically performed the calibration procedure. In contrast, the Basler® cameras were calibrated using an in-house point detection script This script processes several images of a 3D calibration plate positioned in different locations with known coordinates Markers in the images are detected and triangulated to generate 3D coordinates, which are then transformed into the desired reference frame and used to create the epipolar plane To verify the accuracy of the calibration, the 3D points are re-projected back onto the 2D images to calculate the fit error This error ranged between 0.17 and 0.4 pixels for the underwater cameras, while for the above-water was approximately 0.17 pixels These values indicate that the calibration is accurate, meaning that the extrinsic and intrinsic parameters are well-calibrated.

This calibration procedure was performed after every significant change in the setup, such as changing the AR or switching between hydrofoils.

3.4.8. Data Acquisition System

Data acquisition was managed by four dedicated computers: one for speed and acceleration control, two for camera operations, and one for force and position measurements. The arrangement and connections are summarized in the following subsection.

Force, speed, and position signals were initially measured as analog voltages, filtered with a

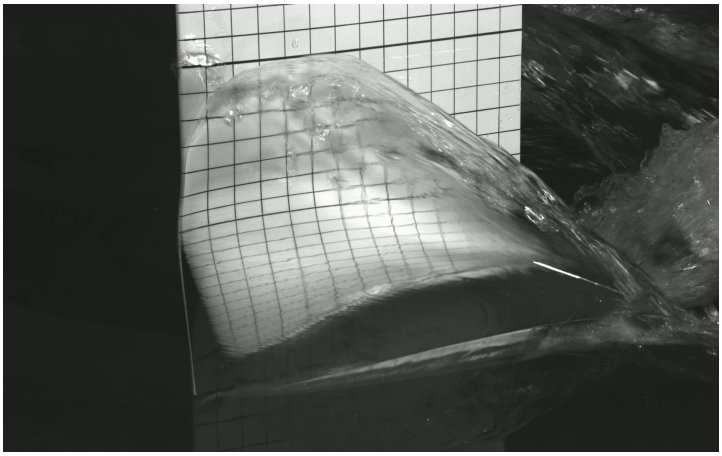

(a) 90 degrees above-water camera

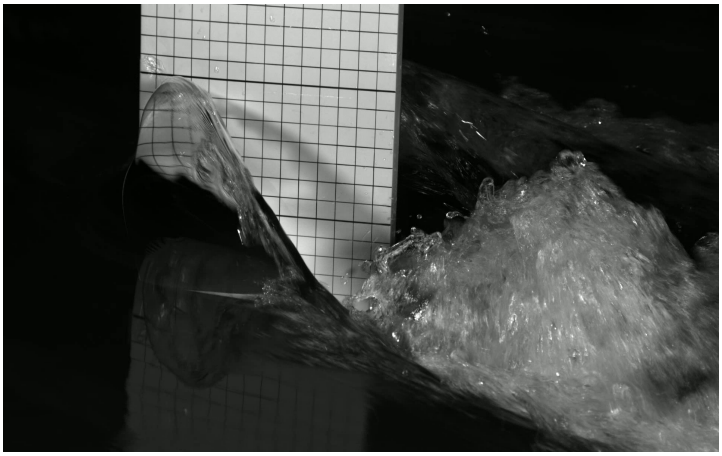

(b) Angled above-water camera

Figure 3.20: Views from Basler® cameras installed during the experimental campaign. Both cameras look at the suction side of the hydrofoil.

100 Hz low-pass filter, and then converted into binary data. The filter specifications are preset by the Delft towing tank system and are integrated within the DAQ unit shown in Figure 3.15. For each run, two binary files containing the force and position data, along with a configuration file, were saved.

Image files from the LaVision® system were saved directly into their commercial software, Davis, while Basler® images were stored as a "pickle" file containing all frames and associated metadata. Additionally, the trigger signal was sent into the DAQ system, where it was converted into a digital format.

3.4.9. Instrumentation overview

A schematic overview of the instrumentation setup is shown in Figure 3.23

3.5. Force Predictions

Force predictions were based on the experimental results of Harwood et al. [2], who used the same semi-ogive hydrofoil. Identical coefficients were assumed for the NACA0010-34 hydrofoil.

Figure 3.21: Programmable Timing Unit that controls the trigger signals received by the cameras.

The maximum forces are expected at an aspect ratio of 1 and a Froude number of 2.5 (see section 3.6 for details on the test matrix). Under these conditions, the predicted maximum drag, lift, and yaw moment values are 200 N, 450 N, and 25 Nm, respectively. The maximum forces for each load cell in the most demanding conditions are presented in Figure 3.24. For this configuration, load cells 1, 2, and 3 require a full-scale capacity of 400 N, while load cells 4, 5, and 6 need a full-scale capacity of 800 N.

The forces and moments acting on the hydrofoil are calculated using the following recalled equations for the lift, drag, and moment coefficients:

$$C_{L_{3D}} = \frac{L}{\frac{1}{2}\rho V^2 hc} \tag{2.11a}$$

$$C_{D_{3D}} = \frac{-D}{\frac{1}{2}\rho V^2 hc} \tag{2.11b}$$

$$C_{M_{3D}} = \frac{M}{\frac{1}{2}\rho V^2 hc^2} \tag{2.11c}$$

where $C_L = 0.65$, $C_D = 0.3$ and $C_M = 0.12$ (Based on experiments by Harwood et al. [2]).

The forces and moments measured in the 6-DOF reference frame are converted into the forces acting on each load cell using the transformation matrix. This matrix describes the geometric configuration of the load cells in the system, taking into account the positions and orientations of the cells. The load cell positions in the system are depicted in Table 3.4. This relation is expressed through the following matrix equation.

$$\begin{bmatrix} F_x \\ F_y \\ F_z \\ M_x \\ M_y \\ M_z \end{bmatrix}_{6DOF} = A_{f6DOF} = \begin{bmatrix} 1.0 & 0.0 & 0.0 & 0.0 & 0.0 & 0.0 \\ 0.0 & 1.0 & 1.0 & 0.0 & 0.0 & 0.0 \\ 0.0 & 0.0 & 0.0 & 1.0 & 1.0 & 1.0 \\ 0.0m & 0.0m & 0.0m & -0.15m & 0.3m & -0.15m \\ 0.0m & 0.0m & 0.0m & -0.26m & 0m & 0.26m \\ 0.0m & 0.2m & -0.2m & 0.0m & 0.0m & 0.0m \end{bmatrix} \begin{bmatrix} F1X \\ F2Y \\ F3Y \\ F4Z \\ F5Z \\ F6Z \end{bmatrix} \tag{3.5}$$

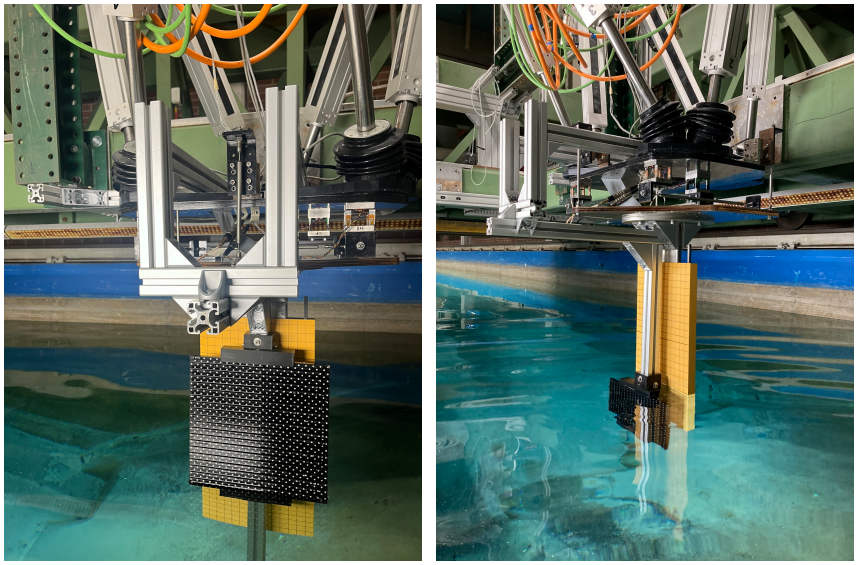

(a) Above-water camera calibratrion **(b)** Underwater camera calibration

Figure 3.22: Type 31 3D calibration plate in front of the hydrofoil.

The forces in each load cell were calculated using the established transformation matrix. The next step is to visualize how these forces evolve as the configuration of the 6-DOF force balance rotates The configuration ranges from 0 degrees, representing the initial setup as shown in Figure 3.12, to 90 degrees, corresponding to a positive rotation about the M_z axis Figure Figure 3.24 illustrates how the forces in each load cell vary with this rotation, providing insight into the distribution of forces across different configurations.

The load cells along the y-axis, FY, reach their maximum value at around 25 degrees, while the load on cell F_1 becomes zero at this point. This angle represents the configuration where the foil is expected to generate its predicted forces. As the rotation continues, the load along the x-axis increases steadily, reaching its peak at 90 degrees, indicating a clear shift in force distribution towards the x-axis as the system approaches full rotation.

Notably, the load cells in the z-direction experience the most significant forces overall, likely due to the location of the centre of effort of the foil. The lift force is mainly distributed between load cells 2 and 3, with F_{2Y} taking a more significant share of the load due to the positive M_z moment. This moment induces an imbalance in the lift distribution, causing F_{2Y} to carry more force than F_{3Y}.

Therefore, based on the maximum expected forces in each load cell, the full-scale capacity can be appropriately selected Load cells $F4Z$, $F5Z$, and $F6Z$, as previously mentioned, will be replaced with non-instrumented load cells, as their measurements are not required For load cells $F2Y$ and $F3Y$, considering that the lab has three types of load cells available—200 N, 400 N, and 800 N—load cells with an 800 N capacity were selected Although 400 N load cells would have been preferable, there were not enough available to equip both load cells in the same direction Therefore, 800 N-load cells were equipped This option provides a broader range for higher-speed conditions while still maintaining accuracy for the lower-speed ranges of 25N Finally, load cell $F1X$ was chosen to have a 400 N capacity, as this best fits the expected force distribution along the x-axis The chosen sensor ranges are shown in Table 3.6

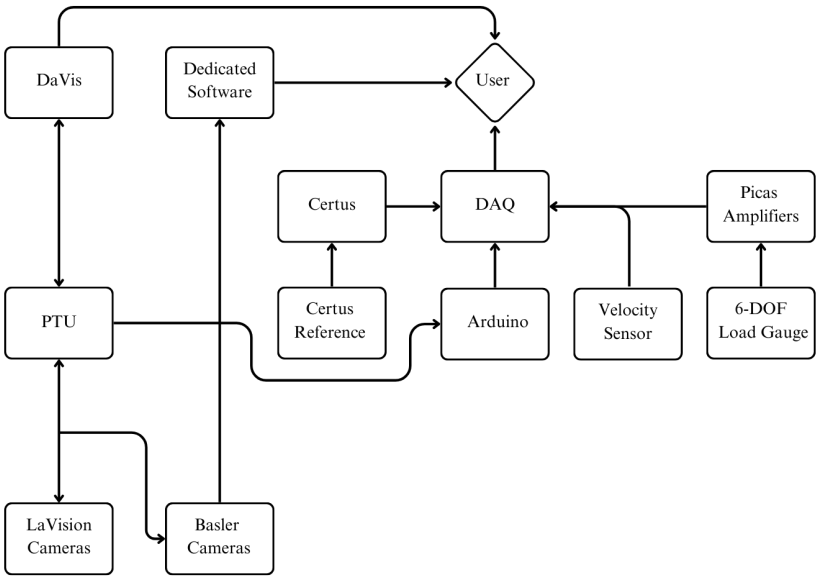

Figure 3.23: Schematic overview of the intruments

Table 3.6: Cell gauge full-range

	Units	F1X	F2Y	F3Y	F4Z	F5Z	F6Z
Full-Load	N	400	800	800	-	-	-

3.6. Method

This section describes the methodology used during the experimental campaign for both hydrofoils. A complete list of all conditions tested in the towing experiments is provided in Appendix C. The methodology was divided into two main phases:

1. **Static tests:** Runs were conducted at a constant angle of attack (AoA) to validate the test geometries by comparing results with previous experimental campaigns.
2. **Quasi-static tests:** Runs involved varying the AoA to evaluate its effect on ventilation susceptibility.

3.6.1. General Considerations

This subsection outlines key considerations for both testing phases and hydrofoils. All tests were conducted in calm water.

Each run followed a standardized procedure. The amplifiers were zeroed before every run to eliminate residual effects from previous measurements. A waiting period of approximately 30 minutes was established between runs to allow the water to return to calm conditions, for higher speed this time as increased. Before each test, a zero run was recorded without moving the hydrofoil or carriage. This run was then subtracted from the test data to obtain the true zero.

The experimental campaign began with tests on the Semi-ogive hydrofoil. Once these tests were completed, the Semi-ogive was replaced with the NACA0010-34 hydrofoil, requiring a

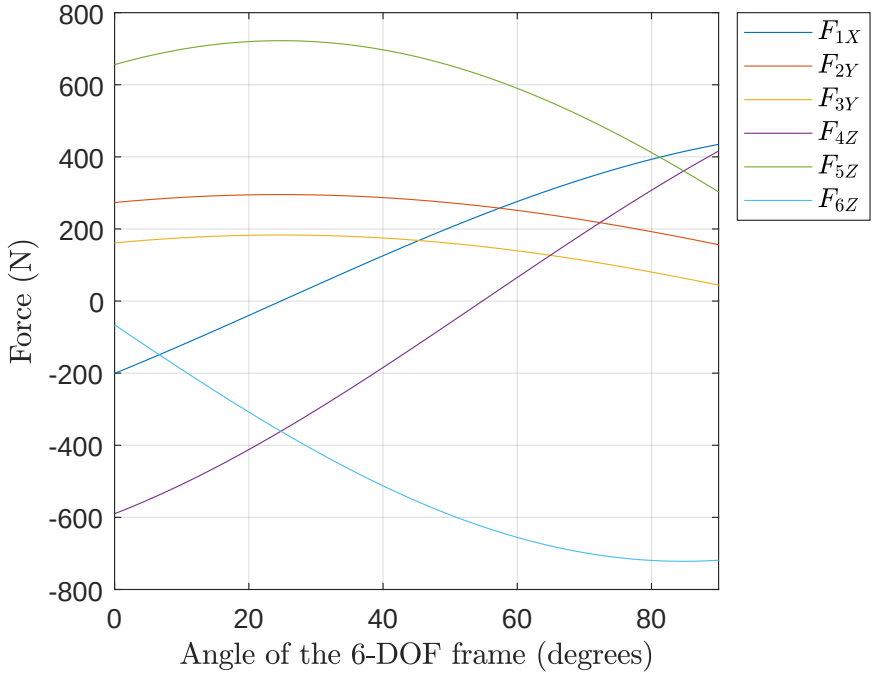

Figure 3.24: Predicted forces for the load gauges in the 6-DOF force balance across a range of configurations from 0 to 90 degrees.

recalibration of all systems. Due to differences in the centre of rotation between the hydrofoils, the camera frame had to be adjusted by a few centimetres and recalibrated. After completing the calm water tests, a campaign was conducted with the NACA0010-34 hydrofoil to assess ventilation inception under wave conditions. However, this is out of the scope of this thesis.

3.6.2. Static Tests

The static tests were designed to replicate previous experiments on ventilated hydrofoils. Specifically, those documented by Harwood et al. [2]. The objective was to induce ventilation at the acceleration stage, following the approach described by Harwood et al. [2]. The approach is illustrated in Figure 3.25.

The approach maintained a constant angle of attack (AoA) as the foil accelerated to a specified speed, after which both speed and AoA were held constant for the remainder of the test. Only a Froude number of $Fn_h = 1.5$ was evaluated. The AoA was adjusted in four-degree increments for non-critical angles and two-degree increments near stall. This setup was chosen to validate the models, as a single Froude number was sufficient to confirm geometric consistency. Additionally, this test aimed to estimate the AoA at which ventilation triggered during acceleration—a crucial insight for the remaining experimental phase, given that the towing tank's limited length prevents starting at an AoA of 0°, if a quasi-static state is to be maintained. A summary of the test conditions follows in Table 3.7

Table 3.7: List of static tests. The angle of attack is fixed at this test.

Aspect Ratio	Froude Number	Angle of Attack
1	1.5	0, 4, 8, 12, 14, 16, 18, 20
1.5	1.5	0, 4, 8, 12, 14, 16, 18, 20

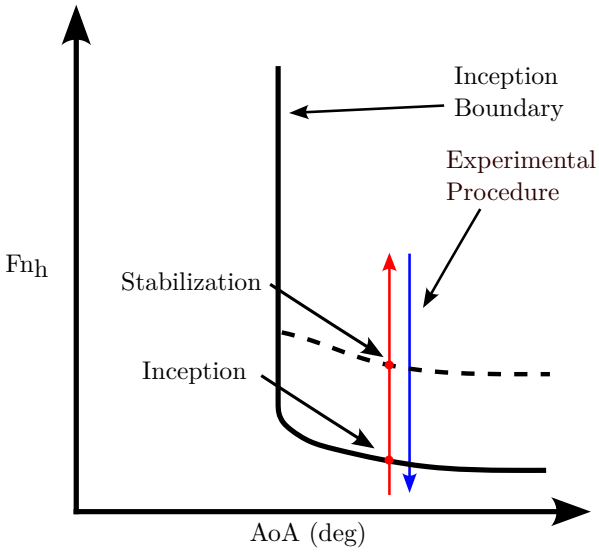

Figure 3.25: Experimental procedure performed by Harwood et al. [2], illustrated in the $\alpha - Fn_h$ parametric space. The two stages are represented as acceleration (red) and deceleration (blue). The inception boundary is based on experiments by Harwood et al. [2].

For certain conditions, the run at $AoA = 20°$ was replaced with a run at an AoA closer to the point where ventilation was triggered. This approach provided greater resolution on the critical AoA associated with ventilation inception.

3.6.3. Quasi-Static Tests

This phase aims to improve the understanding of ventilated flow formation through a methodology that has not yet been experimentally tested. As noted in previous chapters, prior experiments have primarily focused on the transient effects in ventilation inception by quasi-statically varying velocity. Harwood et al. [2] contributed significantly to this area by developing a parametric framework that maps AoA and Fn_h across distinct flow regimes, as shown in Figure 2.11. However, it remains uncertain whether this map fully captures the effects of varying AoA on ventilation, as it was developed by solely adjusting speed and acceleration. To address this gap, the quasi-static tests were designed to vary AoA during the run in a controlled, quasi-static manner. To eliminate any transient effects associated with acceleration, the foil was accelerated at a shallow angle below the thresholds for ventilation formation, identified in the initial phase of the experiments. The anticipated ventilation formation for this phase of testing is through spontaneously induced mechanisms, such LE ventilation, Rayleigh-Taylor ventilation or TE ventilation. However, tip-vortex or TE inception are unlikely, as the test speeds are too low for this mechanisms to trigger ventilation. Harwood et al. reported TE-induced- tip-vortex formation at $Fn_h = 3.5$, leaving LE and Rayleigh ventilation as the primary mechanisms.

Approach

The main approach for each run is presented in the $\alpha - Fn_h$ parametric space in Figure 3.26 and consists of three key stages: the acceleration stage, the AoA variation stage, and the deceleration stage. During the acceleration stage, the strut was brought to the target speed at $0.3 m/s^2$, the maximum achievable by the carriage without causing wheel slip. This stage was executed as quickly as possible to maximize the available time for the AoA variation stage. While an initial AoA estimate was obtained from the previous phase, slight adjustments were

necessary due to its dependency on Fn_h and AR_h.

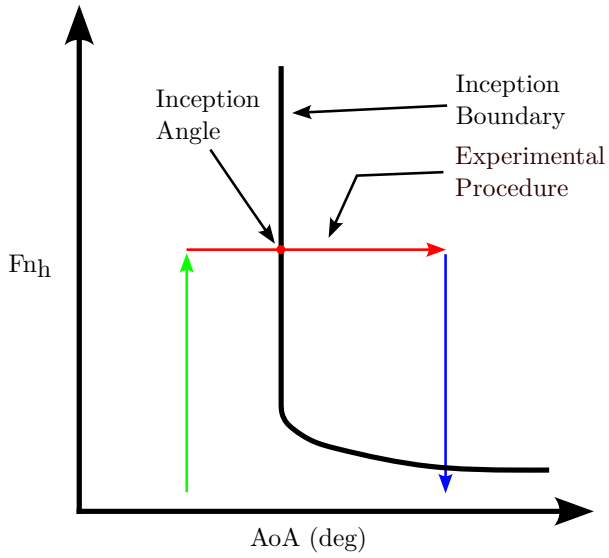

Figure 3.26: Experimental procedure illustrated in the $\alpha - Fn_h$ parametric space. The three stages are represented as follow: acceleration (green), AoA variation (red) and deceleration (blue). The inception boundary is based on experiments by Harwood et al. [2].

The AoA variation stage began near the end of the acceleration phase, with the hexapod executing a calculated rotational motion to adjust the foils from their initial AoA to a target AoA. This stage aimed to create a controlled rotation to facilitate ventilation inception. However, due to manual initiation control, the exact frame marking the transition from acceleration to AoA variation was imprecise, occasionally causing the rotation to start slightly earlier or later. The yaw motion was governed by the turnover rate, set as high as possible in each run to approximate quasi-static conditions, which are discussed further in this subsection.

Initial estimates based on Harwood et al. [2] suggested that ventilation would form around a stall AoA of 15°. However, it became evident that significantly higher angles were required. Consequently, the target AoA was determined through trial-and-error adjustments for each condition, as it varied considerably with changes in Fn_h during the experiments. Ventilation inception was expected to occur during the yaw motion stage, but any runs that exhibited ventilation precisely at the beginning or end of the motion were discarded, as this was likely induced by the motion itself rather than natural flow conditions.

The motion generally concluded before the deceleration stage began, allowing some frames to be recorded under steady-state conditions. However, due to the limited length of the towing tank, this was not always achievable, and in some cases, the deceleration stage started just before the end of the motion, leaving no opportunity for steady-state conditions. During this stage, the cameras were manually triggered, typically capturing 3000 frames.

The deceleration stage was automated, with the carriage programmed to stop upon reaching a specified position and speed within the towing tank. This stage also included the additional time at the end of each run for the instruments to complete data recording.

Figure 3.27 illustrates the typical variations in speed and AoA for a run and in specific run 1152, showing the progression through the three key stages: acceleration (Acc), AoA variation (AoA var), and deceleration (Decel). This figure highlights the adjustments made to achieve the target speed and angle of attack.

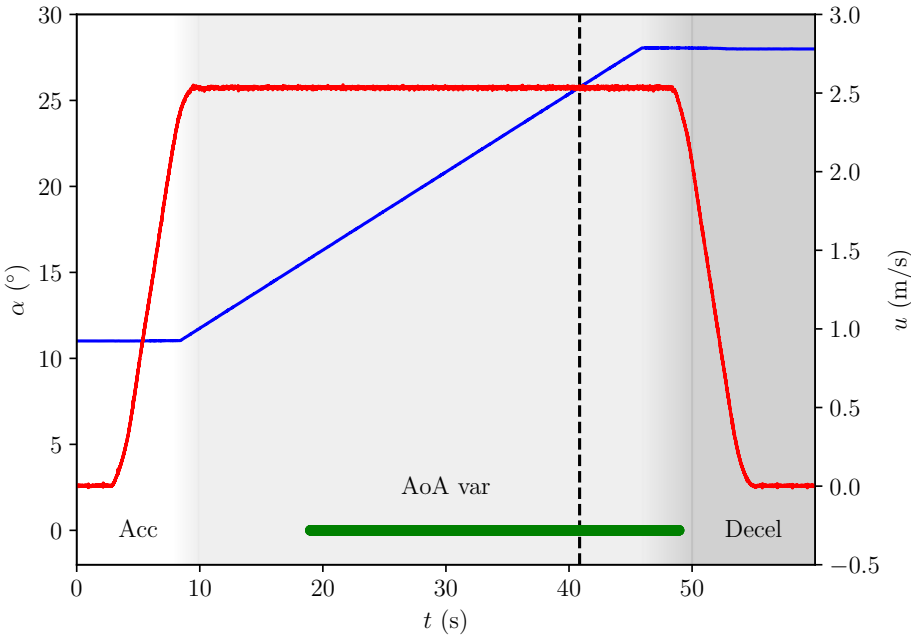

Figure 3.27: Variations in AoA and speed throughout run 1152. Green dots represent the acquired images, and the horizontal line indicates the point of ventilation inception. The three stages are denoted as acceleration (Acc), AoA variation (AoA var) and deceleration (Decel). White and grey backgrounds indicate a transition within stages.

Quasi-static state

As previously noted, the yaw rotation was conducted quasi-statically, with a rate determined by the convective timescale, c/u, to maintain consistent quasi-steady conditions across the range of Froude numbers. The convective timescales per degree were affected by factors including the towing tank length, carriage acceleration, degree range, and Froude number. Given the towing tank specifications and the intended Fn_h range, the minimum rate of angle of attack was set at $(u/c)/20$. This rate change varied between the minimum for the higher Fn_h and $(u/c)/30$ for the lower.

The convective timescale defines the characteristic duration for a fluid particle to traverse a given length scale, specifically the chord length in this context. This selected timescale indicates that for each degree of rotation, 20 to 30 timescales are needed.

To verify the quasi-static condition, it is essential that the yaw rotation does not influence the measured forces. This implies that the results obtained under steady-state and quasi-static conditions should be consistent. Specifically, for the tested scenarios, both static and quasi-static tests were conducted at $Fn_h = 1.5$. When comparing these tests, the slope of the relationship between lift and angle of attack should remain identical. This is illustrated in Figure 3.28 and Figure 3.29 for the two tested geometries.

The lift trend under quasi-static conditions closely follows the same pattern as observed in the static tests. However, at $\alpha \approx 21°$ there is a noticeable shift in the lift trend. This change is likely associated with the interaction between the hydrofoil and fluid dynamics phenomena. By analysing the linear trends, the slope can be determined, allowing for the calculation of the relative error between the quasi-static and static tests. These findings are summarized in

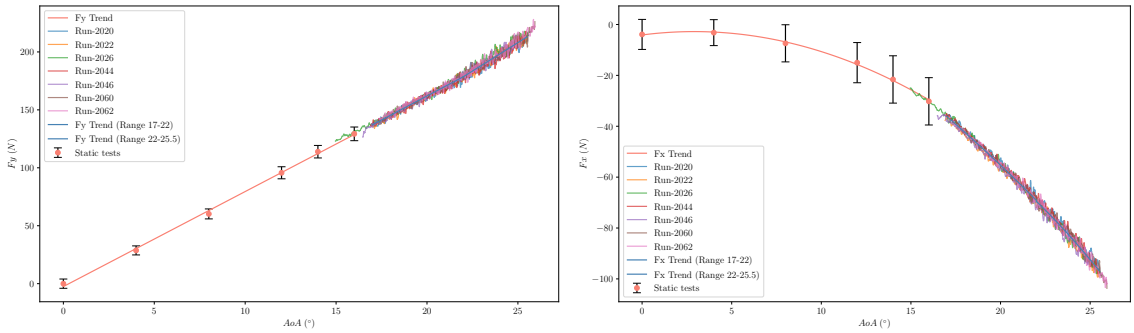

(a) Lift **(b)** Drag

Figure 3.28: Measured hydrodynamic lift and drag for the NACA hydrofoil at an $AR = 1$ and $Fn_h = 1.5$, for the "Static" and "Quasi-static" tests. The data is fitted with a linear trend for lift and quadratic for drag.

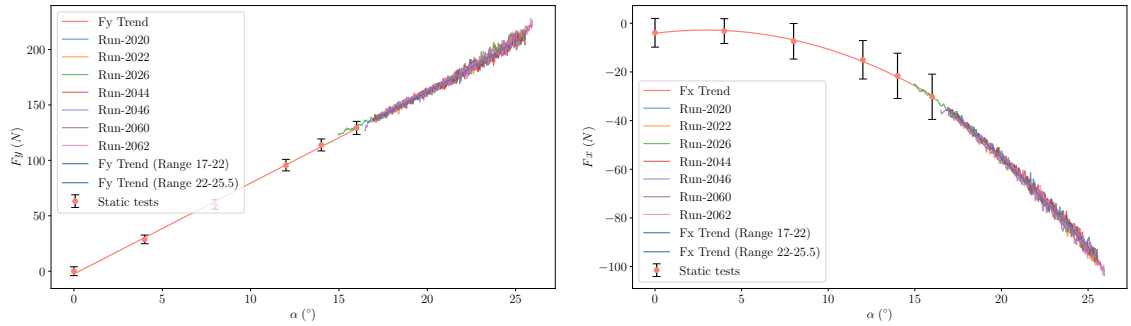

(a) Lift **(b)** Drag

Figure 3.29: Measured hydrodynamic lift and drag for the Semi-ogive hydrofoil at an $AR = 1$ and $Fn_h = 1.5$, for the "Static" and "Quasi-static" tests. The data is fitted with a linear trend for lift and quadratic for drag.

Table 3.8.

Table 3.8: Relative error in the Lift-AoA slope

NACA			Semi-Ogive		
Static	Quasi-Static	Error	Static	Quasi-Static	Error
8.2	8.272	0.87 %	7.178	7.299	1.67 %

The results indicate that the relative error is within the 2% which is below the standard deviation on the measurement for both test conditions. Consequently, it can be assumed that the experiments are conducted under quasi-steady conditions. Several runs were conducted using 20 or 30 convective timescales for $Fn_h = 1.5$ for the NACA hydrofoil. The results indicate no significant variation in the onset of ventilation or the forces.

Test Conditions

Tests were conducted across nine Froude numbers (Fn_h) ranging from 0.5 to 2.5, with aspect ratios (AR) of 1 and 1.5. However, due to the force balance's capacity limitations, tests at $AR = 1.5$ were capped at $Fn_h = 1.5$. For each condition shown in Table 3.9 and Table 3.10, at least three runs were performed to ensure statistical reliability. Additional runs were carried out for cases with high uncertainty in the inception angle of attack (α_i) to improve data robustness. Further tests were also conducted at $Fn_h = 1.5$ and $AR = 1$ for the NACA0010-34 profile, as

this condition was the main focus of the subsequent experimental campaign on ventilation in waves.

Table 3.9: Test Conditions at $AR = 1$ for the Semi-ogive and NACA0010-34 hydrofoils, respectively.

Froude Number	Towing velocity	Turnover	Alpha rate of change
Fn_h	u	t_c	$\dot{\alpha}$
Unit	m/s	deg.	deg./s
0.5	0.83 / 0.86	30 / 30	0.10
0.75	1.24 / 1.29	30 / 30	0.15
1.00	1.66 / 1.72	30 / 30	0.20
1.25	2.07 / 2.14	25 / 25	0.3
1.50	2.48 / 2.57	20 / 25	0.44 / 0.34
1.75	2.90 / 3.00	20 / 25	0.52 / 0.40
2.00	3.31 / 3.43	20 / 25	0.59 / 0.46
2.25	3.73 / 3.86	20 / 20	0.67 / 0.64
2.5	4.14 / 4.29	20 / 20	0.74 / 0.71

Table 3.10: Test Conditions at $AR = 1.5$ for the Semi-ogive and NACA0010-34 hydrofoils, respectively.

Froude Number	Towing velocity	Turnover	Alpha rate of change
Fn_h	u	t_c	$\dot{\alpha}$
Unit	m/s	deg.	deg./s
0.5	1.01 / 1.05	30 / 30	0.12
0.75	1.52 / 1.58	30 / 30	0.18
1.00	2.06 / 2.10	20 / 20	0.36
1.25	2.53 / 2.63	20 / 25	0.45 / 0.35
1.50	3.04/ 3.15	20 / 25	0.54 / 0.42

3.6.4. Experimental Matrix

The following test matrices indicate the conditions of testing for each hydrofil.

Table 3.11: Test matrix

Hydrofoil Models		Semi-ogive	NACA 0010-34	Units
Tip Immersion	h	279.4, 419.1	300, 450	mm
Immersed Aspect Ratio	$AR_h = \frac{h}{c}$	1.0, 1.5	1.0, 1.5	-
Velocity	U	0.83 - 4.14	0.86 - 4.29	m/s
Depth Froude #	$Fn_h = \frac{U}{\sqrt{gh}}$	0.5 - 2.5	0.5 -2.5	-
Chord Reynolds #	$Re_c = \frac{Uc}{\nu}$	2.1×10^5 - 1.1×10^6	2.4×10^5 - 1.2×10^6	-
Yaw angle	α	0 - 30	0 - 30	deg
Weber Number	$We = \frac{\rho U^2 c}{\gamma}$	2.6×10^3 - 6.6×10^4	3×10^3 - 7.6×10^4	-
Vaporous Cavitation #	$\sigma_v = \frac{P_{atm} - P_v}{\rho U^2/2}$	11.44 - 284.78	10.65 - 265.25	-

3.7. Post-processing

A total of 148 runs were conducted, with data collected from each. This includes 80 runs with the semi-ogive hydrofoil and 68 runs with the NACA0010-34. The run identifiers follow the formats 1xxx, 2xxx, or 3xxx, representing the semi-ogive hydrofoil, the NACA0010-34, in

calm water and wave conditions, respectively. Collected data encloses all instrument outputs, including videography, force, and position measurements.

3.7.1. Filtering

Typically, the phenomena of interest occur at low frequencies (below 1 Hz). Therefore, the raw signal, sampled at 1000 Hz, was filtered to remove high-frequency noise caused by facility vibrations. Two filters were applied to the force measurements for optimal noise reduction and data clarity.

First, a notch filter was applied to attenuate the hydrofoil's natural frequency, identified through a decay test. This step was essential to eliminate resonant frequencies inherent to the hydrofoil, providing a clearer view of the primary forces acting on the system. Subsequently, a zero-phase 5th-order low-pass Butterworth filter with a 1 Hz cutoff frequency was applied to isolate the main components and reduce high-frequency noise, effectively retaining only the relevant low-frequency signals.

The carriage velocity and measurements from the Certus system showed a very low standard deviation, making filtering unnecessary for these variables. This is also evident in Figure 3.27, where the speed and yaw rotation are presented as raw data.

3.7.2. Force Rotation

The forces due to hydrodynamic effects are required in the global reference frame. After filtering the data obtained for each load cell, the forces are calculated using Equation 3.3. The resulting force vector is described as $\left[F_x, F_y, M_z\right]^{6DOF}$. To express this force vector in the global reference frame, a rotation by the AoA is required, as shown in Equation 3.6.

$$\begin{bmatrix} F_x \\ F_y \\ M_z \end{bmatrix}^{Ref.frame} = \begin{bmatrix} \cos AoA & \sin AoA & 0 \\ -\sin AoA & \cos AoA & 0 \\ 0 & 0 & 1 \end{bmatrix} \cdot \begin{bmatrix} F_x \\ F_y \\ M_z \end{bmatrix}^{6-DOF} \tag{3.6}$$

The final forces were then used to compute non-dimensional coefficients, including the lift, drag, and moment coefficients (C_L, C_D and C_M), to analyse the effect of ventilation on the forces over time. For the ventilation analysis, the forces were plotted both with and without the low-pass filter applied. The non-dimensional force coefficients were typically calculated over the 1-second interval preceding inception, allowing for comparison with the semi-empirical formula derived by Damley-Strnad et al. [48].

3.7.3. Ventilation

The ventilated flows were investigated visually using the videography from both above and underwater cameras to determine factors such as the inception frame, flow regime, or the free surface's position before ventilating. From this data and the trigger signal, each run's inception angle (α_i) was found and plotted against the Fn_h to obtain the inception boundary. This made it easier to draw conclusions on how these factors affected the flow.

3.8. Uncertainty Analysis

The estimated uncertainties of the measured and derived quantities are summarized in Table 3.12. This uncertainty analysis follows the guidelines for the expression of uncertainty

in measurement as provided by the International Bureau of Weights and Measures (BIPM) et al. [50]. Uncertainty estimates were obtained based on the calibration procedures of the instruments used for measurement and the uncertainty of the measured signal after filtering. The associated uncertainty of the instruments is the positive square root of the uncertainty components of the instrument listed as resolution, repeatability and calibration uncertainty. On the other hand, the associated uncertainty of the signals is estimated as the positive square root of the standard deviation of the mean, expressed as

$$s^2\left(\overline{q}\right) = \frac{s^2\left(q_k\right)}{n} \tag{3.7}$$

where

$$s^2\left(q_k\right) = \frac{1}{n-1}\sum_{j=1}^{n}\left(q_j - \overline{q}\right)^2 \tag{3.8}$$

The associated uncertainty of the derivated quantities is estimated as the positive square root of the combined variance, expressed as

$$u_c^2(y) = \sum_{i=1}^{N} u_{x_i}^2(y) \tag{3.9}$$

where

$$u_{x_i}^2(y) = \left(\frac{\partial y(x_i)}{\partial x_i}\right)^2 u^2(x_i) \tag{3.10}$$

and $u(x_i)$ is the uncertainty associated for each independent quantity listed in Table 3.12. This formulation also applies to the combination of signal and instrumentation uncertainty for measured quantities.

Table 3.12: Estimated uncertainties in baseline variables, measured and derived quantities. Baseline variables and measured quantities are obtained a 95% confidence interval.

Baseline Variables	Description		Uncertainty	
h	Tip immersion depth		0.003m	
ν	Kinematic viscosity		3%	
Measured Quantities	Description	Measurement Method		
α	Yaw angle	Certus	0.04°	
U	Flow speed		0.3%	
F_x	X Force component	6-DOF load gauge	0.36%	
F_y	Y Force component	6-DOF load gauge	0.2%	
M_z	Z Moment component	6-DOF load gauge	1.28%	
T_w	Water temperature	Thermometer	$0.1^{\circ}C$	
Derivated Quantities	**Description**	**Formula**	$AR_h = 1$	$AR_h = 1.5$
Fn_h	Froude number	$Fn_h = \frac{U}{\sqrt{gh}}$	0.6%	0.5%
AR_h	Inmersed aspect ratio	$AR_h = \frac{h}{c}$	1.07%	0.72%
Re_c	Reynolds number	$Re_c = \frac{Uc}{\nu}$	3%	3%
σ_c	Vaporous cavitation number	$\sigma_v = \frac{P_{atm}-P_v}{\rho U^2/2}$	0.61%	0.61%
$C_{L_{3D}}$	Lift coefficient	$C_{L_{3D}} = \frac{F_y}{\rho U^2 hc/2}$	1.39%	1%
$C_{D_{3D}}$	Drag coeffiecient	$C_{D_{3D}} = \frac{-F_x}{\rho U^2 hc/2}$	1.36%	0.96%
$C_{M_{3D}}$	Yawing moment coefficient	$C_{M_{3D}} = \frac{M_z}{\rho U^2 hc^2/2}$	1.85%	1.58%

4

Results

This chapter presents a discussion of the experimental data and findings. The chapter begins by validating the Semi-ogive by comparing previous experiments with the same geometry, examining the forces coefficients, α_i and the inception mechanism. The chapter then maps the flow regimes by identifying the inception boundary within the $\alpha - Fn_h$ parametric space and providing visual documentation that illustrates transitions between these boundaries.

Next, the mechanisms of ventilation inception are investigated, describing the distinct types observed in the experiments, including leading-edge, Rayleigh-Taylor, and TE-induced tip vortex ventilation. This analysis is further extended by examining the impact of the Froude number on inception mechanisms and its effects on α_i. A comparative analysis of the two tested hydrofoils follows, highlighting performance differences.

To conclude, the findings are integrated with data from previous experimental studies to enrich the understanding of ventilation phenomena. Additionally, a historical semi-empirical formulation for lift and drag is introduced, evaluated against experimental data, and discussed with proposed improvements.

Ultimately, this chapter aims to answer the research sub-questions, contributing directly to resolving the primary research question in the final chapter.

4.1. Semi-Ogive Validation

The Semi-ogive hydrofoil was constructed following Model 0 from the experiments by Harwood et al. [2]. Therefore, to compare the results obtained in both experiments, it is necessary to confirm that the geometries are similar. It should be noted that the NACA 0010-34 is not validated against Harwood's experiments since having a different geometry will make the coefficients differ. However, the flow characteristics and inception angles will be compared. The Semi-ogive hydrofoil was validated by replicating the experimental procedure in Harwood's experiments, named Static Tests in this experimental campaign. The force and moment coefficients obtained were plotted against those obtained by Harwood. et al. [2] for $AR = 1$ and $AR = 1.5$ (Figure 4.1 and Figure 4.2). Then, a polynomial fit was plotted for each regime in Harwood's experiments, and an uncertainty band of 8%, corresponding to the uncertainty in the measurement reported by Harwood et al. [2] for these coefficients. It should be noted that the moment coefficient is calculated at mid-chord, which replicates Harwood's results.

The results observed in Figures 4.1a-4.1b and 4.2a-4.2b show that the force coefficients for the Semi-ogive are within the uncertainty region in Harwood's results for the ventilated and non-ventilated results. However, the moment coefficient is not in this region. A possible explanation for this is where the yaw moment is obtained, which can result in different outcomes. Harwood et al. [2] reported that the yaw moment was obtained about mid-chord but did not specify the exact position. Thereafter, the moment coefficient deviation is not considered in validating the Semi-Ogive hydrofoil. The deviation for each point is obtained to validate the hydrofoil regarding the force coefficients. A summary can be observed in Table 4.1.

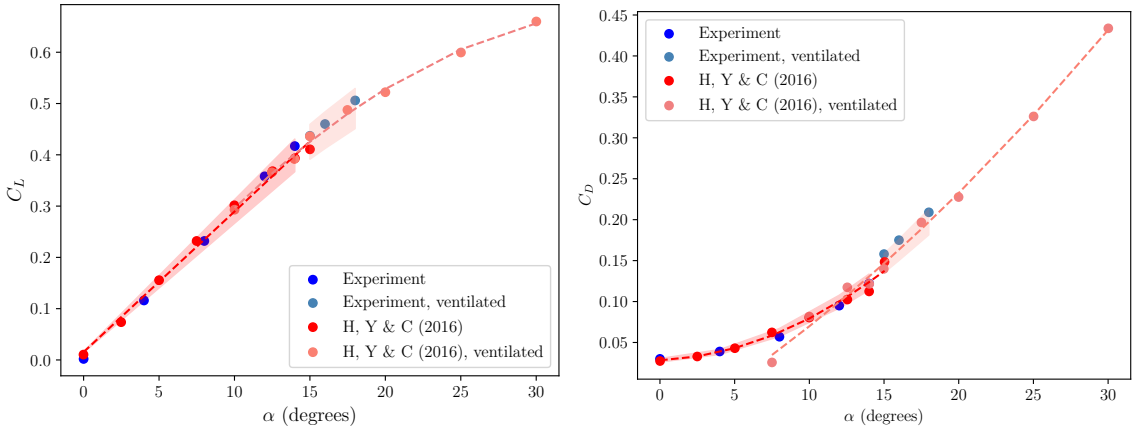

(a) Lift coefficient

(b) Drag coefficient

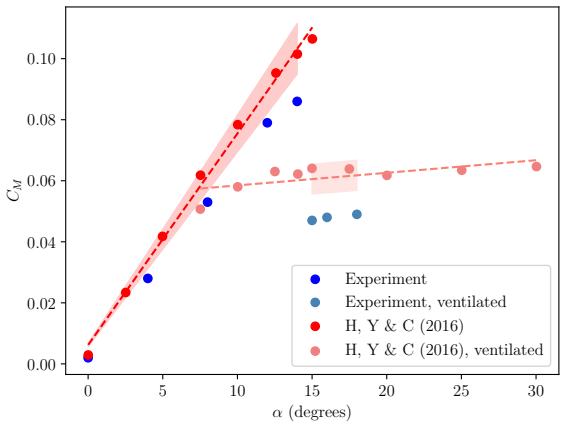

(c) Moment coefficient

Figure 4.1: Measured hydrodynamic lift and drag coefficients for the semi-ogive hydrofoil at an $AR = 1$ and $Fn_h = 1.5$, compared against historical experimental data under identical conditions and geometry. The experimental data aligns within an 8% uncertainty band around the polynomial fit of Harwood et al. [2] data. H, Y & C: Harwood et al. (2016) [2].

The results indicate that, across all cases, the mean deviation remains within 6%, which can be attributed to measurement uncertainty and differences in the experimental setups used in the campaigns. It should be noted that the lift coefficients are closer, while for the drag conditions, this deviation increases. This can be explained by the greater sensitivity of the drag coefficient to small variations in the flow around the hydrofoil, primarily due to induced drag. Consequently, any variation in experimental conditions, such as temperature, pressure, or precise angle of attack, can have a greater impact on C_D. Additionally, the higher deviation may be associated with the relative magnitudes of the forces, as drag is smaller than lift, making it more susceptible to measurement uncertainty.

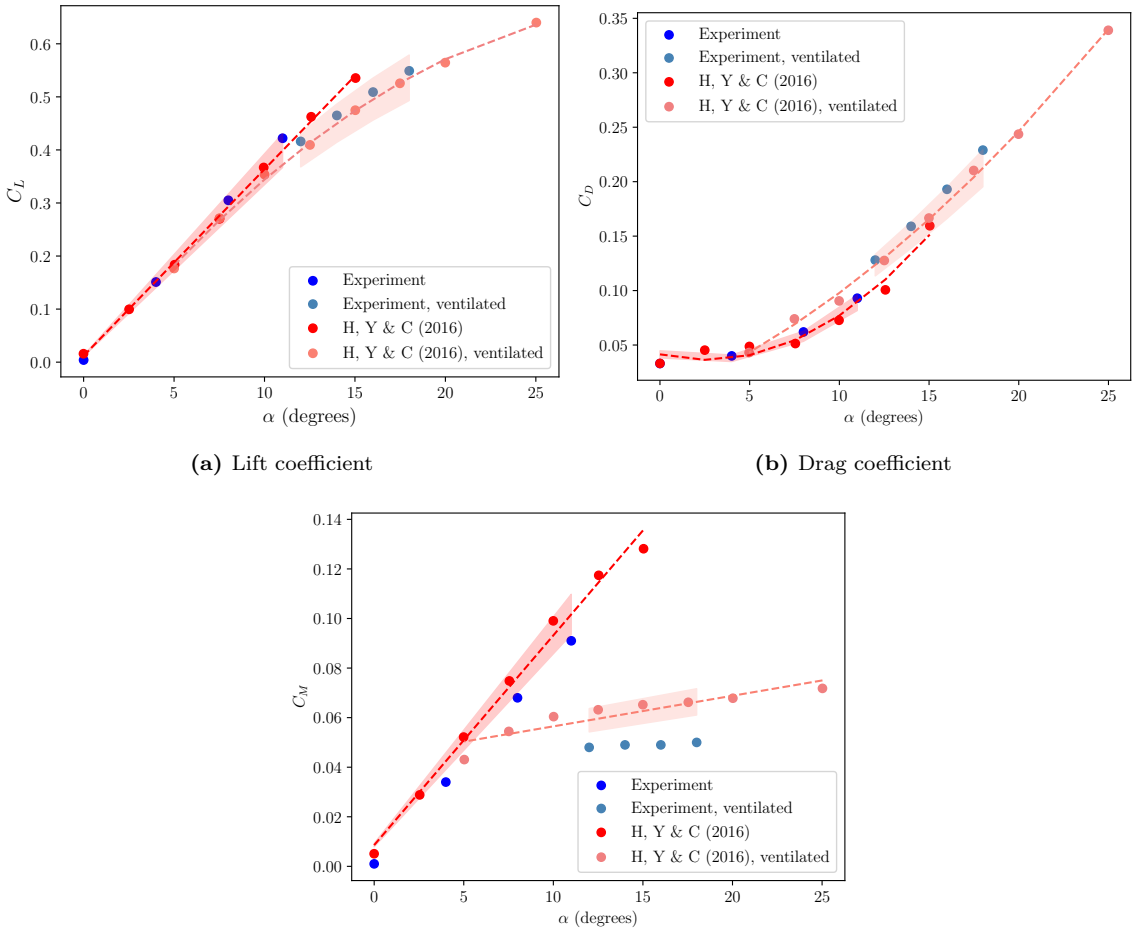

(a) Lift coefficient

(b) Drag coefficient

(c) Moment coefficient

Figure 4.2: Measured hydrodynamic lift and drag coefficients for the semi-ogive hydrofoil at an $AR = 1.5$ and $Fn_h = 1.5$, compared against historical experimental data under identical conditions and geometry. The experimental data aligns within an 8% uncertainty band around the polynomial fit of Harwood et al. [2] data. H, Y & C: Harwood et al. (2016) [2].

Overall, the results show that the Semi-Ogive and Model 0 from Harwood et al. [2] exhibit similar force coefficients, suggesting their geometries are comparable.

To validate the ventilation inception mechanism and determine the lowest angle of attack (AoA) at which the hydrofoil naturally ventilates, visual documentation for Run 1108 and for Harwood's experiments is provided (see Figure 4.4 and Figure 4.3). The experiments by Harwood et al. [2] named the inception mechanism during acceleration as stall-induced ventilation formation (see Figure 2.13); for the present dissertation, this is termed Rayleigh-Taylor inception at acceleration. In Figure 4.4a, the low pressures on the hydrofoil surface and the associated transient effect to the acceleration create a steep depression of the free surface, forcing proximity to the separated flow. At the same time, this proximity generates Rayleigh-Taylor disturbances that can momentarily breach the surface seal and admit air into the flow, (see Figure 4.4b). Figure 4.4c and Figure 4.4d show the development of the cavity as the speed increases and ultimately reaches the FV condition. The same mechanism is observed in Figure 4.3, which ultimately connects the behaviour of both hydrofoils.

Ventilation inception for the Semi-Ogive occurs at approximately $Fn = 0.5$ during acceleration in all cases shown in Table C.1, aligning with the inception boundary at $Fn = 0.5$ for Model

Table 4.1: Measured percentage deviation between the experimental results and Harwood's data.

α (°)	$AR = 1$ (%)		$AR = 1.5$ (%)	
	C_L	C_D	C_L	C_D
4	7.2	1.69	1.05	5.74
8	1.10	8.36	4.0	6.85
11	-	-	5.83	7.86
12	4.02	4.81	4.02	3.79
14	4.52	1.41	3.23	5.38
15	2.76	7.72	-	-
16	2.69	7.27	2.66	6.89
18	3.22	6.02	2.42	7.89
Mean	**3.19**	**4.66**	**2.90**	**5.55**

0 in Figure 2.11. The lowest angle of attack (α_i) at which ventilation is triggered is 14° for $AR = 1$ and 12° for $AR = 1.5$, closely matching the last point on the inception boundary in Figure 2.11.

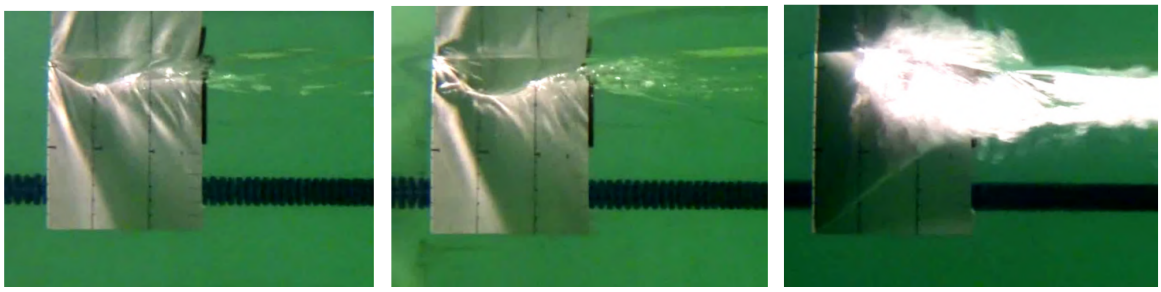

(a) $Fn_h = 0.44$ **(b)** $Fn_h = 0.60$ **(c)** $Fn_h = 1.16$

Figure 4.3: Rayleigh-Taylor (RT) ventilation inception observed during the acceleration phase by Harwood et al. [2], with an aspect ratio, $Ar_h = 1.5$. The Froude number, Fn_h, represents the value at the instant of each photograph.

Based on the results, we can conclude that the Semi-Ogive hydrofoil and Model 0 from Harwood et al. [2] have comparable behaviour in relation to ventilation, as evidenced by their similar force coefficients and ventilation inception characteristics. Validation tests, including comparisons of lift and drag coefficients, confirm that the force behaviour of the Semi-Ogive closely aligns with Harwood's findings for $AR = 1$ and $AR = 1.5$. Additionally, the observed Rayleigh-Taylor ventilation inception during acceleration at $Fn_h = 0.5$ and the consistent angle of attack further support the comparability of the two hydrofoils.

4.2. Flow Regimes

For all the runs listed in Table C.2, the inception angle of attack (α_i) and the flow regime after ventilation were measured at a given Froude number for both hydrofoils. The outcome of this procedure can be found in the following subsections.

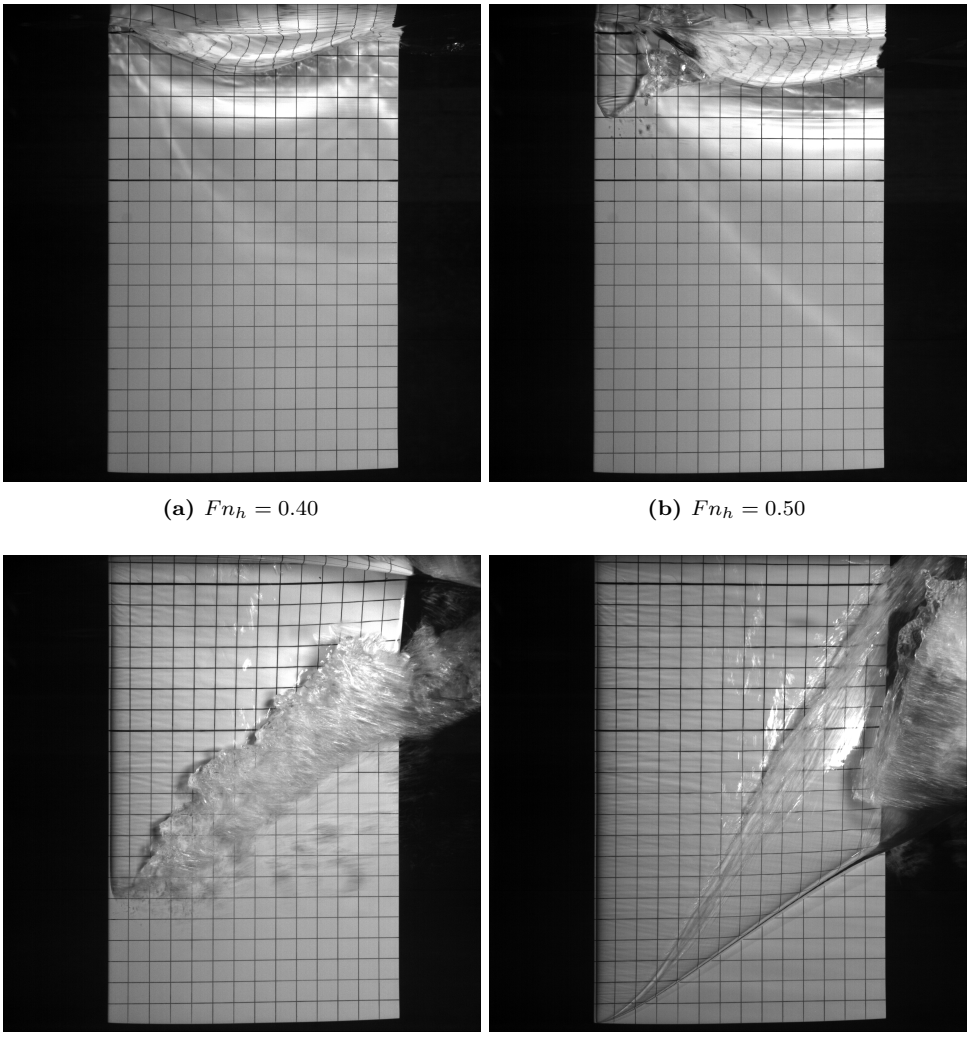

(a) $Fn_h = 0.40$ **(b)** $Fn_h = 0.50$

(c) $Fn_h = 1.13$ **(d)** $Fn_h = 1.47$

Figure 4.4: Rayleigh-Taylor (RT) ventilation inception observed during the acceleration phase at an angle of attack, $\alpha = 12^{\circ}$, with an aspect ratio, $Ar_h = 1.5$, Run 1108. The Froude number, Fn_h, represents the value at the instant of each photograph. This approach follows the methodology described by Harwood et al. [2].

4.2.1. $AoA - Fn_h$ inception boundary

The inception boundary is obtained by plotting the mean value of α_i for each test condition shown in Table 3.9 and Table 3.10. This boundary is represented in the $AoA - Fn_h$ parametric space for each AR in Figure 4.5 and Figure 4.6. The standard error is plotted as a shaded area on each point.

The inception boundary defines the transition between the FW regime and the PV or FV regime. Below this boundary, the flow remains naturally FW, with ventilation only triggered by an artificial perturbation. Previously, researchers, in particular Harwood et al. [2], represented this boundary as a vertical line fixed at the stall angle of attack, $\alpha_S \approx 15^{\circ}$. However, this simplification is not consistent with the results of this experimental campaign. As shown in Figure 4.5 and Figure 4.6, by quasi-statically varying the AoA, the hydrofoil can reach inception angles, α_i, up to 29° in the FW regime, expanding the stability region represented in Figure 2.11 for this regime. This finding applies not only to the Semi-Ogive hydrofoil but also to the NACA profile, with minor differences in trends and inception angles.

The experimental procedure was designed to eliminate any effects associated with the transient effects of acceleration. By doing so, the hydrofoils did not ventilate through the mechanism described in the previous section, allowing the flow to remain wetted at higher AoA. The inception mechanisms are further explained in section 4.3.

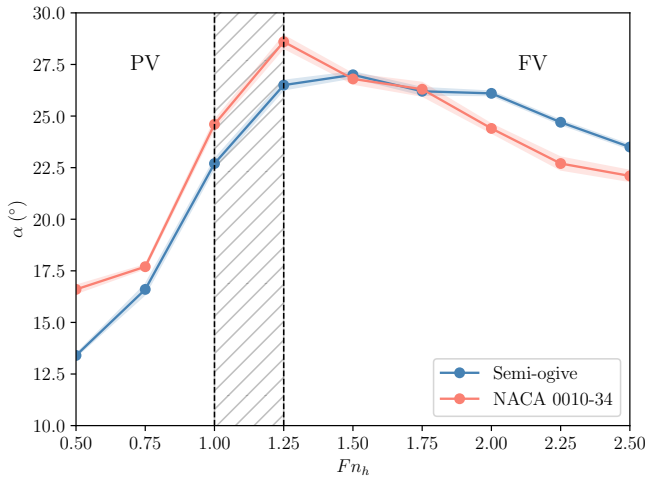

Figure 4.5: Ventilation inception angle of attack as a function of the depth Froude Number for $AR = 1$. The hatched region indicates the transition between PV and FV regimes. Uncertainty on the measurement is plotted as a shaded area on each point.

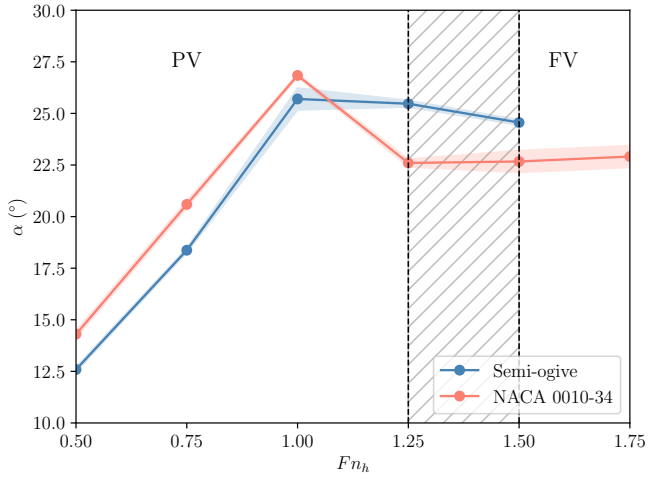

Figure 4.6: Ventilation inception angle of attack as a function of the depth Froude Number for $AR = 1.5$. The hatched region indicates the transition between PV and FV regimes. Uncertainty on the measurement is plotted as a shaded area on each point.

4.2.2. Repeatability of the AoA

Ventilation was previously described as a stochastic mechanism, where ventilation could trigger at any time or angle of attack, during the acceleration phase or at a steady state. However, this uncertainty has been reduced by quasi-statically varying the AoA and reaching for the inception boundary, as described in subsection 3.6.3. The experimental results in Table 4.2 and Table 4.3 show that the standard error over the mean inception angle has a maximum of

Table 4.2: Measured $\overline{\alpha_i}$, σ, and σ_M for the Semi-Ogive and NACA 0010-34 hydrofoils at various Fn_h across test conditions for $AR = 1$.

Fn_h	Semi-Ogive			NACA 0010-34		
	$\overline{\alpha_i}$	σ	σ_M	$\overline{\alpha_i}$	σ	σ_M
0.5	13.4	0.132	0.066	16.6	0.338	0.195
0.75	16.6	0.610	0.249	17.7	0.156	0.090
1	22.7	0.479	0.214	24.6	0.336	0.194
1.25	26.5	0.549	0.224	28.6	0.531	0.306
1.5	27.0	0.323	0.145	26.8	0.647	0.244
1.75	26.2	0.394	0.176	26.3	0.566	0.327
2	26.1	0.229	0.103	24.4	0.371	0.214
2.25	24.7	0.103	0.103	22.7	0.613	0.307
2.5	23.5	0.103	0.103	22.1	0.524	0.262

Table 4.3: Measured $\overline{\alpha_i}$, σ, and σ_M for the Semi-Ogive and NACA 0010-34 hydrofoils at various Fn_h across test conditions for $AR = 1.5$.

Fn_h	Semi-Ogive			NACA 0010-34		
	$\overline{\alpha_i}$	σ	σ_M	$\overline{\alpha_i}$	σ	σ_M
0.5	12.59	0.268	0.120	14.3	0.310	0.179
0.75	18.37	0.268	0.120	20.59	0.310	0.179
1	25.70	1.197	0.535	26.84	0.161	0.093
1.25	25.47	0.362	0.162	22.6	0.338	0.195
1.5	24.56	0.295	0.132	22.67	0.922	0.532
1.75	-	-	-	22.91	0.922	0.532

only $\pm 0.5°$, with a mean standard error of $\pm 0.195°$ for $AR = 1$ and $\pm 0.25°$ for $AR = 1.5$. This corresponds to a relative variation of approximately 1% to 2% around the mean value at each point, indicating that the mean inception angle at each Froude number is highly accurate, with ventilation likely occurring near that angle. This could indicate a natural mechanism that, in those specific conditions, can trigger ventilation around that AoA.

Notably, the highest uncertainties generally occur when α_i is close to its maximum value, possibly reflecting the involvement of different inception mechanisms and thus contributing to higher uncertainty. The standard deviation is typically around $0.5°$, with only two specific cases reaching $1°$, which could likely be reduced by increasing the sample size

4.2.3. Flow Regime Transition

As previously described, the transition from FW to a ventilated flow can occur as PV or FV. For the Semi-Ogive hydrofoil, a representative frame for each Fn_h and Run at $AR = 1$ has been plotted in Figure 4.7. It is clear that as the Fn_h is increased, the ventilated area becomes larger until it reaches full ventilation at around $Fn_h = 1.25$. This phenomenon is due to the ratio between increased inertial forces and reduced gravitational as Fn_h increases. At higher Froude numbers, the high water flow velocity creates a strong low-pressure region on the hydrofoil surface, which entrains air from the free surface and facilitates ventilation. With the increasing dominance of inertial forces over gravity, gravity's downward acceleration becomes less effective in keeping water attached to the hydrofoil. This reduced gravitational constraint allows ventilated areas to expand more easily.

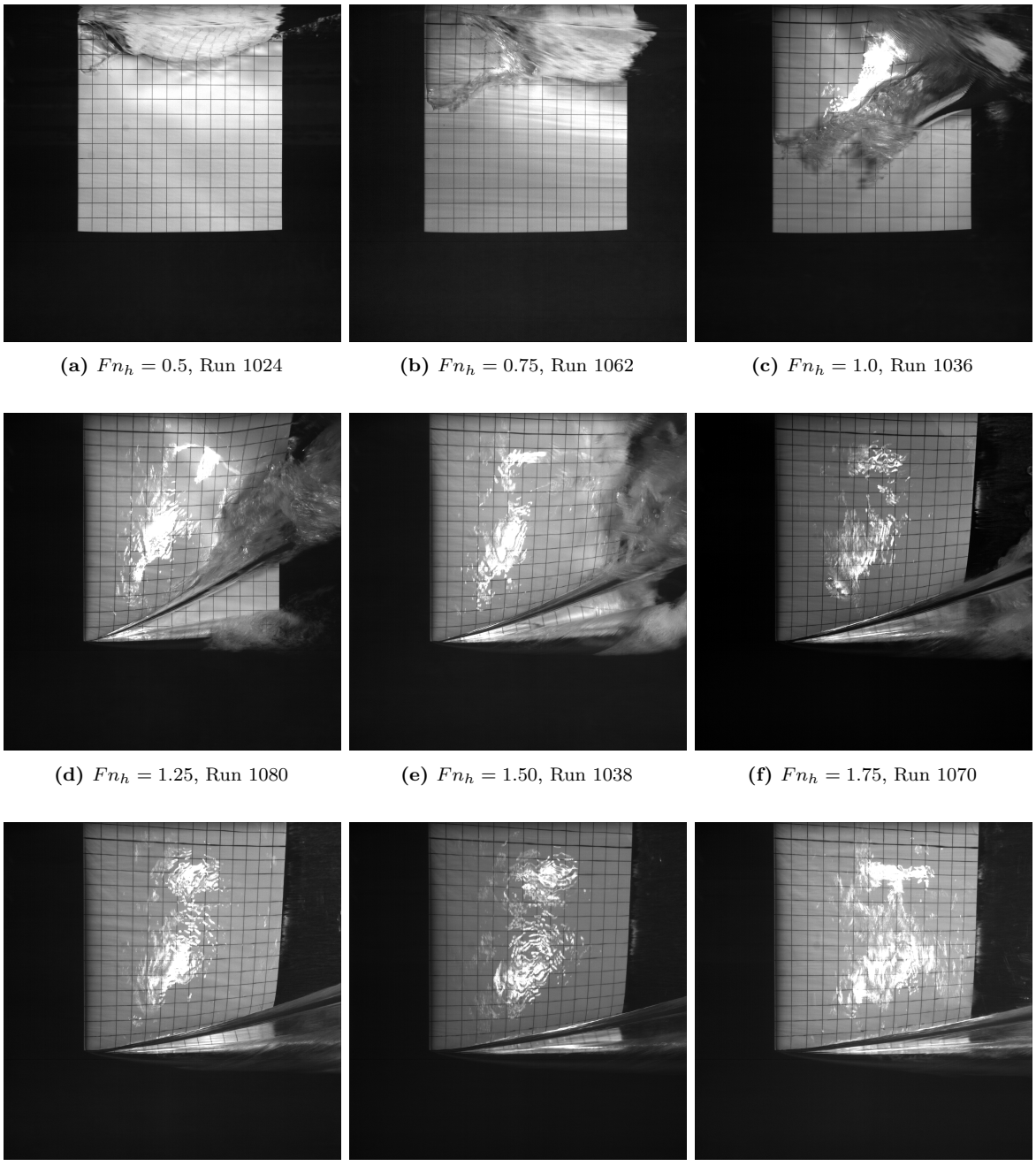

(a) $Fn_h = 0.5$, Run 1024 **(b)** $Fn_h = 0.75$, Run 1062 **(c)** $Fn_h = 1.0$, Run 1036

(d) $Fn_h = 1.25$, Run 1080 **(e)** $Fn_h = 1.50$, Run 1038 **(f)** $Fn_h = 1.75$, Run 1070

(g) $Fn_h = 2.0$, Run 1086 **(h)** $Fn_h = 2.25$, Run 1088 **(i)** $Fn_h = 2.50$, Run 1090

Figure 4.7: Visualization of the flow transition for the Semi-Ogive hydrofoil at various Fn_h with $AR = 1$. Each frame represents the flow state for each tested Fn_h value after ventilation, showing the progressive transition from partially ventilated (PV) to fully ventilated (FV) regimes.

4.3. Ventilation Inception Mechanisms

This section analyses the mechanisms of ventilation inception, beginning with an overview of the different types of inception mechanisms observed in the experiments. Next, the specific triggers for ventilation are examined. Furthermore, the influence of Re_c, Fn_h, and AoA on these mechanisms is discussed.

4.3.1. Types of inception mechanisms

During the experimental campaign, three types of inception mechanisms are observed: LE Ventilation, Rayleigh-Taylor Ventilation, and TE Ventilation. This list combines the Semi-ogive Hydrofoil's possible tip-vortex ventilation and TE ventilation.

LE Ventilation

As described in the literature review, LE ventilation occurs when natural disturbances have enough momentum to disrupt the free surface near the leading edge and reach the small separation bubble at this location. During the experiments, two primary types of LE ventilation were observed: LE ventilation due to a laminar separation bubble (LSB) at low Fn_h and LE ventilation due to the collapse of the run-up at the LE at moderate Fn_h. As Fn_h increased, the collapse of the run-up occurred later, ultimately enabling for higher values of the inception AoA for this mechanism. This inception mechanism is the most sporadic of the three observed, with LE-LSB inception occurring within approximately $1/10^{\text{th}}$ of a second and LE inception occurring between $2/10^{\text{th}}$ and $5/10^{\text{th}}$ of a second as Fn_h increases. A schematic of this inception mechanism is shown in Figure 4.8, along with three experimental runs providing visual representations of the LE-LSB, Figure 4.9, LE to partial ventilated flow, Figure 4.10, and LE to fully ventilated flow, Figure 4.11.

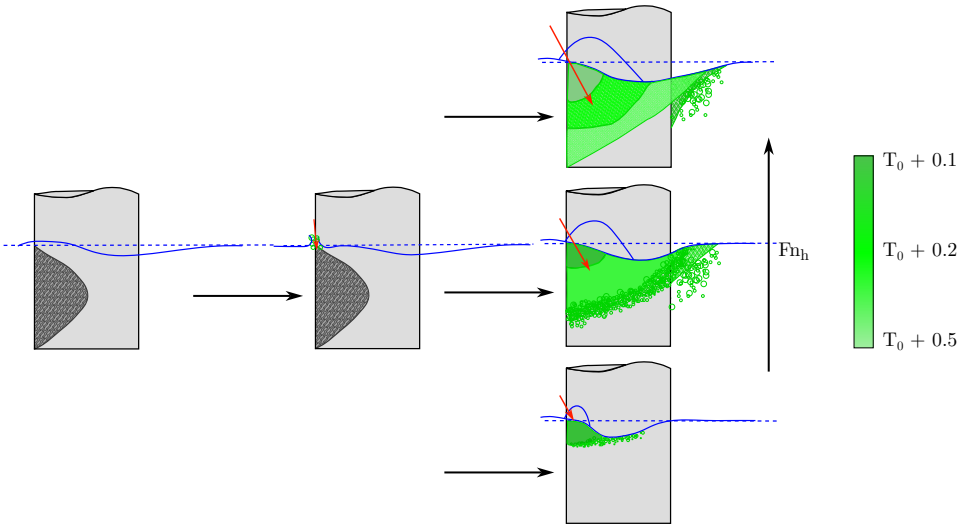

Figure 4.8: Schematic of LE ventilation inception across different Froude numbers. The blue lines represent streamlines, highlighting the flow field around the hydrofoil. Green areas with hatching indicate regions of entrained air. Black hatching denotes boundary layer separation zones, and red arrows show the paths of air ingress. T_0 represents the moment of inception. The diagram is inspired by the schematics in Harwood et al. [2].

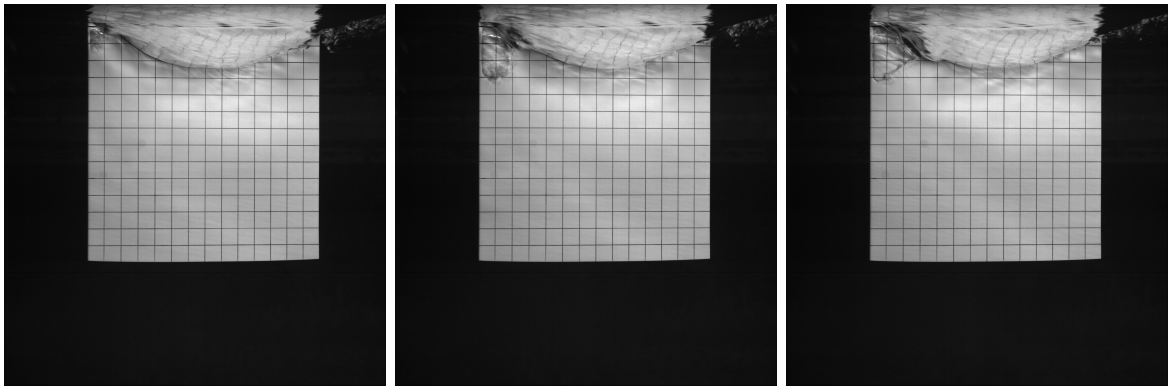

(a) $T_0 + 0.02$ **(b)** $T_0 + 0.06$ **(c)** $T_0 + 0.1$

Figure 4.9: Leading edge - LSB ventilation inception, $Fn_h = 0.5$; $AR_h = 1$; Run 1024; Semi-Ogive. The time is given at the instant of each photograph relative to the initiation of the mechanism.

(a) $T_0 + 0.03$ **(b)** $T_0 + 0.08$ **(c)** $T_0 + 0.19$

Figure 4.10: Leading edge ventilation inception, $Fn_h = 1.0$; $AR_h = 1$; Run 1036; Semi-Ogive. The time is given at the instant of each photograph relative to the initiation of the mechanism.

Rayleigh-Taylor Ventilation

Previous research has observed this type of mechanism at high velocities, but in the current experimental campaign, it occurred at speeds as low as $U = 2\ m/s$. In this inception mechanism, Taylor's instabilities along the free surface create a pathway for air. The low-pressure region on the suction side of the hydrofoil induces a downward acceleration of the free surface, forming a depression. When this downward acceleration is strong enough, small disturbances on the surface, such as ripples or capillary waves, rapidly grow in amplitude, becoming unstable and collapsing as the low-pressure region and downward acceleration subside. The vortices generated by these perturbations then facilitate air ingress. Once an air path is established and sufficient air has entered the separated region, the air reaches the LE, creating a secondary air pathway that ultimately triggers ventilation.

In the present experiment, the run-up generates the surface ripples that initiate the disturbance. As the AoA increases, the run-up becomes unstable, releasing droplets along the free surface. A schematic of this inception mechanism is shown in Figure 4.12, along with visual representations from two experimental runs, one for each hydrofoil in Figure 4.13 and Figure 4.14.

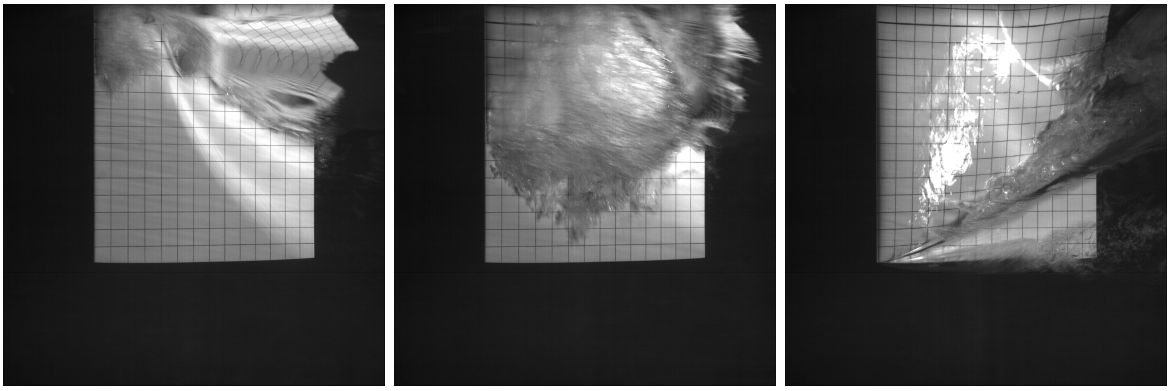

(a) $T_0 + 0.04$ **(b)** $T_0 + 0.13$ **(c)** $T_0 + 0.50$

Figure 4.11: Leading edge ventilation inception, $Fn_h = 1.25$; $AR_h = 1$; Run 1058; Semi-Ogive. The time is given at the instant of each photograph relative to the initiation of the mechanism.

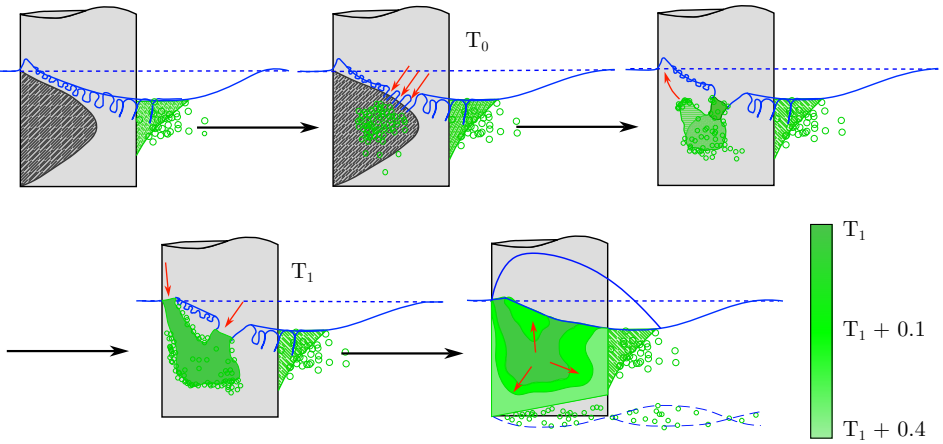

Figure 4.12: Schematic of Rayleigh-Taylor ventilation inception. T_0 represents the moment of inception and T_1 is when enough air has entered for ventilation to trigger. The diagram is inspired by the schematics in Harwood et al. [2].

TE - Tip-Vortex Ventilation

These two inception mechanisms were not explicitly observed during the towing tank experiments. However, for the Semi-Ogive hydrofoil at $Fn_h = 2.5$, ventilation inception occurs through a combination of Rayleigh-Taylor and trailing edge inception. At this speed, tip-vortex inception also appears to develop, with air supplied from the blunt TE, suggesting that ventilation via this mechanism could occur at higher speeds. The blunt TE is crucial for these mechanisms, as it serves as the primary air ingress point. For tip-vortex inception, air enters the vortex through the bubbly wake, eventually reaching the leading edge (LE) and resulting in sporadic inception. In contrast, TE inception aligns more closely with the RT mechanism; air also enters through the bubbly wake but travels directly to the flow separation region. From there, it reaches the free surface at the LE and ultimately triggers full ventilation. A schematic of this inception mechanism is shown in Figure 4.16 and Figure 4.15 along with visual representations from Run 1090 illustrating the two specific scenarios.

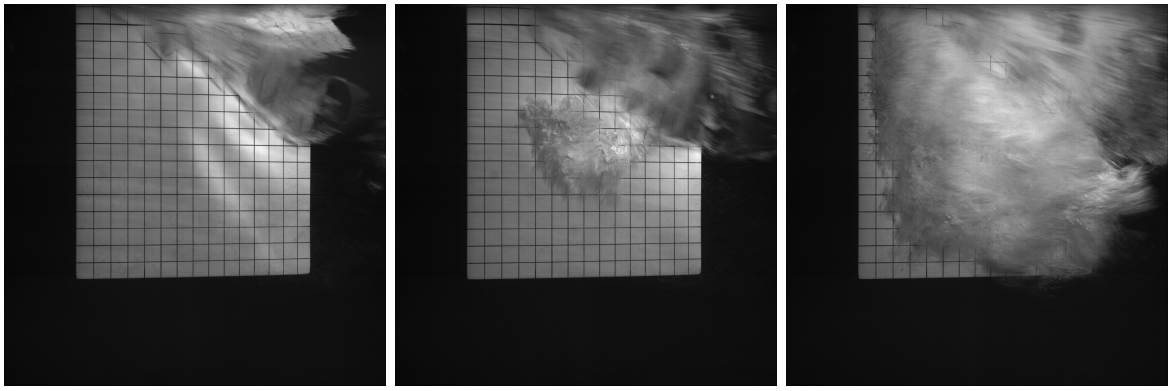

(a) $T_0 + 0.02$ **(b)** $T_0 + 0.04$ **(c)** $T_0 + 0.14$

Figure 4.13: Rayleigh-Taylor ventilation inception, $Fn_h = 2.0$; $AR_h = 1$; Run 2042; NACA 0010-34. The time is given at the instant of each photograph relative to the initiation of the mechanism.

4.3.2. Triggering Mechanisms

For the inception mechanisms to develop, a perturbation must pierce the free surface. In the experimental campaign, these perturbations arose naturally due to the hydrofoil's geometry and the specific flow conditions in each run. Three distinct mechanisms were observed.

First of all, LE-LSB inception is primarily driven by the transition from laminar to turbulent flow as the angle of attack increases. During the experimental campaign, it was observed at $Fn_h \leq 0.75$. At higher AoA, the LSB near the leading edge becomes increasingly unstable, eventually transitioning to a turbulent state and shedding vortices.

These turbulent disturbances introduce enough energy and fluctuations to pierce the free surface, allowing air to enter the separation region and trigger ventilation. Therefore, as the AoA increases, the instability of the LSB grows, creating the conditions necessary for air entrainment and ventilation through the LE-LSB mechanism.

Figure 4.19 illustrates the progression of LE-LSB ventilation inception as the AoA increases over time. The figure contains four frames (a-d), showing the growth of instabilities at the leading edge and corresponding AoA. The time stamps and AoAs are given to display the chronological development of the phenomenon.

Secondly, leading-edge inception is primarily driven by the dynamics of the run-up phenomenon. This mechanism involves a column of water at the LE that rises above the free surface due to the sharp nose of the tested hydrofoils. During the experimental campaign, this mechanism was observed for $0.75 \leq Fn_h \leq 1.0$. The collapse of this column provides the necessary momentum to reach the separated flow region and initiate ventilation. At low Fn_h, the water column at the LE remains relatively small. As the angle of attack increases, this column becomes unstable and collapses into the LE, triggering ventilation by inducing small vortices that carry air into the separated flow region.

Figure 4.20 depicts the leading-edge ventilation inception through the run-up phenomenon. The sequence of images (a-e) indicates the progression of the water column at the LE as it collapses into the separated flow region. The red circles in frames (c) and (d) highlight the perturbations at the LE that trigger ventilation. It can be noted that once the run-up has collapsed it only takes $4/10^{th}$ of a second for ventilation to trigger.

At $1 \leq Fn_h \leq 1.25 - 1.5$, the water column at the leading edge (LE) becomes taller due to

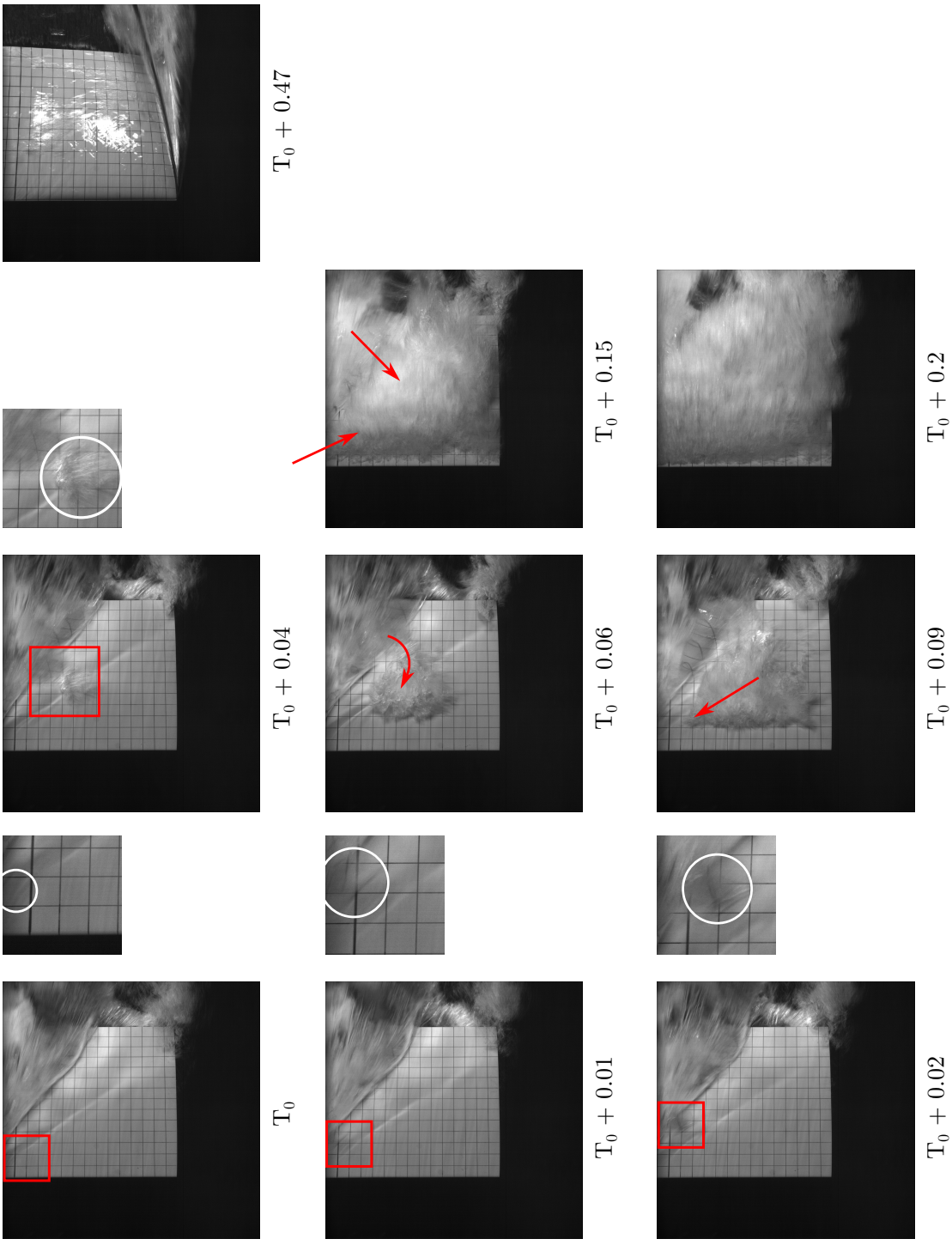

Figure 4.14: Rayleigh-Taylor ventilation inception, $Fn_h = 2.0$; $AR = 1$; Run 1086; Semi-Ogive. The time is given at the instant of each photograph relative to the initiation of the mechanism. The white circles show the droplet's instability, and the red arrows indicate the flow direction.

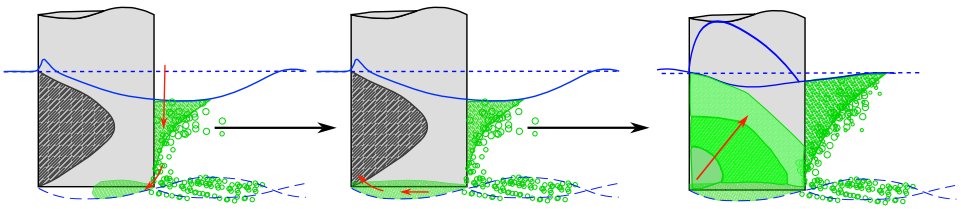

Figure 4.15: Schematic of tip-vortex ventilation inception. The diagram is inspired by the schematics in Harwood et al. [2].

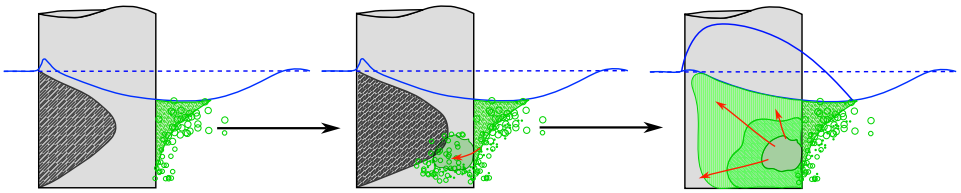

Figure 4.16: Schematic of TE ventilation inception. The diagram is inspired by the schematics in Harwood et al. [2].

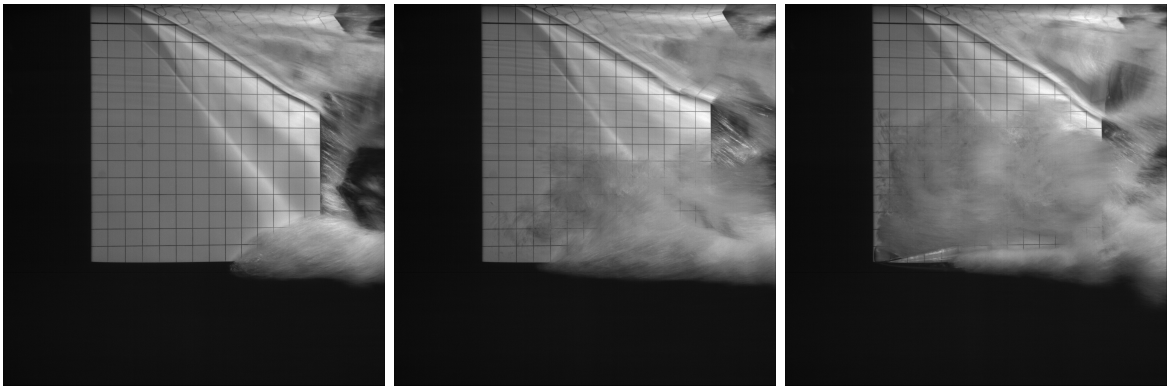

(a) $T_0 + 0.35$ **(b)** $T_0 + 0.59$ **(c)** $T_0 + 0.72$

Figure 4.17: Tip-Vortex inception, $Fn_h = 2.5$; $AR_h = 1$; 1090; Semi-Ogive. The time is given at the instant of each photograph relative to the initiation of the mechanism.

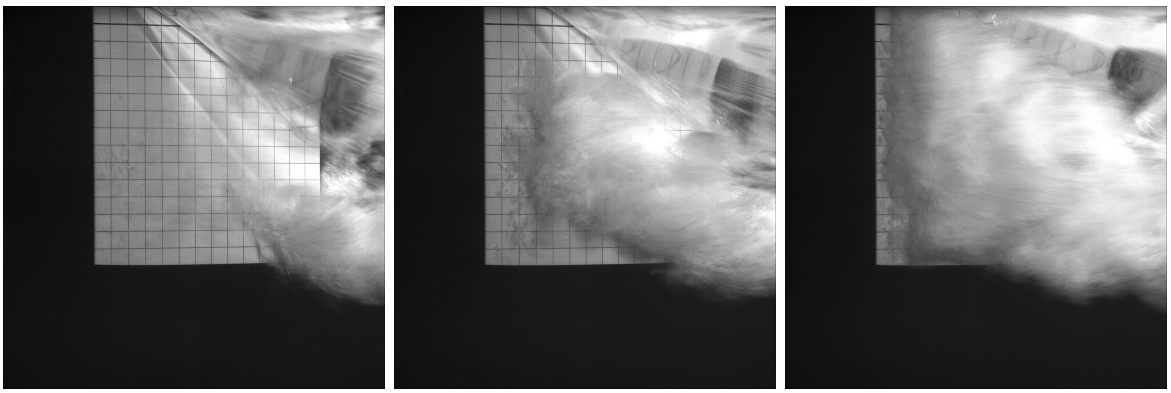

(a) $T_0 + 0.02$ **(b)** $T_0 + 0.15$ **(c)** $T_0 + 0.26$

Figure 4.18: RT-TE inception, $Fn_h = 2.5$; $AR_h = 1$; 1090; Semi-Ogive. The time is given at the instant of each photograph relative to the initiation of the mechanism.

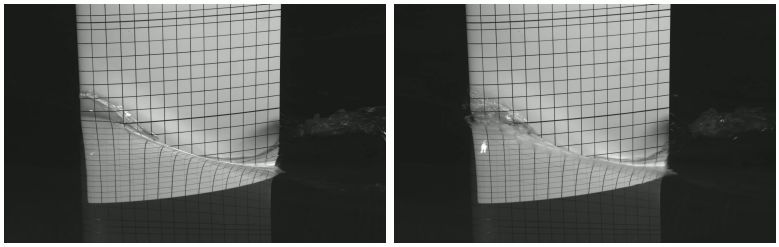

(a) $T = 0\ s$; $AoA = 15.39$ **(b)** $T = 6\ s$; $AoA = 15.94$

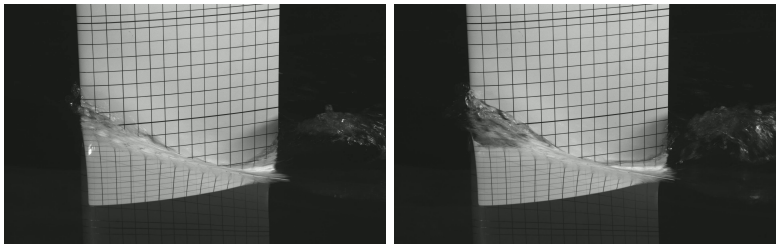

(c) $T = 17.5\ s$; $AoA = 17.58$ **(d)** $T = 18.96\ s$; $AoA = 17.78$

Figure 4.19: LE-LSB ventilation inception, $Fn_h = 0.75$; $AR_h = 1$; Run 2050; NACA 0010-34. The flow can be seen as instabilities grow near the leading edge. The time is given from the start of the recording.

the increased flow velocity. Rather than collapsing entirely, it becomes unstable and releases droplets at the LE. These droplets create sufficient perturbations to reach the separated flow region and trigger ventilation. However, as Fn_h continues to increase, the stability of the flow further inhibits the formation of disturbances at the LE. At this stage, the high-speed flow prevents the droplets from becoming unstable as they reach the free surface, reducing the effectiveness of the run-up mechanism. Consequently, inception begins to rely on other mechanisms as Fn_h increases. The transition between inception mechanisms was observed around $Fn_h = 1.25 - 1.5$, coinciding with the maximum AoA. See the following subsection for more details on the influence of the Fn_h.

Figure 4.21 presents the leading-edge ventilation inception under higher Froude numbers $Fnh = 1.5$. The sequence of images (a-e) captures the release of droplets at the LE and their progression toward the free surface. The specific droplet that triggers ventilation is highlighted in the red circles.

Finally, Rayleigh-Taylor's inception is primarily influenced by the free surface position at the LE. This phenomenon is observed above $Fn_h = 1.25 - 1.5$, up to $Fn_h = 2.5$ which is the maximum tested speed. For Froude numbers above $Fn_h = 1.5$, droplets released by the run-up fall along the free surface without triggering ventilation. However, once the free surface descends to approximately $d/c = 0.5$ below its nominal position at the TE, Rayleigh-Taylor disturbances develop due to its proximity to the separation and low-pressure region. At this stage, the droplets falling at the LE travel along the free surface gaining sufficient momentum to become unstable, which forms small vortices that can trigger ventilation. As the Fn_h increases, the d/c ratio shows a decreasing trend, resulting in a reduction in the condition of $d/c = 0.5$. Figure 4.22 illustrates the variation of the d/c ratio as a function of F_{nh} and speed, providing a clear representation of this relationship. The first four images in Figure 4.14 illustrate the progression of a droplet as it travels along the free surface. Starting from the LE, the droplet gains momentum and moves downstream while remaining attached to the free surface. This process demonstrates how the droplet interacts with the surrounding flow field until it reaches a critical point where it destabilizes, forming perturbations that eventually

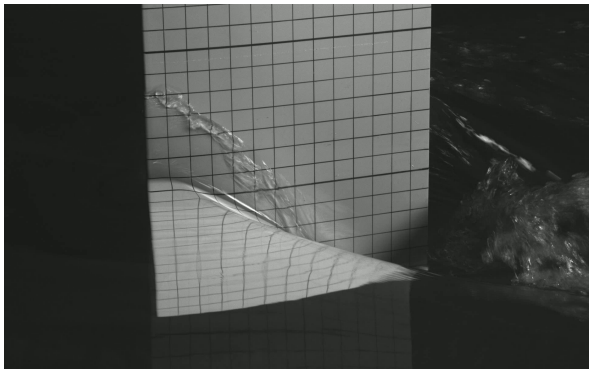

(a) $T = 0\ s$; $AoA = 22.82$

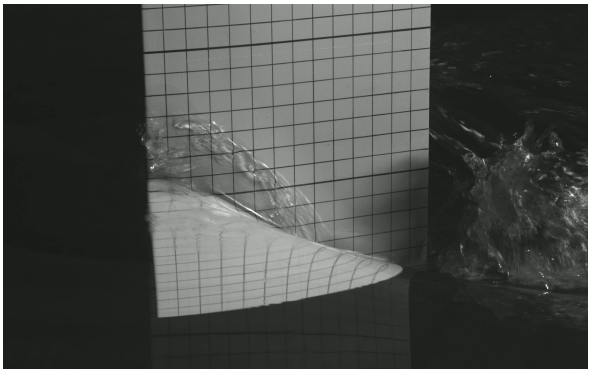

(b) $T = 0.4\ s$; $AoA = 22.97$

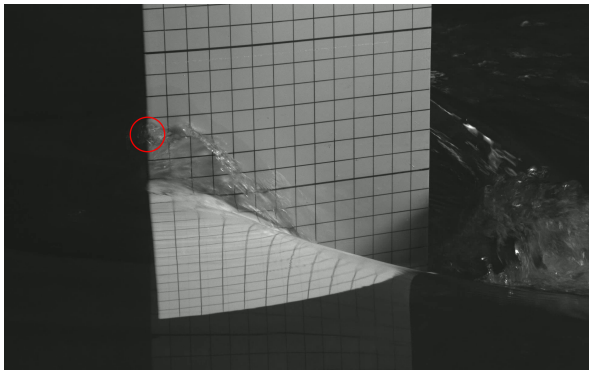

(c) $T = 0.78\ s$; $AoA = 23.04$

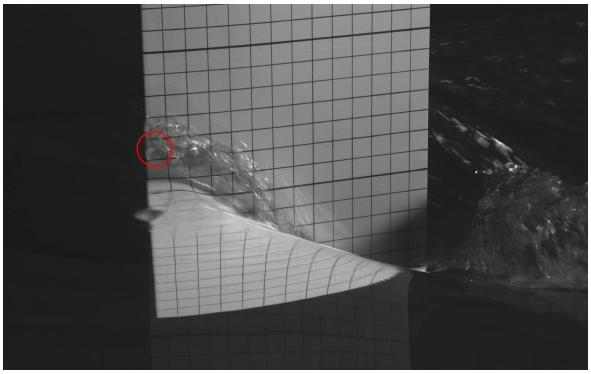

(d) $T = 0.82\ s$; $AoA = 23.05$

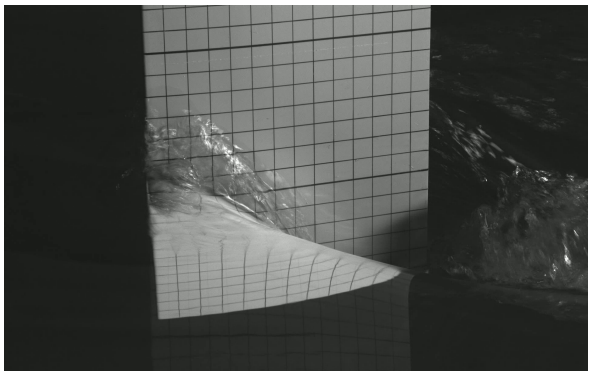

(e) $T = 0.86\ s$; $AoA = 23.05$

Figure 4.20: LE ventilation inception, $Fn_h = 1$; $AR_h = 1$; Run 1036; Semi-Ogive. The run-up can be seen to collapse onto the LE. The red circle indicate the perturbation that ultimately triggers ventilation. The time is given from the start of the recording.

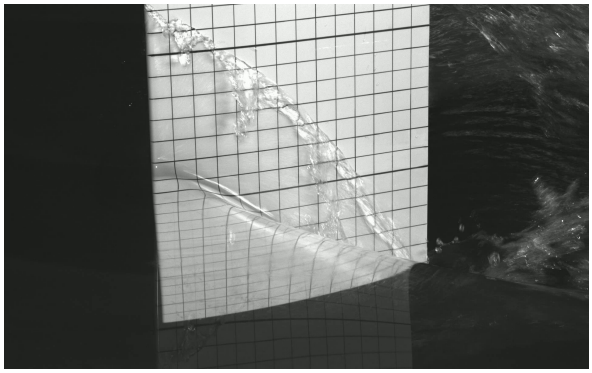

(a) $T = 0\ s$; $AoA = 26.93$

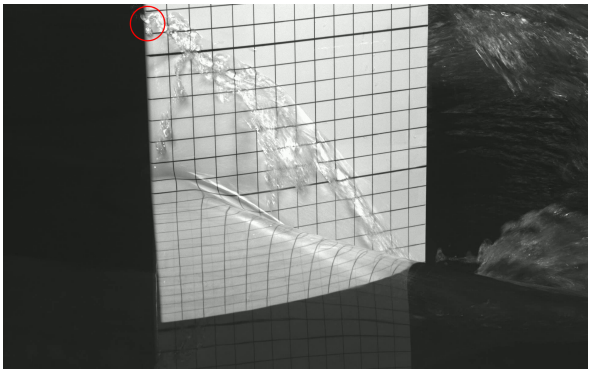

(b) $T = 0.12\ s$; $AoA = 26.98$

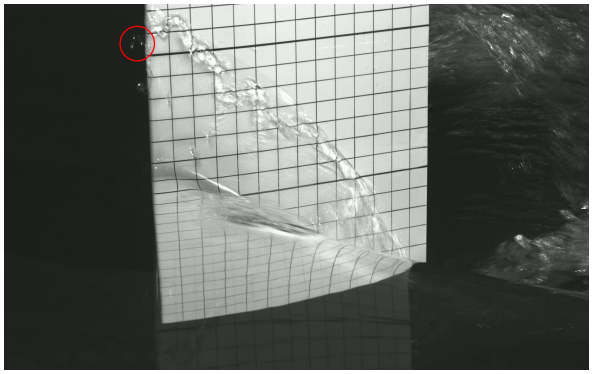

(c) $T = 0.16\ s$; $AoA = 27.00$

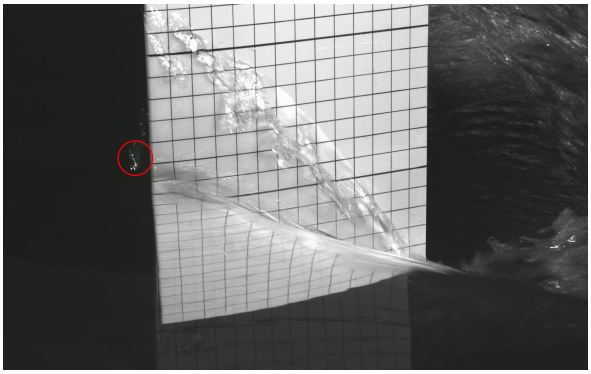

(d) $T = 0.2\ s$; $AoA = 27.02$

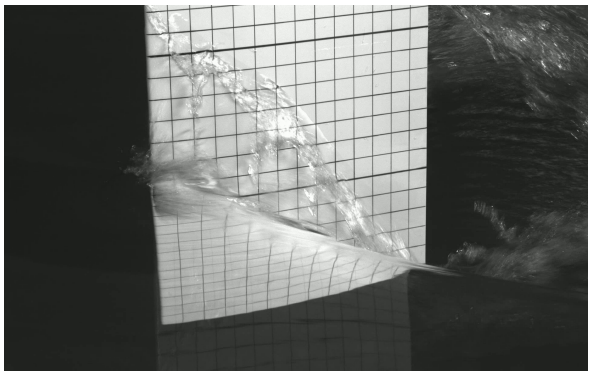

(e) $T = 0.22\ s$; $AoA = 27.03$

Figure 4.21: LE ventilation inception, $Fn_h = 1.5$; $AR_h = 1$; Run 1038; Semi-Ogive. The run-up can be noticed to be releasing droplets toward the free surface and the LE. The red circle indicate the perturbation that ultimately triggers ventilation. The time is given from the start of the recording.

trigger Rayleigh-Taylor disturbances.

4.3.3. Influence of the Fn_h and Re_c on the Inception Mechanisms

The following section provided an analysis of the influence of the Fn_h and Re_c on the inception of ventilation.

Figure 4.23 categorizes the inception mechanisms for the test runs across the tested Froude numbers ($0.5 \leq Fr_h \leq 2.5$) for both geometries and aspect ratios. The figure distinguishes between two primary inception mechanisms: Leading Edge LE inception and Rayleigh-Taylor RT inception and their combinations with other mechanisms. Additionally, Figure 4.24 illustrates the relationship between the chord Reynolds number (Re_c) and the angle of attack (α) at which ventilation inception occurs for different geometries and aspect ratios. These figures highlight how both Fr_h and Re_c influence the transition between inception mechanisms. At low Fr_h and low $Re_c \approx 0.4 \times c$, Leading edge ventilation with LSB (LE-LSB) is identified as the dominant mechanism for both geometries. This indicates that flow instabilities caused by adverse pressure gradients at the leading edge are more prevalent in this regime. The presence of LSBs can be associated with a slight increase in lift. This phenomenon occurs because ventilation creates a stabilized bubble of air near the suction side, which smooths the transition from laminar to turbulent flow, maintains attached flow, and slightly enhances lift.

At intermediate conditions, particularly around $Fr_h = 1.25$ or $Re_c \approx 0.6 \times 10^6$, the angle of attack reaches its maximum for all configurations. In this range, the inception mechanisms transition from laminar separation bubble-dominated mechanisms to a combination of leading-edge and Rayleigh-Taylor instabilities. This transition introduces greater uncertainty, as shown in Table 4.2 and Table 4.3, as ventilation can be triggered by either mechanism independently or through their interaction. For higher aspect ratios ($AR = 1.5$), the transition to Rayleigh-Taylor-dominated mechanisms occurs at lower Fr_h, associated with the earlier compliance of the condition presented in Figure 4.22. The peak in the angle of attack observed corresponds to this transition between inception mechanisms and is related to the behaviour of the boundary layer. The flow begins shifting from predominantly laminar to more turbulent characteristics.

At high Fr_h and Re_c ($Re_c > 0.8 \times 10^6$), Rayleigh-Taylor instabilities dominate the ventilation inception process for both geometries. For the Semi-Ogive geometry, trailing-edge (TE) instabilities begin to emerge, reflecting the influence of its blunt trailing edge. On the other hand, the streamlined body of the NACA profile ensures that the triggering mechanisms remain fully Rayleigh-Taylor driven.

For $Fr_h \geq 2.5$, trailing-edge ventilation or combinations with tip-vortex ventilation are expected for the Semi-Ogive hydrofoil, as these mechanisms are already forming at lower angles of attack before full inception by RT-TE. This behaviour is illustrated in Figure 4.18. The NACA 0010-34, on the other hand, ensures that Rayleigh-Taylor-driven mechanisms remain dominant without significant interference from trailing-edge effects. Figure 4.25 illustrates the contrasting wake structures of the two hydrofoils before ventilation at $Fn_h = 1.5$, $AR = 1$. The ventilated wake behind the Semi-Ogive foil is visible, whereas the NACA 0010-34 maintains a stable flow with no significant wake formation.

At $AR = 1$, the results for the NACA 0010-34 nand Semi-Ogive geometries appear to overlap, as seen in Figure 4.24, while not for $AR = 1.5$. This suggests that, at lower aspect ratios, the influence of the geometry on ventilation inception is reduced.

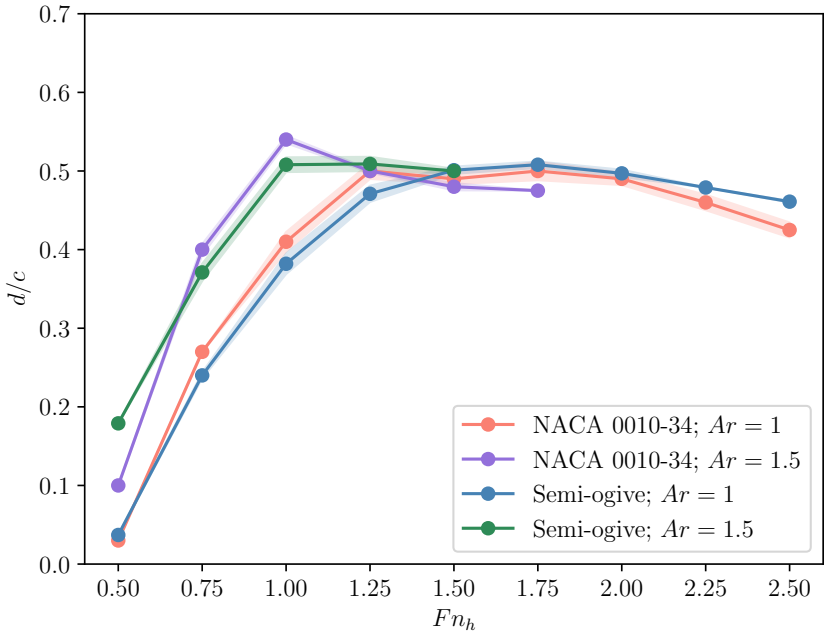

(a) $d/c - Fn_h$

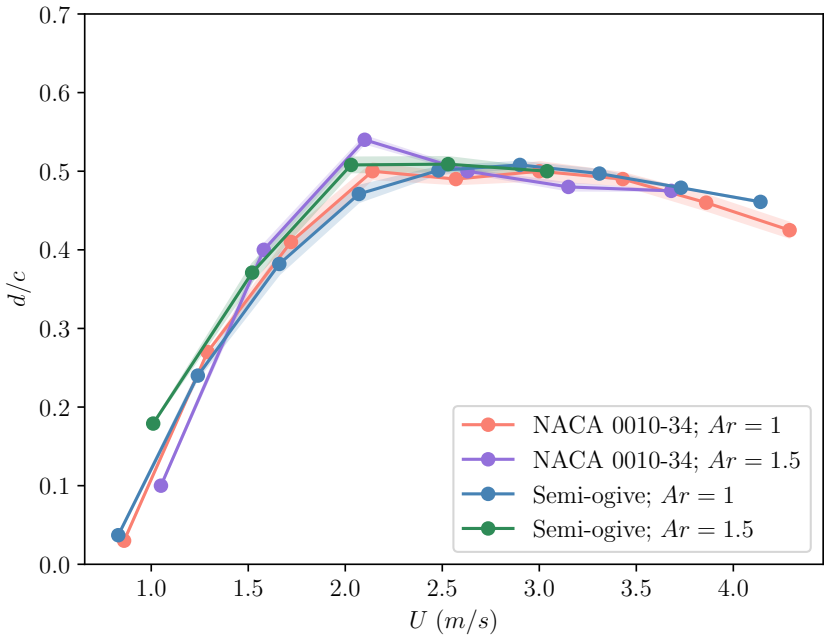

(b) $d/c - U$

Figure 4.22: The surface drawdown ratio, d/c, at the point of ventilation inception is presented as a function of Fn_h and U for both hydrofoil shapes (Semi-Ogive and NACA 0010-34) and aspect ratios (AR).

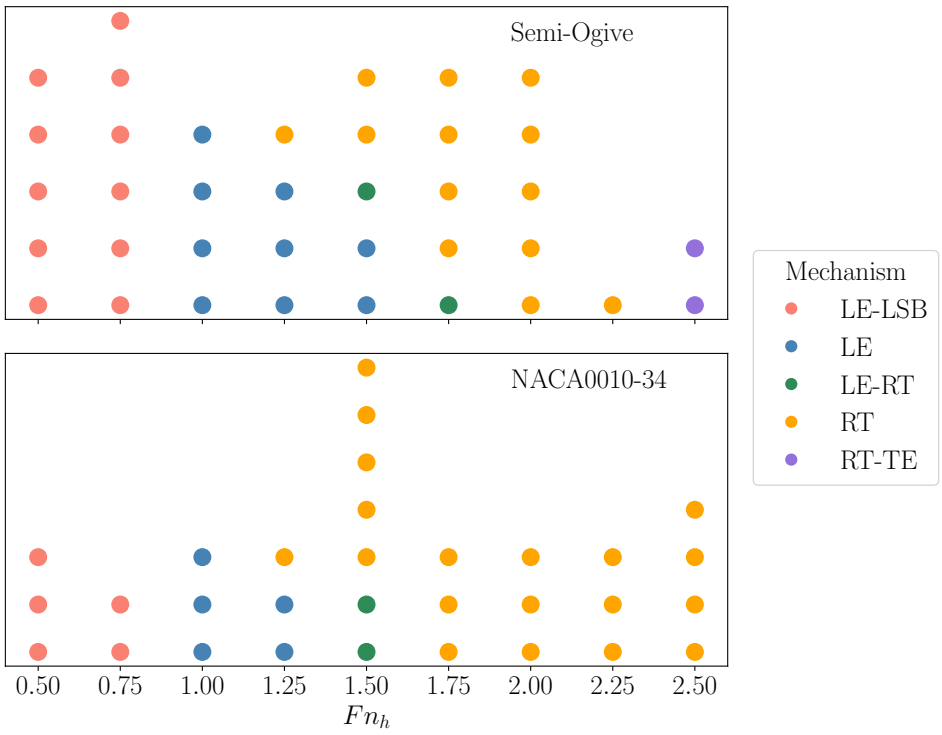

(a) $AR = 1$

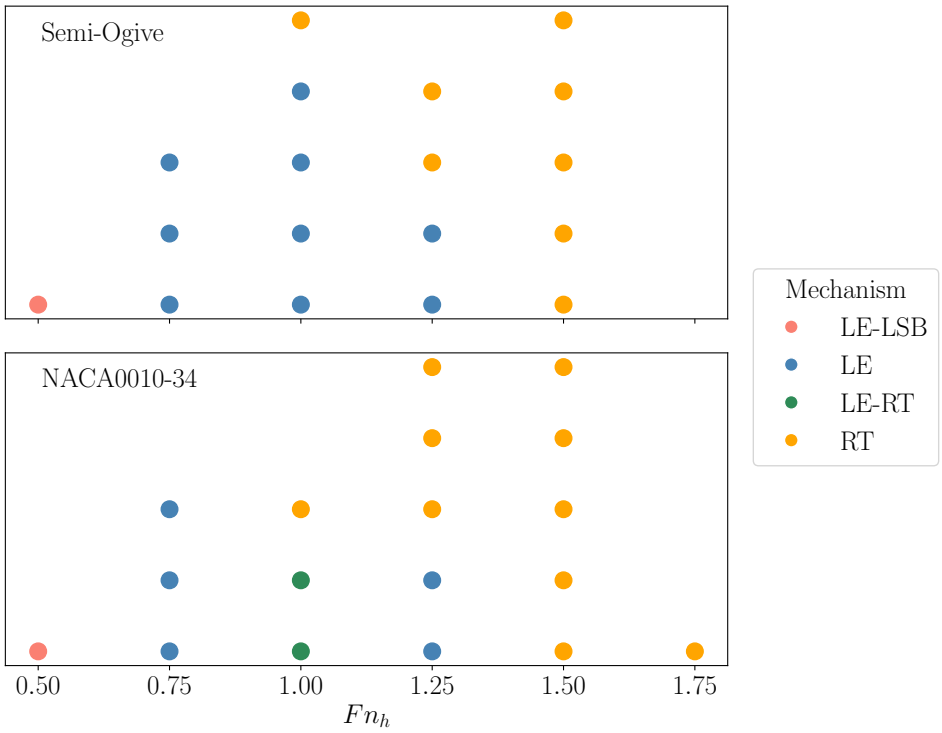

(b) $AR = 1.5$

Figure 4.23: Inception Mechanisms as a Function of Froude Number fpr $AR = 1$ and $AR = 1.5$. Each dot represents an experimental run, excluding those without camera availability. The graph distinguishes two primary mechanisms and three combinations: LE-LSB (Leading Edge inception by laminar separation bubble), LE (Leading Edge inception), LE-RT (Combined Leading Edge and Rayleigh-Taylor inception), RT (Rayleigh-Taylor inception), and RT-TE (Combined Rayleigh-Taylor and Trailing Edge inception).

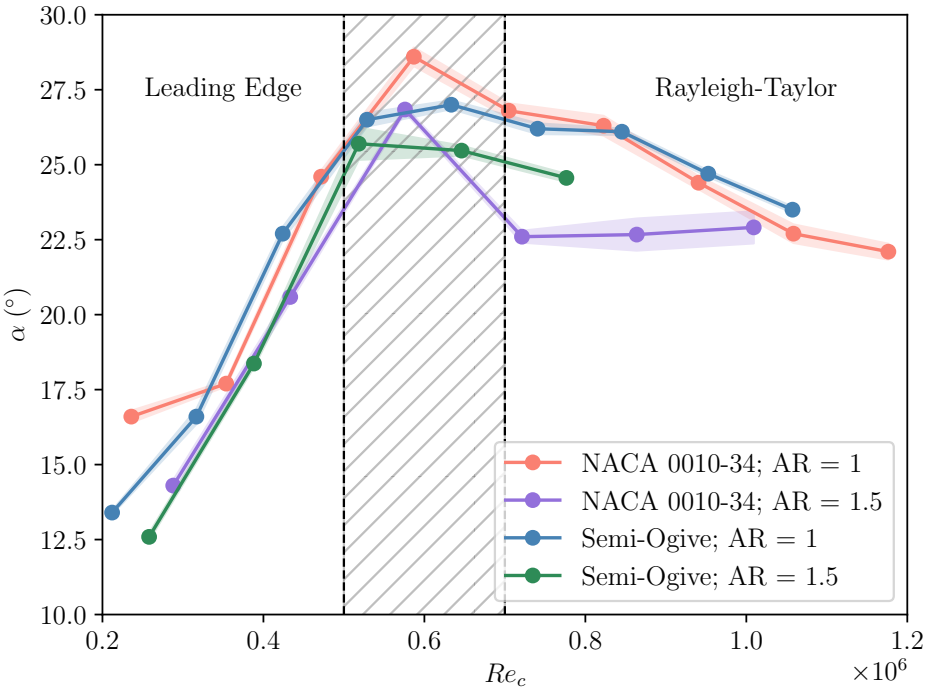

Figure 4.24: Ventilation inception angle as a function of the chord Reynolds Number. Hatched lines indicate a transitional region were there is a combination of LE and RT ventilation

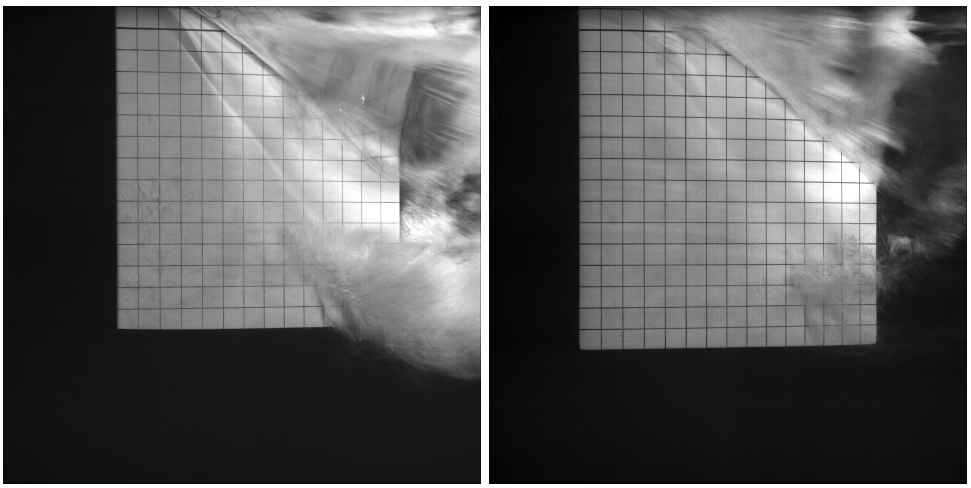

(a) Semi-Ogive **(b)** NACA 0010-34

Figure 4.25: Frame prior to ventilation, $Fn_h = 1.5$; $AR_h = 1$; Run 1090, Run 2132. The ventilated wake behind the Semi-ogive can be noted, while there is no wake behind the NACA profile.

4.3.4. Influence of the Inception Mechanisms and Fn_h on the AoA

Figure 4.26 and Figure 4.27 present the inception boundary in the $AoA - Fn_h$ parametric space for each AR and geometry. These graphs provide insights into the influence of the Froude number (Fn_h) and the corresponding inception mechanisms on the inception angle of attack (α_i).

Two distinct trends are visible in the graphs: an ascending trend associated with leading-edge (LE) ventilation and a descending trend driven by Rayleigh-Taylor ventilation.

For $0.5 \leq Fn_h \leq 1 - 1.25$, depending on the AR, both geometries exhibit a steep increase in α_i. This is linked to the run-up phenomenon described in previous sections. As Fn_h increases, the angle of attack at which the run-up collapses also increases, ultimately leading to a higher inception angle of attack. The Semi-Ogive hydrofoil consistently shows slightly lower α_i values compared to the NACA 0010-34, likely due to small differences in chord length between the two geometries and speed.

The transition between inception mechanisms occurs when the condition $d/c = 0.5$ is met. As reflected in Figure 4.22a, this transition takes place at $Fn_h = 1.25$ for $AR = 1$ and $Fn_h = 1.0$ for $AR = 1.5$. The higher peak observed in α_i for the NACA 0010-34 is likely related to differences in speed, suggesting that the Semi-Ogive's peak would occur slightly later, between $Fn_h = 1.25$ and $Fn_h = 1.5$. However, due to the fixed speeds tested, this delayed peak is not observable. This phenomenon is further supported by Figure 4.24, where, for $AR = 1$, the peak of the NACA 0010-34 lies exactly between these two Froude numbers, indicating that the difference in peak location is a direct consequence of the variation in tested speeds.

At $Fn_h \geq 1.25$, Rayleigh-Taylor ventilation dominates the ventilation inception process. Both geometries exhibit a slight decline in α, which might extend for $Fn_h > 2.5$. This behaviour is driven by a combination of the reduction in the d/c condition as Fn_h increases and the higher downward acceleration, which causes the free surface to meet the condition earlier in the region where d/c remains constant. The slight difference in α_i between the geometries at $Fn_h \geq 2$ can be attributed to the slight differences observed in Figure 4.22a. The condition for these Fn_h values is lower for the NACA 0010-34, which is reflected in a smaller inception angle of attack. However, if d/c is plotted as a function of speed, as shown in Figure 4.22b, there is an overlap in the data. This overlap suggests that the inception boundary as a function of Fn_h for the Semi-Ogive is shifted relative to the NACA 0010-34. Figure 4.24 shows α_i as a function of the Reynolds Number, for $AR = 1$ it can be noted that the data is coinciding.

4.4. Integration of Past Experimental Results - Flow Regime Map

After presenting the results from the towing tank experiments, the data is compared to the findings of Harwood et al. [2]. Figure 4.28 and Figure 4.29 illustrate the flow regime maps for the Semi-Ogive hydrofoil, as presented by Harwood et al. [2] in Figure 2.11, specifically highlighting the inception and stabilization boundaries. These maps define the transitions between fully wetted, partially ventilated, and fully ventilated flow regimes.

The results from Harwood et al. [2] were obtained via towing tank experiments. The methodology employed in their study aligns with the approach used in the present experimental campaign during the "Static Tests." In their experiments, the hydrofoil was set at a fixed α and was quasi-statically accelerated to increasing speeds until ventilation inception was reached. This approach corresponds to a vertical progression in the parametric $\alpha - Fn_h$ space. Conversely,

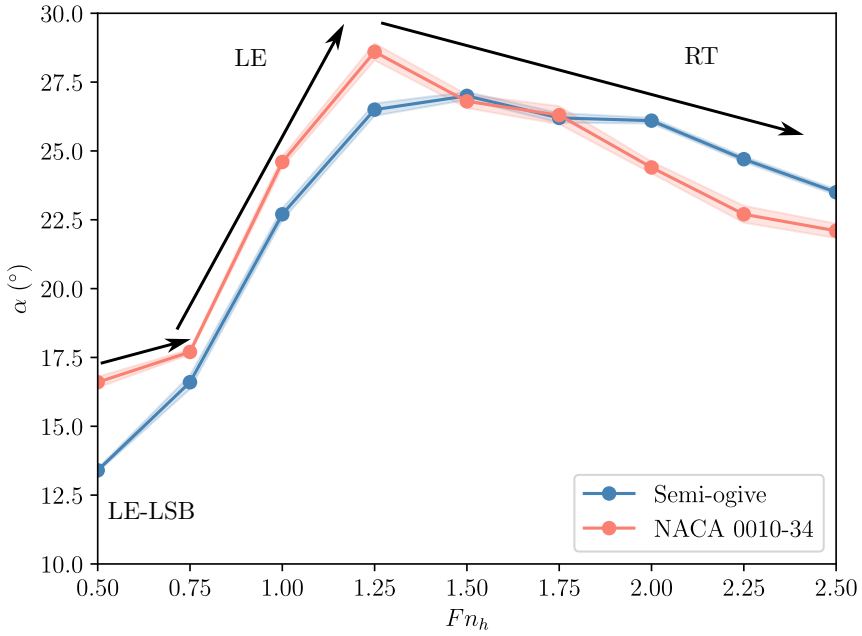

Figure 4.26: Ventilation inception angle of attack as a function of the depth Froude Number for $AR = 1$. The arrows indicate the trends of the AoA as a function of the Fn_h and the inception mechanism.

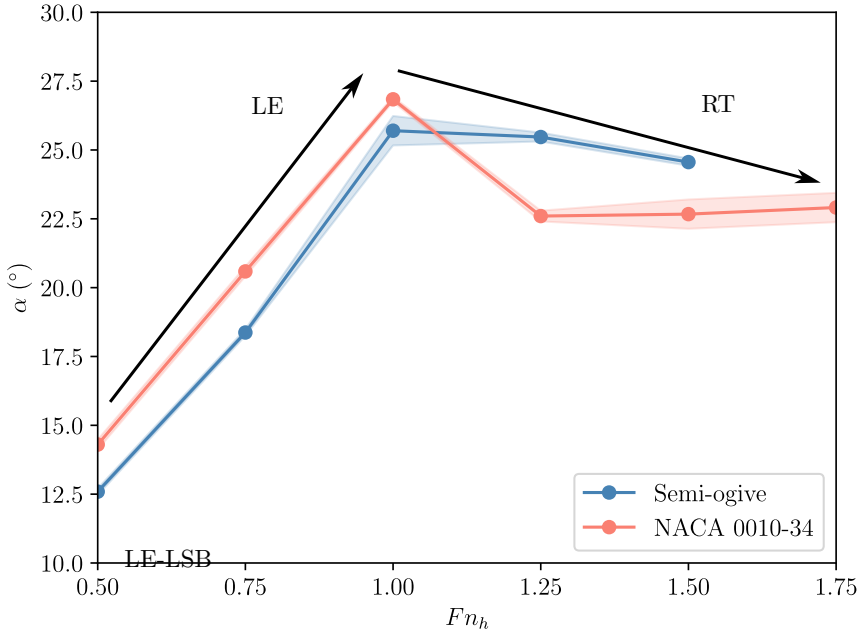

Figure 4.27: Ventilation inception angle of attack as a function of the depth Froude Number for $AR = 1.5$. The arrows indicate the trends of the AoA as a function of the Fn_h and the inception mechanism.

the present experimental campaign used a different methodology, where Fn_h was fixed, and the angle of attack (α) was quasi-statically varied, corresponding to a horizontal progression in Figure 4.28, named "Quasi-Static Tests."

The inception boundary, presented as a dotted line (blue for the present campaign and red for Harwood et al. [2]), represents the transition from a fully wetted to a partially or fully ventilated regime. In the case of moving horizontally, the hydrofoil will ventilate in accordance with the horizontal inception boundary, which is dependent on the acceleration. Conversely, if moving vertically, the foil will encounter the blue line. The data from both experimental campaigns appear to connect, as there is a shared point at the very lowest inception point. Furthermore, during the "Static Tests," the results obtained align well with those reported by Harwood et al. [2].

However, the vertical line at $\alpha = 15°$, as presented in Figure 2.11, was found to deviate significantly from reality, as evidenced by the updated regional map. The triangular dashed line represents the transition from partial ventilation (PV) to full ventilation (FV). In the present experiment, this transition was not explicitly tested. However, during the "Quasi-Static Tests," it was observed that ventilation inception occurred horizontally below this line in the PV regime, while above this line, the flow transitioned to FV.

For $AR = 1$, Harwood et al. [2] reported obtaining a point at $Fn_h = 3.5$ and $\alpha = 15°$. They stated that, after several runs, they were able to bring the hydrofoil through the inception boundary at $\alpha \approx 15°$ without inducing ventilation by decreasing the acceleration to its lowest possible value. Later, at a fixed speed, the hydrofoil naturally transitioned to ventilation via tip-vortex ventilation.

To connect this point with the present experimental campaign, it is possible to speculate about the inception boundary at $Fn_h \geq 2.5$. Two possibilities arise: First, given the blunt trailing edge (TE) of the Semi-Ogive and the growing influence of the ventilated wake it generates, it is possible that the tip-vortex formation, reported in run 1090 at an AoA occurring 3° earlier than full ventilation inception, triggers ventilation at higher Fn_h, resulting in a discontinuity in the data. This scenario is represented in Figure 4.28 by the green dashed line. Following this pathway, α_i would continue to decrease until coinciding with Harwood's data.

Second, following the trend observed in c/d, the foil could simply continue decreasing its α_i at the same rate as observed above $Fn_h = 2.0$. This path is more likely to be followed by the NACA 0010-34, as the absence of a blunt trailing edge minimizes the influence of wake. This scenario is represented by the purple dashed line in Figure 4.28.

In summary, the comparison with Harwood et al. [2] highlights the importance of proper experimental methodology in interpreting ventilation behaviour and provides a foundation for speculative trends at higher Fn_h.

4.5. Lift and Drag Semi-empirical Formulation

This section builds upon a semi-empirical formulation for lift and drag coefficients, derived from the work of Damley-Strnad et al. [48]. The formulation is designed to predict the force coefficients, C_L and C_D, in the regime prior to ventilation inception. The semi-empirical approach is expected to provide a good approximation for $Fn_h \geq 2$, as the authors state that at lower speeds, experimental results are dominated by surface tension and viscous effects. The results obtained from the semi-empirical model are compared to the experimental data from the present campaign, serving to validate the model's effectiveness in predicting the coefficients.

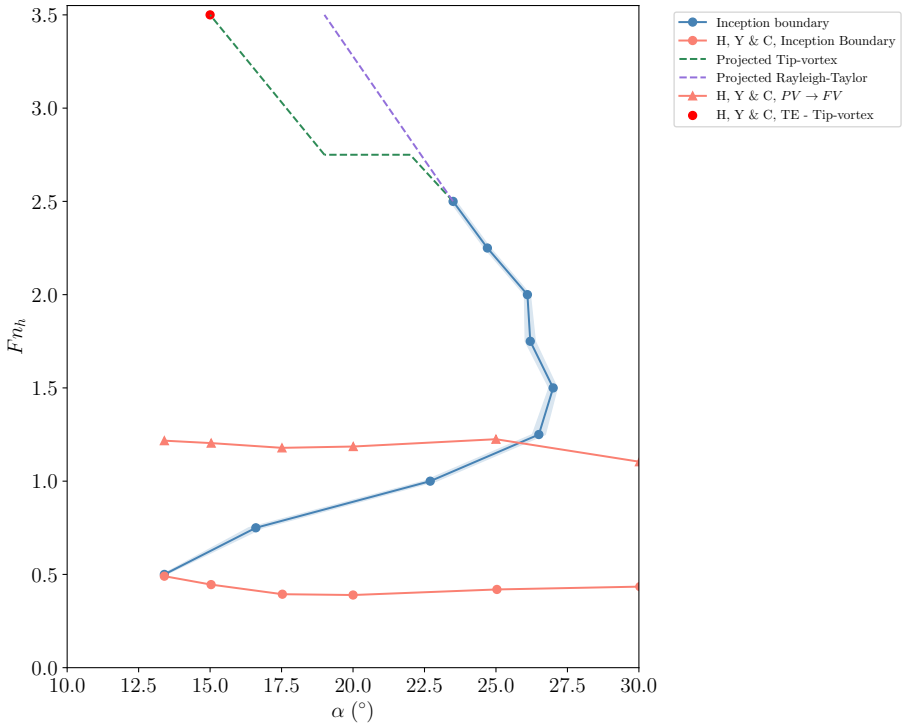

Figure 4.28: Flow regime map for the Semi-Ogive hydrofoil as a function of α and Fnh at a fixed aspect ratio of $AR_h = 1.0$. The inception boundary delineates the transition between fully wetted and partial or full ventilation regimes. Symbols mark experimentally observed boundaries for the Semi-Ogive hydrofoil, including boundaries documented in previous research by Harwood et al. [2] marked as H, Y & C. The dashed lines indicate projected trends for the inception and bifurcation boundaries based on empirical data. This figure is adapted from Harwood et al. [2].

4.5.1. Semi-empirical Lift and Drag Formula

The lift and drag coefficients are expressed using a semi-empirical formulation derived from the work of Damley-Strnad et al. [48]. The drag coefficient (C_D) is decomposed into three components: the frictional drag (C_{D_f}), the induced drag (C_{D_i}), and the wave drag (C_{D_w}). Each component is defined as follows:

$$C_{D_f} = \frac{0.075\left(1 + 2\frac{\tau_{\max}}{c} + \left(60\frac{\tau_{\max}}{c}\right)^4\right)}{\left|\log Re_c - 2\right|^2}, \tag{4.1}$$

$$C_{D_i} = \frac{2C_L^2}{\pi AR_h}, \tag{4.2}$$

$$C_{D_w} = C_L^2 e^{\frac{-2}{Fn_h^2}} \frac{1}{2Fn_h^2}. \tag{4.3}$$

In these equations:

- C_{D_f} represents the frictional drag, where $\tau_{\max}$ is the maximum thickness of the hydrofoil and c is the chord length.
- C_{D_i} represents the induced drag, which depends on the lift coefficient C_L, the aspect ratio AR_h, and the Froude number F_n.

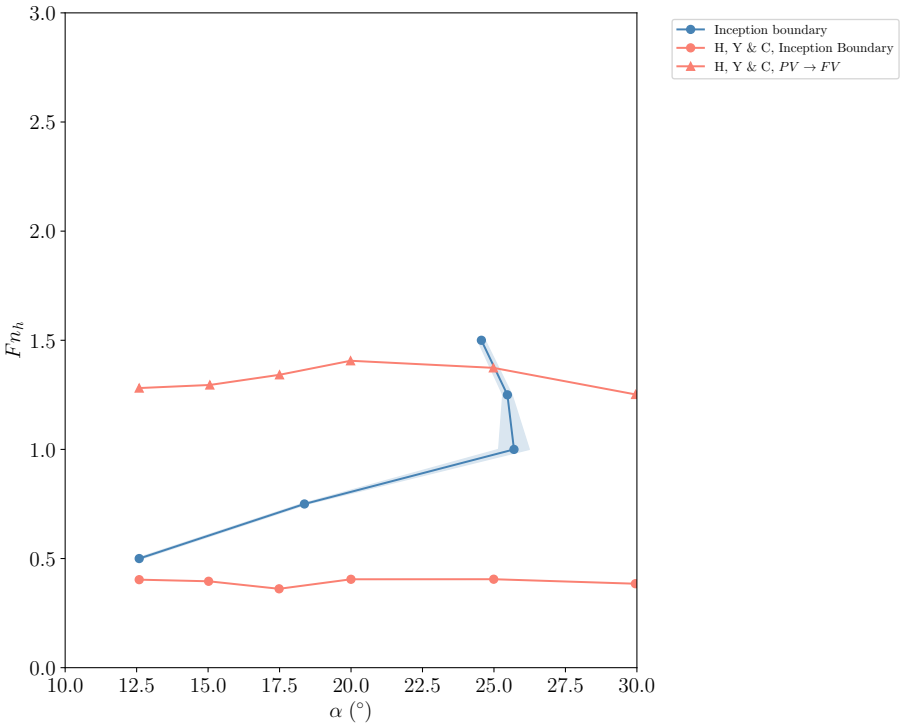

Figure 4.29: Fow regime map for the Semi-Ogive hydrofoil as a function of α and Fnh at a fixed aspect ratio of $AR_h = 1.5$. Data are from the experimental campaign and previous research [2]. Figure inspired from Harwood et al. [2].

- C_{D_w} represents the wave drag, which accounts for free-surface effects through an exponential decay term that depends on F_n.

The general expression for the drag coefficient is the following:

$$C_{D_{wet}} = 2C_{D_f} + C_{D_i} + C_{D_w} \tag{4.4}$$

In addition to the drag coefficients, the semi-empirical formulation provides an expression for the lift coefficient at ventilation inception, $C_{L_{\text{incep}}}$. This coefficient is expressed as a function of the Froude number, F_n, and a ventilation parameter, σ_v, which modulates the influence of ventilation effects. The general formulation is given by:

$$C_{L_{\text{incep}}} = F_n^{-0.5} \left[1 - e^{-\sigma_v F_n}\right], \tag{4.5}$$

where $C_{L_{\text{incep}}}$ represents the lift coefficient prior to full ventilation.

The behavior of $C_{L_{\text{incep}}}$ can be described under two limiting conditions:

$$C_{L_{\text{incep}}} = \begin{cases} 0, & \sigma_v F_n \to 0, \\ F_n^{-0.5}, & \sigma_v F_n \to \infty. \end{cases} \tag{4.6}$$

- When $\sigma_v F_n \to 0$, the lift coefficient approaches zero, representing conditions where ventilation effects are negligible or absent.

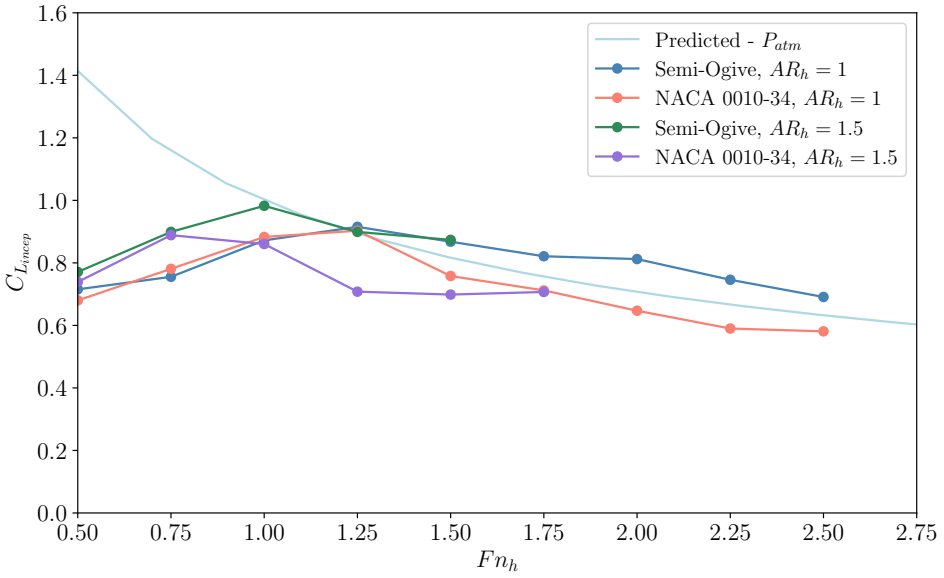

Figure 4.30: Maximum lift coefficients at the ventilation inception boundary, ($C_{L_{incep}}$), as a function of the Froude number, (Fn_h), for both hydrofoil geometries (Semi-Ogive and NACA 0010-34) and aspect ratios ($AR_h = 1$ and $AR_h = 1.5$). The plot includes a predicted curve at atmospheric pressure, calculated using Equation 4.5.

- When $\sigma_v F_n \to \infty$, the lift coefficient asymptotically reaches $F_n^{-0.5}$, indicating the maximum attainable lift in the presence of significant ventilation effects.

4.5.2. Comparison with Experimental C_L and C_D

The semi-empirical model for lift (C_L) and drag (C_D) coefficients was evaluated against experimental results from the present campaign and additional data from the literature. The comparison of predicted and experimental C_L, in Figure 4.30, shows that the predicted curve provides an upper limit for the lift coefficient, capturing the general trend of decreasing lift with increasing Fn_h. Experimental results for both the Semi-Ogive and NACA 0010-34 geometries follow this trend but consistently fall below the predicted curve, particularly at higher $AR_h = 1.5$. The Semi-Ogive exhibits higher C_L values compared to the NACA 0010-34 for both $AR_h = 1$ and $AR_h = 1.5$. Agreement between the predicted and experimental C_L improves at $F_n \geq 1.25$ which is when the inception mechanism transitions from LE to RT ventilation.

For drag comparisons, in Figure 4.31, the predicted curves for $AR_h = 1$ and $AR_h = 1.5$ capture the general trend of drag reduction with increasing F_n. Experimental C_D values are generally lower. The Semi-Ogive has slightly higher C_D values compared to the NACA 0010-34, particularly at $AR_h = 1.5$, due to trailing-edge effects and increased wake turbulence. At $F_n \geq 1.75$, the experimental C_D values align closely with the predicted trends, demonstrating the model's reliability in high F_n regimes.

The inclusion of literature data highlights the significance of the results obtained in the present experimental campaign. Except for the data from Vaughan and Ramsen [51], the literature data fails to reproduce the semi-empirical formula, likely due to differences in the methodologies employed to achieve ventilation compared to the present experimental campaign. Notably, the experiments conducted by Harwood et al. [2] used the same geometry as the present experiments. However, the significant discrepancies between their results and those obtained in this campaign further underscore that the experimental approach used by Harwood et al.

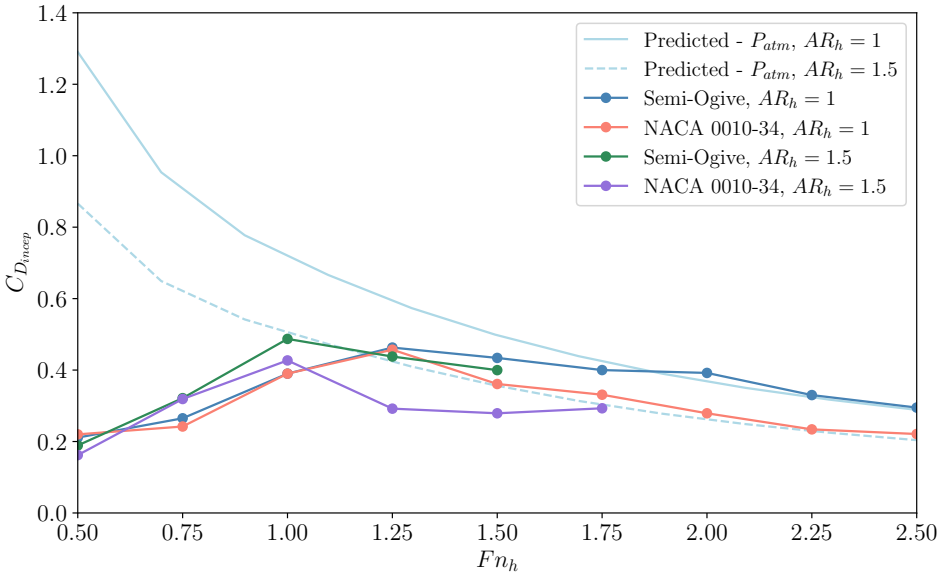

Figure 4.31: Maximum drag coefficients at the ventilation inception boundary, ($C_{D_{incep}}$), as a function of the Froude number, (Fn_h), for both hydrofoil geometries (Semi-Ogive and NACA 0010-34) and aspect ratios ($AR_h = 1$ and $AR_h = 1.5$). The plot includes a predicted curve at atmospheric pressure, calculated using Equation 4.4.

did not fully capture the essence of ventilation inception.

The differences in the lift coefficient below Fn_h are associated with the geometry of the tested foils. The geometries selected are of the thin airfoil type, which allows for separation at the leading edge, resulting in LE ventilation. For thicker, more streamlined bodies, the flow tends to separate at the trailing edge, increasing the angle of attack at which ventilation occurs at low speeds. This scenario would likely lead to ventilation dominated by Rayleigh-Taylor instabilities and, consequently, bring the values of C_L closer to the predicted ones.

Overall, the experimental data closely aligns with the semi-empirical model for $Fn_h \geq 1.0$. In contrast, the literature data appears scattered and deviates significantly from the model, highlighting the importance of consistent methodologies and geometries in achieving accurate results.

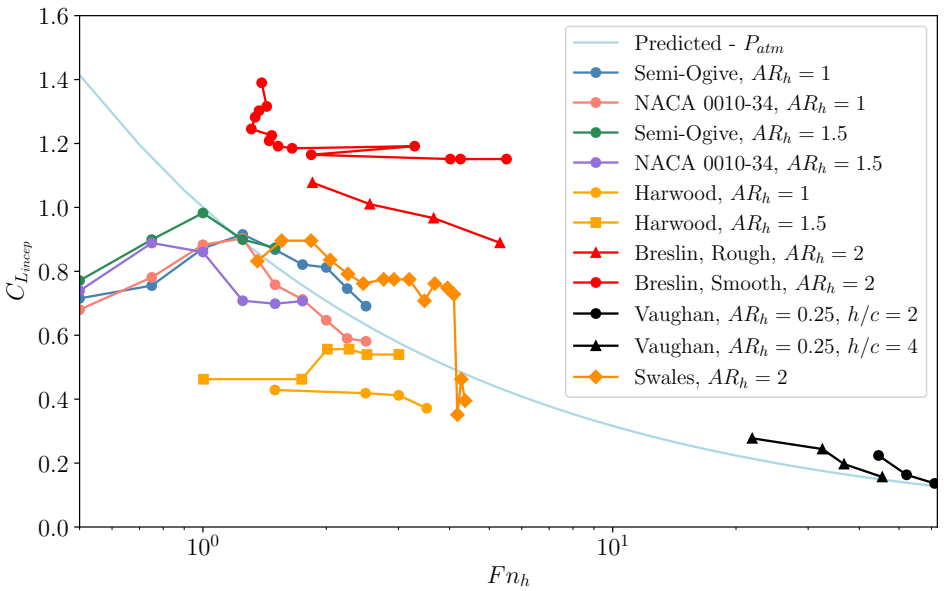

Figure 4.32: Maximum lift coefficients at the ventilation inception boundary, $C_{L_{incep}}$, as a function of the Froude number, Fn_h. This figure compares the experimental results with prior experimental data. Harwood: Harwood et al. [2], Breslin: Breslin & Skalak [7], Vaughan & Ramsen [51], Swales: Swales et al. [12]. Reprinted with modifications from Damley-Strnad et al. [48].

5

Conclusions and Recommendations

The results obtained in this study can serve as guidelines for a deeper understanding of the mechanisms associated with ventilation inception. Two experimental methods were used to describe the behaviour of ventilation in the $\alpha - Fn_h$ parametric space: one based on previous experimental campaigns (Static Tests) and one new methodology not previously studied (Quasi-Static Tests). The study concludes that the results obtained using the "Quasi-Static Tests" methodology differ significantly from those obtained using the historical method "Static Tests", and the previously assumed inception boundary. This section will conclude the study based on the answers provided to the research questions.

5.1. Conclusions on the Research Question

The research questions accompanying the thesis described in this report were formed in section 1.5. The answers to them were found throughout the project. In this section, the supporting questions are first answered, followed by an answer to the main research question.

SQ 1: How repetitive is the AoA at which ventilation inception occurs for a given Fn_h and AR?

In section 4.2, it is demonstrated that, for the "Quasi-Static Tests," at a given AR and for the combination of all Fn_h, the standard error of the mean has an average value of only 0.195° for $AR = 1.0$ and 0.25° for $AR = 1.5$. This corresponds to a relative error of 1% to 2% over the mean α_i at each Fn_h. The mean α_i at each Fn_h deviates by no more than 0.5°, with the maximum deviations occurring at the transition between flow regimes around $Fn_h = 1.25$ for $AR = 1.0$ and $Fn_h = 1.0$ for $AR = 1.5$. This last increased uncertainty is associated with the combination of the inception mechanisms, LE ventilation dominates when $Fn_h \leq 1.25$ while RT ventilation is associated with $Fn_h \geq 1.25$. Therefore, based on the repeatability analysis over the α_i, the inception boundaries described in Figure 4.5 and Figure 4.6 are considered reliable.

SQ 2: How do varying Froude numbers affect α_i for a given geometry?

In subsection 4.2.1, the inception boundary is presented in the $\alpha - Fn_h$ parametric space. The initial hypothesis, supported by the literature analysis, suggested that the inception angle of attack would remain constant as Fn_h increased, at an angle referred to as the stall angle (α_s) with an approximate value of $\alpha_s \approx 15°$. However, the present work has demonstrated that this assumption is not realistic. For a sharp-nose hydrofoil, the inception boundary follows the trends shown in Figure 4.5 for $AR = 1$ and Figure 4.6 for $AR = 1.5$.

Two main trends for α_i were identified in subsection 4.3.4. Firstly, in the region dominated by leading-edge ventilation, α_i shows a sharp increase as Fn_h rises to approximately $Fn_h = 1.25$. This phenomenon is associated with the run-up behaviour described in this study. Conversely, for streamlined, thicker hydrofoils, this trend is speculated to be absent due to the flow's tendency to separate at the trailing edge (TE) rather than the leading edge (LE), as these foils lack the separated flow region at the LE necessary for LE-driven ventilation. Secondly, in the region dominated by Rayleigh-Taylor ventilation, α_i shows a consistent decrease as Fn_h rises. This phenomenon is speculated to be associated with the d/c condition described in subsection 4.3.4. The transition between trends and inception mechanisms coincides with the maximum value of α_i. For higher Fn_h for values beyond the tested range ($F_n \geq 2.5$), the trend is expected to persist. The results indicate that the hydrofoils follow the trend described by Equation 4.5. As C_L decreases with increasing F_n, the angle of attack is expected to continue decreasing. This behaviour aligns with the experimental observations.

SQ 3: How are the inception mechanisms affected by the Fn_h and the Re_c?

The variation of the inception mechanisms with respect to Fn_h and Re_h is presented in subsection 4.3.3. At low Fn_h and low Re_c ($Re_c \approx 0.4 \times 10^6$), leading-edge ventilation driven by laminar separation bubbles (LE-LSB) is the dominant mechanism. This regime is characterized by flow instabilities caused by adverse pressure gradients at the leading edge, resulting in slightly increased lift due to the stabilization of the laminar separation bubble.

As Fn_h and Re_c increase, particularly around $Fn_h = 1.25$ or $Re_c \approx 0.6 \times 10^6$, the inception mechanisms transition from laminar separation-dominated behaviour to a combination of leading-edge and Rayleigh-Taylor instabilities. For higher aspect ratios ($AR = 1.5$), this transition occurs at lower Fn_h. At high Fn_h and Re_c ($Re_c > 0.8 \times 10^6$), Rayleigh-Taylor instabilities dominate the inception process.

SQ 4: How does varying the hydrofoil geometry, particularly the trailing edge shape, impact the inception AoA and mechanisms at moderate to low Fn_h?

This study conducted towing tank experiments with two distinct hydrofoil geometries: a Semi-Ogive profile with a chord length of $c = 0.2794$ m and a blunt trailing edge, and a NACA 0010-34 profile with $c = 0.3$ m and a streamlined trailing edge.

For the Semi-Ogive hydrofoil, trailing-edge dominance begins to emerge at $Fn_h = 2.5$, highlighting the influence of its blunt trailing edge. This geometry enhances the coupling between Rayleigh-Taylor and trailing-edge mechanisms, making RT-TE combinations increasingly prevalent at moderate to high Fn_h. In contrast, the NACA 0010-34, with its streamlined trailing edge, minimizes trailing-edge-induced instabilities and maintains mechanisms dominated entirely by RT instabilities.

At low Fn_h there is no significant difference between the two tested geometries. The small differences in AoA can be associated to the difference in speed to match the Fn_h. The NACA 0010-34 experiences a higher α_i peak at $Fn_h = 1.25$ while this is not observed for the Semi-ogive. However, a peak is expected for the Semi-ogive at $1.25 \leq Fn_h \leq 1.5$ due to the observations in Figure 4.24.

At $AR = 1$, the results for the NACA 0010-34 and Semi-Ogive geometries show significant overlap in the Re_h, as illustrated in Figure 4.24, suggesting that at lower aspect ratios, the impact of geometry on ventilation inception mechanisms is diminished. However, at $AR = 1.5$, the divergence between the two profiles becomes more pronounced, emphasizing the increased sensitivity of the inception mechanisms to geometric differences at higher aspect ratios.

MRQ: How is the inception of ventilation affected by a quasi-static variation of the angle of attack?

The inception of ventilation under quasi-static variations of α is governed by a complex interplay of parameters, including Fn_h, Re_c, AR, and hydrofoil geometry. Ventilation inception is highly repeatable, with minimal deviation in α_i for given Fn_h and AR conditions. However, uncertainties increase in transitional flow regimes, particularly at $Fn_h = 1.25$ for $AR = 1.0$, where leading-edge and Rayleigh-Taylor mechanisms interact.

The relationship between α_i and Fn_h is dynamic, with α_i increasing sharply at low Fn_h due to LE-driven mechanisms and decreasing steadily at higher Fn_h as RT-driven instabilities dominate. This transition aligns with changes in the stability of flow structures, which are influenced by Re_c. At low $Fn_h \leq 1.25$ and Re_c, laminar separation bubbles (LE-LSB) dominate the flow dynamics, while at intermediate values, a mix of LE and RT instabilities emerges. At higher $Fn_h \geq 1.25$ and Re_c, RT instabilities become the primary driver of ventilation. The unexpectedly high angles of attack observed during this phase, exceeding the initially hypothesized stall angle of $\alpha_s \approx 15°$, challenge prior assumptions reported in the literature and highlight the dynamic nature of ventilation inception in sharp-nose hydrofoils.

Hydrofoil geometry further modulates these dynamics, particularly the trailing-edge shape. Blunt trailing edges, such as those in the Semi-Ogive hydrofoil, introduce trailing-edge instabilities (RT-TE) at moderate Fn_h, while streamlined designs like the NACA 0010-34 predominantly follow RT-driven mechanisms. For higher aspect ratios ($AR = 1.5$), the impact of geometry becomes more pronounced, leading to divergence in inception AoA and mechanisms compared to lower aspect ratios.

Overall, the inception of ventilation is not governed by a single mechanism but results from a dynamic interaction of flow conditions, hydrofoil design, and operating parameters. For sharp-nose hydrofoils, α_i is driven by LE mechanisms at low Fn_h, while RT instabilities dominate at high Fn_h. Geometry accentuates these effects, with trailing-edge shapes introducing additional complexities.

This study has successfully established a new inception boundary inspired by the work of Harwood et al. [2] depicted in Figure 2.11, this is illustrated in Figure 4.28 and Figure 4.29. By integrating Harwood's findings with the results from the present experimental campaign, the refined flow regime map offers a more precise and comprehensive representation of ventilation inception dynamics.

5.2. Future Recommendations

This section provides recommendations for further related research, arranged by the different topics addressed in the present work.

- **Develop computational tools to track the free surface and identify instabilities:** This thesis has generated extensive visual data of the free surface using stereo-mode above and underwater cameras. Future research could focus on developing advanced computational tools or software capable of detecting and reconstructing key structures in the captured images, such as closure boundaries and free-surface deformation. These tools should leverage image processing and machine learning techniques to automate the identification of flow features and instabilities. Such advancements would enable a more precise analysis of ventilation mechanisms and offer deeper insights into the complex interactions of flow dynamics near the free surface.
- **Perform PIV on the suction side to observe flow separation before ventilation:** This thesis, drawing from the observations of Wadlin [10] and Harwood [15], has hypothesized that a region of flow separation exists on the suction side before ventilation, which subsequently expands as ventilation progresses. While this phenomenon was indicated using oil painting techniques, these methods have significant limitations in capturing the transient flow behaviour. Future studies should focus on visualizing the flow dynamics immediately preceding ventilation inception. Time-resolved PIV measurements on the suction side are recommended to capture the unsteady flow separation dynamics leading to ventilation. This approach would provide more detailed insights into the mechanisms driving ventilation initiation and development.
- **Investigate the influence of waves on ventilation inception:** This thesis has focused on the dynamics of ventilation in calm water conditions. However, this is an unrealistic approximation as sea states are far from flat and typically involve waves. Further experiments should aim to elucidate the mechanisms of ventilation inception in waves by challenging the current understanding, which is limited to qualitative observations by McGregor et al. [31]. The proposed study would systematically decouple and quantify the contributions of a_h and a_w to the earlier onset or delay of ventilation under various sea state conditions. This would include testing in regular and irregular waves, both in head and following seas.
- **Develop a CFD model to compare with experimental results:** Given the significant amount of visual data provided by this thesis, future work could focus on developing a CFD code to simulate the observed ventilation mechanisms and compare these results with experimental data. The CFD model should aim to replicate the results observed in the experiment. This effort would allow for predictive modelling of ventilation in conditions that are challenging to replicate experimentally.
- **Investigate the inception of ventilation in streamlined, thick hydrofoils:** The present work has focused on sharp-nose leading-edge hydrofoils, which are thin airfoils where flow separates at the leading edge. Future studies should investigate streamlined, thicker hydrofoil designs optimized for reduced separation. This would provide a clearer understanding of how trailing-edge separation affects ventilation mechanisms, particularly at low Fn_h. Testing such designs would extend the applicability of the findings to a broader range of hydrofoil geometries.
- **Perform towing tank testing at $Fn_h \geq 2.5$:** This thesis has focused on $Fn_h \leq 2.5$ due to limitations in the towing tank. However, predictions have been made for higher

Fn_h based on observations and trends identified in this work. Future research should conduct towing tank testing using the same geometries and quasi-static conditions at $Fn_h \geq 2.5$. This would validate the scaling relations and trends established here and improve the reliability of predictions for real-world applications, particularly in high-performance hydrofoils.

References

[1] C. M. Harwood et al. "Experimental and Numerical Investigation of Ventilation Inception and Washout Mechanism of a Surface-Piercing Hydrofoil". In: *30th Symposium on Nabal Hydrodynamics*. Tasmania, Australia, 2014.

[2] C. M. Harwood, Y. L. Young, and S. L. Ceccio. "Ventilated Cavities on a Surface-Piercing Hydrofoil at Moderate Froude Numbers: Cavity Formation, Elimination and Stability". In: *J. Fluid Mech.* 800 (2016), pp. 5–56.

[3] S. Subramaniam. "Multiphase flows: Rich physics, challenging theory, and big simulations". In: *Physical Review Fluids* 5.110520 (2020), pp. 1–36.

[4] O. Faltinsen. *Hydrodynamics of High-Speed Marine Vehicles*. Cambridge University Press, 2006.

[5] A. J. Acosta. "Hydrofoils and Hydrofoil Craft". In: *Annual Review on Fluid Mechanics* 5.5 (1973), pp. 161–184.

[6] Y. L. Young et al. "Ventilation of Lifting Bodies: Review of the Physics and Discussion of Scaling Effects". In: *Applied Mechanics Reviews* 69 (2017), pp. 1–38.

[7] J. P. Breslin and R. Skalak. *Exploratory Study of Ventilated Flows About Yawed Surface-Piercing Struts*. Tech. rep. 2-23-59W. Washington, DC: National Aeronautics and Space Administration, 1957.

[8] B. W. Pearce and P. A. Brandner. "Experimental Investigation of a Base-Ventilated Supercavitating Hydrofoil with Interceptor". In: *8th International Syposium of Cavitation*. Singapore, 2012.

[9] J. M. Wetzel. *Experimental Studies of Air Ventilation of Vertical, Semi-Submerged Bodies*. Tech. rep. 57. Minneapolis, MN: St. Anthony Falls Hydraulic Laboratory, University of Minnesota, 1957.

[10] K. L. Wadlin. "Mechanics of Ventilation Inception". In: *Second Symposium on Naval Hydrodynamics*. 1958, pp. 425–446.

[11] R. S. Rothblum, D. A. Mayer, and G. M. Wilburn. *Ventilation, Cavitation and Other Characteristics of High Speed Surface-Piercing Struts*. Tech. rep. E-55.2. Pasadena, CA: Carolina Institute of Technology, 1969.

[12] P. D. Swales et al. "The Mechanism of Ventilation Inception on Surface Piercing Foils". In: *J. Mech. E.* 16.1 (1974), pp. 18–24.

[13] C. E. Brennen. *Cavitation and Bubble Dynamics*. Pasadena, Calif: Oxford University Press, 1995.

[14] J.-P. Franc and J.-M. Michel. *Fundamentals of Cavitation*. Dordrecht: Kluwer Academic Publishers, 2004.

[15] C. M. Harwood. "The Hydrodynamic and Hydroelstic Responses of Rigid and Flexible Surface-Piercing Hydroofils in Multi-Phase Flows". PhD thesis. University of Michigan, 2016.

[16] R. L. Waid. *Experimental Investigation of the Ventilation of Vertical Surface-Piercing Strutrs in the Presence of Cavitation*. Tech. rep. AD738493. Sunnyvele, CA: Naval Ship Research and Development Center, 1968.

[17] Y. L. Young and S. Brizzolara. "Numerical and Phisycal Investigation of a Surface-Piercing Hydrofoil". In: *Thrid International Symposium of Marine Propulsors*. Tasmania, Australia, 2013.

[18] B. Perry. *Experiments on Struts Piercing the Water Surface*. Tech. rep. E-55.1. Pasadena, CA: Carolina Institute of Technology, 1954.

[19] T. Kiceniuk. *A Preliminary Experimental Study of Vertical Hydrofoils of Low Aspect Ratio Piercing a Water Surface*. Tech. rep. E-55.2. Pasadena, CA: Carolina Institute of Technology, 1954.

[20] G. Fridsma. *Ventilation Inception on a Surface Piercing Dihedral Hydrofoil with Plan Surface Wedge Section*. Tech. rep. 952. Hoboken, NJ: Davidson Laboratory, Stevens Institute of Technology, 1963.

[21] H. W. Emmons, C. T. Chang, and B. C. Watson. "Taylor instability of finite surface waves". In: *Journal of Fluid Mechanics* 7.2 (1960), pp. 177–193.

[22] R. S. Rothblum. "Investigation of Methods of Deleyiong or Controlling Ventilation on Surface Piercing Struts". PhD thesis. University of Leeds, 1977.

[23] T. Fuwa et al. "Experimental Study on Spray Shape, Spray Drag and Flow Field of Surface-Piercing Vertical Strut Advancing at High Speed". In: *Papers Ship Res. Inst.* 30.1 (1993), pp. 1–31.

[24] E. M. Pogozelski, J. Katz, and T. T. Huang. "The flow structure around a surface piercing strut". In: *Physics of Fluids* 9.5 (1997), pp. 1387–1399.

[25] M. Charlou and J. Wackers. "Numerical simulation of bi-stable ventilated flows around surface-piercing hydrofoils". In: *22th Numerical Towing Tank Symposium, NUTTS'19*. Topar, Portugal, 2019.

[26] M. Andrun et al. "CFD Analysis of Surface-Piercing Hydrofoil Ventilation Inception". In: *22nd Symposium, on Theory and Practice of Shipbuilding*. Croatia, 2016.

[27] R. Huang, R. Qiu, and Y. Zhi et al. "Investigations into the Ventilated Cavities around a Surface-Piercing Hydrofoil at High Froude Numbers". In: *Physics of Fluids* 34.043304 (2022), pp. 1–19.

[28] Y. Wang et al. "Research on Ventilation and Supercavitation Mechanism of High-Speed Surface-Piercing Hydrofoil". In: *Physics of Fluids* 34.023316 (2022), pp. 1–17.

[29] A. Yu et al. "Experimental and numerical study of ventilation cavitation around a NACA0015 hydrofoil with special emphasis on bubble evolution and air-vapor interactions". In: *Engineering Computations* 25.3 (2018), pp. 1528–1542.

[30] H. Zhou et al. "Interaction between Natural and Ventilated Cavitation around a Base Ventilated Hydrofoil". In: *Journal of Applied Fluid Mechanics* 12.6 (2019), pp. 1873–1883.

[31] R. C. McGregor et al. "An Examination of the Infuence of Waves on the Ventilation of Surface-Piercing Struts". In: *J. Fluid Mech.* 61.1 (1973), pp. 85–96.

[32] Y. L. Young et al. "Wave effects on the hydroelastic response of a surface-piercing hydrofoil. Part 1. Fully wetted and ventilated flows". In: *J. FLuid Mech.* 963 (2023a), A37.

[33] Y. L. Young et al. "Wave effects on the hydroelastic response of a surface-piercing hydrofoil. Part 2. Cavitating and ventilating flows". In: *J. FLuid Mech.* 965 (2023b), A3.

[34] C. M. Harwood et al. “The hydroelastic response of a surface-piercing hydrofoil in multiphase flows. Part 1. passive hydroelasticity”. In: *J. Fluid Mech.* 881 (2019a), pp. 313–364.

[35] C. M. Harwood et al. “The hydroelastic response of a surface-piercing hydrofoil in multiphase flows. Part 2. Modal parameters and generalized fluid forces”. In: *J. Fluid Mech.* 884 (2019b), A3.

[36] C. W. Jr. Coffee and R. E. McKann. *Hydrodynamic drag of 12- and 21-percent-thick surface-piercing struts*. Tech. rep. 3963. Washington, DC, US: NACA Tech. Note, 1953.

[37] J. A. Ramsen. *An Experimental Hydrodynamic Investigation of the Inception of Vortex Ventilation*. Tech. rep. 3903. Washington, DC: National Advisory Committee for Aeronautics, 1957.

[38] V. Ageorges, J. Peixinho, and G. Perret. “Flow and Air-Entraiment Around Partially Submerged Vertical Cylinders”. In: *Physical Review Fluids* 4.064801 (2019), pp. 1–14.

[39] Y. Zhi et al. “Numerical Investigation into the Ventilation Elimination Mechanism of a Surface-Piercing Hydrofiol”. In: *Ocean Engineering* 243.110225 (2022), pp. 1–12.

[40] Y. Wang et al. “Experimental Study on the Mechanism of Cavitation-Induced Ventilation”. In: *International Journal of Multiphase Flow* 170.104633 (2024), pp. 1–11.

[41] I. H. Abbott and A. E. Von Doenhoff. *Theory of Wing Sections*. 2nd ed. Toronto, ON: General Publishing Company, Ltd., 1959.

[42] Y. A. Çengel and J. M. Cimbala. *Fluid Mechanics: Fundamentals and Applications*. 1st ed. New York, NY: McGraw-Hil, 2006.

[43] W. H. Michel et al. *Hydrodynamic Characteristics of Components*. Tech. rep. NONR-507(00). New York, NY: Office of Naval Research, 1954.

[44] S. S. Kulkarmi et al. “Design stdy of Horizontal Axis Tidal Turbine Blade”. In: *Mindanao Journal of Science and Technology* 15 (2017), pp. 12–34.

[45] E. S. Hostmark. *Experimental and numerical investigations on wave profiles and ventilation on a surface-piercing hydrofoil*. 2021.

[46] D. F. De Lange and G. J. De Bruin. “Sheet Cavitation and Cloud Cavitation, Re-Entrant Jet and Three-Dimensionality”. In: *Fascination of Fluid Dynamics*. 1998, pp. 91–114.

[47] R. Arndt, W. Hambleton, and E. Amromin. “Creation and maintenance of cavities under horizontal surfaces in steady and gust flows.” In: *Kournal of Fluid Engineering* 131.11 (2009).

[48] A. Damley-Strnad, C. M. Harwood, and Y. L. Young. “Hydrodynamic Performance and Hysteresis Response of Hydrofoils in Ventilated Flows”. In: *6th Internatinal Symposium on Marine Propulsors*. Rome, Italy, 2019.

[49] Meet In Holland. *TU Delft Towing Tank*. URL: `https://www.meetinholland.nl/projecten/tu-delft-towing-tank`.

[50] BIMP I et al. *Evaluation of measurement data -Guide to the expression of uncertainty in measurement*. Tech. rep. 100. JCGM, 2008.

[51] V. L. Vaughan and J. A: Ramsen. *Hydrodynamic characteristics over a range of speed up to 80 feet per secod of a rectangular modified flat plate having an aspect ratio of 0.25 and operating at several depths of submersion*. Tech. rep. Langley Field, Va: Langley Aeronautical Laboratory, 1957.

[52] S. F. Hoermer and H. V. Borst. *Fluid-Dynamic Lift: Practical information on Aerodynamic and Hydrodynamic Lift*. New York, NY, 1985.

[53] J. D. Anderson. *Fundamentals of Aerodynamics*. 6th ed. New York, NY: McGraw-Hill Education, 2017.

[54] A. Llopis-Pascual. "Supercritial coanda jets for flight control effectors". PhD thesis. University of Manchester, 2017.

[55] Tom Benson. *Inclination effects on drag*. URL: `https://www.grc.nasa.gov/www/k-12/VirtualAero/BottleRocket/airplane/inclind.html`.

[56] E.J. Kerschen and P. W. Hammertin. *Effects of Nose Radius and Aerodynamic Loading on Leading Edge Receptivity*. Tech. rep. Tucson, AZ: University of Arizona, 1998.

[57] R. W. Kermeen. *NACA 4412 and Walchner Profil 7 Hydrofoils in Noncavitating and Cavitating Flows*. Tech. rep. 47.5. Pasadena, CA: Carolina institute of Technology, 1956.

[58] D. E. Gault. *A correlation of low-speed, airfoil, section stalling characteristics with reynolds number and airfoil geometry*. Tech. rep. 3963. NACA: Ames Aeronautical Laboratory, 1998.

[59] P. K. Chang. "Laminar Sepatation of Flow around Symmetrical Struts at Zero Angle of Attack". In: *J. Frankl. Inst.* 270.5 (1960), pp. 382–396.

[60] P. K. Chang. "Separation of Flow". In: *J. Frankl. Inst.* 272.6 (1961), pp. 433–448.

[61] R. Hecker and G. Ober. *Flow Separation, Reattachment, and Ventilation of Foils with Sharp Leading Edge at Low Reynolds Number*. Tech. rep. AD-787500. Bethesda, MD: Naval Ship Research and Development Center, 1974.

[62] S.Kumar and S. Narayanan. "Airfoil thickness effects on flow nd acoustic characteristics." In: *Alexandria Engineering Jounal* 61 (2021), pp. 4679–4699.

[63] N. Thomareis and G. Papadakis. "Effect of trailing edge shape on the separated flow characteristics around an airfoil at low Reynolds number: A numerical study". In: *Physics of Fluids* 29.014101 (2017), pp. 1–18.

[64] M. T. Beierle. "Investigation of effects of surface roughness on symmetric airfoil lift and lift-to-drag ratio". PhD thesis. University of Maryland, College Park, 1998.

[65] R. S. Rothblum, R. C. McGregor, and P. D. Swales. "Effect of roughness, wettability and speed on the ventilation characteristics of surface piercing hydrofoil struts". In: *Intl Hovering Crafts, Hydrofoil, and Adv. Transit Sys. Conf.* 1974, pp. 235–243.

A

Foil Theory

This appendix covers foil theory, emphasizing the physical aspects and theoretical background. Foil theory includes the study of lift, drag, and the behaviour of foils in different fluid conditions.

A.1. Kutta-Joukowki Theorem

The Kutta-Joukowki theorem is a simplified version of the classic Prandtl lifting-line theory to model flow around a foil [43]. This theorem can be derived from a rectilinear vortex advancing in a fluid in a direction normal to the vortex axis [43]. According to Bernoulli's theorem, the sum of the static, dynamic and hydrostatic pressure is a constant along a streamline. Note that the hydrostatic component is assumed to be zero for a hydrofoil. Therefore, it can be concluded that the pressure must decrease when the velocity of the fluid decreases.

$$p + \frac{1}{2}\rho V^2 + \rho g z = constant \tag{A.1a}$$

$$p + \frac{1}{2}\rho V^2 = constant \tag{A.1b}$$

Assuming a uniform flow around the foil, an upward vortex forms at the trailing edge due to viscous effects. Initially, this vortex flows down to the trailing edge and forward along the boundary layer, looping back when it meets the stagnation point. As the stagnation point moves backwards, part of the rear vortex is squeezed below the trailing edge, establishing a circulation flow around the entire airfoil. According to the Kutta condition, the flow must leave the trailing edge smoothly, needing a specific circulation leading to a clockwise circulation around the foil. This circulating flow reduces the incoming flow on the lower side and accelerates the flow on the upper side of the foil [52]. Leading to a decrease of the static pressure on the suction side and an increase on the pressure side. The overall flow around the foil combines the uniform incoming and circulating flow; see Figure A.1.

The resultant lift force is perpendicular to the incoming flow and has the magnitude:

$$L = \rho V \Gamma \tag{A.2}$$

The relation between circulation and the lift coefficient of a foil section can be expressed as:

$$\Gamma = C_{L_{2D}} c \frac{V}{2} \tag{A.3}$$

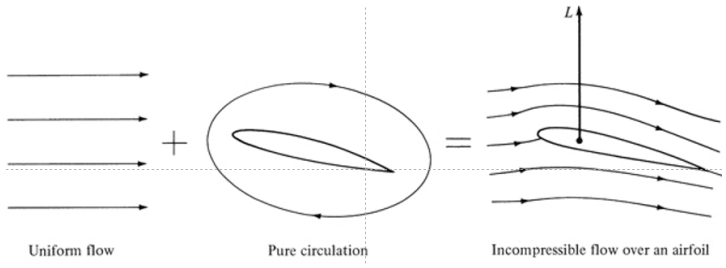

Figure A.1: Superposition of flow around a foil

A.1.1. Thin foil theory

The thin foil theory simplifies the Kutta-Joukowki Theorem for a thin airfoil of known geometry. This theory is based on the following assumptions: [4]

- Thickness is much smaller than the chord length ($t << c$)
- Angle of attack is small
- Analysis is based on the camber line
- Pressure distribution is linearized
- Flow is inviscid, incompressible and is attached

With these assumptions, the flow around a thin foil can be modelled by considering the components of the lifting force. This includes the lift due to the effect of the camber and the angle of attack. The lift generated by the angle of attack can be computed by solving the boundary conditions on the airfoil surface. By using potential flow theory, the circulation is found to be:

$$\Gamma_\alpha = \pi c V \alpha \tag{A.4}$$

By combining Equation A.4 and Equation A.3, the non-dimensional lift component is computed. Note that the theory is limited as it assumes a linear relation ($sin(\alpha) \approx \alpha$) between lift and angle of attack. Therefore, as mentioned before, the flow separation is not accounted for.

$$C_{L_{2D}} = 2\pi\alpha \tag{A.5}$$

For a cambered foil, the lift curve is shifted by an angle α_0. This particular angle is called the zero-lift angle of attack, at which it produces no lift. The circulation due to the camber can be related to α_0:

$$\Gamma_f = -\pi c V \alpha_0 \tag{A.6}$$

The total lift coefficient is the sum of the effect of the angle of attack and the camber. This gives the following expression: [43]

$$C_{L_{2D}} = C_{L_\alpha} + C_{L_{camber}} \tag{A.7}$$

$$C_{L_{2D}} = 2\pi(\alpha - \alpha_0) \tag{A.8}$$

A.2. Lifting-line theory

Prandtl's lifting-line theory is an analytical method to predict the aerodynamic properties of a finite wing [53]. The theorem is based on the concept of representing the wing by a series of horseshoe vortices superimposed along the span as illustrated in Figure A.2.

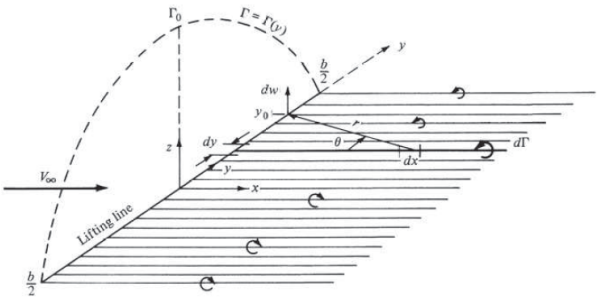

Figure A.2: Superposition of an infinite number of horseshoe vortices along the lifting line. Reprinted from Anderson [53].

The theory states that for an elliptic lift distribution along the foil span, the result is a constant value of downwash or induced angle along the span as shown in Figure A.3. [43]

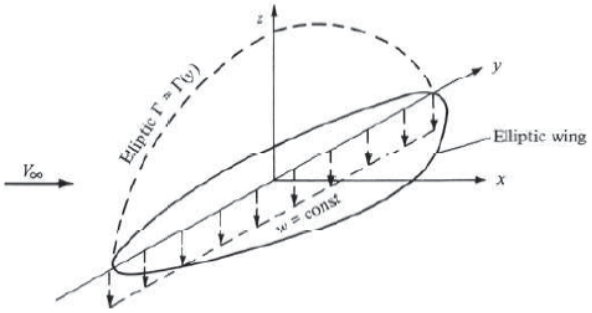

Figure A.3: Elliptic loading and constant downwash. Reprinted from Anderson [53].

For this specific case, the derived value of the induced angle and induced drag are the following:

$$\alpha_i = \frac{C_{L_{2D}}}{\pi AR} \tag{A.9a}$$

$$C_{D_{3D}} = C_L \alpha_i = \frac{C_{L_{3D}}^2}{\pi AR} \tag{A.9b}$$

Where $AR = s/c$ is the aspect ratio, and s is the total span of the airfoil. For a surface piercing hydrofoil $s = h$, the submergence depth is h.

The expression of the two-dimensional lift coefficient can be modified by considering the induced angle. Thus,

$$C_{L_{3D}} = 2\pi \left(\alpha - \frac{C_{L_{2D}}}{\pi AR} \right) \tag{A.10a}$$

$$C_{L_{3D}} = \frac{C_{L_{2D}}}{1 + \frac{2}{AR}} \tag{A.10b}$$

A.3. Foil Characteristics

A.3.1. Characteristic Graphs of a foil

A typical variation of the lift coefficient with the angle of attack is shown in Figure A.4. At low to moderate angles of attack, the lift coefficient varies linearly with α [53]. The slope of this line is called the lift slope. The flow is considered attached in this region as it moves smoothly over the foil surface. As the angle of attack increases, the flow separates from the top surface of the foil, caused by viscous effects [54]. The lift coefficient will increase until a sudden drop in lift and an increase in drag are observed [5]. Under such conditions, the airfoil is said to be stalled [53]. The stall angle (α_s) is the angle of attack at which the airfoil stalls. The maximum value of C_L achieved just before the stall is determined as the maximum lift coefficient C_{Lmax} [53].

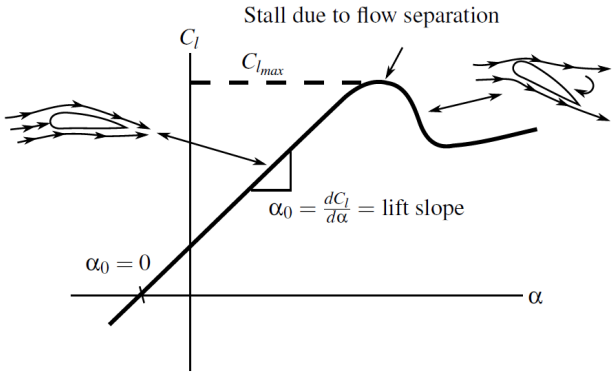

Figure A.4: Schematic of lift-coefficient variation with angle of attack for an airfoil. Figure reproduced from Anderson[53].

The variation of the drag coefficient is denoted as linear for small angles of attack. As the angle increases, the drag rises because of increased frontal area and boundary layer thickness [53]. At post-stall angles, the flow separation causes a large wake behind the airfoil, significantly increasing the pressure drag. This leads to a sharp increase in drag [55].

The moment coefficient tends to have a negative slope and is in the negative region for the typical range of angle of attack. This characteristic is designed to be as close as zero to ensure equilibrium on the airfoil. The moment coefficient is zero for a symmetrical foil at the aerodynamic centre [4].

Figure A.5 illustrates the typical variation of lift-to-drag ratio versus angle of attack. This parameter is a measurement of the aerodynamic efficiency of an airfoil. A higher ratio indicates a more efficient foil that produces more lift for a given drag amount. The AOA at which the ratio has a maximum is depicted as the operational angle of attack. As the AOA increases above the stall point, the ratio decreases due to the increase in drag.

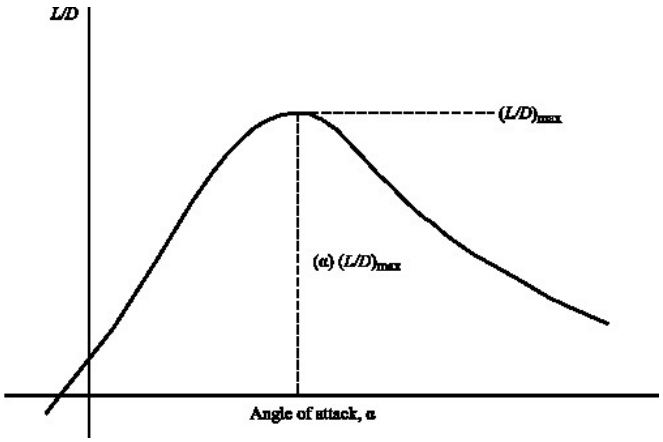

Figure A.5: Schematic of the variation of lift-to-drag ratio with angle of attack. Reprinted with modifications from Anderson et al. [53]

Shape Characteristics

An introduction to the most relevant shape-related parameters of a foil is given. These parameters are the nose radius ratio R/c, thickness ratio t/c, camber, camber location and trailing edge angle.

The nose radius (R) is the curvature radius of the LE. This parameter influences the flow behaviour around the foil. A larger nose radius tends to smooth out the flow for high Reynolds Numbers, reducing sharp velocity gradients and delaying flow separation [56]. On the other hand, Kermeen [57] experiments showed that a more prominent nose radius was associated with an increase in drag force and a decrease in lift-drag ratio for low Reynolds Numbers. This was observed in non-cavitating and cavitating flows. According to Kermeen [57], larger nose radii also decrease the cavitation number. Hoerner [52] defined, for the maximum lift, the optimum nose radius as a percentage of the chord length (R/c) to be between 1.5% and 2.0%. This applies to foils with a thickness between 6 and 18%. Hoerner [52] also found that for sharper leading edges, there is a decrease in the lift and an earlier boundary layer transition. In addition, Rothblum et al. [11] stated that in undisturbed flow, the ventilation resistance would increase with increasing sharpness of the nose. At low speeds, the sharpest model created unexpected ventilation when acted upon by a transient disturbance. This reflects that sharper lean edges induce flow separation at low velocities and angles. Other works indicate that separation on foils with sharp leading edges is of the laminar type (thin-airfoil type) and is primarily a function of the angle attack [58, 59, 60, 61].

The thickness ratio (t/c) is the maximum thickness of the foil divided by its chord length. Hoerner's experiments determined a reduction in lift for conventional foils at a thickness ratio above 10% or 12%. Hoerner considered conditions with a high Reynolds number ($Re > 10^5$) [52]. These findings are supported by Kumar, who observed a decrease in lift with an increase in thickness above the critical (t/c) [62]. The primary effect of the thickness ratio is on drag; increasing this parameter raises skin friction due to a larger surface area, and pressure drag due to a more significant pressure difference. Kumar also noted that higher thickness ratios delay flow separation at high Reynolds numbers. Additionally, Perry stated that an increased thickness ratio increases the chances of ventilation inception. [18].

The camber of a foil is defined as the maximum separation between the mean line and the chord line [43]. This parameter increases the lift compared to a symmetrical foil shift at the zero-lift angle, meaning that a smaller angle of attack is needed to produce lift in a cambered

foil [52, 4]. Additionally, cambered foils avoid the pressure peak at and above the leading edge in symmetrical sections. However, these peaks can prevent laminar separation by making the boundary layer turbulent under high loads. Hoerner states that a camber of 1% to 2% can improve the performance of a foil [52]. Experiments conducted by Hoerner indicate that placing the maximum camber between 30% and 50% of the chord length maximizes lift, with no significant distinction in the lift coefficient within this range [52].

The shape and design of an airfoil's trailing edge significantly affect its aerodynamic characteristics. The trailing edge configuration can be sharp or blunt. The trailing edge angle (TE angle) is crucial in sharp configurations. The edge can be further classified within blunt configurations as blunt or round.

The typical shape of streamlined bodies for such subsonic speeds is such that the after-body is more slender than the fore-body. This avoids or postpones separation [52]. A round trailing edge leads to a separated turbulent wake, which results in increased pressure drag [53]. In contrast, a sharp TE is essential for optimizing aerodynamic efficiency [52]. The lift-curve slope tends to reduce as the trailing edge increases. At angles between 16° and 22°, the lift-curve slope can switch from positive to negative [52]. This behaviour is observed at high Reynolds number ($Re > 10^6$).

Blunt trailing edges have an effect opposite to that of large TE angles. The angle included by the upper and lower surfaces naturally reduces when the trailing edge is thickened. This design can improve lift characteristics, especially at small angles of attack, which is crucial for control surfaces like ailerons. A blunt trailing edge can increase the lift-curve slope compared to a sharp trailing edge. For instance, Hoerner [52] experiments showed that a section with a blunt edge experienced a 10% increase in lift-curve slope in two-dimensional conditions and a 5% increase in lift for the tested wing section.

Harwood [2] noted that blunt trailing edges eliminate adverse pressure gradients and wetted flow separation, confining air ingress to the area near the leading edge. Additionally, base ventilation was observed, providing an alternate path for air at moderate angles of attack and high speeds. This process influenced the location of vortex aeration in tip-vortex-induced formations. Similarly, Thomareis [63] investigated the effect of a blunt trailing edge on separated flow characteristics. This study noted that periodic vortex shedding occurs at the trailing edge. This shedding, resulting from global instability, has an upstream effect that forces the separating shear layer.

Surface Characteristic

The influence of surface roughness on foils has been extensively studied, showing increased drag. According to experiments performed by Beierle [64], for a NACA 0015 airfoil with standard leading edge roughness, the minimum drag coefficient increased by 63% compared to a smooth airfoil. This increase in drag is attributed to the roughness causing a premature transition from laminar to turbulent flow, which increases the boundary layer thickness and thus the skin friction drag [22, 53].

Rothblum et al. [65, 22] noted that applying roughness to a surface-piercing strut reduced the AoA at which ventilation prompts for a given speed. This effect was strengthened with increasing roughness and speed. Wetzel [9] observed the same trends with increasing roughness.

B

Construction Drawings

B.1. Semi-Ogive Hydrofoil

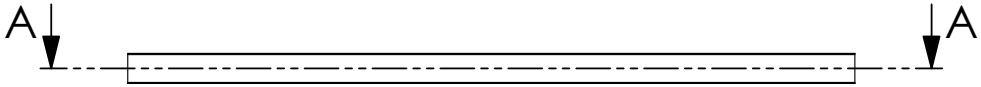

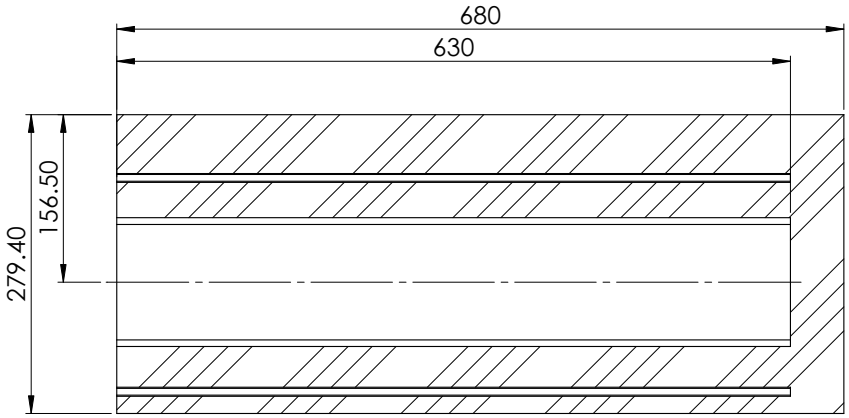

A-A

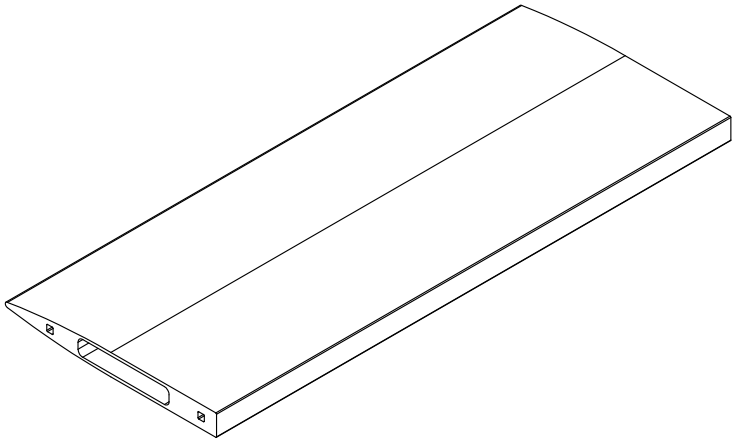

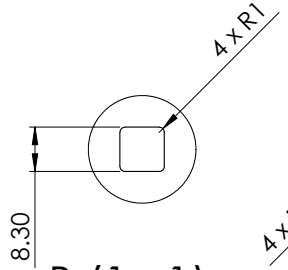

B (1 : 1)

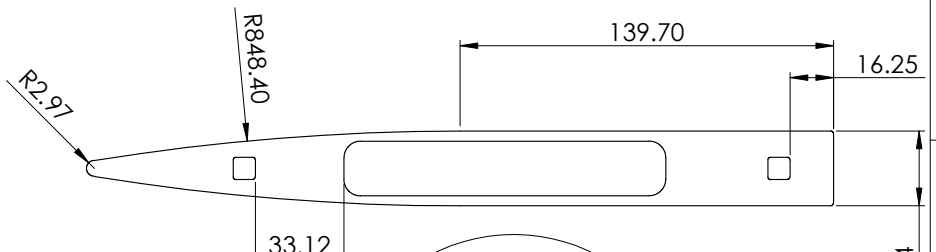

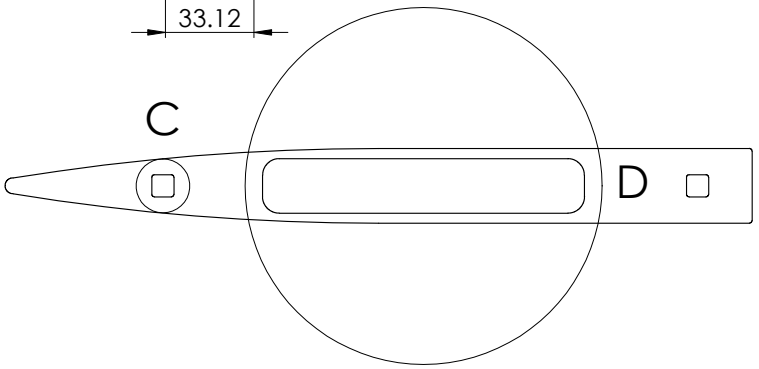

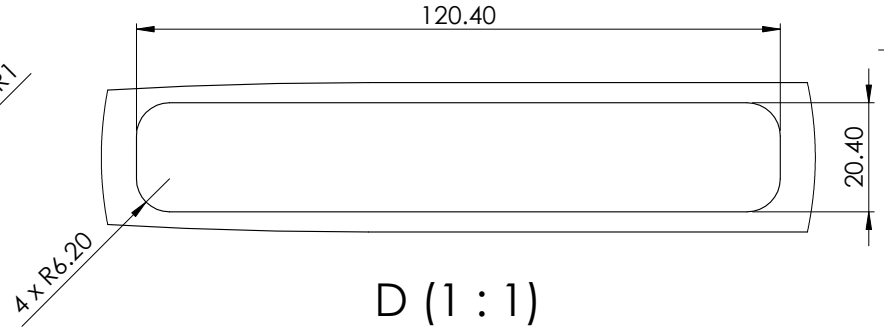

D (1 : 1)

Material: Not specified	This drawing and any information or descriptive material set out on it are the confidential and copyright property of ***Delft University of Technology***. © and MUST NOT BE DISCLOSED, COPIED, LOANED in whole or part or used for any purpose without the written permission of ***Delft University of Technology***.	Description: Component	
Finish: Not specified			
Unless Otherwise Stated: Linear Tol.: ±0.2, Angular Tol.: 0 °15' Surface Finish: 0.8µm All Dimensions: mm	Document Type: Hydrofoil Body	Drawn by: Carlos Navas Rodríguez	Drawn Date: 14/02/2024
Drawing Scale: 1:5	Company Confidential	Checked/Approved by: Carlos Navas Rodríguez	Checked/Approved Date: 14/02/2024
Approx Weight: Kg; Drawing Produced In Accordance With: ISO 2768	Legal Owner: TU Delft	Part Number: 1	
Projection Method: FRIST ANGLE; Sheet Size: A3		Drawing Number: 1	Sheet: 1 of 1; Revision: 1

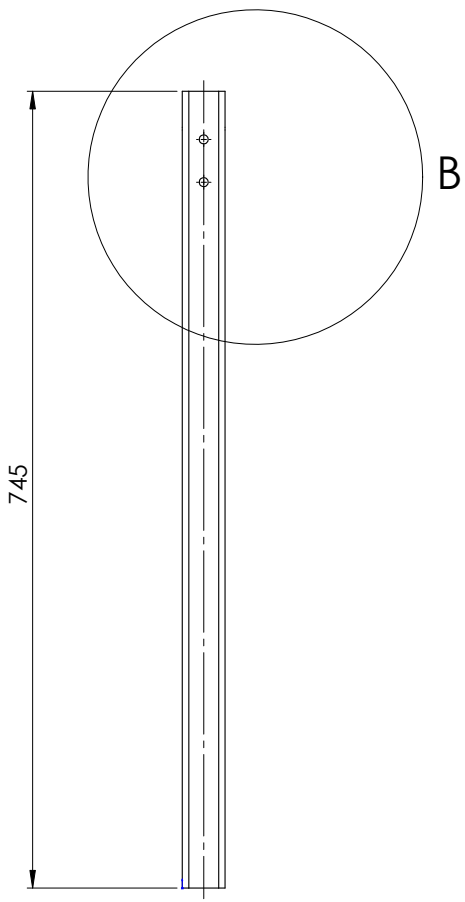

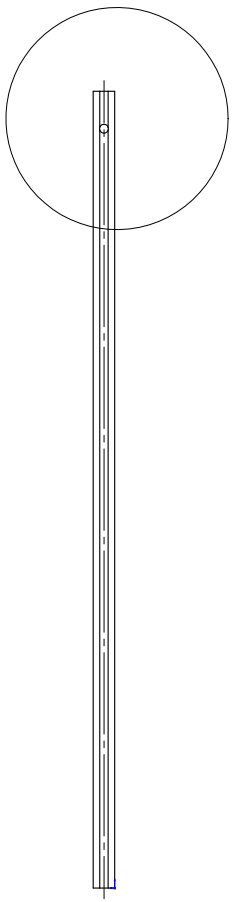

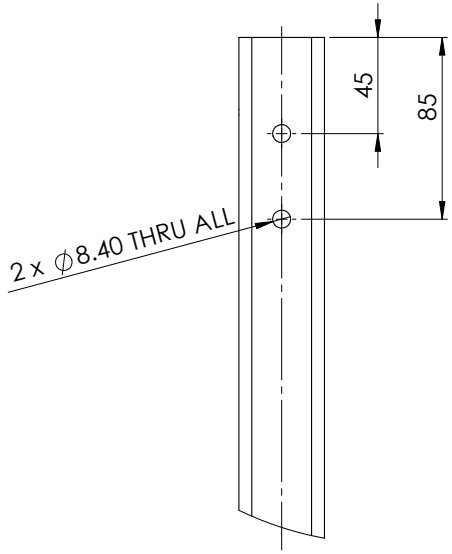

Detail B
Scale 2 : 5

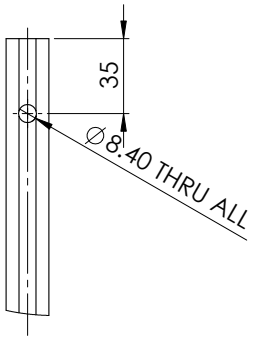

Detail C
Scale 2 : 5

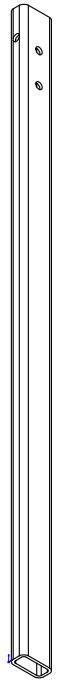

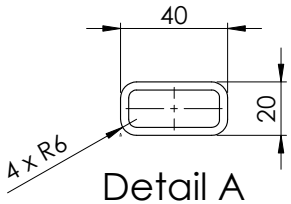

Detail A
Scale 1 : 2

A

Material: Acero aleado	This drawing and any information or descriptive material set out on it are the confidential and copyright property of ***Delft University of Technology***. © and MUST NOT BE DISCLOSED, COPIED, LOANED in whole or part or used for any purpose without the written permission of ***Delft University of Technology***.	Description: Component	
Finish: Not specified			
Unless Otherwise Stated: Linear Tol.: ±0.2, Angular Tol.: 0°15' Surface Finish: 0.8µm All Dimensions: mm	Document Type: Hydrofoil Spar	Drawn by: Carlos Navas Rodríguez	Drawn Date: 14/02/2024
Drawing Scale: 1:5	Company Confidential	Checked/Approved by: Carlos Navas Rodríguez	Checked/Approved Date: 14/02/2024
Approx Weight: 2.09 Kg; Drawing Produced In Accordance With: ISO 2768	Legal Owner: TU Delft	Part Number: 2	
Projection Method: FRIST ANGLE; Sheet Size: A3		Drawing Number: 2	Sheet: 1 of 1; Revision: 1

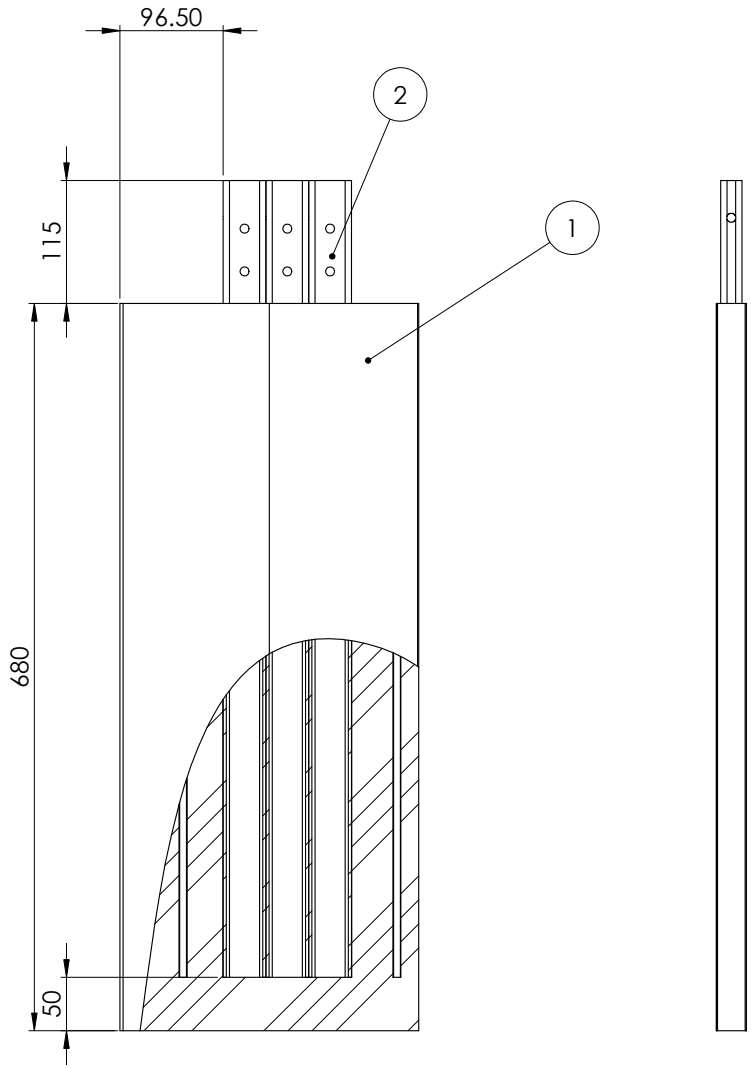

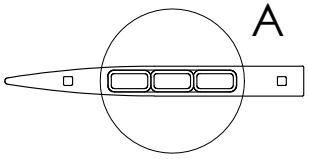

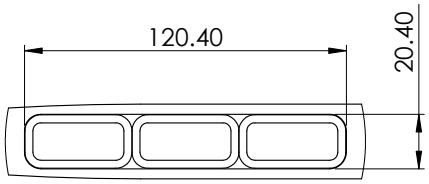

Detail A
Scale 1 : 2

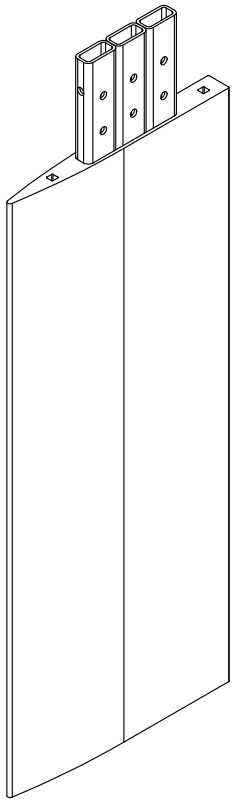

ITEM N°	PART NUMBER	DESCRIPTION	QTY.
1	Foil	Hydrofoil Body	1
2	steelbar		3

Material: **Not specified**
Finish: **Not specified**
Unless Otherwise Stated:
Linear Tol.: **±0.2**, Angular Tol.: **0 °15'**
Surface Finish: **0.8µm**
All Dimensions: **mm**
Drawing Scale: **1:5**
Approx Weight: Kg
Drawing Produced In Accordance With: **ISO 2768**
Projection Method: **FRIST ANGLE**
Sheet Size: **A3**

This drawing and any information or descriptive material set out on it are the confidential and copyright property of ***Delft University of Technology***. © and MUST NOT BE DISCLOSED, COPIED, LOANED in whole or part or used for any purpose without the written permission of ***Delft University of Technology***.

Document Type: **Hydrofoil Assembly**
Company Confidential
Legal Owner: TU Delft

Description:
Drawn by: **Carlos Navas Rodríguez**
Drawn Date: 14/02/2024
Checked/Approved by: Carlos Navas Rodríguez
Checked/Approved Date: 14/02/2024
Part Number: 4
Drawing Number: 4
Sheet: **1 of 1**
Revision: 1

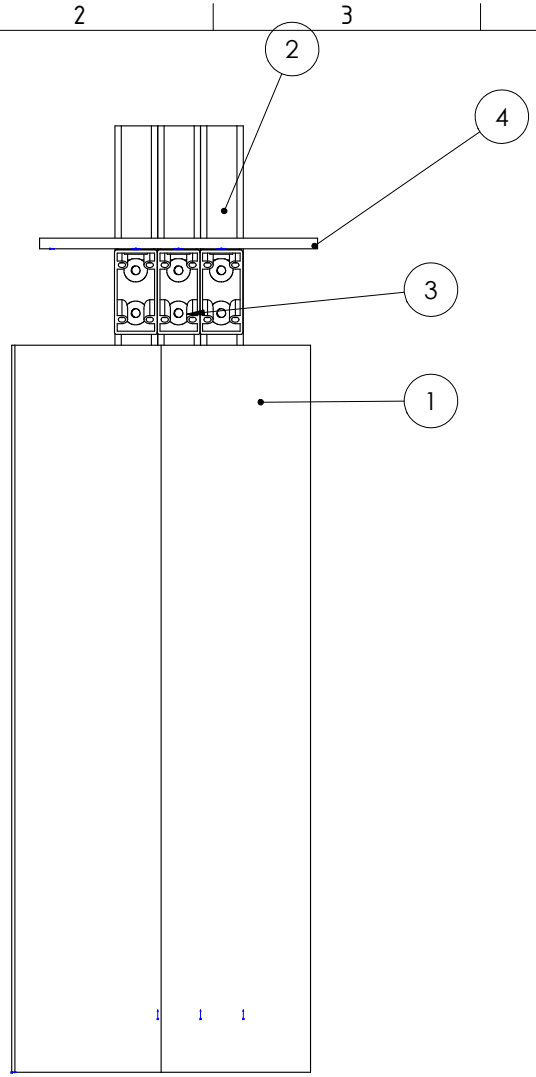

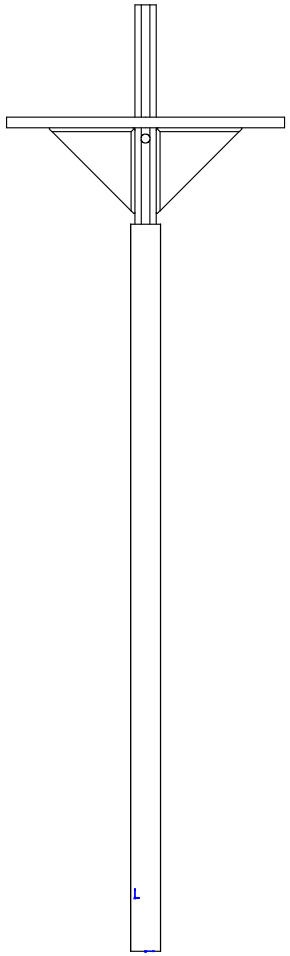

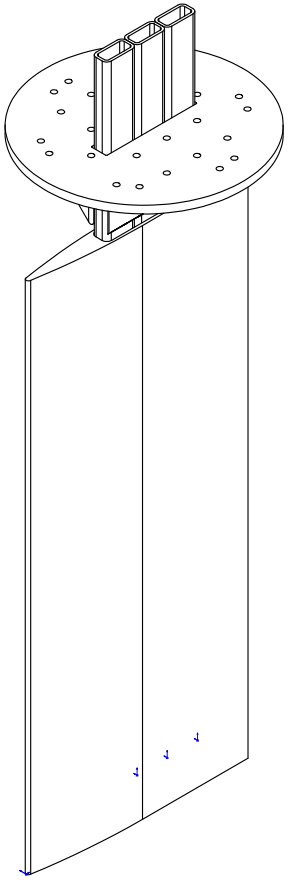

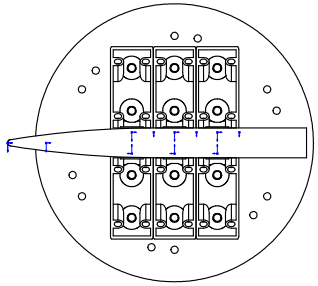

ITEM N°	PART NUMBER	DESCRIPTION	QTY.
1	Foil	Hydrofoil Body	1
2	steelbar		3
3	angle bracket	Item 0.0411.23	6
4	hydrofoil flange		1

Material: **Not specified**

Finish: **Not specified**

Unless Otherwise Stated:
Linear Tol.: **±0.2**, Angular Tol.: **0 °15'**
Surface Finish: **0.8µm**
All Dimensions: **mm**

Drawing Scale: **1:5**

Approx Weight: Kg

Drawing Produced In Accordance With: **ISO 2768**

Projection Method: **FRIST ANGLE**

Sheet Size: **A3**

This drawing and any information or descriptive material set out on it are the confidential and copyright property of ***Delft University of Technology***. © and MUST NOT BE DISCLOSED, COPIED, LOANED in whole or part or used for any purpose without the written permission of ***Delft University of Technology***.

Document Type: **Hydrofoil set up**

Company Confidential

Legal Owner: TU Delft

Description:

Drawn by: **Carlos Navas Rodríguez**

Drawn Date: 14/02/2024

Checked/Approved by: Carlos Navas Rodríguez

Checked/Approved Date: 14/02/2024

Part Number: 3

Drawing Number: 3

Sheet: **1 of 1**

Revision: 1

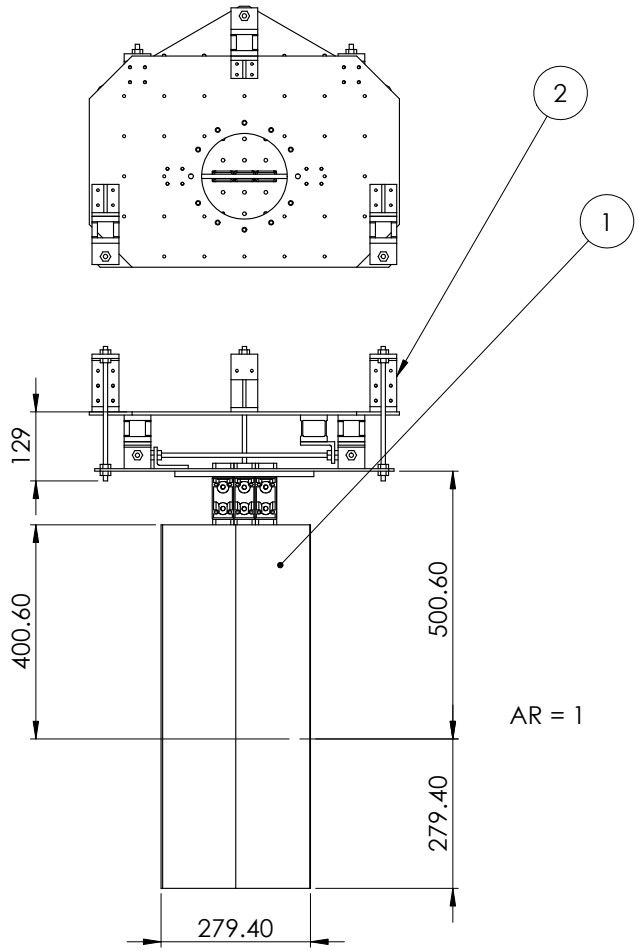

AR = 1

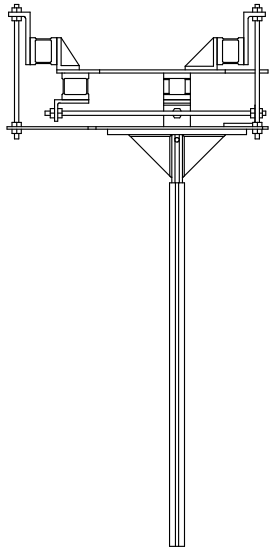

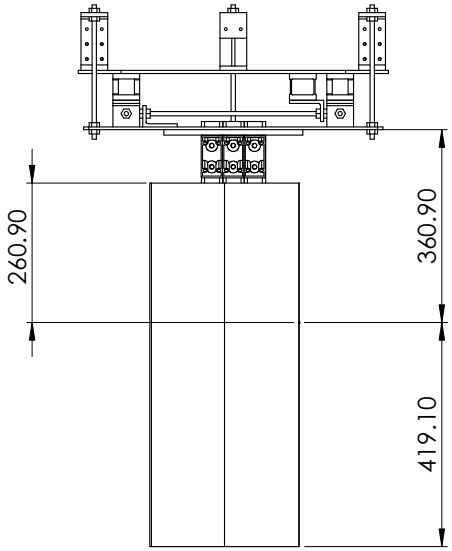

AR = 1.5

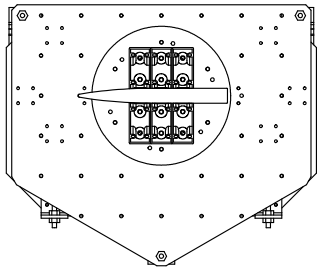

Minimum of 0.5c of foil above water
Minimum clearance 0.75c
Water level: 2.2m

ITEM N°	PART NUMBER	DESCRIPTION	QTY.
1	Hydrofoil setup		1
2	Force Balance		1

Material: **Not specified**

Finish: **Not specified**

Unless Otherwise Stated:
Linear Tol.: **±0.2**, Angular Tol.: **0 °15'**
Surface Finish: **0.8µm**
All Dimensions: **mm**

Drawing Scale: **1:10**

Approx Weight: Kg

Drawing Produced In Accordance With: **ISO 2768**

Projection Method: **FRIST ANGLE**

Sheet Size: **A3**

This drawing and any information or descriptive material set out on it are the confidential and copyright property of ***Delft University of Technology***. © and MUST NOT BE DISCLOSED, COPIED, LOANED in whole or part or used for any purpose without the written permission of ***Delft University of Technology***.

Document Type: **Experimental setup**

Company Confidential

Legal Owner: TU Delft

Description:

Drawn by: **Carlos Navas Rodríguez**

Drawn Date: 14/02/2024

Checked/Approved by: Carlos Navas Rodríguez

Checked/Approved Date: 14/02/2024

Part Number: 4

Drawing Number: 4

Sheet: **1 of 1**

Revision: 1

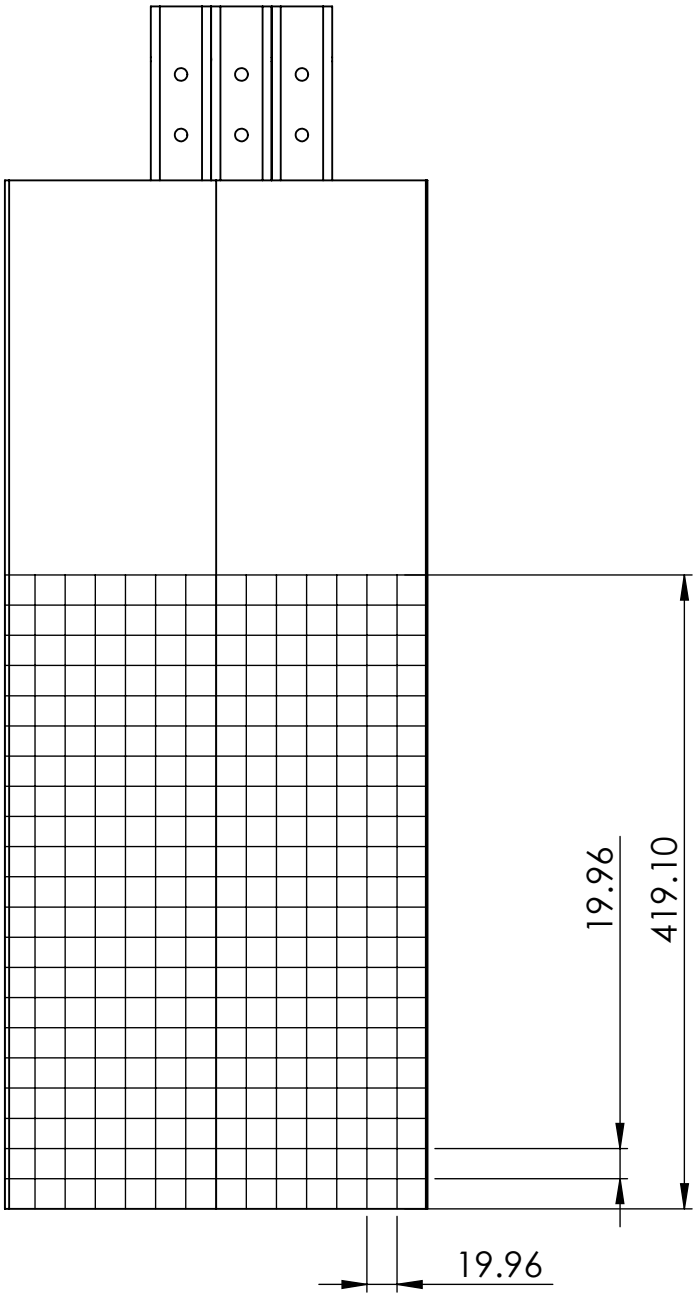

Material: Not specified	This drawing and any information or descriptive material set out on it are the confidential and copyright property of *Delft University of Technology*. © and MUST NOT BE DISCLOSED, COPIED, LOANED in whole or part or used for any purpose without the written permission of *Delft University of Technology*.	Description: Component	
Finish: Not specified			
Unless Otherwise Stated: Linear Tol.: ±0.2, Angular Tol.: 0°15' Surface Finish: 0.8µm All Dimensions: mm	Document Type: Hydrofoil Grid	Drawn by: Carlos Navas Rodríguez	Drawn Date: 11/03/2024
Drawing Scale: 1:5	Company Confidential	Checked/Approved by: Carlos Navas Rodríguez	Checked/Approved Date: 11/03/2024
Approx Weight: Kg; Drawing Produced In Accordance With: ISO 2768	Legal Owner:	Part Number: 4	
Projection Method: FRIST ANGLE; Sheet Size: A4		Drawing Number: 4	Sheet: 1 of 1; Revision: 1

TUDelft

B.2. NACA0010-34 Hydrofoil

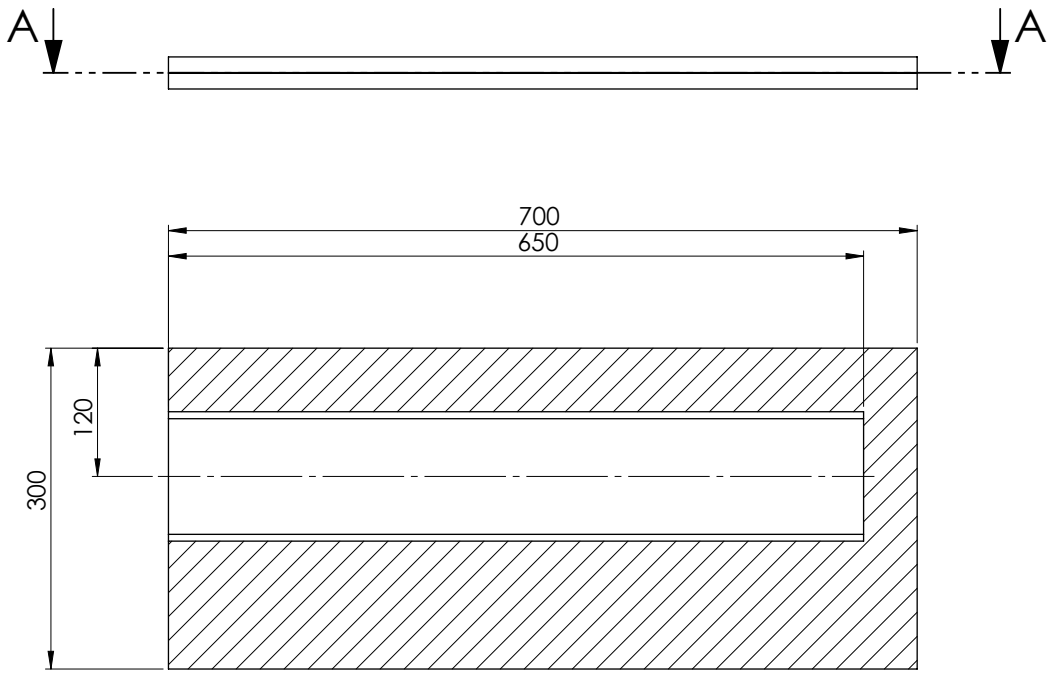

SECTION A-A
SCALE 1 : 5

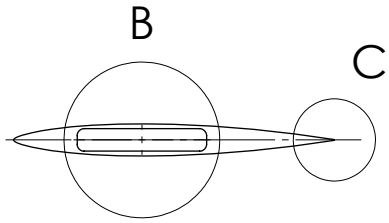

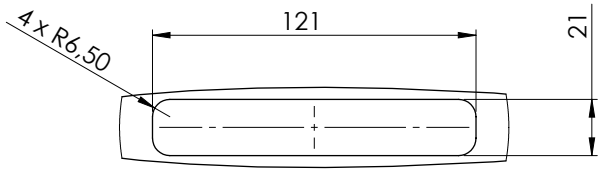

DETAIL B
SCALE 1 : 2

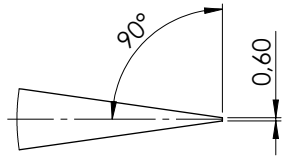

DETAIL C
SCALE 1 : 1

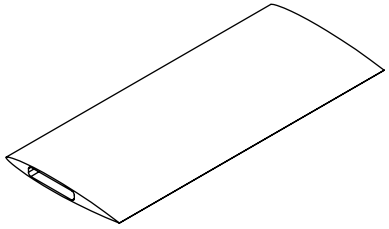

Responsible dept. Process & Energy	Technical reference Manuel Ferreira	Document type Component	Document status Development design	Material Material <not specified>
TU Delft	Created by Manuel Ferreira	Title hydrofoil-body	Tolerance ISO 2768	Weight
	Aproved by Manuel Ferreira		Projection method: Firstangle	Scale 1:5
This drawing and any information or descriptive material set out on it are the confidential and copyright property of Delft University of Technology and MUST NOT BE DISCLOSED, COPIED, LOANED in whole or part or used for any purpose without the written permission of Delft University of Technology.			Rev 1	Date of issue dinsdag 13 februari 2024
			Lang English	Sheet 1 / 1

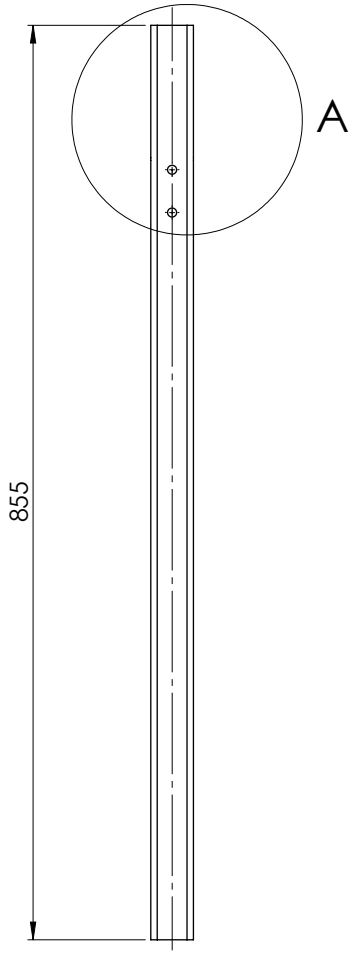

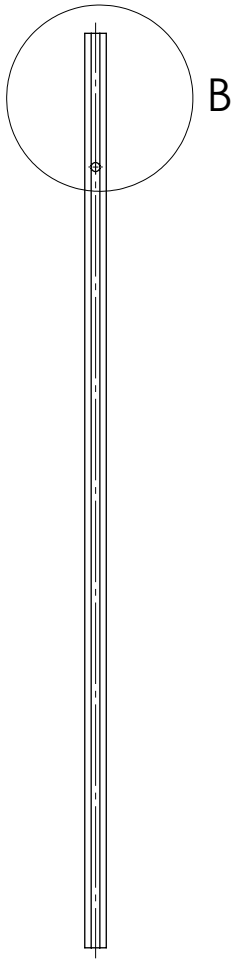

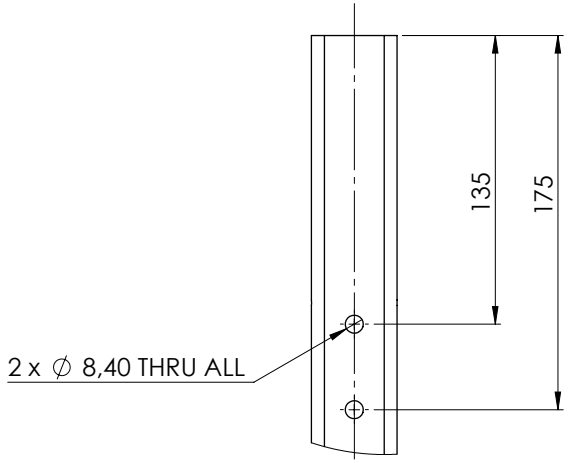

DETAIL A
SCALE 2 : 5

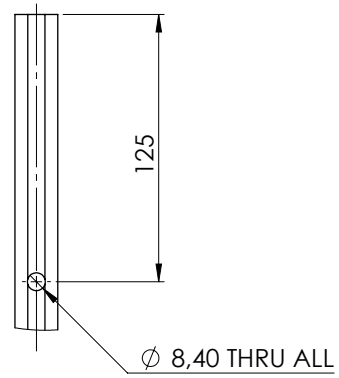

DETAIL B
SCALE 2 : 5

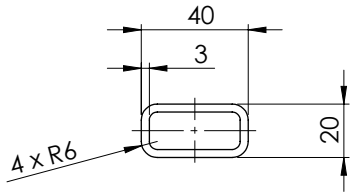

DETAIL C
SCALE 1 : 2

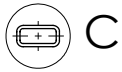

Responsible dept. Process & Energy	Technical reference Manuel Ferreira	Document type Component	Document status Development design	Material Alloy Steel
TU Delft	Created by Manuel Ferreira	Title hydrofoil-spar	Tolerance ISO 2768	Weight 1972.79
	Aproved by Manuel Ferreira		Projection method: Firstangle	Scale 1:5

This drawing and any information or descriptive material set out on it are the confidential and copyright property of Delft University of Technology and MUST NOT BE DISCLOSED, COPIED, LOANED in whole or part or used for any purpose without the written permission of Delft University of Technology.

Rev	Date of issue	Lang	Sheet
1	dinsdag 13 februari 2024	English	1 / 1

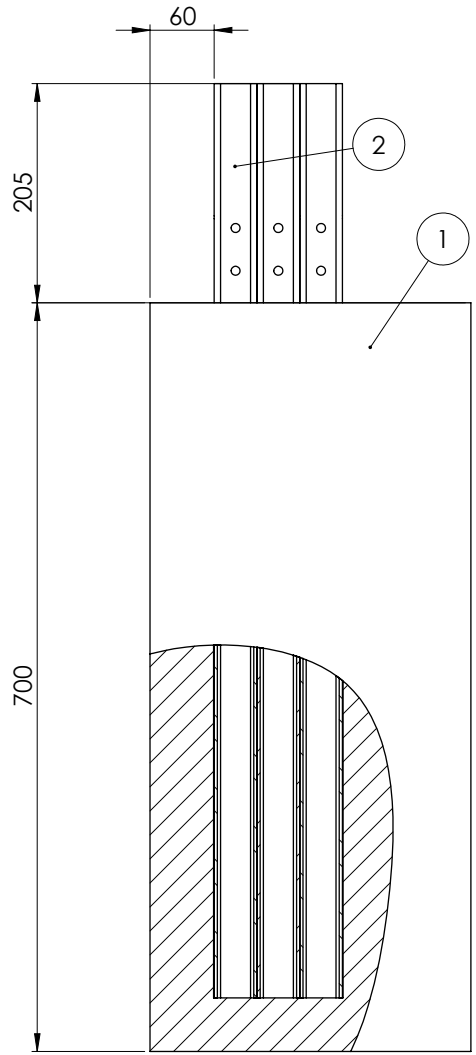

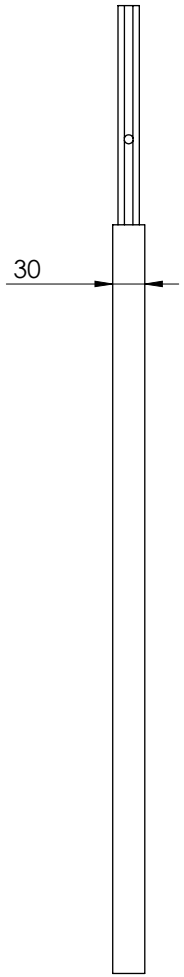

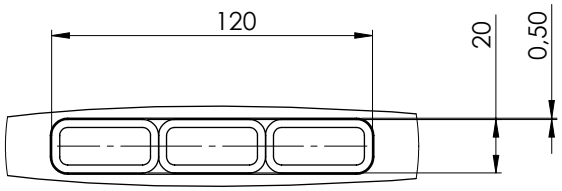

DETAIL A
SCALE 1 : 2

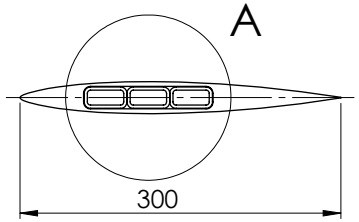

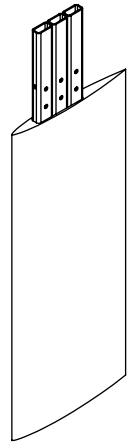

ITEM NO.	PART NUMBER	DESCRIPTION	QTY.
1	hydrofoil-body		1
2	hydrofoil-spar		3

Responsible dept. Process & Energy	Technical reference Manuel Ferreira	Document type Sub-assembly level 1	Document status Development design	Material Material <not specified>
TU Delft	Created by Manuel Ferreira	Title hydrofoil-A	Tolerance ISO 2768	Weight
	Aproved by Manuel Ferreira		Projection method: Firstangle	Scale 1:5

This drawing and any information or descriptive material set out on it are the confidential and copyright property of Delft University of Technology and MUST NOT BE DISCLOSED, COPIED, LOANED in whole or part or used for any purpose without the written permission of Delft University of Technology.

Rev	Date of issue	Lang	Sheet
1	dinsdag 13 februari 2024	English	1 / 1

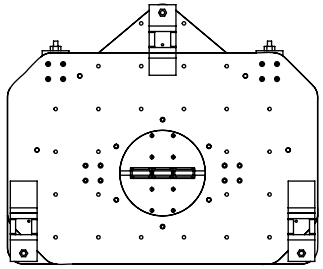

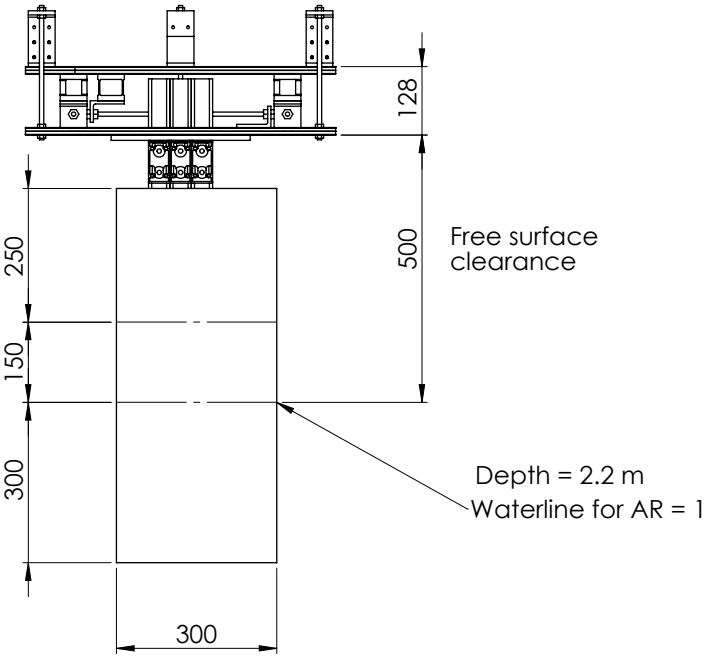

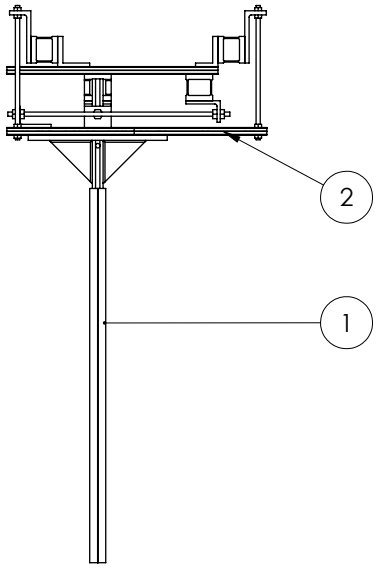

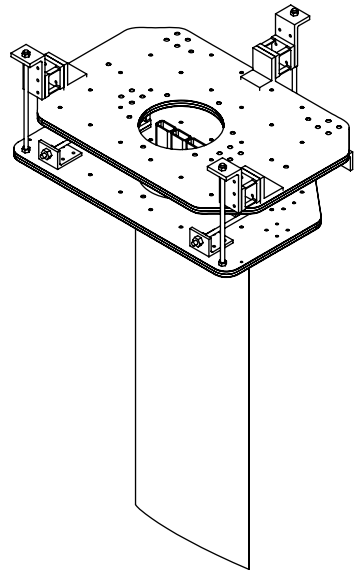

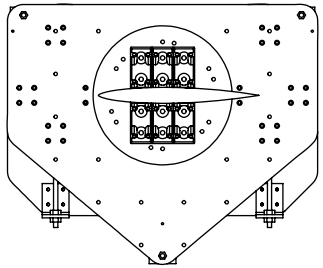

ITEM NO.	PART NUMBER	DESCRIPTION	QTY.
1	hydrofoil-A		1
2	force_balance-force_balance		1

Responsible dept. Process & Energy	Technical reference Manuel Ferreira	Document type Sub-assembly level 1	Document status Development design	Material Material <not specified>
TU Delft	Created by Manuel Ferreira	Title experimental_setup-A	Tolerance ISO 2768	Weight
	Aproved by Manuel Ferreira		Projection method: Firstangle	Scale 1:10

This drawing and any information or descriptive material set out on it are the confidential and copyright property of Delft University of Technology and MUST NOT BE DISCLOSED, COPIED, LOANED in whole or part or used for any purpose without the written permission of Delft University of Technology.

Rev	Date of issue	Lang	Sheet
1	dinsdag 13 februari 2024	English	1 / 1

C

Experimental Run Log

Table C.1: Run list - Fixed Angle of Attack

Date	Time	Run	Zero	Model	AR	α_0	α_t	Fn	Speed	Turnover	Rate of change	P	Water temp	Comments	Flow regime	Inception
-	-	-	-	-	-	deg	deg	-	m/s		deg/s	hPa	C	-	-	deg
26-03-2024	13:20	1002	1001	Ogive	1.00	0	0	1.50	2.48	30	0.30	1013	16.4		FW	
26-03-2024	13:56	1004	1003	Ogive	1.00	4	4	1.50	2.48	30	0.30	1013	16.4		FW	
26-03-2024	14:50	1006	1005	Ogive	1.00	8	8	1.50	2.48	30	0.30	1013	16.4		FW	
27-03-2024	8:29	1008	1007	Ogive	1.00	12	12	1.50	2.48	30	0.30	1013	16.4		FW	
27-03-2024	9:00	1010	1009	Ogive	1.00	14	14	1.50	2.48	30	0.30	1013	16.4		FW	
27-03-2024	9:55	1012	1011	Ogive	1.00	16	16	1.50	2.48	30	0.30	1013	16.4		FV	
27-03-2024	10:29	1014	1013	Ogive	1.00	18	18	1.50	2.48	30	0.30	1013	16.4		FV	
27-03-2024	11:34	1016	1015	Ogive	1.00	15	15	1.50	2.48	30	0.30	1013	16.4		FV	
04-04-2024	11:44	1102	1101	Ogive	1.50	0	0	1.50	3.04	30	0.36	999	16.6		FW	
04-04-2024	12:16	1104	1103	Ogive	1.50	4	4	1.50	3.04	30	0.36	999	16.6		FW	
04-04-2024	12:45	1106	1105	Ogive	1.50	8	8	1.50	3.04	30	0.36	999	16.6		FW	
04-04-2024	13:51	1108	1107	Ogive	1.50	12	12	1.50	3.04	30	0.36	999	16.6	LaVision camera one (ID 22324380) lagging.	FV	
04-04-2024	14:31	1110	1109	Ogive	1.50	14	14	1.50	3.04	30	0.36	999	16.6	LaVision camera one (ID 22324380) lagging.	FV	
04-04-2024	15:16	1112	1111	Ogive	1.50	16	16	1.50	3.04	30	0.36	999	16.6	LaVision camera one (ID 22324380) lagging.	FV	
04-04-2024	16:00	1114	1113	Ogive	1.50	18	18	1.50	3.04	30	0.36	999	16.6	LaVision camera one (ID 22324380) lagging.	FV	
04-04-2024	16:40	1116	1115	Ogive	1.50	11	11	1.50	3.04	30	0.36	999	16.6		FW	
10-04-2024	12:08	2004	2003	NACA	1.00	0.0	0.0	1.50	2.57	30	0.29	1029	17.1		FW	
10-04-2024	12:30	2006	2005	NACA	1.00	4.0	4.0	1.50	2.57	30	0.29	1029	17.1	LaVision live mode on triggered Basler before recording started.	FW	
10-04-2024	13:06	2008	2007	NACA	1.00	8.0	8.0	1.50	2.57	30	0.29	1029	17.10		FW	
10-04-2024	13:39	2010	2009	NACA	1.00	12.0	12.0	1.50	2.57	30	0.29	1029	17.10		FW	
10-04-2024	14:13	2012	2011	NACA	1.00	14.0	14.0	1.50	2.57	30	0.29	1029	17.10		FW	
10-04-2024	14:44	2014	2013	NACA	1.00	16.0	16.0	1.50	2.57	30	0.29	1029	17.10		FW	
10-04-2024	15:17	2016	2015	NACA	1.00	18.0	18.0	1.50	2.57	30	0.29	1029	17.10	LaVision camera one (ID 22324380) lagging. Pulse stretcher not working (faulty cable).	FV	
10-04-2024	15:49	2018	2017	NACA	1.00	20.0	20.0	1.50	2.57	30	0.29	1029	17.10	LaVision camera one (ID 22324380) lagging. Wave probe ventilating throughout.	FV	
16-04-2024	15:53	2082	2081	NACA	1.50	0.0	0.0	1.50	3.15	30	0.35	999	16.7		FW	
16-04-2024	16:22	2084	2083	NACA	1.50	4.0	4.0	1.50	3.15	30	0.35	999	16.7		FW	
16-04-2024	16:56	2086	2085	NACA	1.50	8.0	8.0	1.50	3.15	30	0.35	999	16.7		FW	
17-04-2024	8:26	2088	2087	NACA	1.50	12.0	12.0	1.50	3.15	30	0.35	1013	17.0	Ignore first set of pictures. LaVision camera one (ID 22324380) lagging.	FW	
17-04-2024	8:52	2090	2089	NACA	1.50	14.0	14.0	1.50	3.15	30	0.35	1013	17.0		FW	
17-04-2024	9:56	2092	2091	NACA	1.50	16.0	16.0	1.50	3.15	30	0.35	1013	17.0		FW	
17-04-2024	10:27	2094	2093	NACA	1.50	18.0	18.0	1.50	3.15	30	0.35	1013	17.0	LaVision camera one (ID 22324380) lagging.	FV	
17-04-2024	11:09	2096	2095	NACA	1.50	20.0	20.0	1.50	3.15	30	0.35	1013	17.0	LaVision camera one (ID 22324380) lagging.	FV	

Table C.2: Run List - Angle of Attack Quasi-Static Variation

Date	Time	Run	Zero	Model	AR	α_0	α_t	Fn	Speed	Turnover	Rate of change	P	Water temp	Comments	Flow regime	Inception
-	-	-	-	-	-	deg	deg	-	m/s		deg/s	hPa	C	-	-	deg
27-03-2024	12:16	1018	1017	Ogive	1.00	12	20	0.50	0.83	30	0.10	1013	16.4	Pump setting: 40 rpm, (x, y) = (1000, 0), pump 2mm, dropplet 2 mm.	PV	
27-03-2024	13:35	1020	1019	Ogive	1.00	8	16	0.50	0.83	30	0.10	1013	16.4	Pump setting: 40 rpm, (x, y) = (1000, 0), pump 2mm, dropplet 2 mm.	PV	13.49
27-03-2024	14:22	1022	1021	Ogive	1.00	8	16	0.50	0.83	30	0.10	1013	16.4	Pump setting: 40 rpm, (x, y) = (1000, 0), pump 2mm, dropplet 2 mm.	PV	13.30
27-03-2024	15:10	1024	1023	Ogive	1.00	8	16	0.50	0.83	30	0.10	1013	16.4	Pump setting: 40 rpm, (x, y) = (1000, 0), pump 2mm, dropplet 2 mm.	PV	13.60
27-03-2024	15:40	1026	1025	Ogive	1.00	8	16	0.50	0.83	30	0.10	1013	16.4	Pump setting: 40 rpm, (x, y) = (1000, 0), pump 2mm, dropplet 2 mm.	PV	13.30
02-04-2024	15:05	1060	1059	Ogive	1.00	12	20	0.75	1.24	30	0.15	1002	16.4	Basler cameras not available (trigger issue).	PV	16.34
02-04-2024	15:31	1062	1061	Ogive	1.00	12	20	0.75	1.24	30	0.15	1002	16.4		PV	17.14
02-04-2024	15:52	1064	1063	Ogive	1.00	12	18	0.75	1.24	30	0.15	1002	16.4		PV	16.41
02-04-2024	16:22	1066	1065	Ogive	1.00	12	18	0.75	1.24	30	0.15	1002	16.4	Basler cameras not available.	PV	15.73
02-04-2024	16:54	1068	1067	Ogive	1.00	12	18	0.75	1.24	30	0.15	1002	16.4	Full video at 50 Hz.	PV	17.44
03-04-2024	14:44	1028	1027	Ogive	1.00	12	24	1.00	1.66	30	0.20	1013	16.4	Full video at 50 Hz.	PV	21.95
27-03-2024	17:10	1030	1029	Ogive	1.00	14	24	1.00	1.66	30	0.20	1013	16.4	Pump setting: 10 rpm, (x, y) = (300, 0), pump 2mm, dropplet 1 mm.	PV	22.45
28-03-2024	11:45	1032	1031	Ogive	1.00	12	24	1.00	1.66	30	0.20	984	16.1	Pump setting: 10 rpm, (x, y) = (300, 0), pump 2mm, dropplet 1 mm.	PV	23.11
28-03-2024	12:44	1034	1033	Ogive	1.00	12	24	1.00	1.66	30	0.20	984	16.1	Pump setting: 10 rpm, (x, y) = (300, 0), pump 2mm, dropplet 1 mm.	PV	22.78
28-03-2024	13:15	1036	1035	Ogive	1.00	12	24	1.00	1.66	30	0.20	984	16.1	Pump setting: 10 rpm, (x, y) = (300, 0), pump 2mm, dropplet 1 mm.	PV	23.05
02-04-2024	12:23	1054	1053	Ogive	1.00	12	27	1.25	2.07	25	0.30	1002	16.4		FV	25.96
02-04-2024	13:25	1056	1055	Ogive	1.00	13	28	1.25	2.07	25	0.30	1002	16.4		FV	25.87
02-04-2024	14:00	1058	1057	Ogive	1.00	13	28	1.25	2.07	25	0.30	1002	16.4		FV	27.38
03-04-2024	11:55	1080	1079	Ogive	1.00	13	28	1.25	2.07	25	0.30	1002	16.2	Full video at 50 Hz.	FV	26.41
03-04-2024	12:30	1082	1081	Ogive	1.00	13	28	1.25	2.07	25	0.30	1002	16.2	Cameras not available (trigger issue).	FV	26.59
03-04-2024	15:14	1038	1037	Ogive	1.00	12	28	1.50	2.48	20	0.44	1002	16.2	Full video at 50 Hz.	FV	27.11
28-03-2024	16:12	1040	1039	Ogive	1.00	12	28	1.50	2.48	20	0.44	984	16.1	Pump setting: 15 rpm, (x, y) = (375, -25), pump 2mm, dropplet 1 mm.	FV	27.09
28-03-2024	16:45	1042	1041	Ogive	1.00	12	28	1.50	2.48	20	0.44	984	16.1	Pump setting: 15 rpm, (x, y) = (375, -25), pump 2mm, dropplet 1 mm.	FV	26.58
02-04-2024	8:47	1044	1043	Ogive	1.00	12	28	1.50	2.48	20	0.44	1002	16.4	Pump setting: 15 rpm, (x, y) = (375, -25), pump 2mm, dropplet 1 mm.	FV	26.66
02-04-2024	9:15	1046	1045	Ogive	1.00	12	28	1.50	2.48	20	0.44	1002	16.4		FV	27.34
03-04-2024	8:23	1070	1069	Ogive	1.00	12	28	1.75	2.90	20	0.52	1002	16.2		FV	26.24
03-04-2024	8:58	1072	1071	Ogive	1.00	12	28	1.75	2.90	20	0.52	1002	16.2		FV	25.67
03-04-2024	9:37	1074	1073	Ogive	1.00	12	28	1.75	2.90	20	0.52	1002	16.2		FV	26.75
03-04-2024	10:32	1076	1075	Ogive	1.00	12	28	1.75	2.90	20	0.52	1002	16.2	Basler camera not available. Frame rate 50 Hz.	FV	26.33
03-04-2024	11:14	1078	1077	Ogive	1.00	12	28	1.75	2.90	20	0.52	1002	16.2	Full video at 50 Hz.	FV	26.06
02-04-2024	9:57	1048	1047	Ogive	1.00	12	29.5	2.00	3.31	20	0.59	1002	16.4		FV	26.03
02-04-2024	10:44	1050	1049	Ogive	1.00	12	28	2.00	3.31	20	0.59	1002	16.4		FV	26.38
02-04-2024	11:37	1052	1051	Ogive	1.00	12	28	2.00	3.31	20	0.59	1002	16.4		FV	26.36
03-04-2024	13:01	1084	1083	Ogive	1.00	12	28	2.00	3.31	20	0.59	1002	16.2	Cameras not available (lights off).	FV	26.24
03-04-2024	13:32	1086	1085	Ogive	1.00	12	28	2.00	3.31	20	0.59	1002	16.2	Full video at 100 Hz.	FV	26.00
03-04-2024	14:04	1088	1087	Ogive	1.00	13	28	2.25	3.73	20	0.67	1002	16.2	Full video at 100 Hz.	FV	24.74
03-04-2024	16:13	1090	1089	Ogive	1.00	12	26	2.50	4.14	20	0.74	1002	16.2	Full video at 100 Hz. Decelerated before completing the measurement.	FV	23.63
03-04-2024	16:55	1092	1091	Ogive	1.00	12	26	2.50	4.14	20	0.74	1002	16.2	Full video at 100 Hz.	FV	23.28
04-04-2024	8:30	1094	1093	Ogive	1.00	12	18	0.75	1.24	30	0.15	999	16.6	Full video at 50 Hz. LaVision camera 1 missing (it was not configured).	PV	16.57
04-04-2024	9:25	1096	1095	Ogive	1.00	8	16	0.50	0.83	30	0.10	999	16.6	Full video at 25 Hz.	PV	13.36
04-04-2024	9:53	1098	1097	Ogive	1.00	13	28	1.25	2.07	25	0.30	999	16.6	Cameras not available (trigger issue). Insufficient data at a steady AoA.	FV	26.68
04-04-2024	10:24	1100	1099	Ogive	1.00	12	28	2.00	3.31	20	0.59	999	16.6	Full video at 100 Hz. LaVision camera one (ID 22324380) trigger issue. Insufficient data at a steady AoA.	FV	25.80

Date	Time	Run	Zero	Model	AR	α_0	α_t	Fn	Speed	Turnover	Rate of change	P	Water temp	Comments	Flow regime	Inception
-	-	-	-	-	-	deg	deg	-	m/s		deg/s	hPa	C	-	-	deg
11-04-2024	11:37	2028	2027	NACA	1.00	10.0	18.0	0.50	0.86	30	0.10	1029	16.80	Full video at 50 Hz.	PV	16.72
11-04-2024	14:08	2036	2035	NACA	1.00	12.0	20.0	0.50	0.86	30	0.10	1029	16.80		PV	16.92
11-04-2024	14:40	2038	2037	NACA	1.00	12.0	20.0	0.50	0.86	30	0.10	1029	16.80		PV	16.26
15-04-2024	9:01	2048	2047	NACA	1.00	15.0	26.0	0.75	1.29	30	0.14	1028	17.10	Full video at 50 Hz.	PV	17.78
15-04-2024	9:51	2050	2049	NACA	1.00	12.0	22.0	0.75	1.29	30	0.14	1028	17.10		PV	17.78
15-04-2024	10:10	2052	2051	NACA	1.00	12.0	22.0	0.75	1.29	30	0.14	1028	17.10	Cameras not available (trigger issue).	PV	17.51
11-04-2024	12:10	2030	2029	NACA	1.00	16.0	28.0	1.00	1.72	30	0.19	1029	16.8	Full video at 50 Hz.	PV	25.00
11-04-2024	12:49	2032	2031	NACA	1.00	15.0	26.0	1.00	1.72	30	0.19	1029	16.80		PV	24.50
11-04-2024	12:49	2034	2032	NACA	1.00	15.0	26.0	1.00	1.72	30	0.19	1029	16.80		PV	24.36
15-04-2024	11:14	2054	2053	NACA	1.00	16.0	29.0	1.25	2.14	25	0.29	1029	16.80	Full video at 50 Hz.	FV	28.60
15-04-2024	11:48	2056	2055	NACA	1.00	16.0	29.5	1.25	2.14	25	0.29	1029	16.80		FV	28.11
15-04-2024	12:30	2058	2057	NACA	1.00	16.0	29.5	1.25	2.14	25	0.29	1029	16.80		FV	29.17
10-04-2024	17:10	2020	2019	NACA	1.00	14.0	28.0	1.50	2.57	25	0.34	1029	17.10	Full video at 50 Hz.	FV	26.78
11-04-2024	9:52	2022	2021	NACA	1.00	16.0	29.0	1.50	2.57	25	0.34	1029	16.80		FV	27.19
11-04-2024	16:15	2044	2043	NACA	1.00	16.0	28.0	1.50	2.57	25	0.34	1029	16.80		FV	25.72
11-04-2024	16:47	2046	2045	NACA	1.00	16.0	28.0	1.50	2.57	25	0.34	1029	16.80		FV	27.75
11-04-2024	10:49	2026	2025	NACA	1.00	14.0	29.0	1.50	2.57	20	0.43	1029	16.80		FV	26.66
15-04-2024	13:09	2060	2059	NACA	1.00	16.0	28.0	1.50	2.57	25	0.34	1028	17.10		FV	26.55
15-04-2024	13:45	2062	2061	NACA	1.00	16.0	28.0	1.50	2.57	25	0.34	1028	17.10		FV	27.27
15-04-2024	14:22	2064	2063	NACA	1.00	16.0	28.0	1.75	3.00	25	0.40	1028	17.10	Full video at 50 Hz. LaVision camera one (ID 22324380) lagging.	FV	26.83
15-04-2024	15:01	2066	2065	NACA	1.00	16.0	28.0	1.75	3.00	25	0.40	1028	17.10		FV	26.22
16-04-2024	8:23	2072	2071	NACA	1.00	16.0	28.0	1.75	3.00	25	0.40	999	16.7		FV	25.70
11-04-2024	10:24	2024	2023	NACA	1.00	15.0	29.0	2.00	3.43	20	0.57	1029	16.80	Full video at 100 Hz.	FV	24.77
11-04-2024	15:15	2040	2039	NACA	1.00	15.0	26.0	2.00	3.43	25	0.46	1029	16.80	Full video at 100 Hz.	FV	24.45
11-04-2024	15:46	2042	2041	NACA	1.00	15.0	26.0	2.00	3.43	25	0.46	1029	16.80	Full video at 100 Hz.	FV	24.03
15-04-2024	15:39	2068	2067	NACA	1.00	15.0	26.0	2.25	3.86	20	0.64	1028	17.10	Full video at 100 Hz.	FV	23.49
16-04-2024	8:50	2074	2073	NACA	1.00	15.0	26.0	2.25	3.86	20	0.64	999	16.70	Cameras not available (trigger issue).	FV	22.82
16-04-2024	9:34	2076	2075	NACA	1.00	15.0	26.0	2.25	3.86	20	0.64	999	16.70	Full video at 100 Hz.	FV	22.00
16-04-2024	10:14	2078	2077	NACA	1.00	15.0	26.0	2.25	3.86	20	0.64	999	16.70	Full video at 100 Hz.	FV	22.63
15-04-2024	16:20	2070	2069	NACA	1.00	15.0	24.0	2.50	4.29	20	0.71	1028	17.10	Full video at 100 Hz. LaVision camera one (ID 22324380) lagging.	FV	22.23
16-04-2024	11:31	2080	2079	NACA	1.00	15.0	24.0	2.50	4.29	20	0.71	999	16.70	Full video at 100 Hz. LaVision camera one (ID 22324380) lagging.	FV	21.93
18-04-2024		2130	2129	NACA	1.00	14.0	24.0	2.50	4.29	20	0.71	1019	16.90	Full video at 100 Hz.	FV	23.12

Date	Time	Run	Zero	Model	AR	α_0	α_t	Fn	Speed	Turnover	Rate of change	P	Water temp	Comments	Flow regime	Inception
-	-	-	-	-	-	deg	deg	-	m/s		deg/s	hPa	C	-	-	deg
05-04-2024	8:26	1118	1117	Ogive	1.50	10	20	0.75	1.52	30	0.18	1006	16.6		PV	18.05
05-04-2024	13:52	1132	1131	Ogive	1.50	11	20	0.75	1.52	30	0.18	1006	16.6	Full Video 50 Hz	PV	18.44
05-04-2024	14:40	1134	1133	Ogive	1.50	11	20	0.75	1.52	30	0.18	1006	16.6	Cameras not available	PV	18.01
05-04-2024	16:31	1136	1135	Ogive	1.50	11	20	0.75	1.52	30	0.18	1006	16.6		PV	18.28
05-04-2024	17:00	1138	1137	Ogive	1.50	11	20	0.75	1.52	30	0.18	1006	16.6	Cameras not available	PV	18.38
05-04-2024	9:22	1120	1119	Ogive	1.50	11	28.0	1.00	2.03	20	0.36	1006	16.6		PV	24.82
08-04-2024	9:07	1140	1139	Ogive	1.50	11	28	1.00	2.03	20	0.36	1006	17.1	Full video at 50 Hz.	PV	26.84
08-04-2024	9:38	1142	1141	Ogive	1.50	11	28	1.00	2.03	20	0.36	1006	17.1		PV	25.69
08-04-2024	10:12	1144	1143	Ogive	1.50	11	28	1.00	2.03	20	0.36	1006	17.1		PV	26.91
08-04-2024	10:42	1146	1145	Ogive	1.50	11	28	1.00	2.03	20	0.36	1006	17.1	LaVision camera one (ID 22324380) lagging.	PV	24.22
05-04-2024	9:58	1122	1121	Ogive	1.50	11	29	1.25	2.53	20	0.45	1006	16.6		PV-FV	25.74
08-04-2024	11:53	1148	1147	Ogive	1.50	11	28	1.25	2.53	20	0.45	1006	17.1	Full video at 50 Hz.	PV-FV	25.02
08-04-2024	12:28	1150	1149	Ogive	1.50	11	28	1.25	2.53	20	0.45	1006	17.1		PV-FV	25.13
08-04-2024	13:05	1152	1151	Ogive	1.50	11	28	1.25	2.53	20	0.45	1006	17.1		PV-FV	25.77
08-04-2024	13:41	1154	1153	Ogive	1.50	11	28	1.25	2.53	20	0.45	1006	17.1	LaVision camera one (ID 22324380) lagging.	PV-FV	25.68
05-04-2024	10:36	1124	1123	Ogive	1.50	11	29	1.50	3.04	20	0.54	1006	16.6	Pulse stretcher for sampling the trigger not working properly.	FV	24.82
05-04-2024	12:00	1128	1127	Ogive	1.50	11	28	1.50	3.04	20	0.54	1006	16.6	Full video at 50Hz.	FV	24.91
05-04-2024	12:33	1130	1129	Ogive	1.50	11	26	1.50	3.04	20	0.54	1006	16.6	Full video at 100 Hz.	FV	24.32
08-04-2024	15:29	1156	1155	Ogive	1.50	11	26	1.50	3.04	20	0.54	1006	17.1	Full video at 100 Hz.	FV	24.25
08-04-2024		1158	1157	Ogive	1.50	11	26	1.50	3.04	20	0.54	1006	17.1		FV	24.49
05-04-2024	11:31	1126	1125	Ogive	1.50	8	18	0.50	1.01	30	0.12	1006	16.6		PV	12.59
17-04-2024	11:51	2098	2097	NACA	1.50	14.0	24.0	0.75	1.58	30	0.18	1013	17.0	Full video at 50 Hz.	PV	20.89
18-04-2024	8:17	2114	2113	NACA	1.50	14.0	24.0	0.75	1.58	30	0.18	1019	16.9		PV	20.60
18-04-2024	8:51	2116	2115	NACA	1.50	14.0	24.0	0.75	1.58	30	0.18	1019	16.9		PV	20.27
17-04-2024	13:05	2100	2099	NACA	1.50	14.0	29.0	1.00	2.10	20	0.35	1013	17.0	Full video at 50 Hz.	PV	26.86
18-04-2024	9:30	2118	2117	NACA	1.50	14.0	28.0	1.00	2.10	20	0.35	1019	16.9		PV	26.67
18-04-2024	9:59	2120	2119	NACA	1.50	14.0	28.0	1.00	2.10	20	0.35	1019	16.9	LaVision camera one (ID 22324380) lagging.	PV	26.99
17-04-2024	13:48	2102	2101	NACA	1.50	14.0	29.0	1.25	2.63	20	0.44	1013	17.0	Full video at 50 Hz.	PV	22.52
17-04-2024	14:27	2104	2103	NACA	1.50	14.0	28.0	1.25	2.63	25	0.35	1013	17.0	Full video at 50 Hz.	PV	22.32
17-04-2024	15:09	2106	2105	NACA	1.50	14.0	28.0	1.25	2.63	25	0.35	1013	17.0		PV	22.98
17-04-2024	15:49	2108	2107	NACA	1.50	14.0	24.0	1.50	3.15	25	0.42	1013	17.0	Full video at 100 Hz.	FV	22.50
17-04-2024	16:32	2110	2109	NACA	1.50	14.0	24.0	1.50	3.15	25	0.42	1013	17.0	Full video at 100 Hz.	FV	23.67
17-04-2024	17:00	2112	2111	NACA	1.50	14.0	24.0	1.50	3.15	25	0.42	1013	17.0	Full video at 100 Hz.	FV	21.85
18-04-2024	10:34	2122	2121	NACA	1.50	12.0	20.0	0.50	1.05	30	0.12	1019	16.9		PV	14.30
18-04-2024	12:12	2124	2123	NACA	1.50	14.0	28.0	1.25	2.63	25	0.35	1019	16.9		PV	22.96
18-04-2024	12:56	2126	2125	NACA	1.50	14.0	28.0	1.25	2.63	25	0.35	1019	16.9		PV	22.55
18-04-2024	13:32	2128	2127	NACA	1.50	14.0	24.0	1.50	3.15	25	0.42	1019	16.9	Full video at 100 Hz.	FV	21.98
18-04-2024	16:16	2134	2133	NACA	1.50	14.0	24.0	1.50	3.15	25	0.42	1019	16.9		FV	21.88
18-04-2024	15:39	2132	2131	NACA	1.00	14.0	24.0	2.50	4.29	20	0.71	1019	16.9	Full video at 100 Hz.	PV	22.15
18-04-2024		2136	2135	NACA	1.50	14.0	25.0	1.75	3.68	20	0.61	1019	16.9		FV	22.91